ATTACHMENT A1

The California Public Utilities Commission

FINAL REPORT

Hydrogen Blending Impacts Study

Prepared by: University of California, Riverside
Principal Investigators:
Arun SK Raju, Ph.D.
Alfredo Martinez-Morales, Ph.D.

Subcontractor: Gas Technology Institute
Principal Investigator:
Oren Lever, Ph.D.

Prepared For: California Public Utilities Commission
Project Manager
Love Asiedu-Akrofi

Agreement Number: 19NS1662

TABLE OF CONTENTS

LIST OF FIGURES

Page

LIST OF TABLES

Page

EXECUTIVE SUMMARY

Background

California is committed to the reduction of greenhouse gases (GHGs) while simultaneously increasing renewables use in the energy sector. Renewable hydrogen is increasingly expected to play an important role as a renewable fuel in various sectors including transportation and industry also as an energy storage medium that can help the State transition to a carbon neutral economy. The existing natural gas storage, transmission, distribution, and end-use infrastructure has evolved over 200 years since early "town gas" systems. These early systems, which often consisted of greater than 50% hydrogen have transitioned into natural gas based systems storing, transporting, and supplying primarily methane, with small amounts of propane, ethane and other components allowed by standards. This project aims to determine the viability of blending hydrogen with natural gas in California's existing natural gas infrastructure based on existing information and targeted experimental and modeling work.

Project Purpose and Approach

This study, sponsored by the California Public Utilities Commission, assesses the operational and safety concerns associated with injecting hydrogen into the existing natural gas pipeline system at various percentages. in compliance with Senate Bill 1369 and the California Public Utilities Commission (CPUC) Rulemaking 13-02-008. Senate Bill 1369 requires CPUC to undertake specified actions to advance the state's clean energy and pollution reduction objectives, including, where feasible, cost effective, and consistent with other state policy objectives and that green electrolytic hydrogen is targeted for increased use.

Hydrogen has significantly different properties than methane including combustion properties and is known to have a degrading effect on a number of materials used in the natural gas infrastructure. The major areas of concern associated with hydrogen blending include:

- Maximum hydrogen percentage at which no or minor modifications are needed for natural gas infrastructure and end-use systems

- Types of modifications that may be required for higher percentages of hydrogen.

- Impacts on end-use appliances and safety implications

- Impacts, including degradation, on durability of the existing natural gas pipeline system

- Impacts on natural gas pipeline leakage rates

- Impacts on valves, fittings, materials, and welds due to hydrogen embrittlement

- Impacts on natural gas storage facilities

- Impacts on pipelines under cathodic protection

The project team conducted a review of relevant literature to identify materials and components requiring further investigation. The experimental and modeling work and analysis were then designed to address safety and performance concerns related to most commonly used materials and fill knowledge gaps.

Project efforts are identified and organized by task with subtasks focusing on specific areas of concern. The project tasks are listed below:

Task 1: Literature survey

Task 2: Potential impacts of mixed gas hydrogen injection on the natural gas infrastructure:

a. Modeling and/or experimental assessment of the potential impacts on natural gas pipeline leakage rates

b. Modeling assessment of the impacts, including degradation, on durability/integrity of the existing natural gas pipeline systems, including effects of transient/non-homogeneous gas compositions

c. Modeling and experimental assessment of any impacts on valves, fittings, materials, and welds due to hydrogen embrittlement

d. Degradation analysis

Task 3: Maximum hydrogen blending potential evaluation

Task 4: Presentations to the sponsor and stakeholders

Project Results

Safety and performance concerns associated with injecting hydrogen into the existing natural gas pipeline system at various percentages were assessed in order to develop recommendations on allowable hydrogen blending percentages and the next steps. The project focuses on three areas that are important towards developing a better understanding of the impacts of hydrogen on materials and components commonly used in the California natural gas pipeline network. A combination of literature review, modeling, and experimental work was performed in these areas:

1) Leakage rates of methane and hydrogen blends compared to pure methane,

2) Hydrogen impacts on polymeric materials, and

3) Hydrogen impacts on metals and alloys

A summary of the experimental and modeling analysis performed as part of the project is provided below:

- Assessment of components and systems – evaluation of hydrogen impacts on leakage rates, and on degradation and durability materials, components, and

systems. The project team conducted a review of relevant literature and data from ongoing efforts to identify materials, applications, and components requiring further investigation. These findings were summarized in the literature review and were used to design experimental and modeling tasks. The tasks were designed to focus on priority materials, components, and system conditions that require further analysis.

- Hydrogen blend leakage analysis – comparison and analysis of methane and hydrogen blend leakage rates under varying system conditions. The project team evaluated leakage rates using experimental and modeling techniques under varying hydrogen percentages, flow rates and system pressures. The results were compared against unblended methane leakage rates to evaluate deviations from natural gas leakage rates. The results show that blends with higher hydrogen percentages leak faster compared to methane, although hydrogen does not leak preferentially through orifices.

- Hydrogen impacts on metals and alloys – the project team exposed select metals and alloys used in the natural gas transmission systems to hydrogen through gaseous exposure and electrochemical charging. The exposed metal samples were then subjected to tensile strength tests and impact tests to assess material toughness, followed by characterization using a number of techniques. The results show that hydrogen charged steel samples showed characteristics of hydrogen induced embrittlement which affects the material's strength and toughness.

- Dynamic thermo-mechanical analysis – Dynamic thermo-mechanical analysis (DTMA) testing was performed on the MDPE material to obtain the shift-factors that allow translation of pressure test results obtained under elevated temperatures to equivalent performance under a reference (operating) temperature. The results suggest a reduction in the creep performance of the MDPE. Failure assessment to identify failure vs. safe condition for pipe system in the hydrogen environment was developed. The polymeric material results identify limitations in material integrity for mixtures of 20% hydrogen. The results also indicate that the pipe formation process may influence the susceptibility of polymeric materials and requires further investigation.

- Morphology and elemental analysis – the team performed morphological and elemental analysis to characterize hydrogen impacts on pipeline materials. Exposed materials were analyzed using optical microscopy and scanning electron microscopy. Surface, cross-sectional, and physically/mechanically damaged areas

were analyzed to identify hydrogen exposure related degradation. Elemental analysis using electron beam was conducted to understand and explore the degradation process and further characterize the influence of hydrogen on exposed materials.

Recommendations

Completion of the project tasks has led the project team to conclusions and recommendations that are influenced by many overlapping variables and conditions. A single injection standard that applies systemwide would have to consider the most susceptible conditions observed throughout all infrastructure components. This type of scenario would also be required to consider all end-uses, appliances, and associated industrial processes. This systemwide blending injection scenario becomes concerning as hydrogen blending approaches 5% by volume. As the percentage of hydrogen increases, end-use appliances may require modifications, vintage materials may experience increased susceptibility, and legacy components and procedures may be at increased risk of hydrogen effects.

Hydrogen blending into California's natural gas pipeline infrastructure can help accelerate the transition towards the use of clean hydrogen as a fuel and energy storage medium, and help the state meet a number of climate and air quality goals. However, the hydrogen blending must be carefully planned and conducted in stages to address the effect of hydrogen on materials, components, facilities, and equipment. As there are knowledge gaps in several areas, including those that cannot be addressed through modeling or laboratory scale experimental work, it is critical to conduct real world demonstration of hydrogen blending under safe and controlled conditions. Based on data from the literature and ongoing research and demonstration efforts, we make the following recommendations on the next steps. A three year timeline is proposed to complete these activities and the adopt a hydrogen blending standard.

	Year 1	Year 2	Year 3
A. Large Scale Demonstration		Lead: Utilities	
B. Laboratory R&D	Lead: R&D Organizations		
C. Planning Activities	Lead: State Agencies		
D. Stakeholder Engagement		Lead: State Agencies/Community Organizations	

Key Activities:
A. Demonstrations: Blending under real world conditions over extended periods, develop and demonstrate mitigation strategies to address safety and performance issues
B. R&D: Address knowledge gaps and assess higher hydrogen percentages blending, mitigation strategies, support demonstration activity
C. Planning: Develop inventories, update and develop specifications, safety/maintenance protocols, workforce development
D. Engagement: Understand priorities and concerns, outreach and consensus building

A discussion of the activities is provided below.

- Conduct demonstration of hydrogen blending in a section of the infrastructure that is isolated or is custom-built to include the commonly present materials, vintages, facilities, and equipment of the generic California natural gas infrastructure with appropriate maintenance, monitoring and safety protocols over extended periods. The recommended hydrogen percentages for this demonstration are 5 to 20%. Such demonstration projects will allow critical knowledge gaps to be filled, including the effect of parameters such as weather induced temperature changes, pressure cycling, length of exposure, effect of natural gas components and contaminants, and potential mitigation techniques.

- Conduct laboratory scale research and analysis to address critical technological and scientific issues and unknowns to provide support to the demonstration and deployment projects, with a specific focus on higher hydrogen percentage blends. The immediate focus should be on 0-20% and 20-50% hydrogen with longer term research focused on blends with higher than 50% hydrogen. The analysis should include the development of a comprehensive inventory of materials and equipment in the California natural gas infrastructure, along with available information on vintages, operational data, hydrogen tolerance levels and potential impacts. This inventory can be used to identify materials with known hydrogen related safety and performance concerns and materials that have not been assessed from a hydrogen blending perspective. Further research and analysis should be conducted to specifically evaluate potential impacts and mitigation strategies, maintenance procedures, and replacement timelines. Working groups consisting of different stakeholder sectors, including domestic and international entities involved in ongoing major research and demonstration efforts should be created to develop a hydrogen blending blueprint that creates a recommended timeline for injection standards; policies and procedures necessary to enable safe and planned hydrogen blending, potential hydrogen sources, and costs. The direct and indirect costs associated with the transition, including cost savings, environmental and public health benefits should be better understood.

- Engage the gas utilities, material and equipment manufacturers, suppliers, and regulatory agencies to anticipate hydrogen injection over a predetermined timeframe. The core activities would include updating existing manufacturing, procurement, installation, maintenance, and safety procedures, developing new procedures and protocols as needed; and developing and updating material and equipment specifications as needed. The group would also develop alternate strategies for portions of the infrastructure where hydrogen blending is not recommended in the near term (ex., select storage facilities and end use sectors). Activities will include workforce training and education.

- Engage stakeholder groups including community and environmental organizations, industry, government, academia, and the general public to provide perspectives on hydrogen blending, conduct outreach to address technological, societal, economic, and safety concerns and to build consensus on hydrogen production, storage, transport, and use including blending into the natural gas infrastructure.

Task 1: Literature Review

Maximum Hydrogen Blending Percentage Recommendation

Maximum hydrogen percentage at which no or minor modifications are needed for natural gas infrastructure and end-use systems

The maximum hydrogen gas blending concentration, at which no or only minor modifications of the existing natural gas infrastructure are required, depends greatly on many individual factors. These factors are related to the current natural gas processing and use, which involve gathering, storage, transmission, regulation, distribution, metering, and end-use applications.

Integrity of existing natural gas infrastructure is a primary concern due to hydrogen embrittlement in metals and degradation impacts on some elastomers. However, the impacts of hydrogen embrittlement with respect to integrity of the system depend on operating conditions such as pressure, temperature, and cycle loading, to name a few. Thus, it is more appropriate to use partial hydrogen gas pressure, rather than hydrogen concentration in the gas blend, when discussing impacts on material integrity upon subjection to hydrogen gas. Due to the plethora of different metal alloys and polymeric materials employed throughout the natural gas system and varying operating conditions, large scale demonstration projects would be required to evaluate impacts of hydrogen gas on all materials and components involved. Such projects could identify degradation effects of hydrogen on materials and evaluate the associated reduction in physical properties, and reduction in life-time in service or time-to-failure. At the very least, injection of hydrogen in the natural gas system, even at very small concentrations, would require modifications to existing integrity management systems, including monitoring and maintenance schedules and practices.

Safety is another major concern with hydrogen blending, mainly because hydrogen has a significantly lower ignition energy than natural gas, among other properties which also make it more hazardous. The primary concern is the probability of ignition in the case of large gas blend leaks or gas blend accumulation in confined spaces. Consequently, to reduce the probability of ignition, modifications to existing leak detection and leak repair procedures would be required.

Since hydrogen gas has very different physical and chemical properties compared to natural gas, if the concentration of hydrogen in the gas blend is increased significantly, major changes would be required in the transmission, distribution, regulation and metering processes. Likewise, major modifications of end-use equipment and appliances would be required due to differences in the combustion of hydrogen gas, and also the existing standards and regulations for fuel requirements. Due to strict requirements on gas turbines on fuel specifications, end-use equipment could be the

7

limiting factor of maximum concertation of hydrogen blending in the natural gas infrastructure, without any major modification.

Types of modifications that may be required for higher percentages of hydrogen

Larger concentration of hydrogen may present significant challenges to the operation of the natural gas infrastructure, since the energy content of natural gas is three times higher than that of hydrogen gas, thus a higher volumetric flow rate is required to deliver the same amount of energy with gas blends containing higher concentration of hydrogen. This can be accomplished by increasing operating pressure in the pipeline system, or replacing existing pipelines with larger ones.

End-use applications and equipment is another critical sector that would have to undergo significant modifications to accommodate operation with larger concentrations of hydrogen in the gas blend. For household appliances, upgrading burners and recertification may be required. While, in the case of gas turbines, gas engines, and industrial furnaces, more customized and specific modifications might be required.

Hydrogen Blending Impacts on End-use Appliances

Household appliances

There are several concerns with respect to the use of hydrogen-natural gas blends in household appliances, mainly from perspective of combustion process. One concern relates to potentially higher combustion temperatures with hydrogen-natural gas blends. With higher levels of hydrogen, the adiabatic combustion temperature of the fuel blend increases, given that other operational parameters remain constant. The resulting higher temperatures, can in turn, lead to local overheating of components, or lead to increased emissions of nitrogen oxides (NO_X) [1]. Another concern with hydrogen and natural gas blends is the increase in the laminar combustion velocity with addition of hydrogen, which poses a risk of potential flashbacks in household appliances [1].

Several studies have evaluated the maximum hydrogen blending concentration at which no major modifications would be required to end-use equipment [2]. These studies have indicated concentration of hydrogen blended in natural gas in the range of 5%-20% as acceptable, without significant impact on safety and operation of end-use appliances [2].

Engines

It has been reported that blends of compressed natural gas with hydrogen (HCNG), with concentrations of hydrogen from 0% to 20% can be used in a conventional internal combustion engines (ICE) without any tuning. Whereas, gas blends with more than 20% hydrogen require engine retuning and low swirl intakes to run optimally [3].

Experiments performed by the Bureau of Mines Research Center show that ICE ran normally with 20% hydrogen in the hydrogen and natural gas blend [4].

Genovese et al. performed study on urban transportation fueled by HCNG blends with 5%, 10%, 15%, 20% and 25% of hydrogen [5]. The experimental results showed positive performance of blended fuel with no noticeable impacts on the engine. The experiments also showed significant reduction in energy consumption with the blended fuel compared to the 100% methane gas fuel.

Hydrogen Blending Impacts, Including Degradation, on Durability of the Existing Natural Gas Pipeline System

In general the natural gas pipeline system consists of producing wells, gathering lines, transmission lines, compressor stations, pressure regulation stations, processing plants, storage facilities, city gates, distribution main lines, distribution service lines, metering equipment, and commercial/residential end-users as shown in Figure 1.

Figure 1: Natural Gas Pipeline System Overview
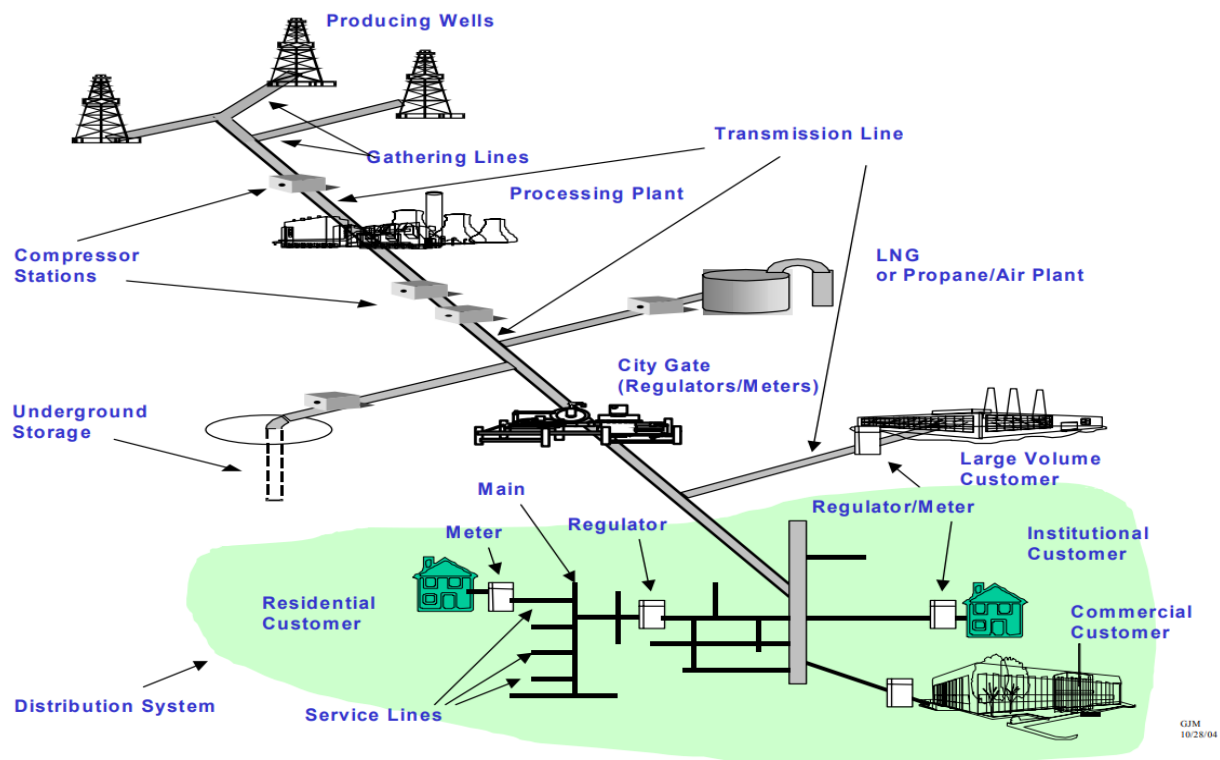
Source: AGF report "Safety Performance and Integrity of the Natural Gas Distribution Infrastructure"

Metals and Metal Alloy Materials

Title 49 Code of Federal Regulations Part 192 (49 CFR 192) [6] lists steel grades approved for transporting natural gas. The majority (99%) of materials employed in the transmission natural gas pipeline system are cathodically protected externally coated steel. Steel types used for transmission and distribution applications primarily fall under

the grade API 5L, according to the American Society for Testing and Materials (ASTM) published standards [7], [8]. A combination of lower strength steels such as ASTM A53 (Grades A and B), ASTM A106 (Grades A and B), API 5L (Grades A, B, 42, and 52) are used in the distribution pipeline system. Ductile iron, cast iron, and copper pipes are also used in the natural gas distribution system, albeit they make-up a much smaller fraction of pipe materials used compared to steels.

A primary concern of hydrogen blending with respect to pipeline durability and integrity, arises from a hydrogen embrittlement phenomenon observed in many metals. Hydrogen embrittlement (HE) is defined as the process of strength and ductility reduction within a metal due to hydrogen induced damage, which makes it more brittle. Main mechanical properties of steel such as tensile strength, toughness and fatigue resistance are adversely affected by hydrogen embrittlement [9].

Different mechanisms that drive hydrogen embrittlement may occur alone or in combination with one another. Hydrogen enhanced decohesion (HEDE) mechanism [10]–[12] takes place when the cohesive strength of a material at the region of the crack tip is reduced upon hydrogen atom adsorption. In hydrogen enhanced localized plasticity (HELP) [13]–[15], accumulated hydrogen near the crack tip decreases resistance to dislocation motion so that dislocation mobility increases. The dislocations then carry plastic deformation within the metal lattice. Adsorption-induced dislocation emission (AIDE) [16], [17] mechanism involves crack growth under sustained stresses, which occurs by dislocation-emission from crack tips and nucleation and growth of microvoids or nanovoids.

Susceptibility to hydrogen embrittlement in a given material depends greatly on its microstructure, since hydrogen transport, diffusion, and solubility in a material are governed by its crystallographic microstructure [18]. Crystal lattice imperfections in the microstructure, such as grain boundaries, dislocations, and vacancies also play critical role. It is generally recognized that martensitic microstructures are most susceptible to hydrogen embrittlement, ferritic microstructures are less susceptible to hydrogen embrittlement than martensitic, while stable austenitic microstructures are least susceptible to hydrogen embrittlement [19]. Other factors that influence hydrogen embrittlement include operating conditions such as temperature, pressure, flow rate, impurities in gas, material surface conditions [20].

According to the European Industrial Gas Association (EIGA) standard on hydrogen pipeline systems, lower strength steels such as ASTM A106 B and API 5L X52 have been used in hydrogen gas service without reported issues [21]. Studies of the impacts of hydrogen on mechanical properties of higher strength steels, including API 5L X60, X70, X80, and X100, have demonstrated reduced tensile ductility, reduced fracture toughness, increased fatigue crack growth rate, and reduced number of cycles to crack initiation [22]–[25]. These adverse impacts on mechanical properties of the API 5L steels were attributed to hydrogen embrittlement.

According to American Society of Mechanical Engineers (ASME) Code B31.12 for Hydrogen Piping and Pipelines [26], cast iron and ductile iron materials are not recommended for hydrogen gas service due to hydrogen embrittlement. Steel grades containing Ni in additions above 0.5 are also not recommended for use with hydrogen gas.

Polymer Materials

With respect to plastics (predominantly polyethylene (PE)), they make up more than half of the pipe materials used in the natural gas distribution system. Other less commonly used plastic materials include Polyvinyl Chloride (PVC) and Acrylonitrile Butadiene Styrene (ABS). According to literature reports, no degradation by pure hydrogen has been reported to date, and little or no interaction between hydrogen gas and polyethylene are expected [2]. The main concern with pipelines comprising of polyethylene is permeability to hydrogen, which may result in leakage of gaseous hydrogen [27]. Permeation though polyethylene pipes is discussed in more detail in the following section.

Hydrogen Blending Impacts on Natural Gas Pipeline Leakage Rates

Gas leaks can be characterized in several ways, depending on the mechanism of mass transfer. They include permeation, diffusion, and pneumatic leaks. With respect to hydrogen gas, permeation through metals consists of adsorption on the metal surface, dissociation of hydrogen molecule, diffusion of hydrogen atoms through the metal, re-association of molecules and desorption on the opposite side of the metal. On the other hand, the permeation of hydrogen gas through polymer materials is accomplished by molecular diffusion. Pneumatic leaks occur through transfer of gas through a physical opening at the presence of a pressure gradient.

The pneumatic gas flow can be described by three types of flow mechanisms, based mainly on the dimension of the physical aperture of the leak and mean free path of the gas molecules. Continuum flow is characteristic for an opening significantly larger than the mean free path of the gas molecules, while molecular flow is characteristic for an opening smaller than the mean free path of the gas molecules. Transitional flow falls between viscous and molecular flow.

Leaks through joints, breaks, cracks, pinhole defects and driven by a pressure gradient fall within the continuum flow regime. In a continuum flow regime, the flow can be laminar, turbulent, or a transition between these two. The flow can be choked or unchoked (sonic or subsonic). Besides the geometry of the opening from which the leak occurs, temperature, pressure, thermodynamic properties, transport properties, and the molecular weight of the gas are factors that determine the extent of the leak [28]–[30].

Permeation leaks

Hydrogen gas is known to permeate through polymer pipes [27], [31]. Hydrogen has a significantly higher permeation rate through polymers compared to natural gas. While the economic loss of hydrogen via permeation may be considered negligible by the industry, it raises safety concerns, especially if hydrogen accumulates in confined spaces [32].

Table 1 shows the calculated gas loss rate of different blends of hydrogen and methane for a high density polyethylene (HDPE) pipe at different pressures [2]. The total volumetric loss of gas increased with both pressure and concentration of hydrogen in the blend.

Hodges et al. report the permeation of hydrogen through polymers to be 6 to 7 times larger than methane. Nevertheless, they consider the leakage rate by permeation compared to the leakage from the small pipe defects is much less than what can be regarded as a safety issue [33].

It is expected that for polyethylene pipes, most gas loss would occur through the pipe wall rather than through joints [2]. In contrast, most of the leaked gas in metal pipes is expected to originate from joints, cracks, and seals, rather than permeation through pipe walls owing to slower diffusion rates of hydrogen in metals.

Table 1: Calculated Gas Loss (ft^3/mile/year) for HDPE Pipes at 0.25, 3, and 60 psig.

Hydrogen Content	At 60 psig			At 3 psig			At 0.25 psig		
	H2	CH4	Total	H2	CH4	Total	H2	CH4	Total
0%	0.0	49.4	49.4	0.0	2.5	2.5	0.0	0.2	0.2
10%	32.9	44.5	77.4	1.6	2.2	3.9	0.1	0.2	0.3
20%	65.9	39.5	105.4	3.3	2.0	5.3	0.3	0.2	0.4
50%	164.7	24.7	189.4	8.2	1.2	9.5	0.7	0.1	0.8
100%	329.3	0.0	329.3	16.5	0.0	16.5	1.4	0.0	1.4

Calculation performed by GTI.

Source: Melaina, M., Antonia, O. & Penev, M. Blending Hydrogen into Natural Gas Pipeline Networks: A Review of Key Issues. *Contract* **303**, 275–3000 (2013).

Physical leaks

Hydrogen can leak through threaded fittings via a pressure gradient when there is a constant gap between the mated screws [29]. A combination of pneumatic leakage and leakage through permeation can occur through the sealing systems, e.g. gasketed joints or a valve stem packing [34]. Under the assumption of continuum flow regime, hydrogen would leak at a volumetric rate of 1.29 times higher than methane for laminar flow, based on ratio of the viscosities of the two gases. Under continuum flow that is turbulent in nature, hydrogen gas would leak at a rate of 2.83 times higher than methane, according to the square root of the ratio of the densities of the two gases. In the case of molecular flow, hydrogen gas would leak at a rate of 3.15 times higher than methane, based on the molecular mass ratio of the two gases [30].

The Gas Technology Institute (GTI) conducted simulated leak experiments through orifices with diameters of 0.003 in, 0.01 in, and 0.03 in, for gas blends of 10%, 20%, and 40% hydrogen in methane [35]. The experiments conducted at three different pressures (54 psig, 9 psig, 0.3 psig), indicated that while there was no preferential leakage of hydrogen through the orifices, the gas blend leaked at higher rate with the increase of hydrogen concentration in the blend. The study concluded that the ratios of flow rates of the simulated leaks were equivalent to the ratios of the square roots of their specific gravities.

In another study GTI constructed three small gas test loops, comprised of components from residential natural gas distribution system, to evaluate operation with hydrogen compared to natural gas over a 6 month period [36]. Several joints, a regulator, and a meter in two of the test loops were monitored individually for leakage. The study concluded that over the duration of the experiment, pure hydrogen gas leaked through joints at rate of 3.8 to 4.6 times higher than natural gas.

There are some reports, which indicated that actual hydrogen gas leak rates can differ from expected flow rates under viscous or molecular flow regime. Swain et al. experimentally investigated the gas leak rates from NPT fitting threads from low-pressure residential service lines, for hydrogen, methane, and propane gases [30]. They found that at lower pressures and smaller sizes of the leak openings, the rate of leakage of the three gases appeared similar, contrary to the expected different flow rates under continuum flow regime. The results were attributed to entrance effects and not fully developed laminar flow. Mejia et al. re-examined Swain & Swain work and concluded that at the residential low-pressure piping system, 1 to 3 kPa (0.15 to 0.44 psig) hydrogen and methane leak at similar rates [28]. These results were attributed to the highly tortuous leakage path of gas molecules and their increased wall collisions frequency. As a result, all gas molecules in the leakage path were expected to move at the same rate and the net flow was the same for all molecules.

Hydrogen Blending Impacts on Natural Gas Valves, Fittings, Materials, and Welds due to Hydrogen Embrittlement

A number of various metal alloys are employed throughout the natural gas infrastructure, in valves, fittings, and joints, including carbon steels, stainless steels, copper, aluminum, brass, cast and ductile irons. The primary concern for these components with hydrogen gas blending, as with metal alloy pipes is related to hydrogen embrittlement. Austenitic stainless steels, such as the 300 series, exhibit better resistance to hydrogen embrittlement than ferritic stainless steels [37]. Low carbon austenitic stainless steel grades 304L and 316L are used in hydrogen gas service, with higher preference for type 316L, due to its higher austenite stability [21].

Copper containing oxygen is subject to hydrogen embrittlement, however pure copper is unaffected by high pressure hydrogen gas [38]. Most copper alloys are deoxidized and thus not susceptible to hydrogen embrittlement [21]. Research work conducted under the European project GRHYD, tested susceptibility to hydrogen embrittlement of copper pipe and two brass alloys (CW617N and CW614N), by smooth and notched tensile tests under exposure to gas blends of up to 20% hydrogen in natural gas [18]. The three materials did not show significant susceptibility to hydrogen embrittlement, however brass CW614N exhibited low hydrogen effect.

Aluminum exhibits low hydrogen solubility and low hydrogen diffusivity. Furthermore, transport of hydrogen through aluminum is further inhibited by a very stable surface oxide [39]. No reduction of toughness or ductility has been observed in tests under dry hydrogen gas [39].

A variety of elastomer materials are used in the natural gas pipeline system as coupling seals and gaskets, meter and regulator diaphragms, o-rings, seals, and valve seats [40]. Commonly used elastomers such as Viton (fluoroelastomer), NBR (Acrylonitrile-butadiene Rubber), and EPDM (Ethylene Propylene Diene Monomer) are compatible with hydrogen gas due to their good chemical resistance [21]. However, likewise to plastics, elastomers suffer from high permeation rates of hydrogen gas.

With the exception of polyethylene, limited studies on the impacts of hydrogen on the broad range of plastics and elastomers have been conducted. Menon at al. examined the effects of hydrogen gas at static conditions under ambient temperature and 100 MPa pressure, on two thermoplastics (HDPE and PTFE) and two elastomers (NBR and Viton A) [41]. The two thermoplastics did not show significant change in physical properties including glass transition temperature, modulus, and tensile strength. However, Viton A showed significant change in modulus, compression set, and percent change in volume upon hydrogen exposure. NBR showed similar changes as Viton A, but to a lower degree.

Duranty et al. devised a method for *in situ* measurement of wear and friction properties of polymers under high pressure hydrogen [42]. Their investigation demonstrated that friction between a steel stationary ball and NBR increased in a high pressure hydrogen environment compared with samples in high pressure argon and ambient air.

Hydrogen Blending Impacts on Natural Gas Storage Facilities

Underground natural gas storage

Underground storage facilities, consisting of porous reservoirs and salt caverns, constitute a critical component of the natural gas infrastructure. While underground facilities have proven to be an effective and stable long-term storage method for natural gas, there are several known problems and anticipated challenges related to storing natural gas-hydrogen blends. Properties of hydrogen, including its lower energy content (12.7 MJ/m^3) compared to that of methane (40 MJ/m^3), and its availability as a substrate for microorganism driven reactions result in specific problems [43].

Hydrogen is known to have serious detrimental effects on underground porous reservoirs. Twenty different hydrogen related phenomena have been observed that have negative effects on porous reservoirs' performance as storage facilities for methane-hydrogen gas blends. The most serious of these is bacterial growth and activity, resulting in loss of gas volume, potential for H_2S production and damage to reservoir itself [44].

Salt caverns, on the other hand, are impervious to gas and the salt's plastic nature avoids fractures and loss of impermeability [43]. Since almost no microorganism can survive in highly concentrated brine, biologically driven reactions are absent in salt caverns except under unusual circumstances. Hence, salt caverns are not only suitable for storage of hydrogen blends, but also pure hydrogen. It should be noted that there are no salt caverns in use in California, according to SoCalGas [45].

Surface storage

Surface storage of natural gas in above-ground manufactured vessels is limited to specific applications. As previously discussed a number of metallic materials in the natural gas pipeline system, including high strength steels, are susceptible to mechanical integrity loss due to hydrogen embrittlement. Therefore, natural gas and hydrogen blends stored in manufactured above-ground natural gas storage containers can result in material degradation and failure, when utilizing materials susceptible to hydrogen embrittlement.

Pipeline storage of hydrogen within the natural gas infrastructure has been proposed as an alternative to underground storage [43]. This approach involves injecting hydrogen into the natural gas pipelines at locations where the blended gas would not be sent to underground storage facilities but would directly be delivered to end use customers or subsequently employing hydrogen separation/extraction downstream.

CNG fuel tanks

Compressed natural gas (CNG) fuel tanks in CNG powered vehicles are an important above-ground natural gas storage mechanism. National and international regulations generally limit hydrogen concentrations to 2% limit in motor fuel CNG because CNG tanks are manufactured with high tensile strength steel, which allows tanks to have

smaller wall thicknesses and therefore reduced weight. However, as indicated previously, these steels are susceptible to hydrogen embrittlement, with resulting serious safety issues. Modern CNG tanks in Europe are manufactured using steels that can accommodate higher hydrogen concentrations, but replacing existing CNG vehicle fuel systems in different regions around the world would be expensive and lengthy process since CNG fuels tanks have life-time guarantee of 20 years [40].

Hydrogen Blending Impacts on Pipelines under Cathodic Protection

Cathodic protection is applied worldwide and across various industrial sectors to protect metallic structures and devices from corrosion, including underground structures, marine exposed structures, ship hulls, or heat exchangers. This technology is also widely used to prevent the corrosion of steel natural gas pipelines. The surface of pipelines is made into the cathode of an electrochemical cell. Corrosion is prevented by converting all of the anodic (active) sites on the metal surface to cathodic (passive) sites by supplying an electrical current (free electrons) from an alternate source [46]. Cathodic protection can usually be divided into two types: 1) galvanic and 2) rectifier systems.

The galvanic technique is a passive method using galvanic anodes, which have a higher potential with respect to the structure being protected. These anodes are made of materials such as magnesium or zinc, which are naturally anodic with respect to steel structures and are connected directly to the steel pipes. However, in structures such a long pipelines, this technique may not provide sufficient corrosion protection and an external DC power source may be necessary to provide sufficient current. Because the power source is almost always a rectifier unit, this type of system is referred to as a rectifier or impressed current type system.

In the rectifier cathodic protection system, anodes are installed in the electrolyte (i.e. ground soil) and are connected to the positive terminal of a DC power source. The protected structure is connected to the negative terminal of that source. In contrast to the galvanic system, a rectifier system is adjustable because its voltage and current can be adjusted, allowing for controlling the corrosion process and monitoring the corrosion status of the pipelines [47]. More importantly, a rectifier system can be applied in any resistivity environment and can be used on any size structure [48]. A rectifier system is suitable for natural gas pipelines which have a significant length and usually are placed underground.

The most critical issue brought by the cathodic protection is hydrogen embrittlement. In the case of cathodic protection of steel pipelines for natural gas transfer, the hydrogen source is mainly from water and moisture. With direct current applied in the rectifier system, H_2O can produce corrosion on steel via a water splitting cathodic reaction. Hydrogen atoms released by this reaction will either recombine and diffuse into the outer environment or without recombining diffuse into the grain of the steel. The latter

case results in hydrogen embrittlement that is caused by cathodic protection [49]. Such an issue would be more serious when the pipeline is installed under water [50], [51]. For the pipelines exposed in air or installed in the soil or concrete, applying a waterproof coating and humidity monitoring, allows for cathodic protection to work in normal condition [52]. However, according to DOT PHMSA annual report data there were no offshore natural gas pipelines as of 2020.

In addition to hydrogen embrittlement, hydrogen atoms produced by cathodic protection can also cause hydrogen blistering [53]. Hydrogen Blistering (HB) refers to the formation of subsurface planar cavities (blisters) in a metal that result from excessive internal hydrogen pressure.

These issues associated with cathodic protection are the result of hydrogen generated by the cathodic protection process. However, it is not evident if cathodic protection can increase the risk of hydrogen embrittlement in pipelines transporting hydrogen or hydrogen-natural gas blend, compared to pipelines transporting natural gas. To date, there are no published reports on potential detrimental impacts of cathodic protection on hydrogen service pipelines, with respect to interaction between cathodic protection and the hydrogen gas being transported through the pipelines.

Hydrogen Blending Projects

Table 2 and **Table 3** are the lists of hydrogen blending projects in North America and Europe and Australia, respectively, in chronical order. Acceptable concentration of H2 in the blending varies between 2 % and 20 %.

Table 2: Hydrogen Blending Projects in North America (S=Storage, D = Distribution, T = Transmission, E = End use)

Project Name	Project Period	Location	Participants	Keywords	Network Level	Key Topics and Findings	% H_2 Studied	% H_2 Acceptable
Hawaii Gas [54]	1970-present	US	Hawaii Gas	Blending Demonstration	T D	Successful demonstration of long-term blending in natural gas distribution and transmission pipelines No available measurement on hydrogen leakage, nor hydrogen-related failure	10-12	12
Initial Assessment of the Effects of Hydrogen Blending in Natural Gas on Properties and Operational	2015	US and Canada	Operations Technology Development (OTD) Members GTI	Materials Integrity Metering	D	Impact of 5% H_2 on non-metallic pipeline was examined. Leakage rate of 5% H_2 blend through elastomer couplings was examined.	5	5

Project Name	Project Period	Location	Participants	Keywords	Network Level	Key Topics and Findings	% H$_2$ Studied	% H$_2$ Acceptable
Safety, Phase 1								
University of California Irvine (UCI) National Fuel Cell Research Center (NFCRC) Campus Hydrogen Microgrid	2016-present	US	UCI NFCRC NREL SoCalGas	Blending Demonstration Leakage Combustion	D	Odorants are not sufficient for detecting leaks Gas turbines showed slight drop in total fuel gas flow but overall no negative impact on emissions	0-3.8	3.8
M2018-008 Expansion of NYSEARCH RANGE Model & Study of Siloxane Concentration Limits	2019-2020	US and Canada	NYSEARCH members etaPartners LLC	Blending End use	D E	Results on Wobbe numbers, combustion process, yellow tipping, flame lifting, flame speed, flashback, CO emissions NYSEARCH RANGE spreadsheet updated to implement correlation	2-20	10

Project Name	Project Period	Location	Participants	Keywords	Network Level	Key Topics and Findings	% H₂ Studied	% H₂ Acceptable
						changes developed in the project. An update to the online model is planned.		
Enbridge Low-Carbon Energy Project	2021-present	Canada	Enbridge	Blending Demonstration	D E	An upper limit of 5% by volume hydrogen was applicable for the specific Gas Distribution Network. The upper limit for hydrogen was found to be 2% based on the local gas composition, heating equipment, and appliances.	0-100	5 (D) 2 (E)

Table 3: Hydrogen Blending Projects in Europe and Australia (S=Storage, D = Distribution, T = Transmission)

Project Name	Project Period	Location	Participants	Keywords	Network Level	Key Topics and Findings	% H_2 studied	% H_2 acceptable
P2G Ameland	2008-2012	Netherlands	Municipality of Ameland Joulz GasTerra Stedin Kiwa Technology	Domestic distribution blending Metering End use equipment	D	The blending of hydrogen up to 20% has no impact on the infrastructure materials and service lines.	20	20
Underground Sun Storage [55]	2013-2018	Austria	Axiom Montan Universitat RAG Austria AG (RAG) Energie Institute Verbund	Storage	S	The underground storage facilities are capable to tolerate hydrogen content up to 10%.	10	10
Permeation of Hydrogen Test on Polyamide (Distribution) Pipelines of Different	2014-2015	Europe	GasNatural Gaz de France E.On Ruhrgas	Integrity Permeability Materials	D	The permeation in PA12 resins occurs after less than 24 hrs (20 °C and 10 barg) Permeability coefficient	100	Not determined

Project Name	Project Period	Location	Participants	Keywords	Network Level	Key Topics and Findings	% H$_2$ studied	% H$_2$ acceptable
Types of Resins (Either PA11 or PA12)						ranges from 80 to 100 ml.mm/m^2/bara/day		
Energy Storage – Hydrogen injected into the Gas Grid via Electroly-sis Field Test – Phase 1 [56]	2014-2020	Denmark	Energinet Evida Danish Gas Technology Centre IRD Fuel Cells	Blending Demonstration	S T D	The long-term test at the facility has been performed with hydrogen concentrations up to 12% hydrogen.	15	12
GRHYD [57]	2014-present	France	ENGIE CETIAT Other participants	Injection Blending Demonstration	D	Successful operation up to 20% H$_2$ injection Injection was performed for over 5 yrs	0-20	20
ITM Power Thüga Plant	2014-present	Germany	Thüga Group ITM Power	Blending Demonstration	D	A maximum of 2% hydrogen was blended with natural gas. No compressor was required since the	2	2

Project Name	Project Period	Location	Participants	Keywords	Network Level	Key Topics and Findings	% H$_2$ studied	% H$_2$ acceptable
						hydrogen produced was at the same pressure as the gas distribution network.		
P2G Haßfurt	2016-present	Germany	Next-Kraftwerk	Blending Demonstration	D	The project has been operational since 2016 with positive news stories.	5	5
Jupiter 1000 [58]	2017-present	France	GRTGaz Atmostat CEA McPhy Leroux et Lotz Terega	Blending Demonstration	T	Not available	0-6	6
HyNTS Aberdeen Vision [59]	2019-present	UK	SGN National Grid Cadent Energy	Blending Demonstration	D	No critical obstacles have been identified which would prevent the injection of 2%	2	2

Project Name	Project Period	Location	Participants	Keywords	Network Level	Key Topics and Findings	% H$_2$ studied	% H$_2$ acceptable
			Pale Blue Dot Energy DNV GL			hydrogen into the national transmission system (NTS) at St Fergus and its distribution through the gas distribution network		
Wind2Gas Brunsbuttel	2019-present	Gemany	Schleswig-Holstein Netz AG Wind2Gas Energy GmbH Co. KG Other participants	Blending Demonstration	T	Hydrogen produced in the wind power-to-gas plant is compressed using two compressors and fed into the high-pressure natural gas grid at 2%.	2	2
Snam Contursi Trial [60]	2019-present	Italy	Snam	Blending	D	Italy's gas utility, Snam, began a large-scale experiment in 2019 intro-ducing 5% hydrogen into	10	10

Project Name	Project Period	Location	Participants	Keywords	Network Level	Key Topics and Findings	% H_2 studied	% H_2 acceptable
						the Italian Gas Transmission Network. In December 2019, Snam doubled the volume of the hydrogen blend to 10%.		
Australian Hydrogen Centre [61]	2019-present	Australia	Australian Gas Networks (AGN) Department of Energy and Mining (DEM) Department of Environment, Land, Water, and Planning (DELWP) Other participants	Blending Demonstration	D	The project started to supply the hydrogen blend of up to 5% renewable hydrogen through the existing natural gas infrastructure.	5	N/A

Project Name	Project Period	Location	Participants	Keywords	Network Level	Key Topics and Findings	% H$_2$ studied	% H$_2$ acceptable
HyDeploy [62]	2019-present	UK	Cadent Gas Northern Gas Networks Progressive Energy Ltd Keele University Health & Safety Laboratory ITM Power	Blending Demonstration	D E	The HyDeploy has successfully completed the demonstration of hydrogen blending up to 20 mol%. Properly installed and maintained domestic appliances are safe with the blended gas.	20	20

Task 2: Potential Impact of Hydrogen Injection on the Natural Gas Infrastructure

Information about the existing transmission and distribution natural gas pipeline system in California, including mileage, material type, age, diameter, and leaks was obtained from the 2019 Annual Data compiled by Pipeline and Hazardous Materials Administration (PHMSA) at the Department of Transportation (DOT) [63].

As shown in Figure 2, the transmission pipeline system in CA is mainly comprised of cathodically protected externally coated steel pipe (99.57% of total miles). Other materials include unprotected externally coated steel (0.14%), plastic (0.12%), cathodically protected bare steel (0.11%), and unprotected bare steel (0.06%) [64].

Figure 2: Miles of Transmission Pipeline by Material in CA
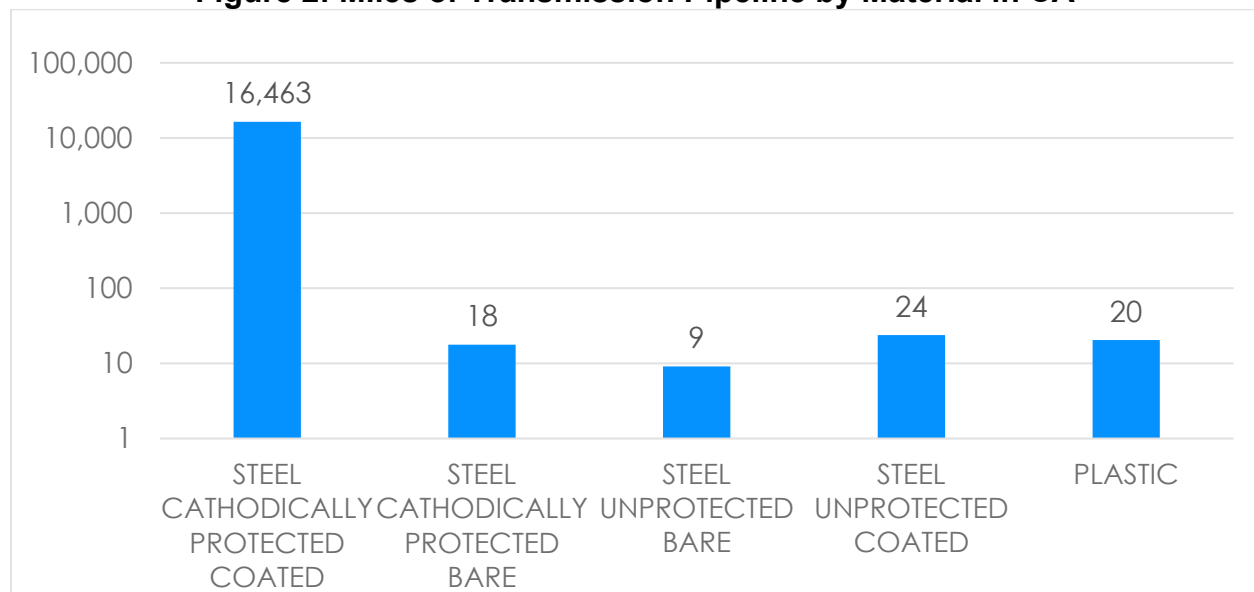
Source: PHMSA 2019 Annual Data

The age of pipe installed as part of California's transmission pipeline system, spans over nine decades. However, the vast majority of pipeline has been installed after 1950. Transmission pipe diameter ranges from smaller than 4" to a maximum of 48" in diameter.

The total number of incidents in high consequence areas (HCA) and non-HCA along the transmission pipeline network in California for 2019 are plotted in Figure 3, categorized by the source of incident. The most frequent cause of incident is equipment failure, followed by external corrosion.

Figure 3: Number of Incidents on Transmission Pipeline System in CA

Legend:
- Construction
- Equipment
- Excavation Damage
- Incorrect Operations
- External Corrosion
- Internal Corrosion
- Manufacturing
- Previous Damage
- Stress Corrosion Cracking

ONSHORE NON-HCA LEAK: 9 | 137 | 1 | 22 | 1 | 3

ONSHORE HCA LEAK: 5 | 86 | 5 | 1

FAILURES IN HCA SEGMENT: 26 | 6 | 4 | 24 | 1 | 15
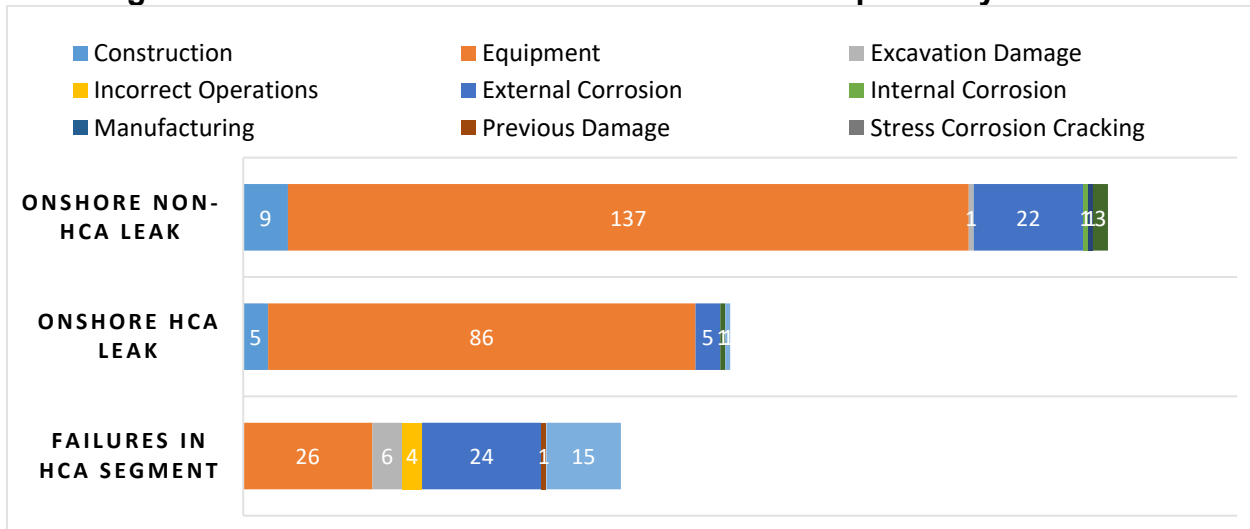
Source: PHMSA 2019 Annual Data

Distribution Mains in California's pipeline system are comprised of plastic pipe (51.68%), cathodically protected externally coated steel (40.44%), unprotected coated steel (4.46%), unprotected bare steel (3.34%), cast/wrought iron (0.05%), and cathodically protected bare steel (0.03%) [65]. Figure 4 shows the total number of miles of distribution mains lines categorized by material type.

Figure 4: Miles of Distribution Mains by Material in CA

Data points:
- STEEL UNPROTECTED BARE: 3,483
- STEEL UNPROTECTED COATED: 4,644
- STEEL CATHODICALLY PROTECTED..: 26
- STEEL CATHODICALLY PROTECTED..: 42,115
- PLASTIC: 53,830
- CAST/WROUGHT IRON: 56
- OTHER: 0.3
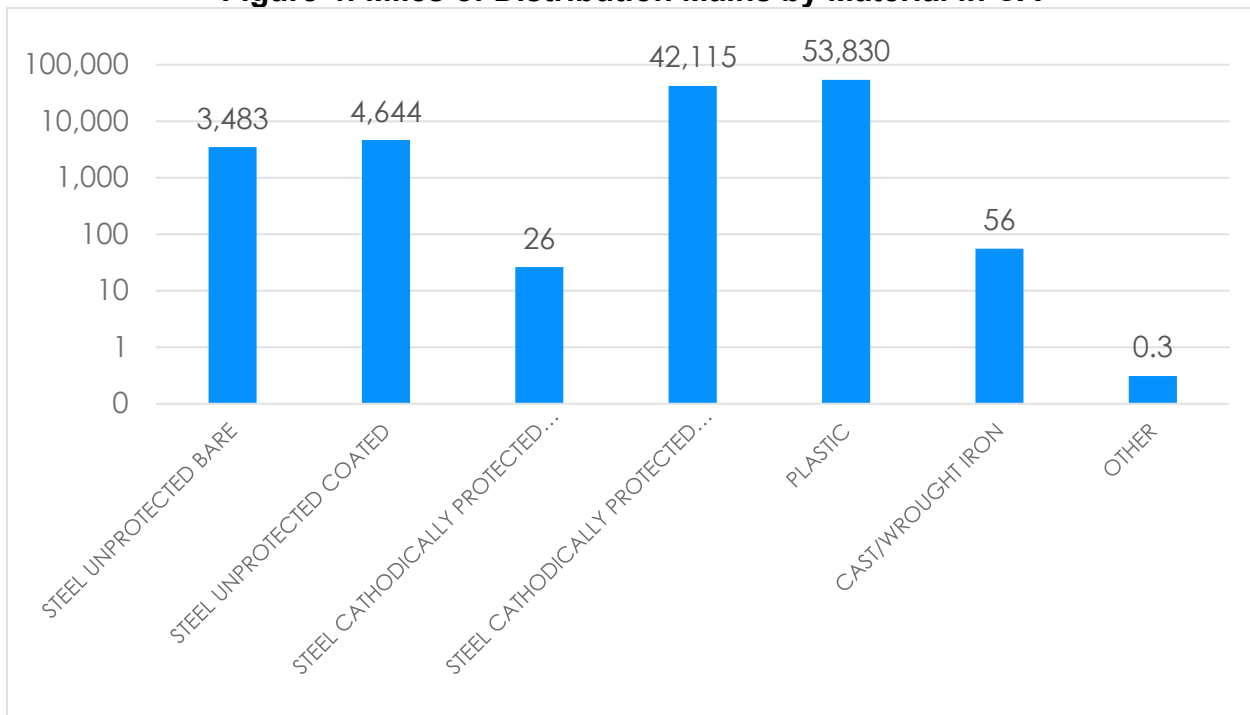
Source: PHMSA 2019 Annual Data

Distribution pipeline system service lines in CA are comprised of plastic pipe (65.55%), cathodically protected coated steel (24.9%), unprotected coated steel (9.53%), cathodically protected bare steel (<0.01%), and other materials (0.01%) [65]. Figure 5 shows the total number of distribution service lines categorized by material type.

Figure 5: Number of Distribution Services by Material in CA
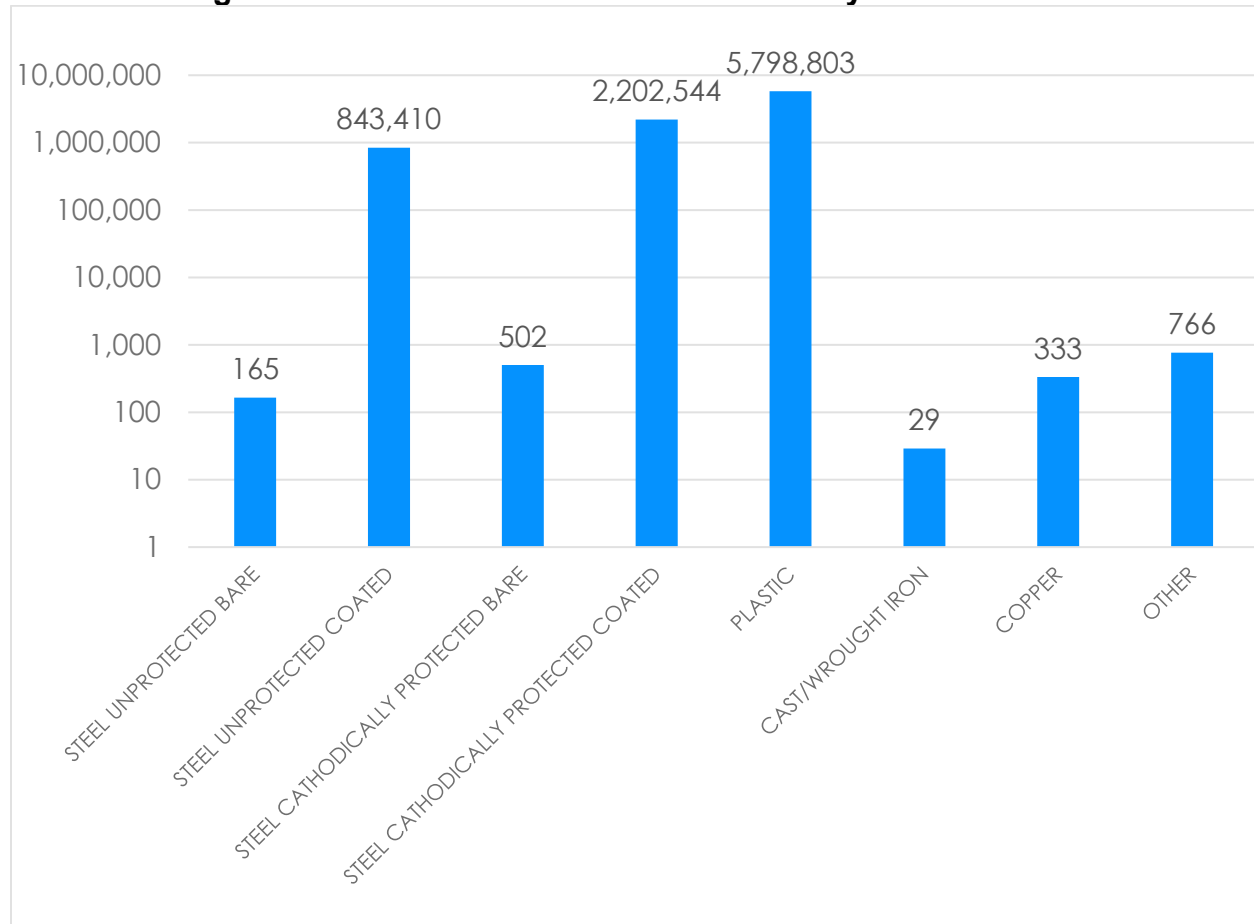
Source: PHMSA 2019 Annual Data

The majority of distribution mains were installed post 1950. However, there are some lines that were installed prior to 1940 still in service. Similarly, the majority of distribution services lines have been installed after 1950.

Incident in the distribution pipeline system include primarily leaks rather than ruptures, due to the low operating pressures [2]. Figure 6 shows the total number of leak incidents in California's distribution pipeline system in 2019, categorized by the cause of incident. Corrosion, followed by joint/weld failure are the most common causes for leaks.

Figure 6: Total Distribution Mains Leaks by Cause in CA
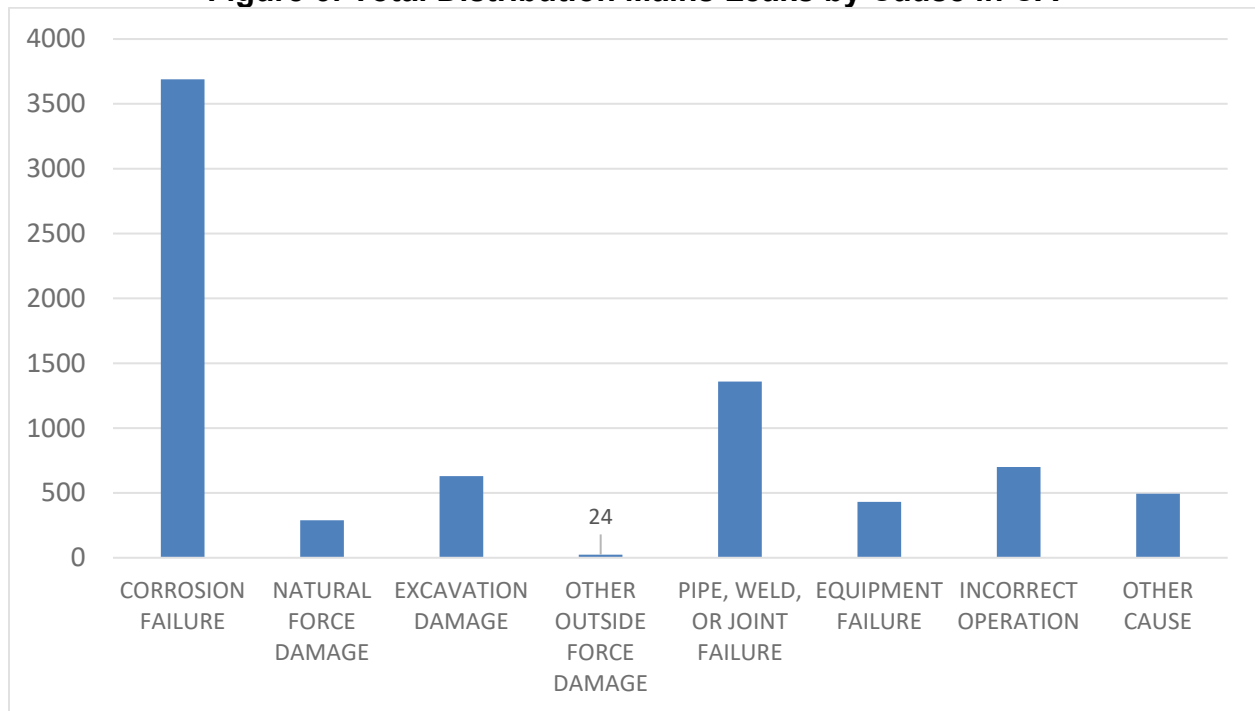
Source: PHMSA 2019 Annual Data

Task 2a - Modeling and/or Experimental Assessment of Potential Impact on Natural Gas Pipeline Leakage Rates

Introduction

Methane (CH_4) the predominant ingredient of natural gas (NG) is a potent greenhouse gas. Recent EPA report [66] estimated that methane emissions, equivalent to 650.3 million metric ton (MMT) CO_2, accounted for 10.9% of the total greenhouse emissions in the U.S.A. during 2020, as shown in Figure 7. Methane emissions from the oil and gas industry represent a significant amount of total annual methane emissions. Figure 8 shows the major emissions sources of methane in the USA during 2020 according to the EPA. The largest source, enteric fermentation, at 175.2 MMT CO_2 eq., accounted for 26.9% of total methane emissions. Natural gas systems were the second largest source of methane emissions in 2020, accounting for 164.5 MMT CO_2 eq., or 25.3% of total methane emissions. The third largest source were landfills, accounting for 109.3 MMT CO_2 eq., or 16.8% of total methane emissions. The methane emissions associated with the natural gas production, transmission and distribution are of particular interest to this study.

Figure 7: 2020 U.S. Greenhouse Gas Emissions by Gas (Percentages based on MMT CO2 22 Eq.)
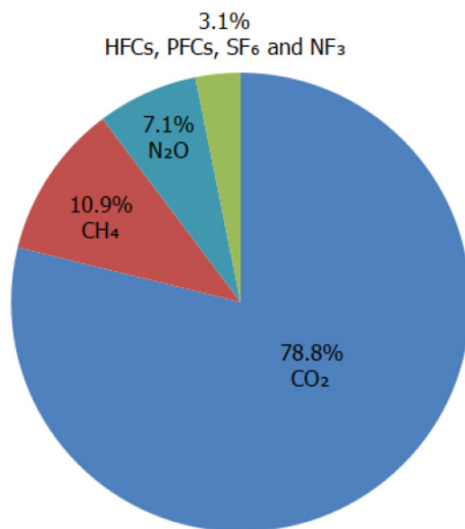
Source: Draft Inventory of U.S. Greenhouse Gas Emissions and Sinks: 1990-2020. U.S. Environmental Protection Agency. EPA 430-P-22-001 https://www.epa.gov/ghgemissions/draft-inventory-us-greenhouse-gas-emissions-and-sinks-1990-2020 (2022).

Figure 8: 2020 Sources of Methane Emissions
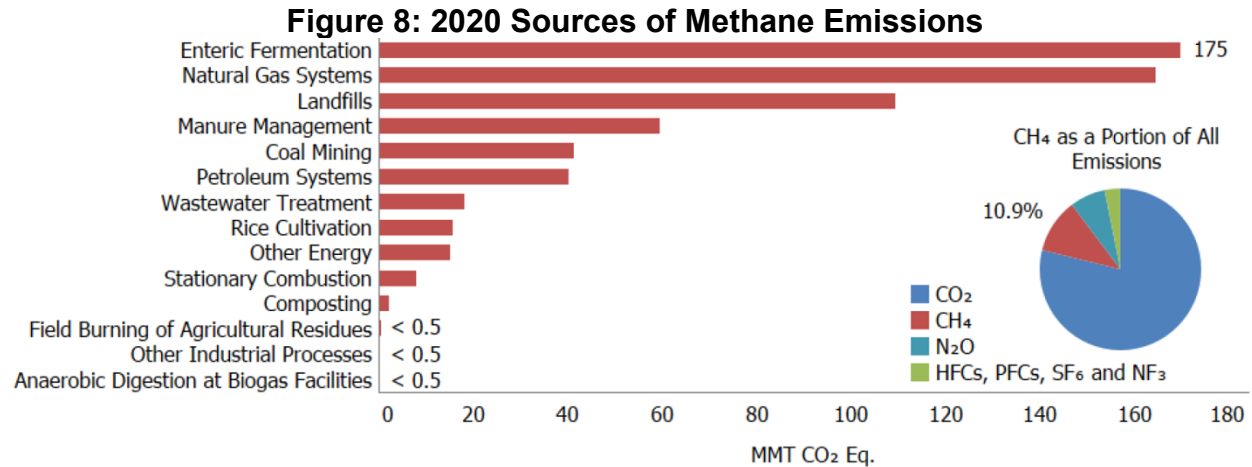
Source: Draft Inventory of U.S. Greenhouse Gas Emissions and Sinks: 1990-2020. U.S. Environmental Protection Agency. EPA 430-P-22-001 https://www.epa.gov/ghgemissions/draft-inventory-us-greenhouse-gas-emissions-and-sinks-1990-2020 (2022).

Methane emissions from the natural gas system consist of large sporadic emissions due to equipment failure, maintenance activities and continuous emissions at smaller rates. A recent study evaluated methane emissions at four of the ten most populous cities in the U.S., located on the U.S. East Coast. Its findings suggest that methane emissions are more than double the estimates from the EPA inventory [67]. Another recent study used satellite imagery to capture some very large methane emission events, occurring between 2019 and 2020 [68]. The study concluded that, while some of the events were due to accidents, most of them were deliberate or controlled emission events.

The California Public Utilities Commission (CPUC) and California Air Resource Board (CARB) have since 2015 released an annual joint staff report on natural gas leak and emissions [69]. Table 4 presents the most recent estimates according to the 2020 report of natural gas in California, divided by system category.

Table 4: Total Natural Gas Emissions by System Category

System Category	2015 Baseline		2019		2020	
	MMscf	% Total	MMscf	% Total	MMscf	% Total
Transmission Pipeline	549	8%	294	5%	261	5%
Transmission M&R Station	1,007	15%	790	14%	760	13%
Compressor Station	163	2%	144	3%	143	3%
Distribution Mains & Services	1,703	26%	1,243	22%	1,178	21%
Distribution M&R Stations	1,348	20%	1,385	24%	1,482	26%
Customer Meter	1,638	25%	1,693	30%	1,704	30%
Underground Storage	193	3%	161	3%	146	3%
Total	**6,601**	**100%**	**5,710**	**100%**	**5,674**	**100%**

Source: Analysis of the Gas Natural Gas Leak and Emission Reports. Joint Staff Report California Public Utilities commission California Air Resource Board https://www.cpuc.ca.gov/-/media/cpuc-website/divisions/safety-policy-division/reports/final-2021-ngla-joint-report_012122.pdf (2022).

The largest aggregated source by volume, customer meter category, accounted for 30% of total emissions, followed by distribution measurement and regulation stations at 26%, and distribution mains and service lines accounting for 21% of total emissions. To that end, in 2020 PG&E conducted a meter leak test survey on one third of all the gas meters on its territory, testing approximately 1.4 million meter sets. The test employed a soap bubble test methodology, classifying the leaks in four groups (A, B, C, D), based on soap bubble size. Figure 9 shows images of soap bubble tests corresponding to the different classification groups and representative flow rates measured in standard cubic foot per hour (SCFH).

Figure 9: Leak Classification Based on Soap Test per PG&E procedure TD-4110P-01 JA-01
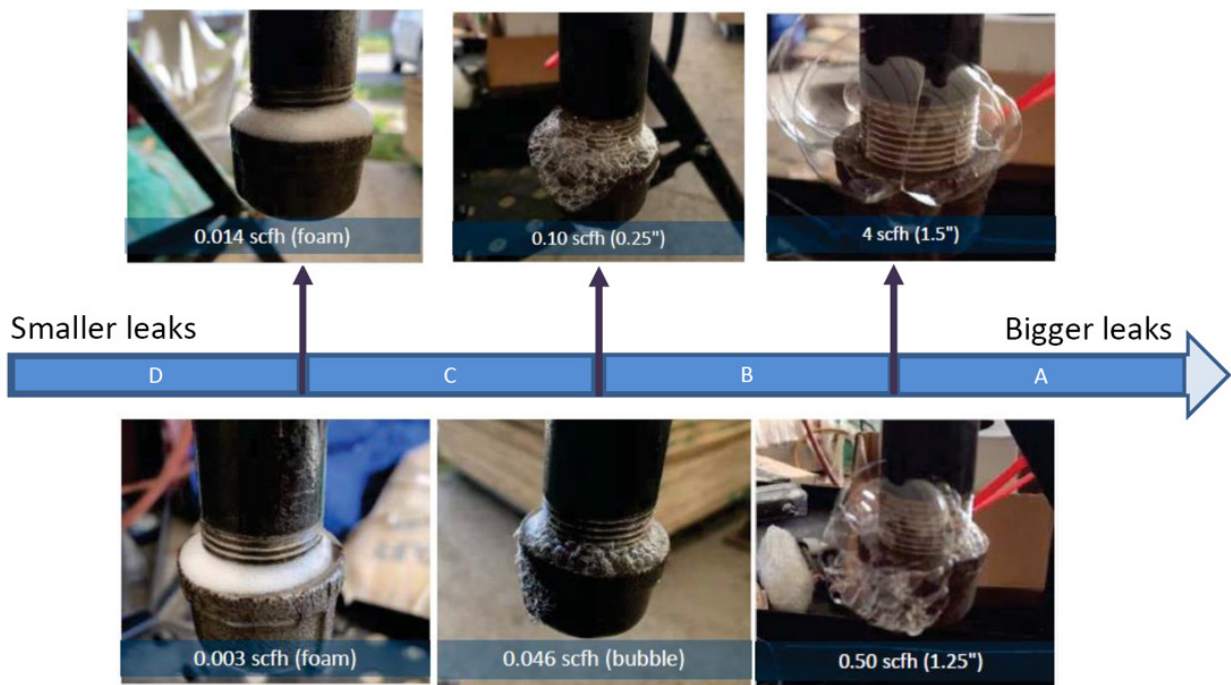
Source: Betran, A. & Ramos, S. *Methane Emissions from Gas Residential Meter Set.* https://www.cpuc.ca.gov/-/media/cpuc-website/divisions/safety-policy-division/documents/day-1-slide-4---pgande---meter-set-emissions_jan2021_corr.pdf (2021).

Out of 1.4 million meters sets tested, leaks were detected in 123,000 of them. Figure 10 shows the number of leaks for each class. Average flow rates and threshold flow rates are also shown in Figure 10. The majority of leaks detected (85% of total) fell under classes C and D, with average flow rates of 0.041 SCFH and 0.0032 SCFH, respectively. However, the largest amount of gas emissions occurred from leaks classified under group A, with mean emission rate of 9.5 SCFH.

Figure 10: Number of Leaks per Class and Flow Rates
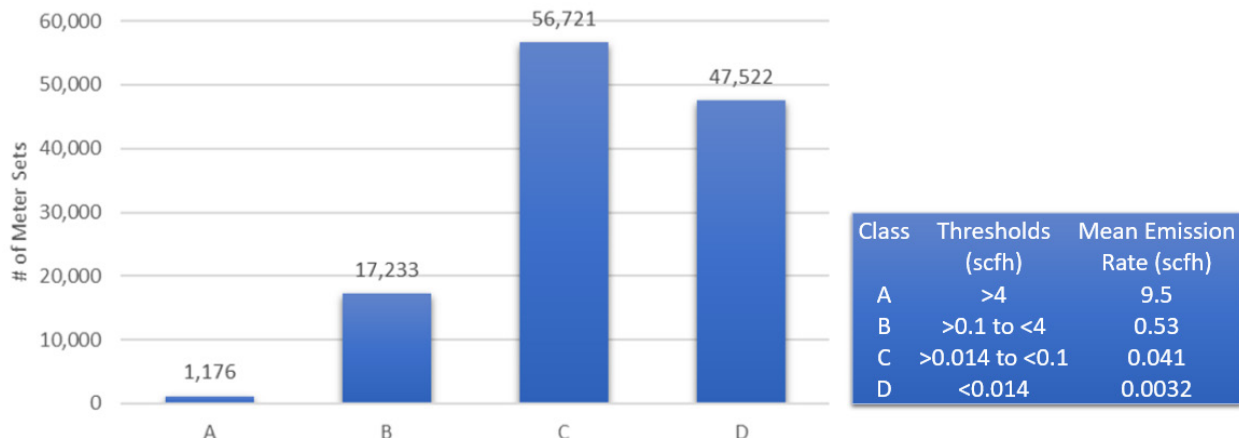
Class	Thresholds (scfh)	Mean Emission Rate (scfh)
A	>4	9.5
B	>0.1 to <4	0.53
C	>0.014 to <0.1	0.041
D	<0.014	0.0032

Source: Betran, A. & Ramos, S. *Methane Emissions from Gas Residential Meter Set*. https://www.cpuc.ca.gov/-/media/cpuc-website/divisions/safety-policy-division/documents/day-1-slide-4---pgande---meter-set-emissions_jan2021_corr.pdf (2021).

With regards to the third largest emission category, distributions pipelines, a CARB study evaluated 78 samples on PG&E, SoCalGas, and SDG&E territories [70]. Figure 11 represents the mean leak rates obtained from the study, compared to a previous study conducted by Washington State University.

Figure 11: Methane Emissions from Distribution Pipelines

	All	Mains	Services	PL	UPS	PS
WSU	1.85	2.52	0.61	0.59	2.22	2.86
CARB	2.48	1.71	2.96	2.58	2.39	2.51

Facility and Material Categories
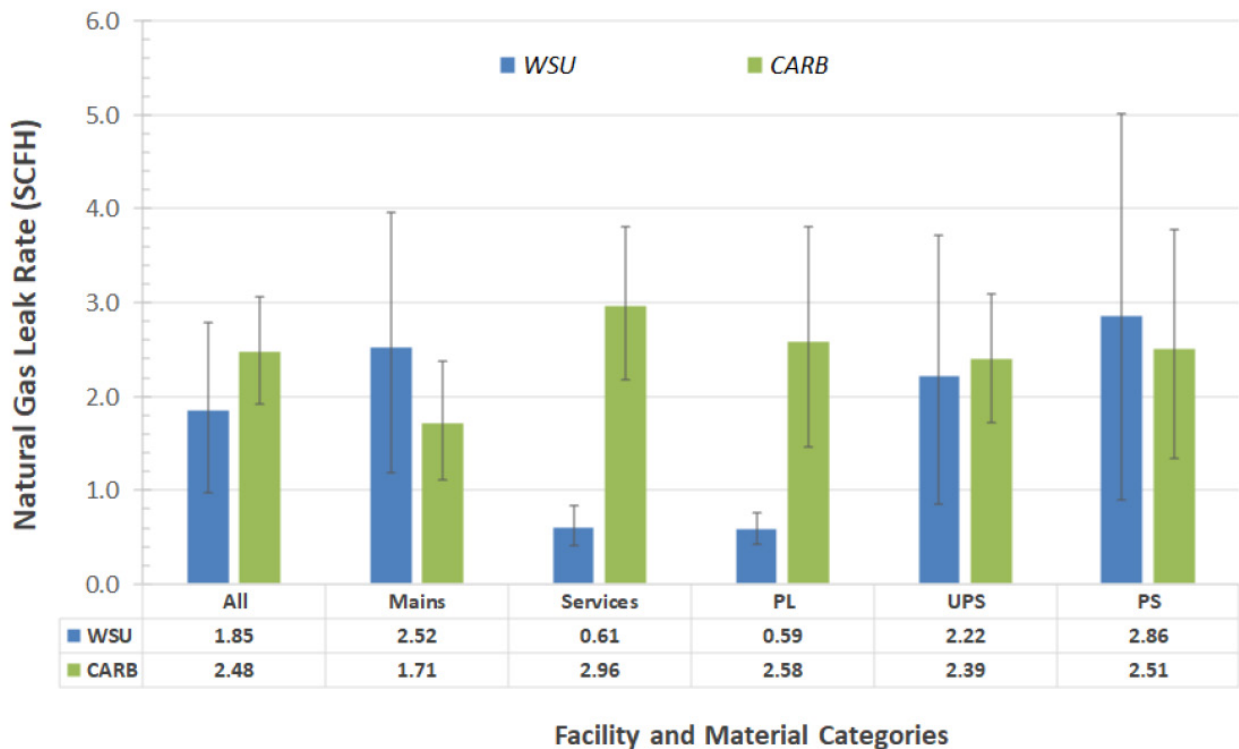
Source: Ersoy, D., Adamo, M. & Wiley, K. *Quantifying Methane Emissions from Distribution Pipelines in California*. https://ww2.arb.ca.gov/sites/default/files/2021-01/Final_CARB_Pipeline Study_1-14-21.pdf (2021).

Based on prior studies and available data it is evident that significant amount of methane is emitted from the natural gas system in the environment. Subsequently, there are numerous efforts aimed at identifying emissions sources, quantifying total emissions, and taking measures to reduce and eliminated emissions. Therefore, it is critical to gain some insights into the potential impacts on emissions from the existing natural gas system that would results from blending hydrogen (H_2) gas with natural gas. The presentation of the experimental work that follows addresses some of these questions.

Experimental Approach

Gas leaks can be described by several mechanisms of mass transfer, which include permeation, diffusion, and pneumatic leaks. Pneumatic leaks occur through transfer of gas through a physical opening (orifice) at the presence of a pressure gradient. With respect to hydrogen gas, permeation through metals consists of adsorption on the metal surface, dissociation of hydrogen molecule, diffusion of hydrogen atoms through the metal, re-association of molecules and desorption on the opposite side of the metal. The process is shown in Figure 12 (a). On the other hand, the permeation of hydrogen gas through plastic materials is more efficient, as permeation through polymers is accomplished by molecular diffusion, as shown in Figure 12 (b). Although hydrogen has much higher permeation rate through metals compared to other common gases, the overall emissions of hydrogen gas by permeation through metal pipes and other metal components is significantly lower than permeation through plastics. It is supposed that the bulk of hydrogen gas leaks from metal pipes and piping components would occur primarily through threads or mechanical joints [2]. These types of pneumatic leaks, shown in Figure 12 (c), in addition to threads and joints, can also occur through cracks or pinhole defects in the material.

Figure 12: Hydrogen Leak Mechanisms
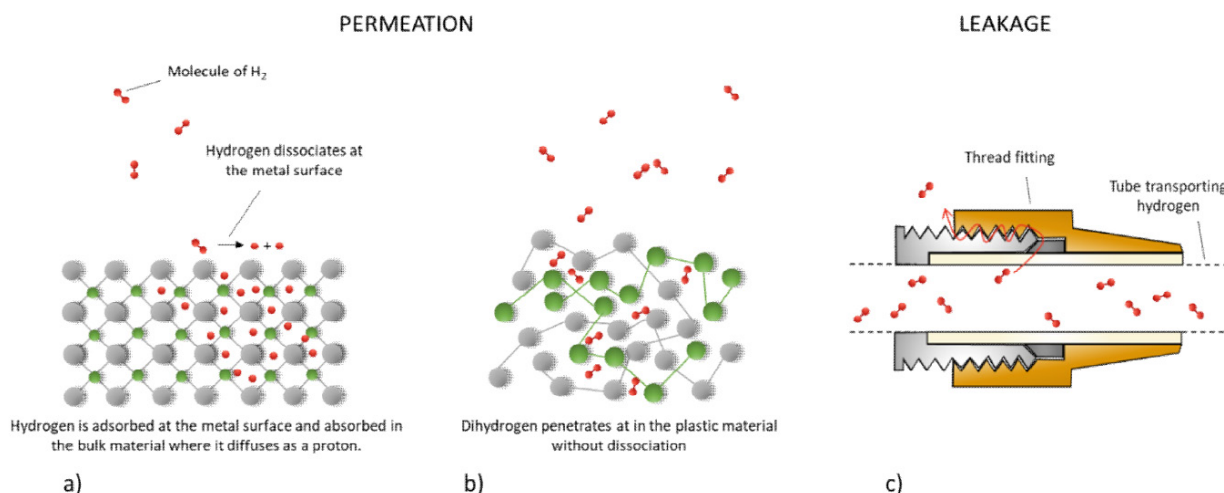
Source: Blanchard, L. & Briottet, L. Testing Hydrogen admixture for Gas Applications - Non-combustion related impact of hydrogen admixture - material compatibility. (2020).

The pneumatic gas flow can be described by three types of flow mechanisms, based mainly on the dimension of the physical aperture of the leak and mean free path of the gas molecules. Viscous flow is characteristic for an opening significantly larger than the mean free path of the gas molecules, while molecular flow is characteristic for an opening smaller than the mean free path of the gas molecules. Transitional flow stands somewhere between viscous and molecular flow. Viscous flow, which is most commonly observed, can be sub-divided into two types, laminar flow and turbulent flow, depending on the geometry of the leak opening and the pressure gradient. Figure 13 (a) depicts the gas molecule movement under turbulent flow, while Figure 13 (b) shows gas molecule movement under laminar flow. Molecular flow is depicted by Figure 13 (c), where the leak aperture is smaller than the mean free path of the gas molecule.

Figure 13: Depiction of Gas Movement in a) Turbulent, b) Laminar, and c) Molecular Leaks
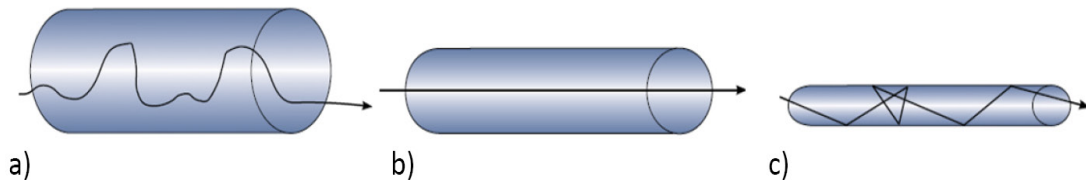
a)   b)   c)

Source: Blanchard, L. & Briottet, L. Testing Hydrogen admixture for Gas Applications - Non-combustion related impact of hydrogen admixture - material compatibility. (2020).

Table 5 lists approximate ranges of volumetric gas flow rates for typical viscous turbulent and laminar flows, as well as transitional and molecular flows, in both SCCS (standard cubic centimeter per second) and SCFH units. Based on the evaluation of methane gas leaks performed on meters sets and distribution pipelines in California, it is reasonable to assume that majority of those gas leaks are in the viscous flow regime, based on flow rates alone.

Table 5: Flow Rates Range of Pneumatic Leaks

Types of flow	Leak Rate (SCCS)	Leak Rate (SCFH)
Turbulent flow	$> 10^{-2}$	$> 10^{-3}$
Laminar flow	$10^{-1} - 10^{-6}$	$10^{-2} - 10^{-7}$
Transitional flow	$10^{-4} - 10^{-5}$	$10^{-5} - 10^{-6}$
Molecular flow	$< 10^{-5}$	$< 10^{-6}$

Source: Gaseous Hydrogen Embrittlement of Materials in Energy Technologies, Vol 1: The Problem, its Characterisation and Effects on Particular Alloy Classes. (ed. Gangloff, RP and Somerday, BP) (2012).

The distinction between turbulent and laminar viscous flow can be established by calculating the Reynolds number given by Equation 1, where D_h is the hydraulic diameter of the opening, Q is the volumetric flow rate of the gas, A is the cross-sectional area of the opening, and v is the kinematic viscosity of the gas. Gas flow with

Reynolds number larger than 4,000 is considered turbulent, while gas flow with Reynolds number of less than 2,000 is considered laminar.

$$R_e = \frac{D_h}{A \cdot v} Q \qquad \text{Equation 1}$$

Laminar flow rate through a tube can be calculated using Equation 2 [9], where d is the tube inner diameter and L is the length, μ is the dynamic viscosity of the gas, P_1 is the upstream pressure, and P_2 is the downstream pressure.

$$Q = \frac{\pi d^4}{128 \mu L} (P_1 - P_2) \,(\text{laminar tube model}) \qquad \text{Equation 2}$$

The flow rate of a compressible fluid, such as gas, through an orifice is given by Equation 3, where C_d is the coefficient of discharge, ε is gas expansion factor given by Equation 4 [71], ρ is the gas density, A is cross-sectional area of the orifice, β is the ratio of orifice diameter to the larger pipe diameter, and k is the specific heat ratio of the gas.

$$Q = C_d \varepsilon A \sqrt{\frac{2(P_1 - P_2)}{r(1 - \beta^4)}} \,(\text{orifice model}) \qquad \text{Equation 3}$$

$$\varepsilon = 1 - (0.351 + 0.256\beta^4 + 0.93\beta^8)\left(1 - \left(\frac{P_2}{P_1}\right)^{1/k}\right) \qquad \text{Equation 4}$$

In order to simulate controlled leaks of hydrogen and methane gas blends, precision orifices of different diameters were employed for the tests. Figure 14 shows a picture of a ruby orifice embedded in a Swagelok fitting used in leak experimental test setup, consisting of solenoid valves, pressure transducers, thermocouples, and flow meters. Two orifices with diameter of 0.0012 in and 0.005 in were used in the experiments.

Figure 14: Orifice Gas Leak Testing Instrumentation Setup
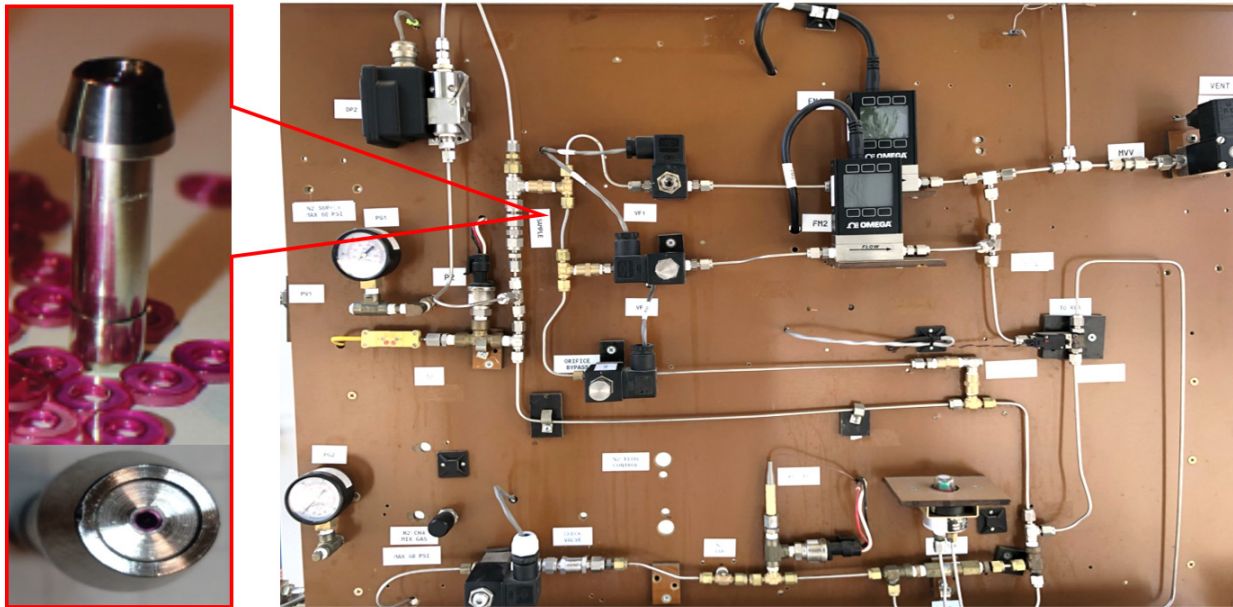
Figure 15 shows a piping and instrumentation diagram of the orifice leak test setup. Four gas blends are used for the test with nominal molar concentration of 5%, 10%, 20% and 50% hydrogen (mol.) in methane. Nitrogen gas is used for purging the system test loop and the vent stack, each regulated by a mass flow controller with flow range of 0 to 5,000 SCCM (0 to 10.59 SCFH). A differential pressure transducer is used to measure the pressure drop across the orifice. Absolute pressure and temperature of the test gas are measured upstream of the orifice. Upstream test gas pressure is regulated to achieve a differential pressure across the office between 1 and 100 psig (6.895 kPag and 689.5 kPag). The test gas flow downstream of the orifice is measured by one of two flow meters, with flow range of 0 to 100 SCCM (0 to 0.21 SCFH) and 0 to 2,000 SCCM (0 to 4.24 SCFH), respectively. The test gas exiting the flow meters is directed to a gas chromatograph (GC) test loop for compositional analysis. An electronic bypass valve, located upstream of the orifice, is used to divert test gas sample directly to the GC, prior to entering the orifice, for source gas compositional analysis. This allows for direct compositional comparison between the source test gas blend and the gas blend leaking out of the orifice.

Figure 15: P&ID of Controlled Gas Leak Testing Instrumentation Setup
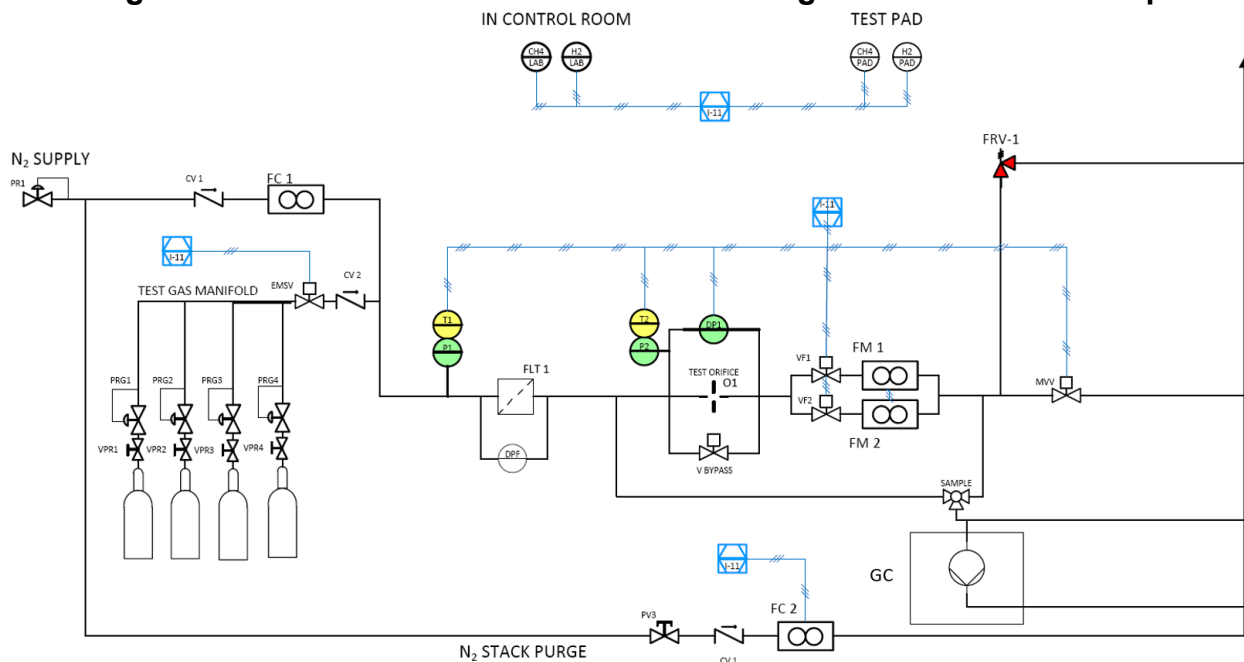
Figure 16 shows a photo of the leak test instrumentation setup with test gas cylinders (brown) and nitrogen cylinders (black). This larger part of the system is located outdoors, adjacent to the testing laboratory room, partly due to the large combined quantity of flammable gases, and the overall fire hazards associated with hydrogen gas. The system is equipped with methane/hydrogen gas detector, UV/IR flame detector, and emergency-off switch, which are set to automatically trigger audible and visible

alarms, disconnect the main test gas supply, and purge the system. The hardware instrumentation controls, gas chromatography equipment, and computers are located inside the lab.

Figure 16: Controlled Gas Leak Testing Instrumentation Setup

The gas chromatograph used for the experiments is Agilent GC 8890, which is equipped with high sensitivity thermal conductivity and flame ionization detectors. With TCD it is capable of detecting hydrogen concentration as low as 100 ppm and methane as low as 200 ppm. Lower detection limit of methane with FID is 5 ppm.

Figure 17 shows a picture of the Omega low pressure drop flow meters used for measuring gas blend flow rates during the controlled leak test experiment. Figure 17 also shows an internal diagram describing the operation of the flow meter. The meter consists of multiple laminar flow elements, through which the flow of gas is restricted to while the pressure drop across the LFEs is used to calculate the flow rate based on the Hagen-Poiseuille equation for laminar flow. The calculation requires accurate values for the density, viscosity, and compressibility factor of the gas blend being measured. Therefore, the Omega flow meters use the latest NIST REFPROP database [72], to estimate density and viscosity of custom gas mixtures entered by the user. The flow meters are also equipped with absolute pressure sensor and temperatures sensor, used to report the gas flow rate measured under different temperature and pressure

condition, in terms of standard measurement conditions of 25° C (77° F) and 14.696 psi (101.3 kPa).

Figure 17: Laminar Flow Element Flow Meter Diagram
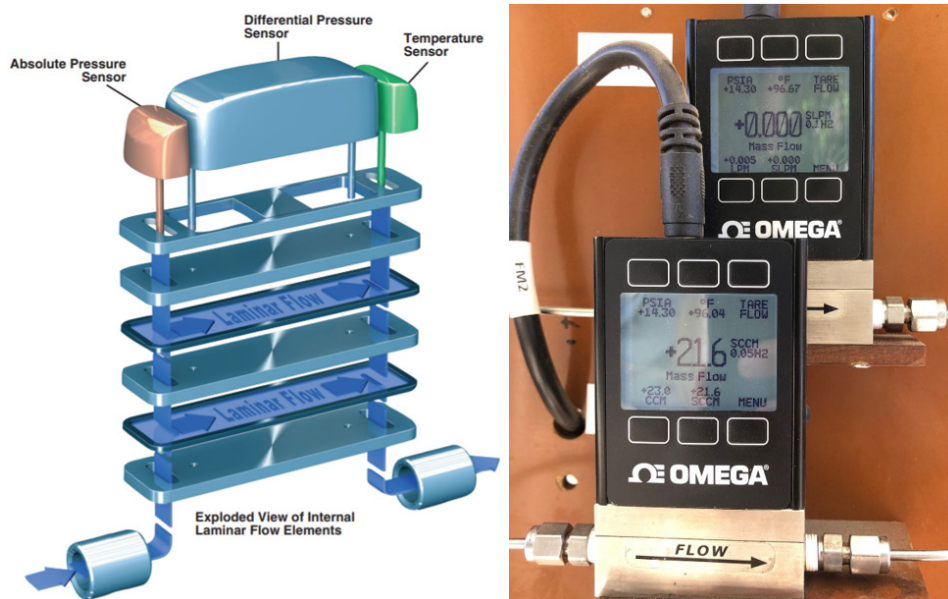
Source: OMEGA Low Pressure Drop Gas Mass Flow Meters Datasheet, https://assets.omega.com/spec/FMA-LP1600A.pdf

Figure 18 shows NI LabVIEW software control panel, designed to monitor and control the gas leak instrumentation setup shown in Figure 15 and Figure 16. NI hardware components, consisting of digital and analog input/output modules are used to interface between the LabVIEW software control application and the gas leak testing devices.

Figure 18: LabVIEW Control Panel of Gas Leak Testing Instrumentation Setup
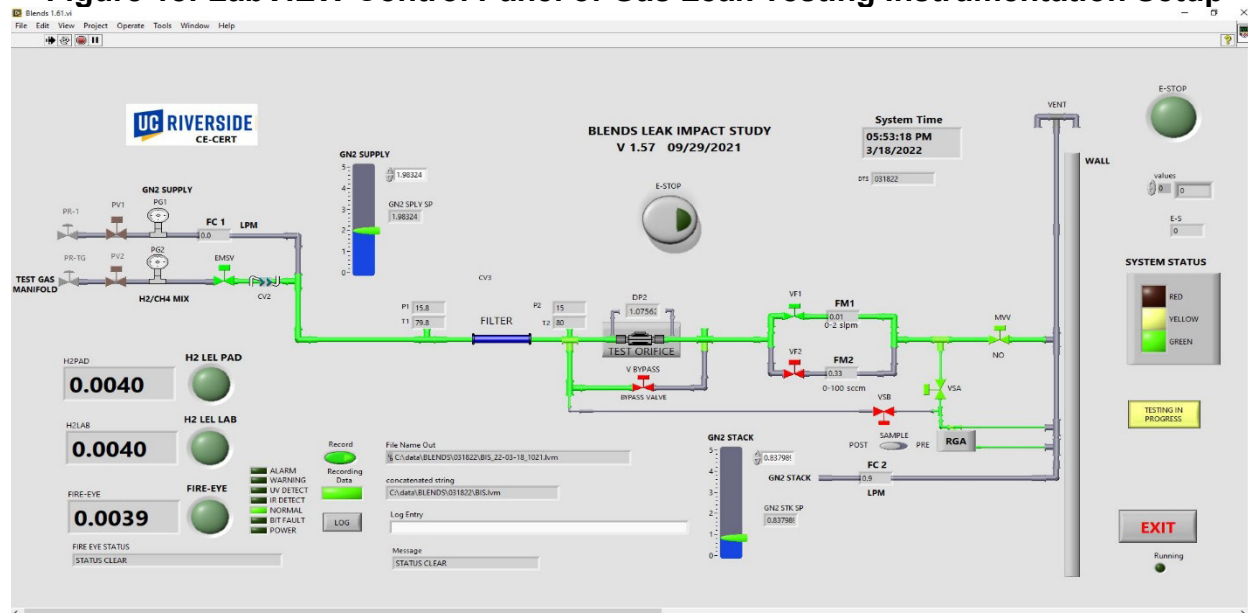
Figure 19 shows a 316L stainless steel chamber added to the gas leak test setup, intended for measurement of gas blend leaks originating from actual natural gas piping components such as valves, fittings, and joints. The chamber has dimensions of 20" x 20" x 10" and is rated for pressures of up to 13 psig.

Figure 19: Steel Chamber for Component Gas Leak Testing
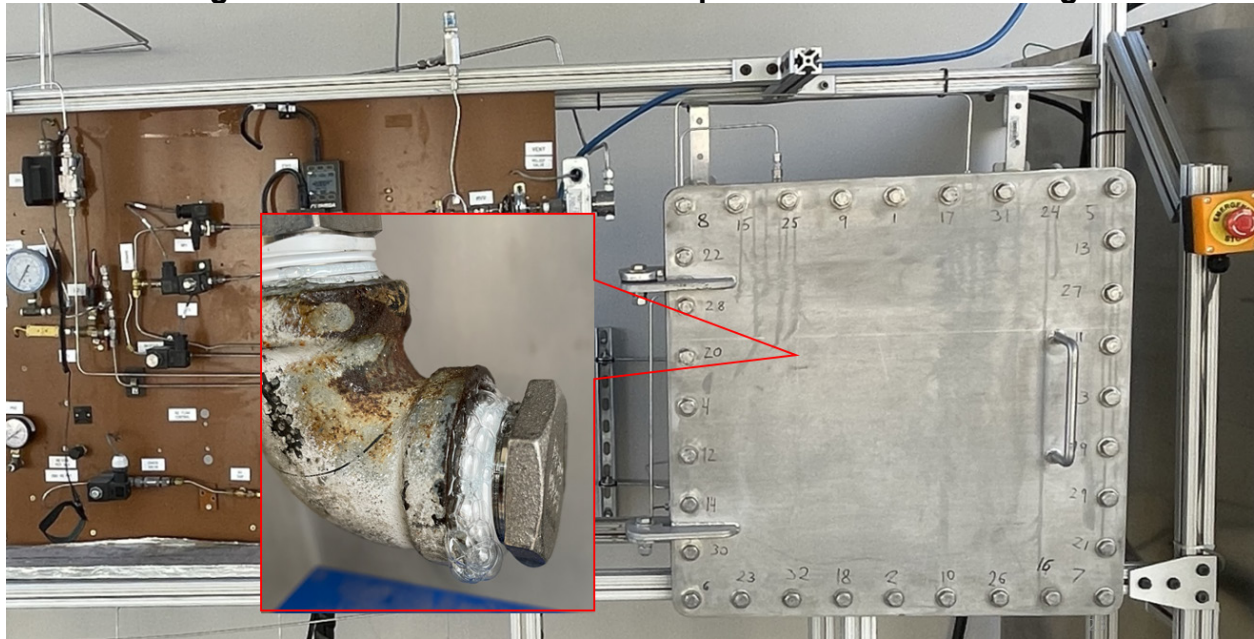
The performance of elastomers, such acrylonitrile butadiene rubber (NBR), can potentially be impacted by hydrogen in two conceivable ways:

1. Loss of elasticity (softening).

2. Acceleration of anti-oxidation stabilizer consumption (aging).

Loss of elasticity in this context assumes hydrogen directly causes micro-scale damage to the NBR, which is suggested by the findings of Pacific Northwest National Laboratory (PNNL) in the H-Mat project [73]; in practical terms, such damage would lead to leaks though NBR seals and performance degradation of NBR components, such as pressure regulator diaphragms.

Accelerated aging also results in premature seal failure, however, the damage mechanism in this case would not be directly induced by hydrogen, but by hydrogen consuming or neutralizing anti-oxidation compounds that protect the polymer from being oxidized [74]. Oxidation leads to polymer chain-scission and loss of elasticity. Empirical testing is needed to determine if loss of elasticity and/or accelerated aging will occur under the operating conditions (temperature, pressure) of natural gas piping systems when hydrogen is present.

Testing of NBR material was performed in conjunction with the medium density polyethylene (MDPE) material testing in Task 2b. The approach was to create NBR gaskets that would be installed with some of the injection molded MDPE specimens (UTV[1] specimens) (see Figure 20). In this configuration, the gaskets affect the seal, and it was assumed that differences in leakage of NBR gaskets exposed to hydrogen versus NBR gaskets not exposed to hydrogen would show the impact of hydrogen. Unfortunately, the NBR gaskets did not properly seal due to the test fixture's design, which was made to seal against polyethylene. This led to excessive gas consumption and the approach of using NBR gaskets had to be abandoned. The NBR gaskets that were put to test were eventually removed from the sealing surface and placed inside the UTV specimens (Figure 21) to continue their exposure to elevated temperature and gas so that oxidation induction time (OIT) test could be performed to assess hydrogen's impact on aging of NBR.

Figure 20: UTV Specimens with (right) and without (left) an NBR Gasket

---
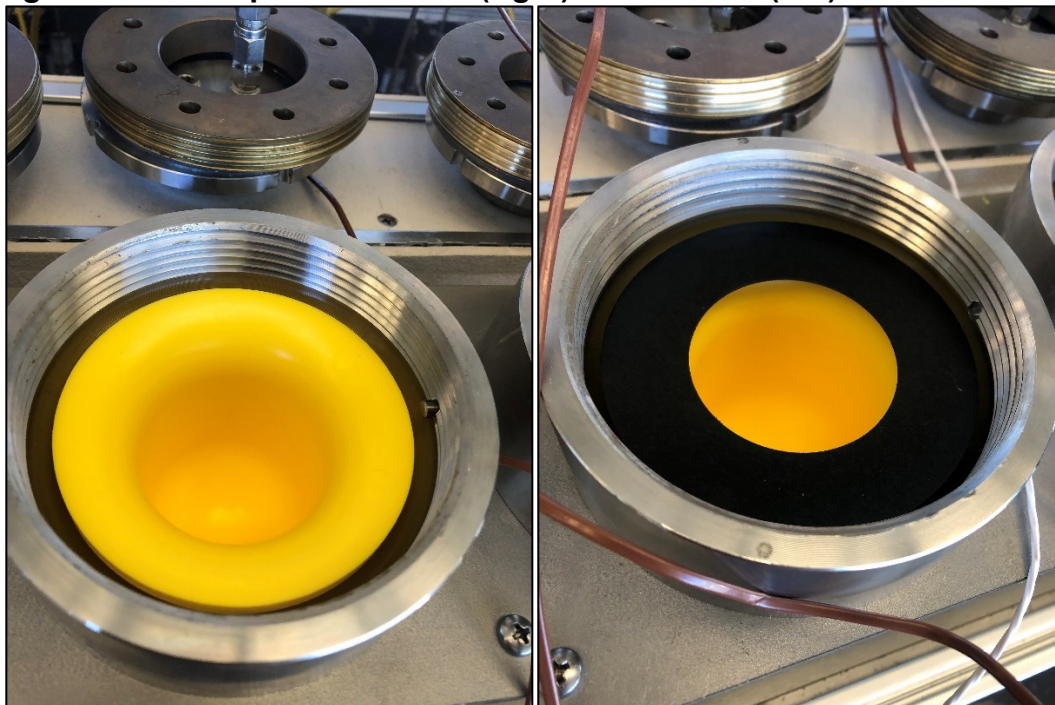
[1] The universal test vessel (UTV) specimens are described in more detail in section Long-Term Pressure Testing.

Figure 21: Example of NBR Gasket Placed inside a UTV Specimen
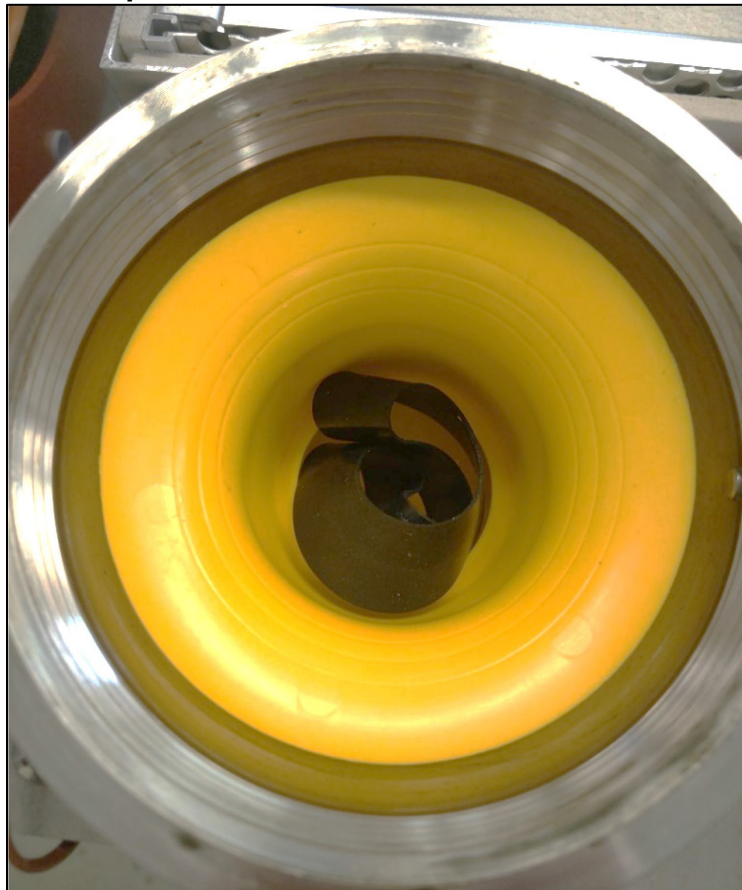
Experimental Results and Discussion

Figure 22 shows the results of the test gas blends flow measurement through an orifice with diameter of 0.0012 in, measured at various differential pressures across the orifice. Four hydrogen/methane gas blends and pure methane gas are compared.

Figure 23 shows the measurement results for an orifice with diameter of 0.005 in. The results from the two orifice tests show that for a given pressure across the orifice, gas flow rates increase as the hydrogen concentration increases in the gas mixture. This behavior can be attributed to the lower density of hydrogen gas and resulting lower density of hydrogen/methane gas mixtures compared to density of pure methane. As previously shown, the flow rated through an orifice, given by Equation 3, is dependent on gas density. It is also evident that the gas flow rate through the two orifices increases with increased differential pressure. The increase of flow rate is higher between 1 and 30 psi, and lower, nearly linear from 30 to 100 psi. This is due to increased resistance of the gas through the orifice as gas velocity increases. As the gas velocity rate of increase diminishes at higher pressures, the increase of gas flow rate with increasing differential pressure is mainly due to gas compression, with increase of gas velocity having a smaller contribution to the overall gas flow rate increase. As a

result, the gas flow rate approaches a linear dependence on differential pressure across the orifice.

Figure 22: Gas Flow Rate through Orifice with Diameter 0.0012"
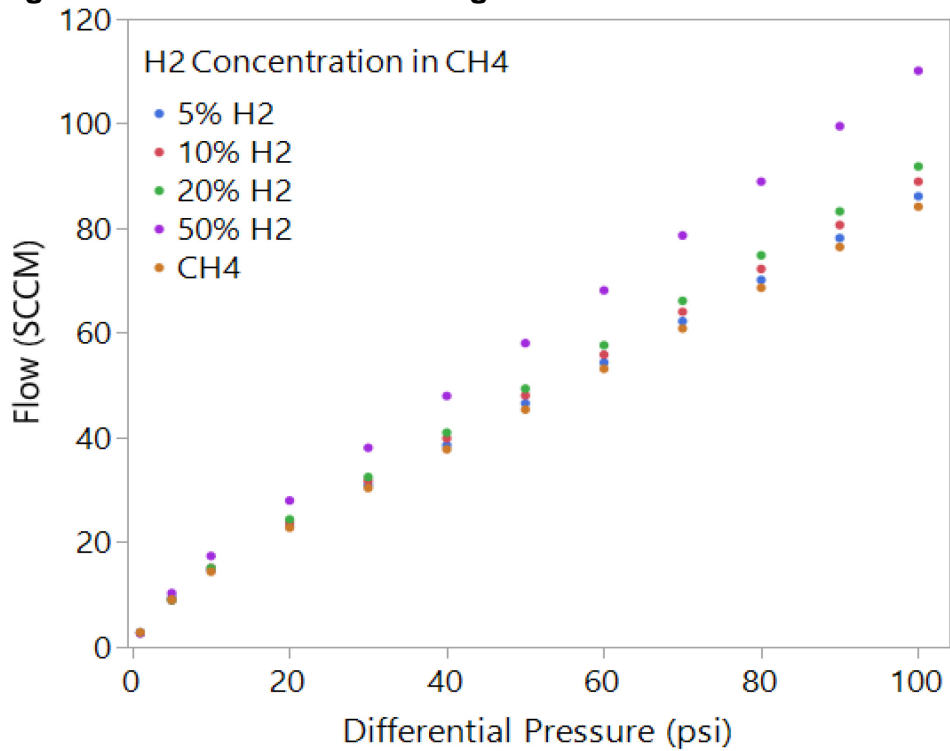
Figure 23: Gas Flow Rate through Orifice with Diameter 0.005"
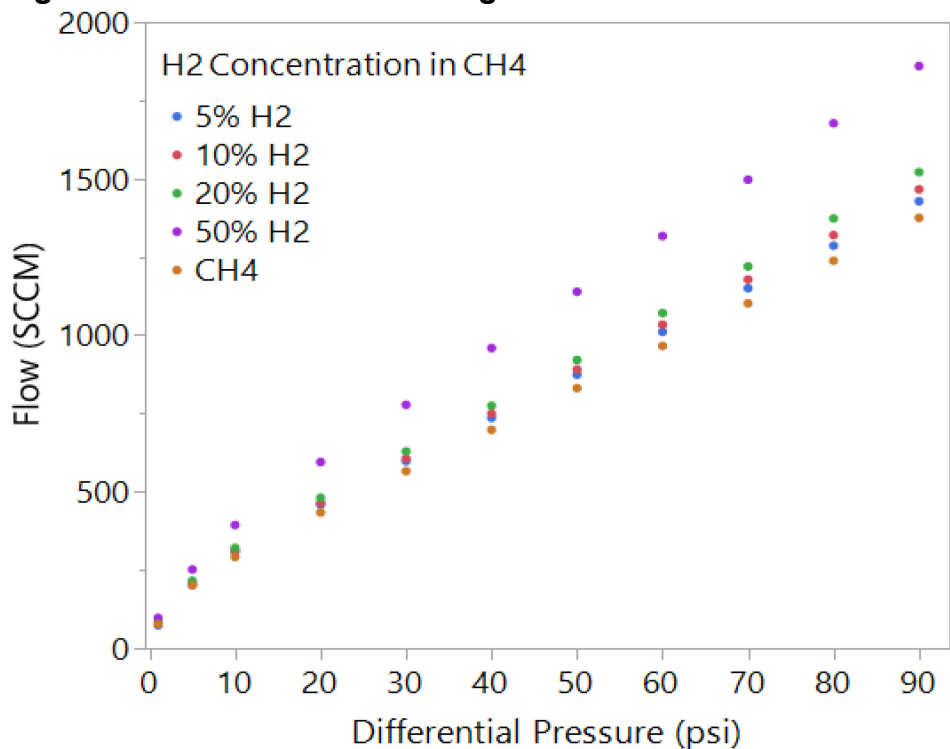
Figure 24: Reynolds Numbers of Flow through Orifice with Diameter 0.0012"
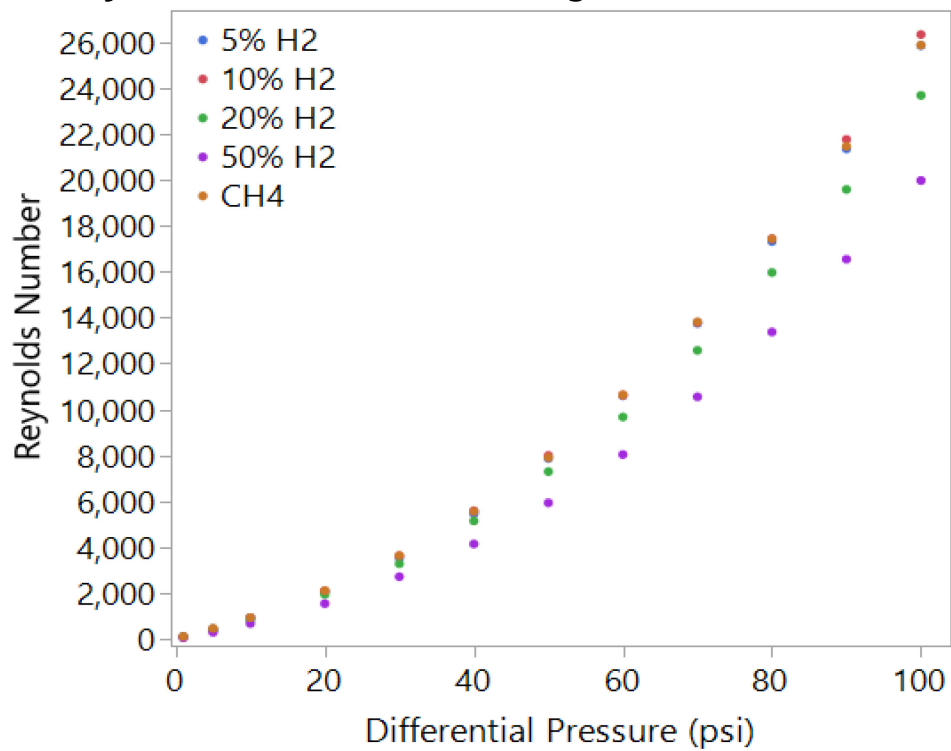
Figure 25: Reynolds Numbers of Flow through Orifice with Diameter 0.005"
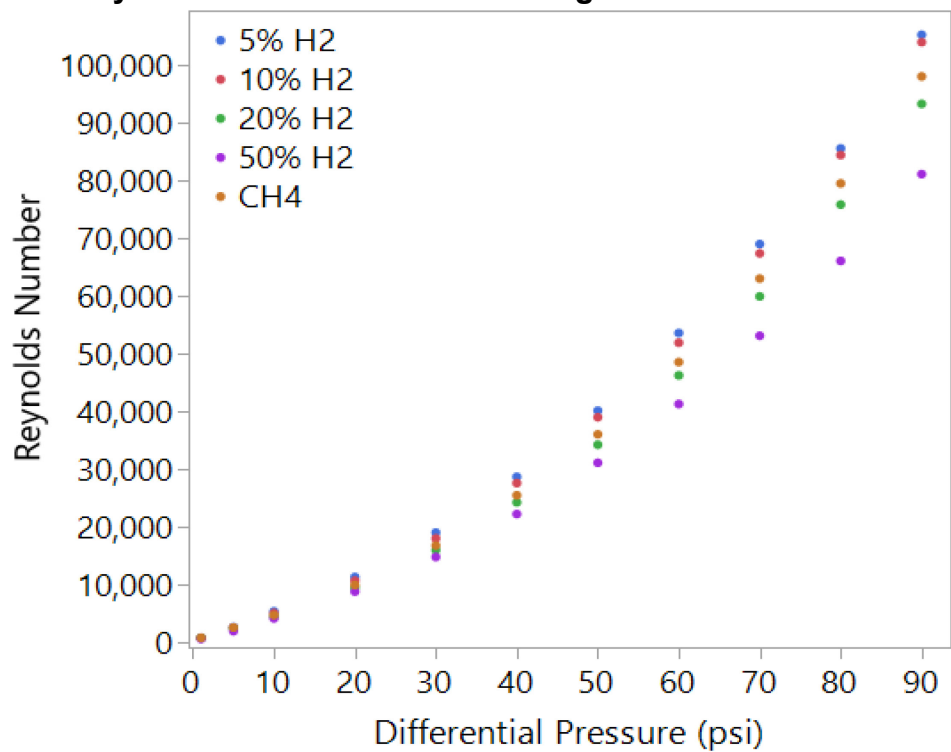
Figure 24 and Figure 25 show the calculated Reynolds numbers for the test gas flow measured trough orifice with 0.0012 in diameter, and orifice with 0.005 in diameter, respectively. The calculation is based on Equation 1, where the kinematic viscosity of specific test gas mixture is obtained from REFPROP database. Reynolds numbers for the flows through the smaller orifice suggest laminar flow differential pressure below 20 psi and turbulent flow for differential pressure above 30 psi. Reynolds numbers for the flows through the larger orifice suggest flow rates become turbulent at differential pressure of 10 psi or greater.

Figure 26 through Figure 29 show the GC compositional analysis of the four different hydrogen/methane test gas mixtures forced at different pressures through the smaller orifice with diameter of 0.0012 in, compared to source test gas mixtures bypassing the orifice. The gas mixture composition of all four test gases passing through the orifice at different pressures, appears unchanged from the original composition of the test gas mixture. This result is expected, since preferential extraction (effusion) of the lighter gas hydrogen over methane would occur with orifice diameter significantly smaller than the mean free path of hydrogen and methane, which are approximately 130 nm and 60 nm, respectively, under normal conditions (mean free path of gas molecules decreases with increasing pressure). The smaller orifice diameter (0.0012 in) corresponds to 30,480 nm, which is much greater than the requirement for gas effusion.

Figure 26: GC Results for 5% H_2 in CH_4 Gas Mixture through 0.0012" Orifice
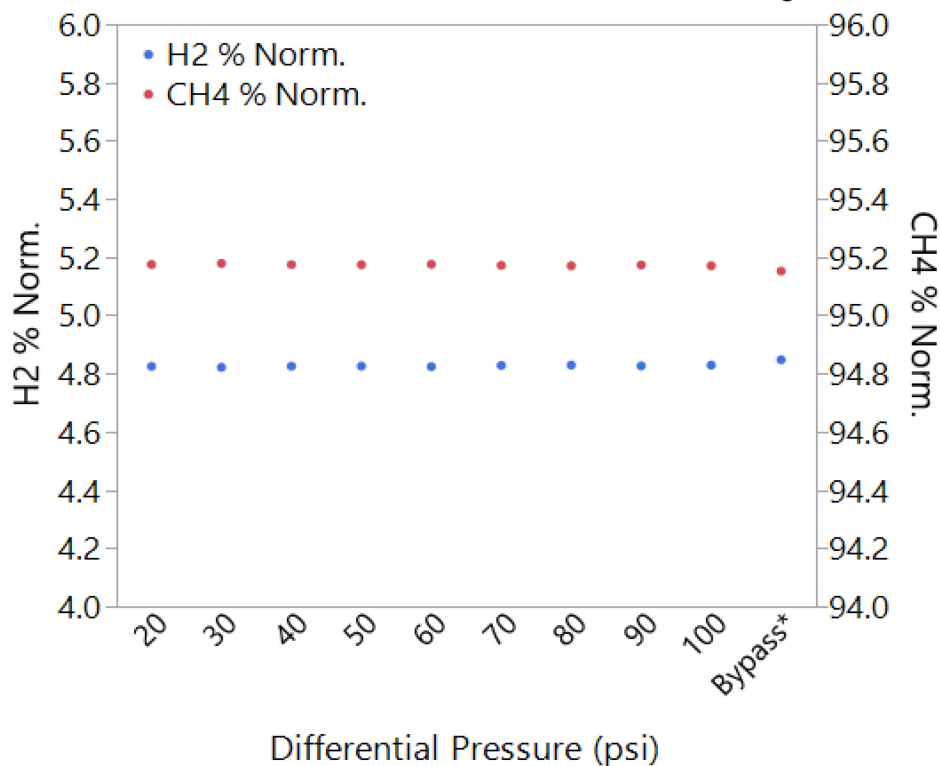
Figure 27: GC Results for 10% H₂ in CH₄ Gas Mixture through 0.0012" Orifice
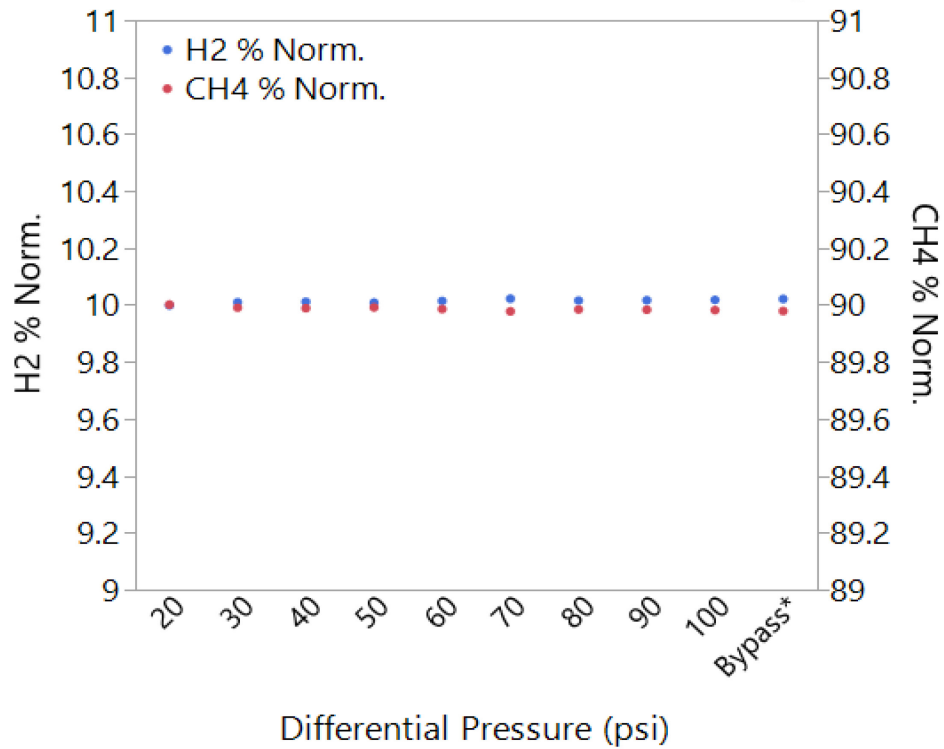
Figure 28: GC Results for 20% H₂ in CH₄ Gas Mixture through 0.0012" Orifice
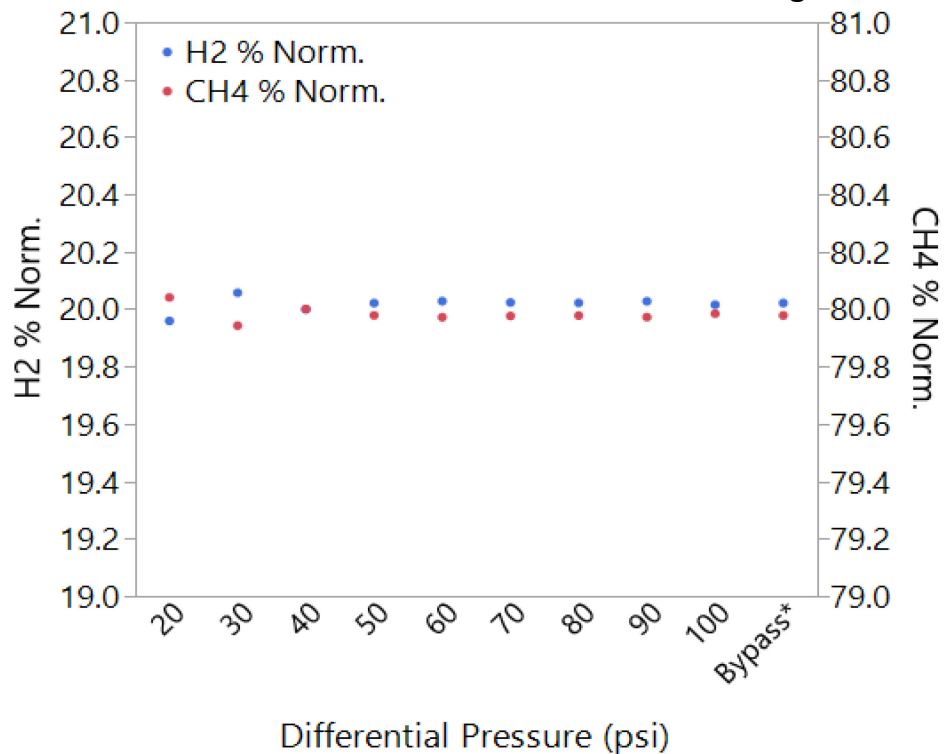
Figure 29: GC Results for 50% H2 in CH4 Gas Mixture through 0.0012" Orifice
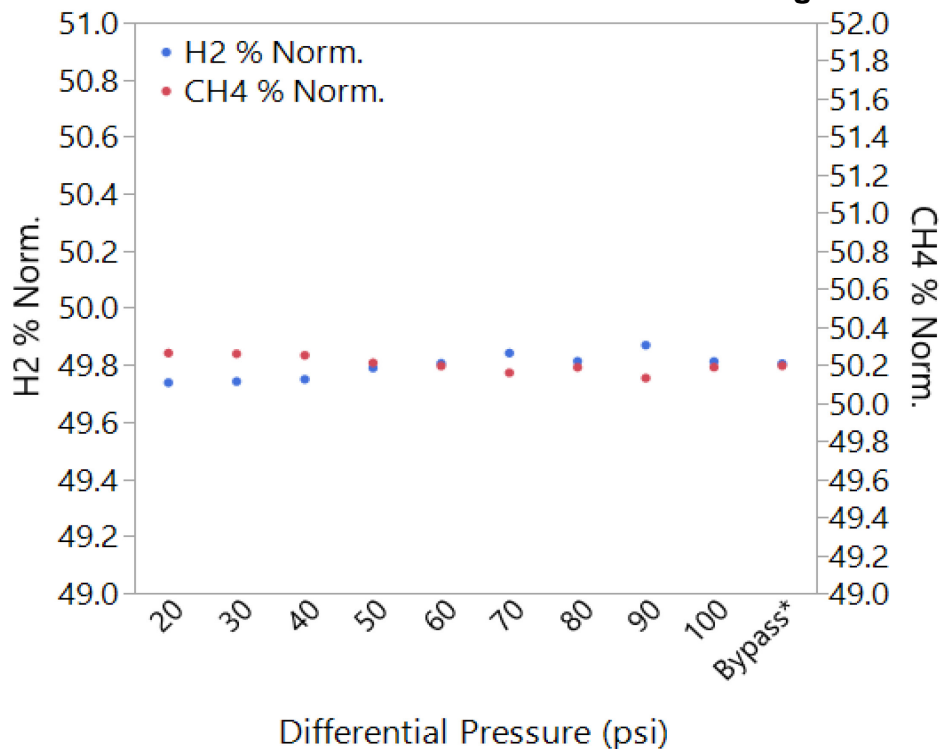
Figure 30 and Figure 31 compare the calculated orifice gas flow rates using Equation 3, to actual measured flow rates through the orifice with diameters of 0.0012 in and 0.005 in, respectively. Discharged coefficient C_d of 0.65 was used for the calculation, expansion factor ε was calculated based on Equation 4, while test gas mixture density was obtained from REFPROP database, using measured gas temperature and absolute pressure upstream of the orifice. The calculated gas flow rates indicated in the graphs by the + symbol agree well with actual measured gas flow rates designated by a circle, for both orifices and all four test gas mixtures and methane.

It can be seen from Equation 3 that with all other variables being equal, including orifice geometry, differential pressure, upstream pressure and temperature, the gas flow rate through the orifice is inversely proportional to the square root of the density of the gas. Thus it is expected that the flow rate for pure hydrogen through an orifice would be approximately 2.8 times the flow rate of pure methane, under viscous turbulent flow assumption. These results are in agreement with the experimental findings from the Gas Technology Institute's evaluation of leak rates for three different hydrogen/methane gas blends through orifices with diameters of 0.03, 0.01, and 0.003 inches [35].

Figure 30: Calculated Gas Flow Rates through Orifice with Diameter 0.0012"
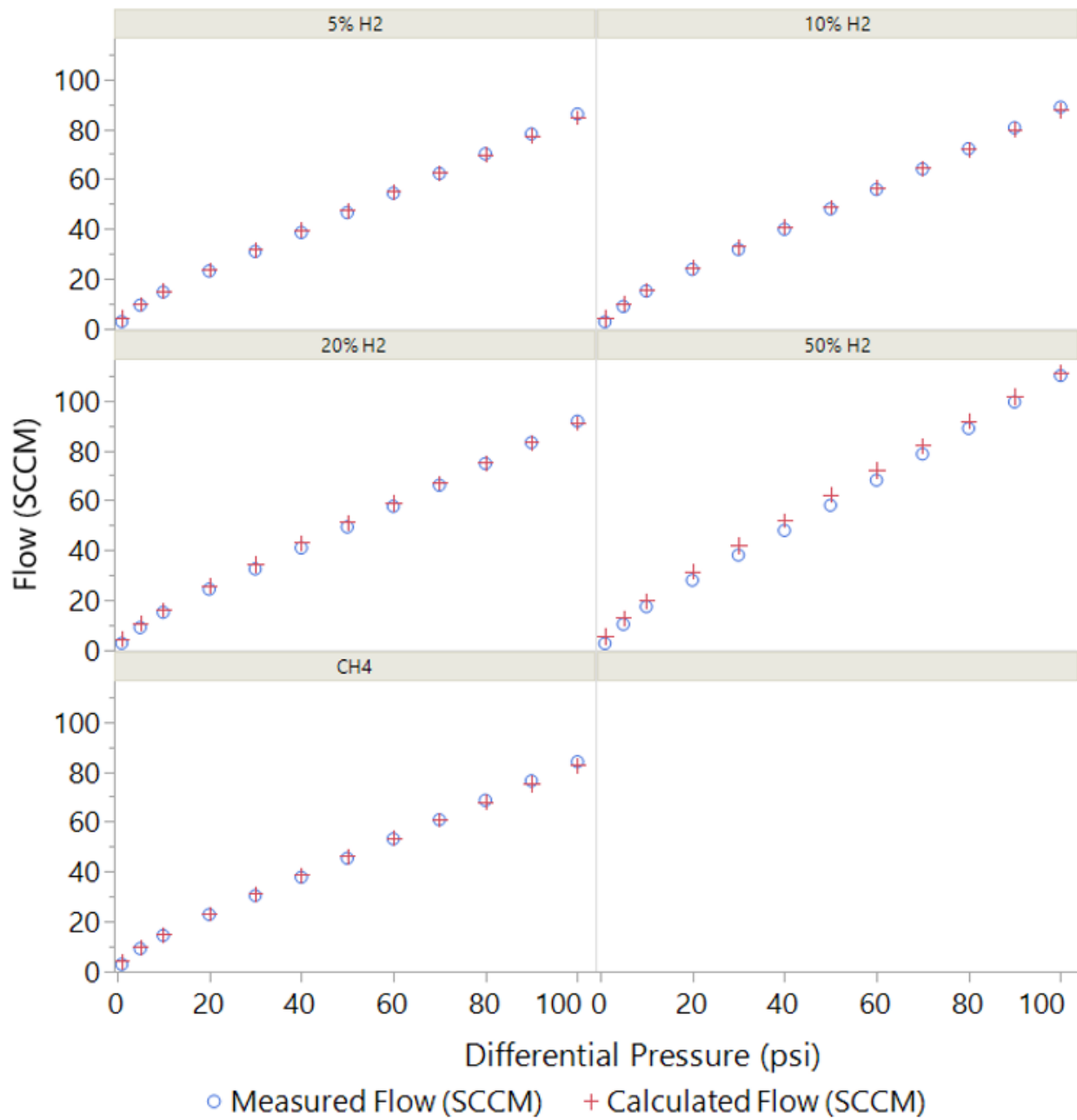
Figure 31: Calculated Flow Rates through Orifice with Diameter 0.005"
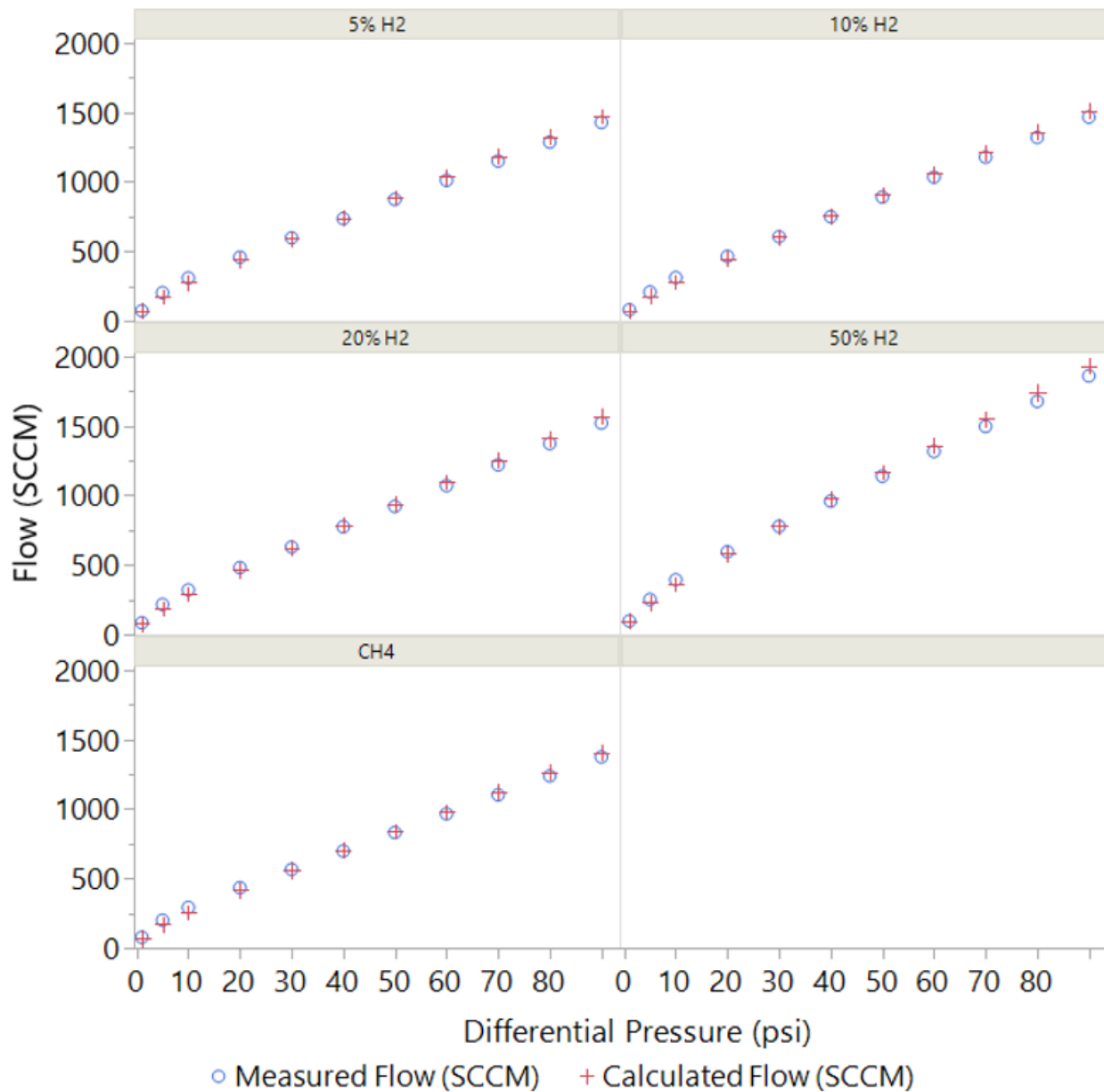
Table 6 lists densities of the four hydrogen/methane gas blends used for leak testing at standard conditions. The square root of the ratio of the gas blend density to 5% hydrogen gas blend density is compared to the ratio of flow rate of the gas blend to the to the flow rate 5% hydrogen gas blend, which were measured through the two orifices with diameters of 0.0012 in and 0.005 in. It can be seen that the gas flow rate increases with increasing concentration of hydrogen in the gas blend, and follows the same trend as the square root of the density of the gas blend. Figure 32 shows the gas bend flow rate percentage increase with corresponding increase of hydrogen concentration in the hydrogen/methane gas blend.

Table 6: Gas Blends Rates Dependence

H$_2$ Gas in CH$_4$	Temp (°F)	Pressure (psia)	Density (mg/cm³)	SQRT Density Ratio to 5% H$_2$	Actual Ratio for 0.0012"	Actual Ratio for 0.005"
50% H2	77	14.696	0.3691	1.30	1.25	1.30
20% H2	77	14.696	0.5422	1.08	1.06	1.06
10% H2	77	14.696	0.5992	1.02	1.03	1.02
5% H2	77	14.696	0.6280	1.00	1.00	1.00

Figure 32: Gas Blend Flow Rate Dependence on Square Root of Gas Blend Density According to Orifice Model

$$\Delta Q \approx \sqrt{\frac{\rho_{CH4}}{\rho_{mix}}}$$
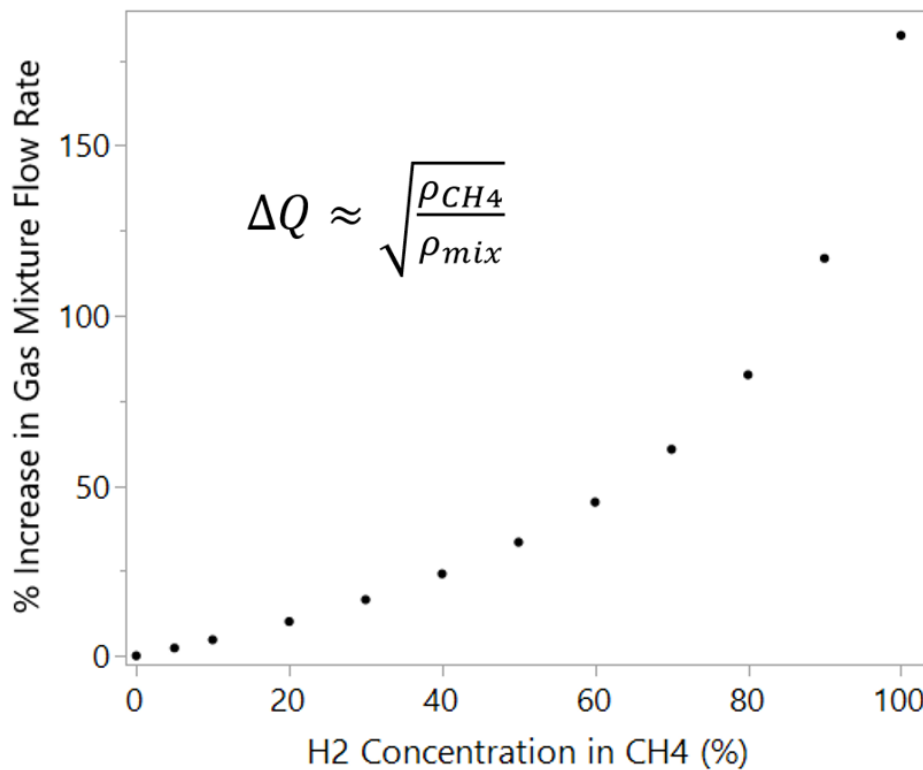
Following controlled gas leak tests through precisions orifices, an attempt was made to test actual piping components in the chamber shown in Figure 19. However, the large volume of the chamber presented some challenges in purging the air out the chamber with nitrogen prior to running experiments, and then purging out all hydrogen/methane mixture prior to opening the chamber. The large volume of the chamber presented further challenges to the elemental composition analysis of the leaked gas by GC, as the leaked gas volume was significantly less than the amount of nitrogen gas in the chamber. Therefore, the project team designed a smaller chamber, based on a 4" diameter pipe, shown in Figure 33, for testing from smaller components such as the riser valve as shown in Figure 33. Due to the changing composition of the gas leaking out of chamber during the experiment, which is a mixture of the leaked

hydrogen/methane gas blend and the nitrogen in the chamber, the flow measurement had to be performed upstream of the leaking component under testing, and thus the upstream pressure was limited to 50 psig, because of the flow meter limitations.

Figure 33: Small Chamber Instrumentation Setup for Component Leak Testing
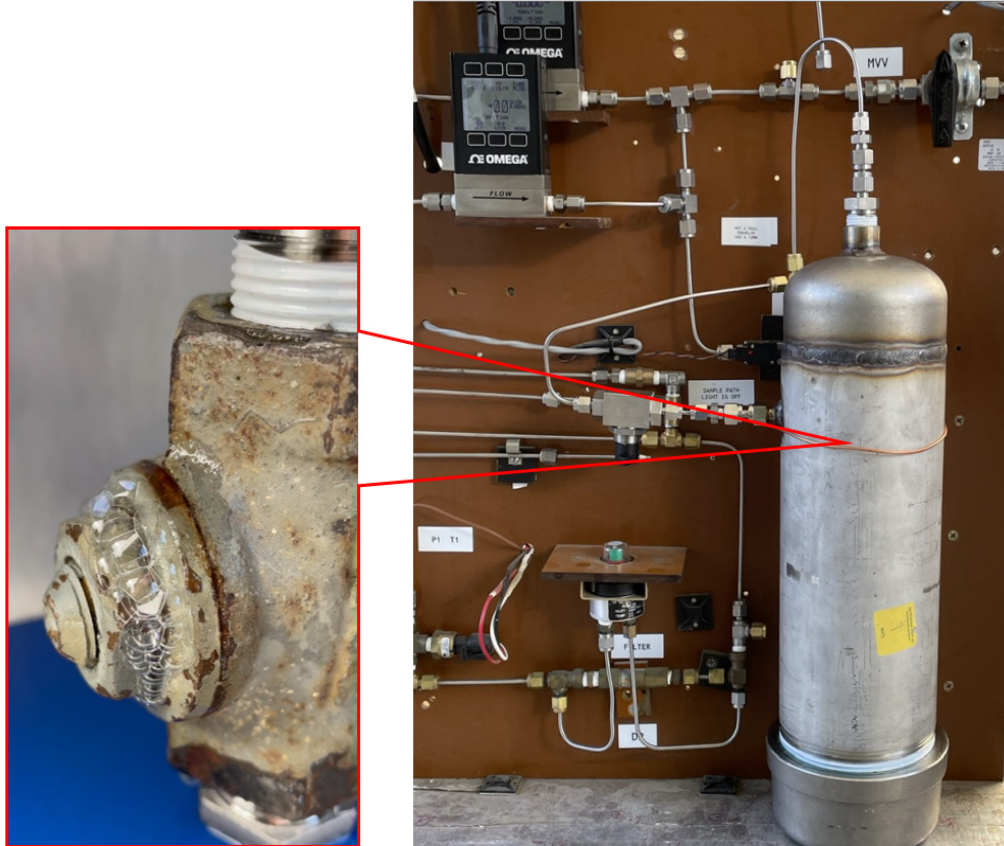
Figure 34 shows the GC analysis of gas from the test chamber after leak testing was conducted for 30 min with gas blend containing 50% hydrogen in methane, at the maximum differential pressure of 50 psi across the leak of the riser valve. The GC chromatogram shows that 60% of the gas was nitrogen, but the hydrogen and methane gases each accounted for 50% of the remaining gas, which is the same ratio in the source test gas blend.

Figure 35 shows the results of the measured leak flow rates through the raiser valve seal, for the four test gas blends under differential pressure ranging from 10 to 50 psi. The measured flow rates did not show dependence on hydrogen concentration, but more importantly the gas flow measurements were not reproducible. Some factors contributing to the lack of measurement reproducibility could be the varying ambient temperature and compression of the seal material under different pressures. Measurements of the gas blend leak rates from threads of an elbow NPT fitting (Figure 19), also failed to demonstrate good reproducibility. The UCR project team is working on modifying its setup for measurement of gas leaks originating from pipe components.

Figure 34: Chromatography Analysis of Leaked Gas in Chamber
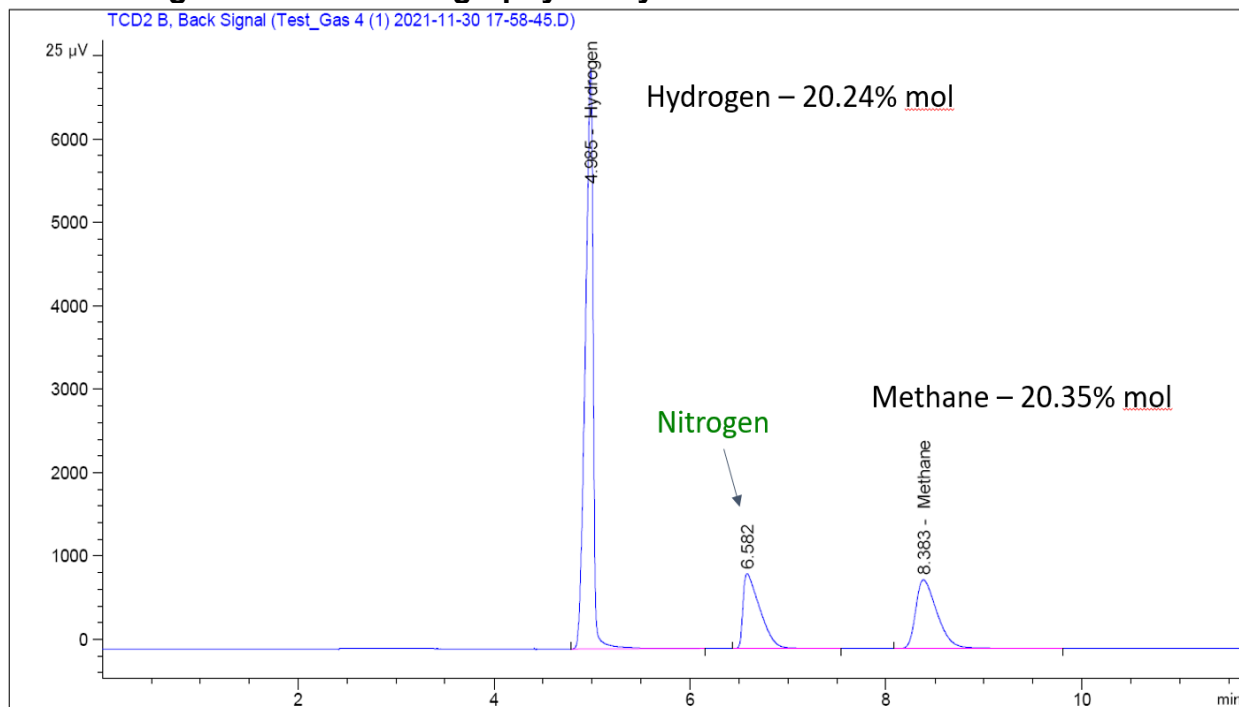
Figure 35: Gas Flow Rates through Leaking Valve Seal
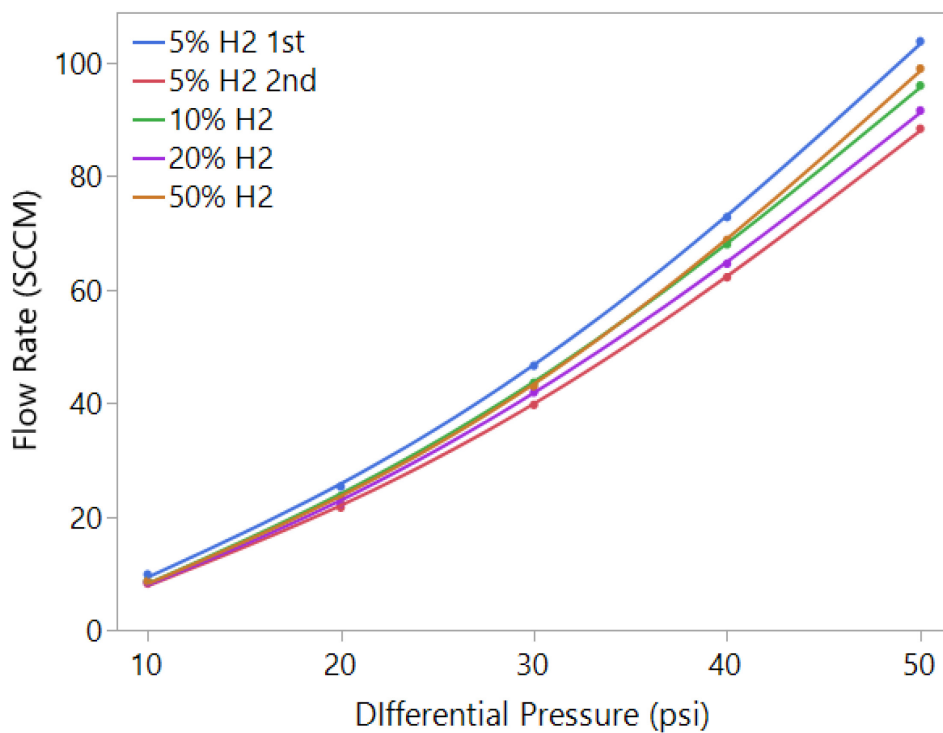
Testing of leak rates through NBR gaskets was abandoned due to excessive leaking and thus no leak rate results are available. As of the writing of this report, the long-term 65°C UTV pressure tests are still ongoing, therefore, no results of post-exposure OIT tests were available to perform an analysis of aging differences between the gaskets exposed to 100% methane and gaskets exposed to the 20% hydrogen-methane blend. Table 7 shows the OIT test results from the virgin NBR material.

Table 7: OIT Results for Virgin NBR

Sample ID	Rep 1 (min)	Rep 2 (min)	Rep 3 (min)	Rep 4 (min)	Rep 5 (min)
NBR gasket	> 220	> 220	> 220	> 220	> 220

OIT tests of the NBR material are planned for all specimens that have been exposed to pressure testing at 65°C; completion of pressure testing is pending as of writing of this report.

Conclusions

Gas leak measurements were performed with pure methane and gas blends of 5%, 10%, 20%, and 50% hydrogen in methane, through orifices with diameters of 0.0012 and 0.005 in. The findings demonstrated volumetric leak rates increase with hydrogen concentration in the gas blend (Figure 22 and Figure 23). Calculated Reynolds numbers (Figure 24 and Figure 25) for the measured flow rates, suggest predominantly turbulent flow through the two test orifices. Calculated leak flow rates based on orifice model (Figure 30 and Figure 31), are in good agreement with the experimental findings. According to this model, gas blend leak flow rate increases with increasing concentration of hydrogen in the gas blend, inversely proportional to the square root of the density of the gas blend.

Based on gas mixture compositional analysis performed by GC, hydrogen did not leak preferentially to methane through the test orifices or tested leaking valve.

Measurements of gas blend flow rates through leaks in actual piping components, including a valve seal and fitting threads, failed to produce reproducibility required to establish a relationship between leak flow rate and hydrogen concentration in the gas blend. The experimental leak measurement setup design is currently being revised, to achieve more accurate measurement of gas blend flow rates from leaks originating in actual piping components.

Testing of NBR gaskets under pressure was abandoned because of excessive leaking. The excessive leaking was due the UTV rig's specimen fixture design, which was designed to seal against the specimens directly. The NBR gaskets were removed and placed inside their respective UTV specimen to at least obtain aging data via OIT testing once the UTV specimens fail. This aging data could not be obtained prior to the contractual end date of this project.

Recommendations

Under the assumption of viscous turbulent flow for gas leaks in the natural gas pipeline system, originating from joints, threads, cracks, and pinhole defects, gas blends of hydrogen and methane would leak at a higher volumetric flow rates compared to pure methane, under the same conditions. The increase of flow rate is inversely proportional to the square root of the specific gravity of the hydrogen/methane gas blend. Thus for a gas blend containing 10% hydrogen the expected increase in flow rate is 5% compared to pure methane, while for 20% hydrogen gas blend the increase in leak flow rate is 10%.

Despite the increase of total volumetric gas flow rate with the blending of hydrogen with natural gas, the overall methane emissions would decrease, while the overall energy loss due to leaks would remain relatively unchanged due to the lower energy density of hydrogen compared to methane.

Even if majority of hydrogen-natural gas blend leaks can be attributed to permeation or viscous flow, which both result in larger volumetric flow rates with increased concentration of hydrogen in the gas blend, other leak mechanisms should be considered. It has been demonstrated by others that hydrogen and methane could leak out of pipe threads at nearly identical flow rates due to highly tortuous leakage path of gas molecules and their increased wall collisions frequency [28]. Therefore, a good understanding of the specific leak flow mechanism is necessary to accurately predict the change of gas leak flow rates with gas blends of varying concentration of hydrogen.

The lower energy content of hydrogen gas compared to methane, means that a volume of hydrogen more than three times that of methane is necessary to deliver the same amount of energy. Therefore, without any changes in the natural gas transmission and distribution pipeline system, larger operating pressures may be required with hydrogen-methane gas blends to deliver the same amount of energy comparable to pure methane. Increasing operating pressure would result in increased leak flow rates. Thus any changes to operating gas pressure should consider gas leak rates, among other factors, such as integrity of the system.

Hydrogen gas has significantly broader flammability range, much lower ignition energy, and higher flame velocity compared to natural gas. Thus, due to the fire hazards associated with hydrogen gas blend leaks from the natural gas system, special considerations need to be made with respect to updating existing leak detection, maintenance, and repair procedures.

Testing of elastomeric component performance in the presence of hydrogen is important as they are used for pressure regulators diaphragms and various seals. GTI recommends that NBR and other elastomers be tested in form-factors applicable to operational conditions, e.g. regulator diaphragms and O-ring seals, with test conditions that address long-term performance. Pressure testing can then provide leak rate evolution and/or time-to-leak data that gas utilities can use to inform their system

integrity management decisions. Aging tests are also recommended to determine if hydrogen reduces the performance of elastomer seals via an accelerated consumption of anti-oxidation stabilizers.

To continue with the NBR evaluation work that was not completed in this project, GTI suggests a dedicated project for testing common NBR components, such as pressure regulator diaphragms. Figure 36 shows an overview of this recommendation in the context of the work completed in this project. The objective of such a project is to obtain the impact of hydrogen on the lifetime expectancy of NBR components and develop an applicable rate-process method (RPM) model for elastomer aging and lifetime prediction.

Figure 36: Overview of current project accomplishments and recommendation for future work on the impact of hydrogen on NBR components
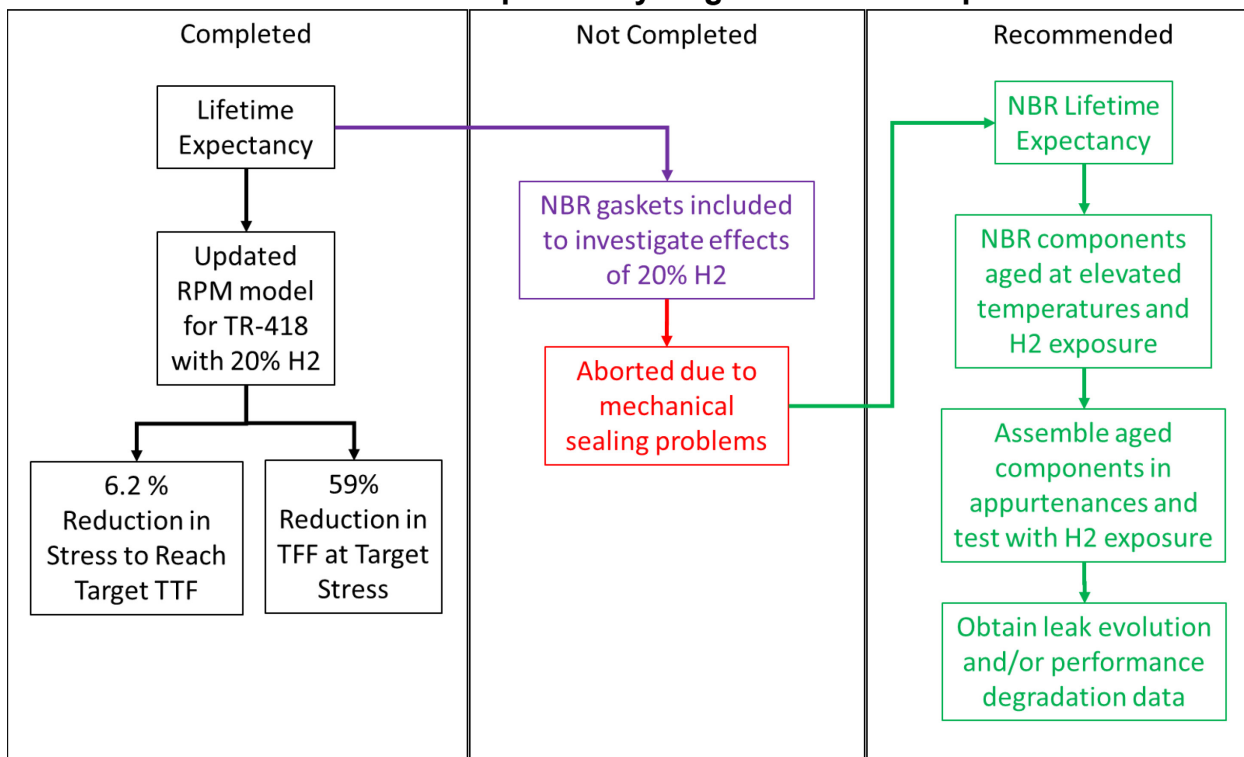
Task 2b - Experimental Assessment of the Impacts, Including Degradation, on Durability/Integrity of the Existing Natural Gas Pipeline System and the Effects of Transient/Non-homogeneous Gas Compositions

Background

The objective of Task 2b was to determine the impact of hydrogen blending on a common medium density polyethylene (MDPE) pipe material. Polyethylene can be potentially impacted by hydrogen in two different ways:

1. Acceleration of creep under stress.

2. Acceleration of anti-oxidation stabilizer consumption (aging).

Creep is the gradual plastic deformation of PE materials under a constant tensile load. This is a natural phenomenon that is inherent to PE. The pressure rating of PE pipes is based on the creep performance of the material [75].

Anti-oxidation stabilizers are chemical compounds that are added to PE to arrest or retard the natural oxidation process of PE when it is exposed to air. The anti-oxidation stabilizers are consumed over time and the amount added to PE pipes and fittings is such that they will not fail via oxidation before they reaches their intended design lifetime (e.g. 80 or 100 years). Oxidation leads to polymer chain-scission, loss of ductility, and premature failure [74].

Additional background on the lifetime of PE pipe is provided in APPENDIX 1 - Lifetime of PE Pipe.

Experimental Approach for Hydrogen Impact on Polyethylene

Long-Term Pressure Testing

Lifetime prediction of PE pipes and fittings is achieved by obtaining time-to-failure (TTF) data where a pipe or fitting is internally pressurized to various stresses at a reference temperature and elevated temperatures. A model that relates the time it takes for the material to rupture as a function of stress and temperature is fitted to the test data, becoming the lifetime prediction model. This modelling approach is called the rate process method (RPM) and it is the PE industry's standard method for predicting the lifetime of PE pipes and fittings [76]–[78].

To assess the impact of hydrogen, pressure testing on injection molded specimens made from a common type of MDPE pipe material was performed. Two sets of specimens were tested, one pressurized with methane, and one pressurized with a blend of 20% hydrogen / 80% methane, by volume. A comparison of the ductile rupture performance curve would determine the impact of hydrogen on the creep performance of the MDPE material.

The impact of hydrogen on aging can be determined by comparing the anti-oxidation stabilizer content in the MDPE before and after the pressure testing. This is done by performing oxidation induction time (OIT) tests that measure the time it takes for the material to fully oxidize under a specific test condition. The OIT test is described further in section Oxidation Induction Time (OIT) Testing.

The injection molded MDPE specimens used for pressure testing were designed by GTI and are called universal test vessels, or UTVs. These specimens were designed specifically to test polyethylene materials' ductile and slow-crack-growth performance via two geometric versions: nominal, and notched. The notched specimen contains a sharp thickness transition which mimics an electrofusion or socket fusion coupling, which represents a typical stress concentration that exists in PE piping system, from which slow-crack growth can initiate [78].

The single-sprue, single cavity tool, injection-molded design of the specimen is designed to obtain the maximum possible specimen quality.

Figure 37: CAD Model Cross-section of a "Notched" UTV in a Fixture

Pin prevents rotation of the cone, thereby preventing torqueing of the UTV

Gas seal formed by compression of the UTV by a ribbed stainless-steel cone (ribs not shown)
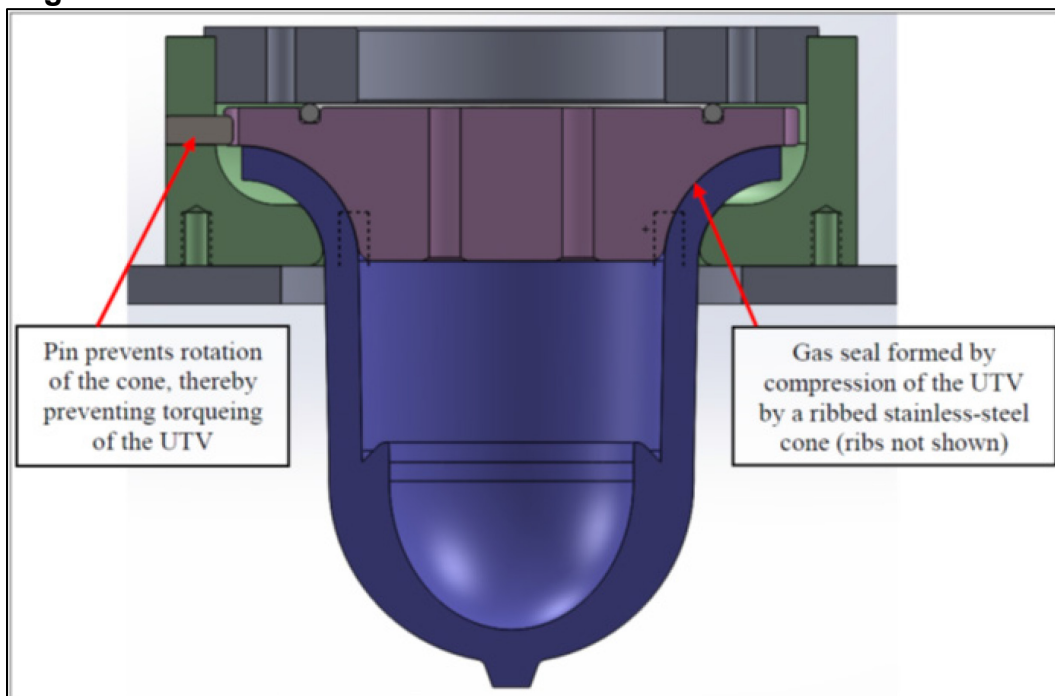
Dynamic Thermo-Mechanical Analysis (DTMA) Testing

Dynamic thermo-mechanical analysis (DTMA) testing was performed on the MDPE material to obtain the shift-factors that allow translation of pressure test results obtained under elevated temperatures to equivalent performance under a reference (operating) temperature. Pressure tests of PE pipe and fittings are conducted at elevated temperatures (typically 60°C to 90°C) in order to accelerate the failure times to within 100 to 10,000 hours. The shifting of material response across temperatures is

based on the time-temperature superposition principle, which is a behavior applicable to viscoelastic materials, such as PE [79], [80].

The results from all DTMA tests are then combined to extract the "vertical" and "horizontal" activation energies, which enable translation of results across temperatures in terms of stress and time, respectively. More information on this method can be found in the work by Mavridis and Shroff [81].

DTMA testing was performed on ASTM D638 [82] Type-V tensile specimens at three temperatures: 23°C, 60°C, and 80°C. The Type-V specimen size is chosen for the convenience of its small size (2.5-inch total length). At each temperature, frequency sweeps (from 0.01 Hz to 30 Hz) of small-displacement oscillation are performed to obtain the viscoelastic response (Figure 38).

Figure 38: DTMA Displacement during a Frequency Sweep from 0.01 HZ to 30 Hz
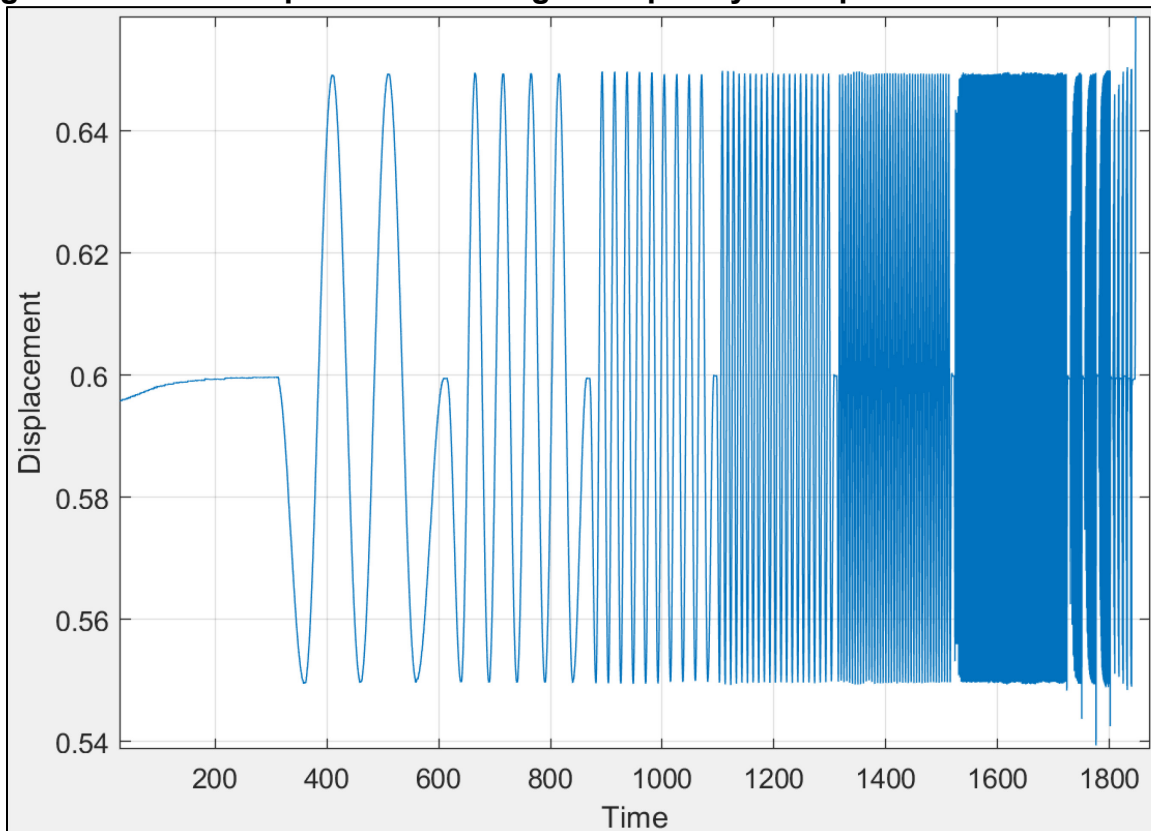
The time (horizontal) shift equation is based on the Arrhenius equation:

$$t_{ref} = t \cdot exp\left[-\frac{H}{R}\left(\frac{1}{T} - \frac{1}{T_{ref}}\right)\right]$$ Equation 5

t_{ref} = equivalent (shifted) time at reference temperature, [h]

t = test time at test temperature, [h]

T_{ref} = reference temperature, [K]

T = test temperature, [K]

H = horizontal activation energy, [cal/(mol*K)] or J/(mol*K)

R = gas constant, 1.9872036 [cal/(mol*K)] or 8.3144598 J/(mol*K)

The stress (vertical) shift equation is also based on the Arrhenius equation:

$$S_{ref} = S \cdot exp\left[-\frac{V}{R}\left(\frac{1}{T} - \frac{1}{T_{ref}}\right)\right]$$ Equation 6

S_{ref} = equivalent (shifted) stress at reference temperature [MPa] or [psi]

S = test stress at test temperature, [MPa] or [psi]

T_{ref} = reference temperature, [K]

T = test temperature, [K]

V = vertical activation energy, [cal/(mol*K)] or J/(mol*K)

R = gas constant, 1.9872036 [cal/(mol*K)] or 8.3144598 [J/(mol*K)]

Tensile Testing

Tensile testing was performed on ASTM D638 [82] Type-V tensile specimens to help determine the vertical intercept of the ductile regression line of the MDPE material (not exposed to hydrogen). The specimens were die cut from molded plaques (Figure 39, Figure 40). Tests were conducted at 23°C, 40°C, and 60°C, at two pull rates to achieve, approximately, 1-hour to break and 1-hour to yield. The 1-hour to yield tests take over 40 hours to reach the break point, therefore only one replicate per temperature was tested at this pull rate. Three replicates were tested at the 1-hour to break pull rate.

A video extensometer that tracks the specimens' smallest width throughout the test enables the measurement of the true stress-strain curve up to break. Figure 41 shows a typical example of a tensile specimen after breaking.

Figure 39: Molded Plaque, with Tensile Specimen Die Cuts
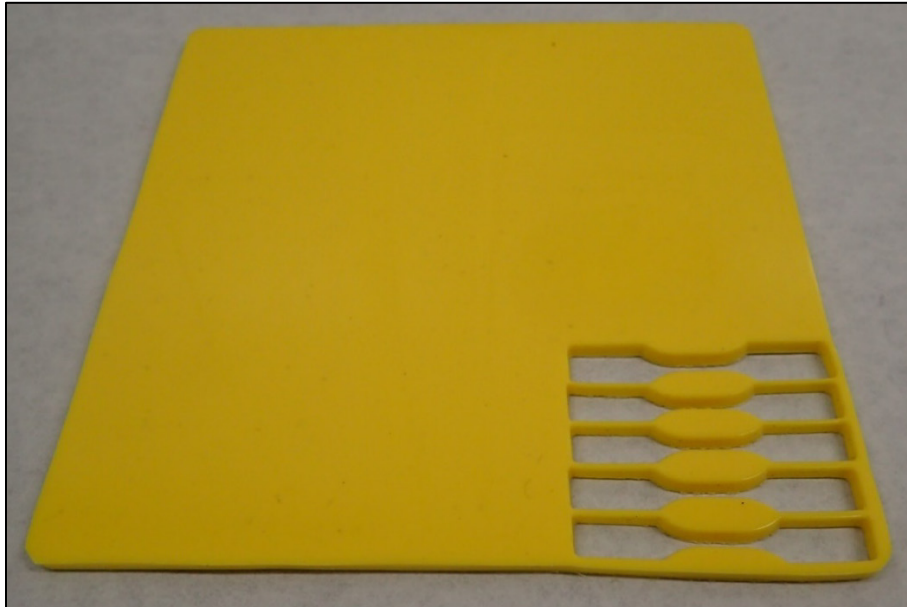
Figure 40: ASTM D638 Type-V Tensile Specimen, Die Cut from Molded Plaque

Figure 41: ASTM D638 Type-V Tensile Specimen, Post-test
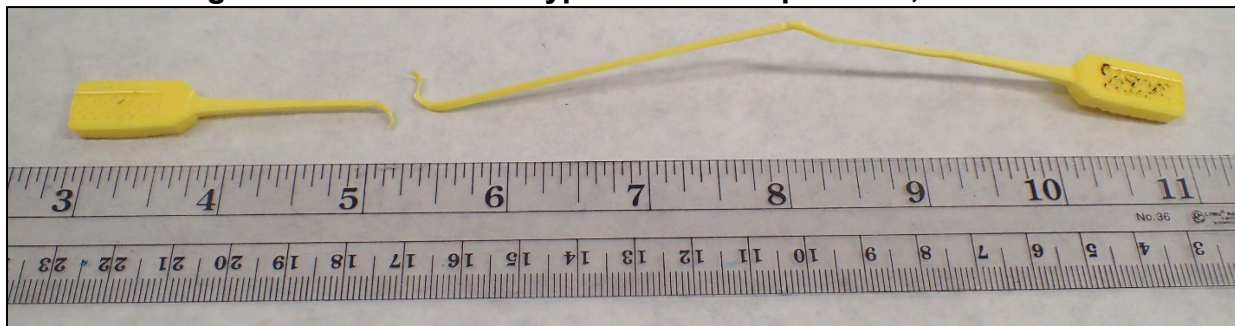
Oxidation Induction Time (OIT) Testing

The oxidation induction time test obtains an indirect measurement of the amount of anti-oxidation stabilizer compounds that are present in a polymeric material. The test is performed in a differential scanning calorimeter (DSC) where a small mass of the material is heated to 210°C under an inert atmosphere and once the set temperature is

reached, oxygen is introduced to induce oxidation [83]. The time it then takes for the material to fully oxidize is the oxidation induction time (OIT).

A relative reduction in OIT between specimens that have been exposed to hydrogen, relative to specimens that have not been exposed to hydrogen would indicate that hydrogen accelerates the consumption of stabilizers, or in other words, accelerates aging.

Experimental Results

Oxidation Induction Time Test Results
OIT test results for the virgin MDPE materials are provided in Table 8.

Table 8: OIT Results for Virgin MDPE

Sample ID	Rep 1 (min)	Rep 2 (min)	Rep 3 (min)	Rep 4 (min)	Rep 5 (min)
Inner Diameter	150.59	152.94	152.46	157.51	152.79

OIT tests of the MDPE material are planned for all specimens that have been exposed to pressure testing at 65°C; completion of pressure testing is pending as of writing of this report.

Dynamic Thermo-Mechanical Analysis
DTMA testing obtained a horizontal activation energy of 23483 cal/(mol*K), and vertical activation energy of 1720 cal/(mol*K). These values are typical for pipe-grade polyethylene [84]. These activation energies are useful for translating the UTV pressure test results – hoop stress and time-to-failure – that are obtained at elevated temperatures to equivalent performance results at a reference temperature (23°C) that is closer to actual pipe operating temperatures.

Tensile
The tensile tests results are shown in Figure 42 through Figure 53. The true stress-strain curves have been derived from these tests. Each figure displays:

- The force versus displacement plot with the yield point and peak force highlighted.

- The true stress-strain curve with the yield point, peak force, and peak true stress highlighted.

Tabulated results are of the highlighted points on in the figures are provided in Table 9.

Figure 42: 1hr-to-break Tensile Test, 23°C, Replicate 1. Force-displacement (left), True Stress-strain (right).
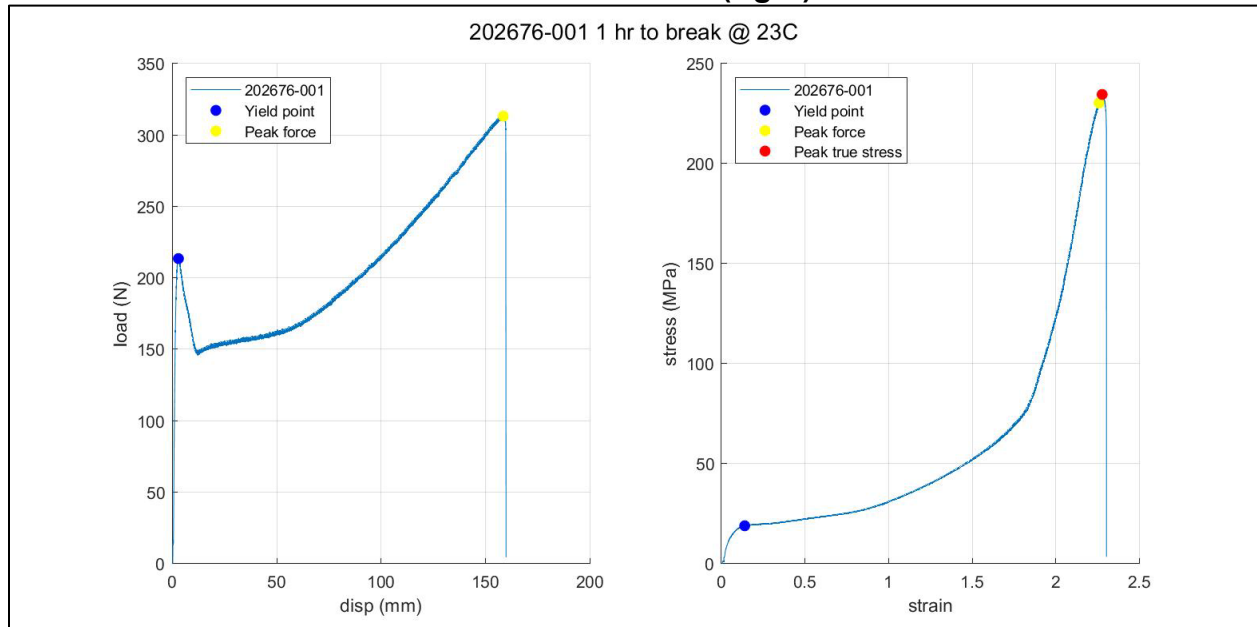
Figure 43. 1hr-to-break Tensile Test, 23°C, Replicate 2. Force-displacement (left), True Stress-strain (right).
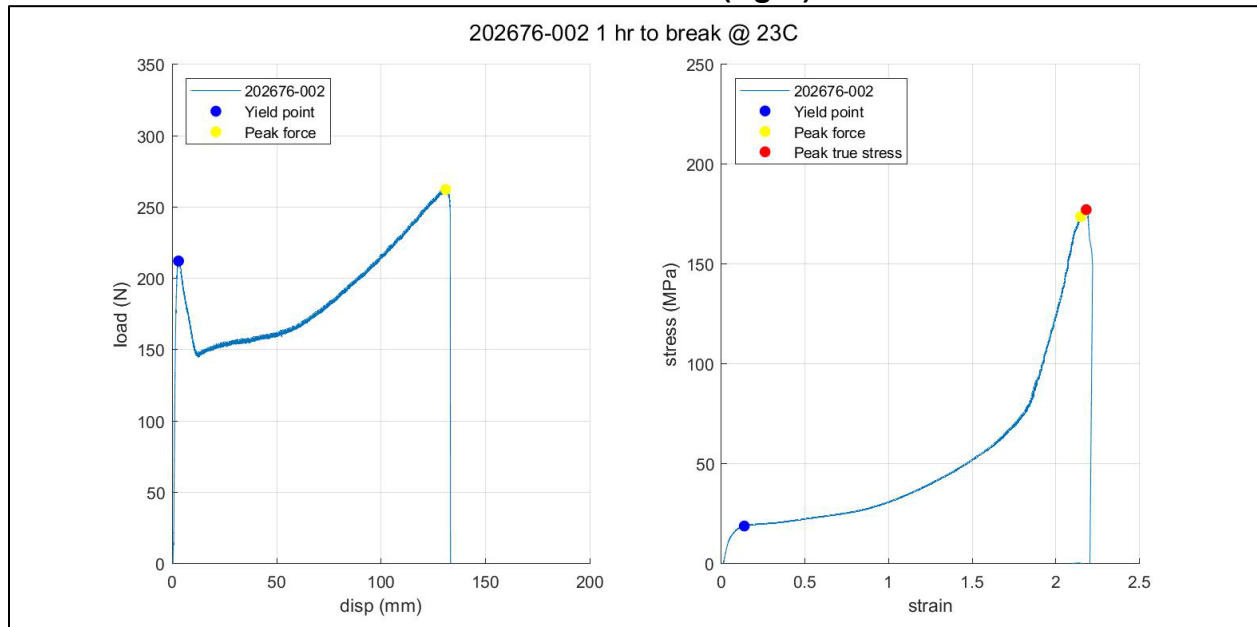
Figure 44: 1hr-to-break Tensile Test, 23°C, Replicate 3. Force-displacement (left), True Stress-Strain (right)
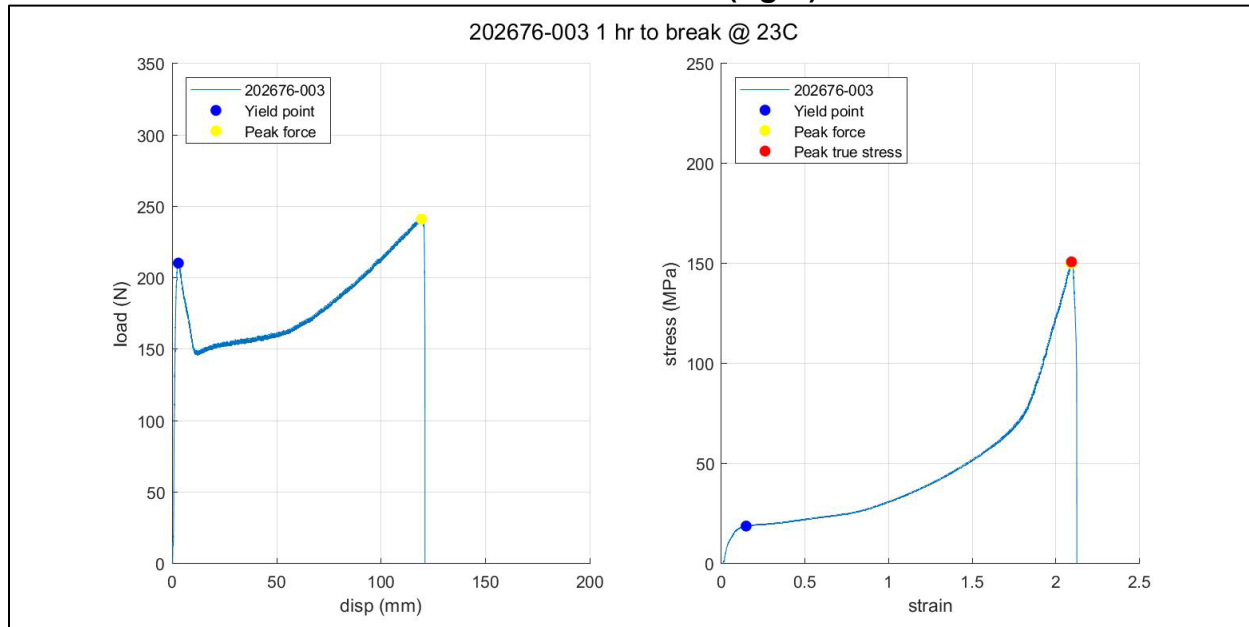
Figure 45: 1hr-to-yield Tensile Test, 23°C, Replicate 1. Force-displacement (left), True Stress-strain (right).
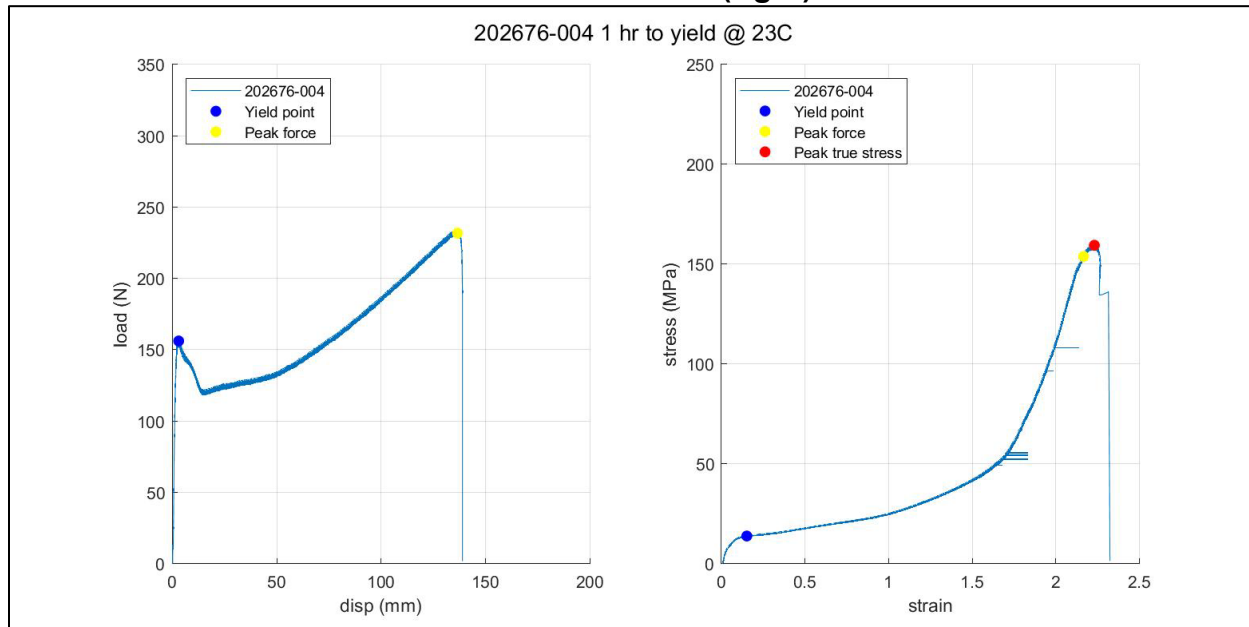
Figure 46: 1hr-to-break Tensile Test, 40°C, Replicate 1. Force-displacement (left), True Stress-strain (right).
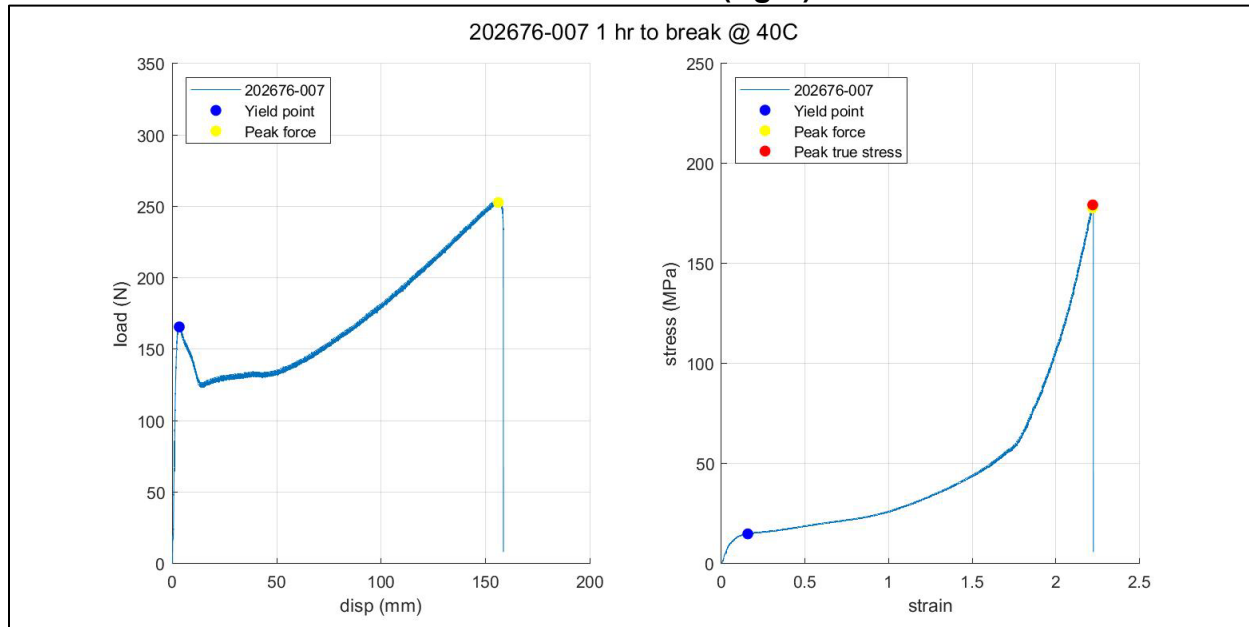
Figure 47: 1hr-to-break Tensile Test, 40°C, Replicate 2. Force-displacement (left), True Stress-strain (right).
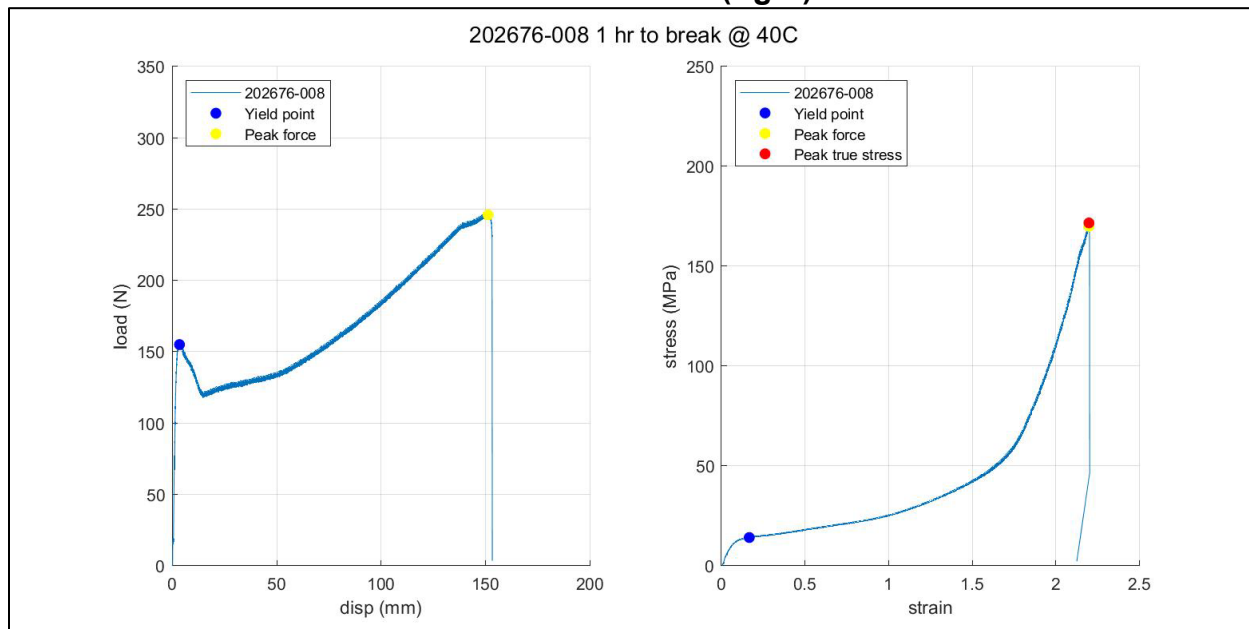
Figure 48: 1hr-to-break Tensile Test, 40°C, Replicate 3. Force-displacement (left), True Stress-strain (right).
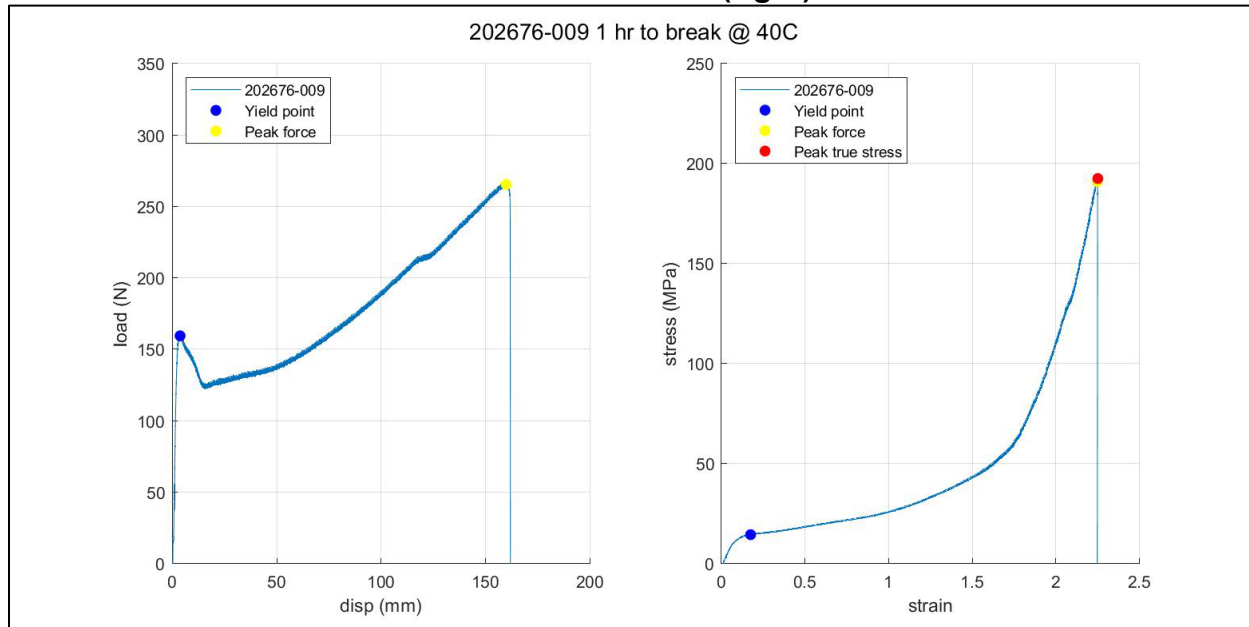
Figure 49: 1hr-to-yield Tensile Test, 40°C, Replicate 1. Force-displacement (left), True Stress-strain (right).
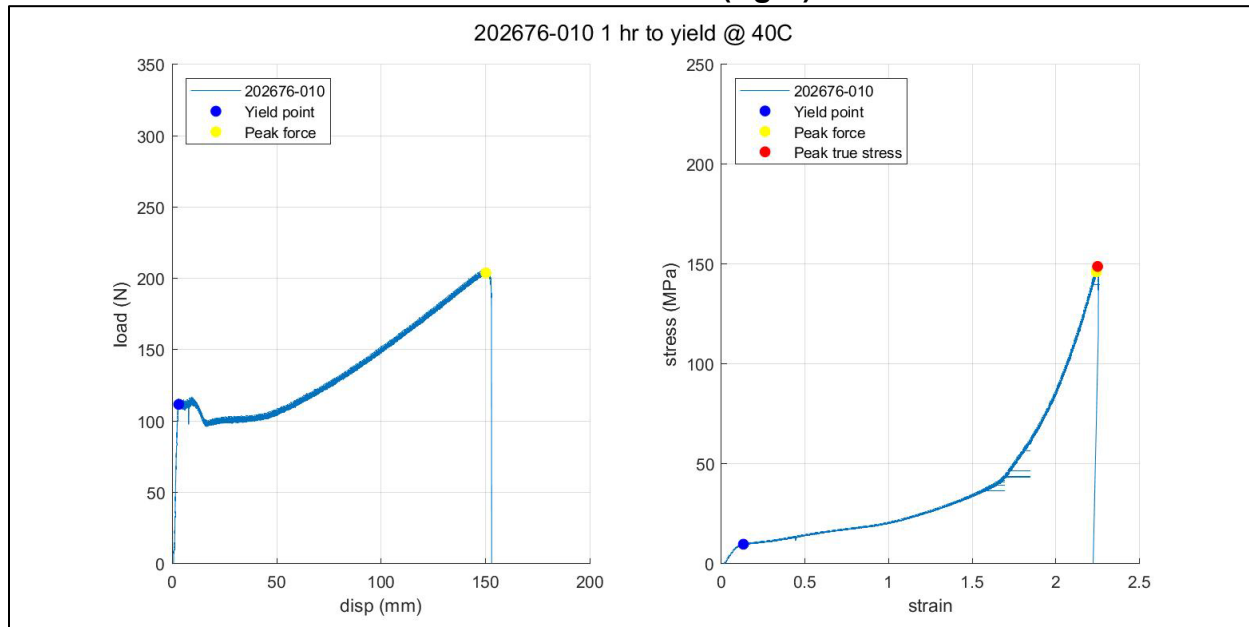
Figure 50: 1hr-to-break Tensile Test, 60°C, Replicate 1. Force-displacement (left), True Stress-strain (right).
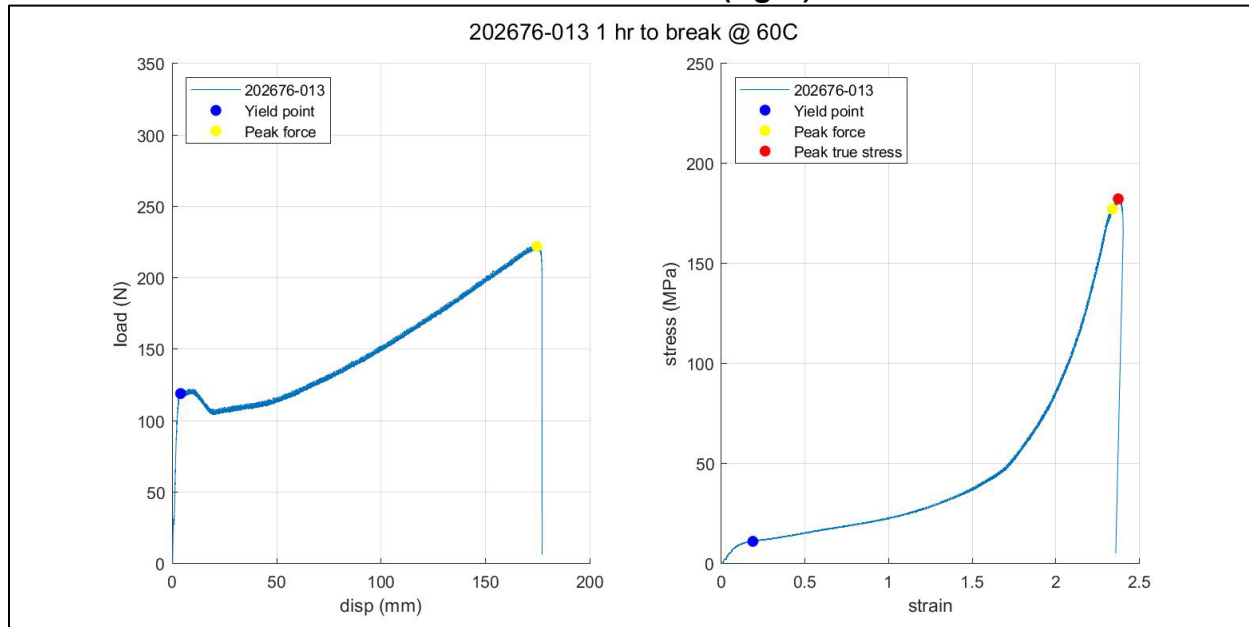
Figure 51: 1hr-to-break Tensile Test, 60°C, Replicate 2. Force-displacement (left), True Stress-strain (right).
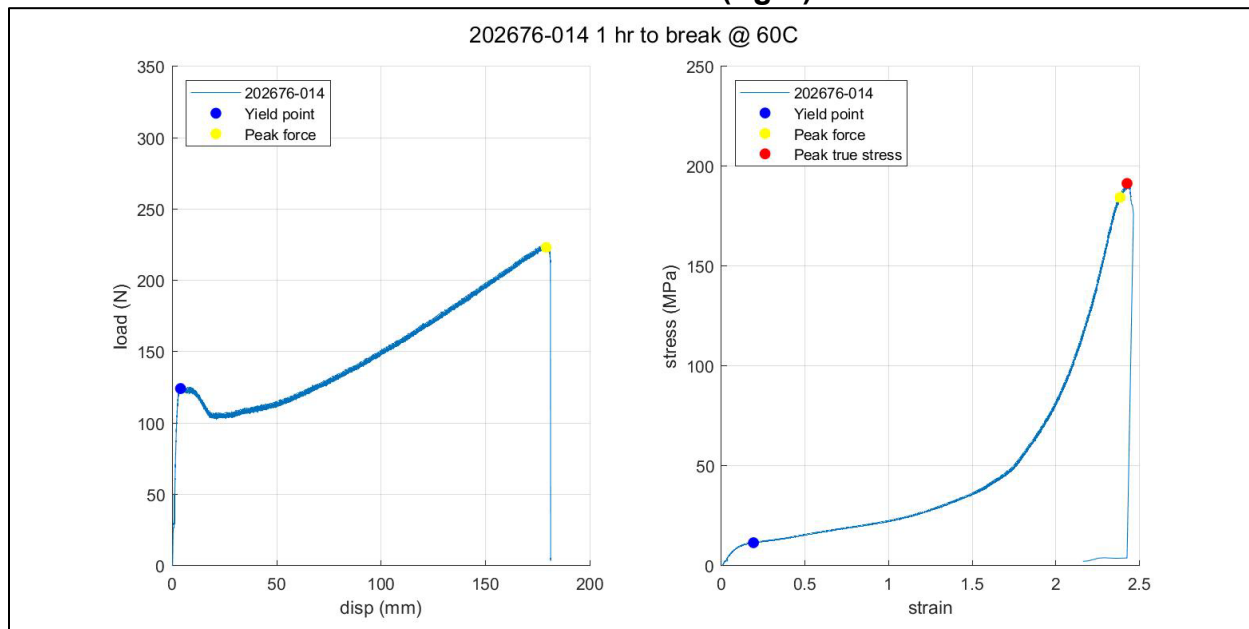
Figure 52: 1hr-to-break Tensile Test, 60°C, Replicate 1. Force-displacement (left), True Stress-strain (right).
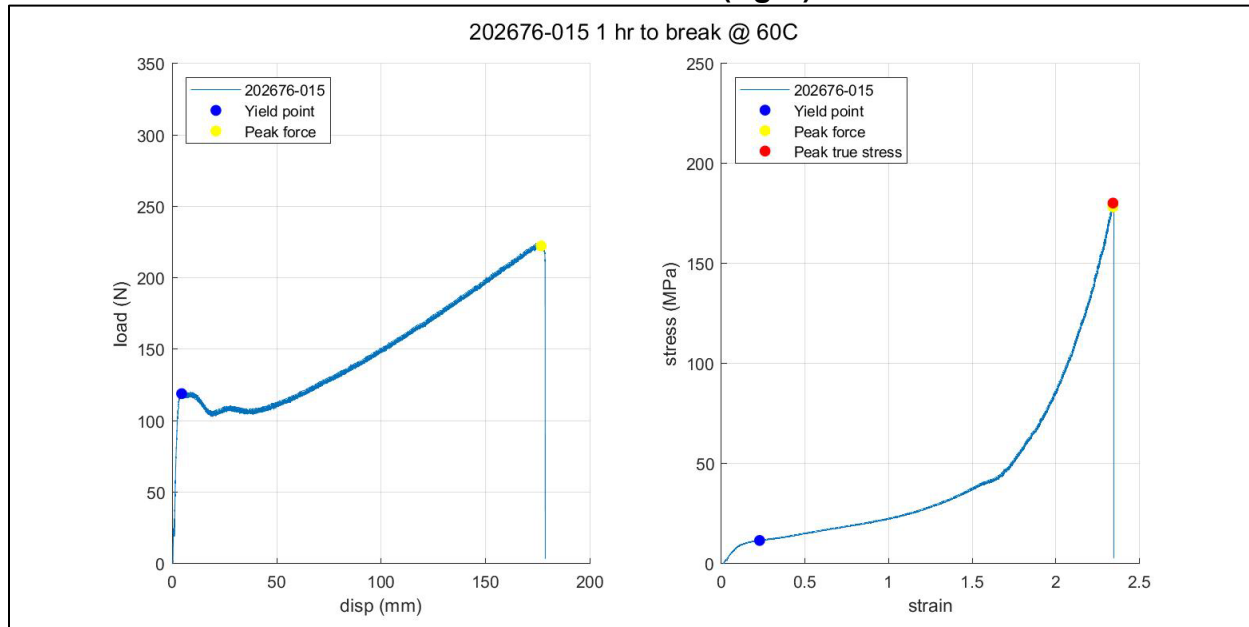
Figure 53: 1hr-to-yield Tensile Test, 60°C, Replicate 1. Force-displacement (left), True Stress-strain (right).
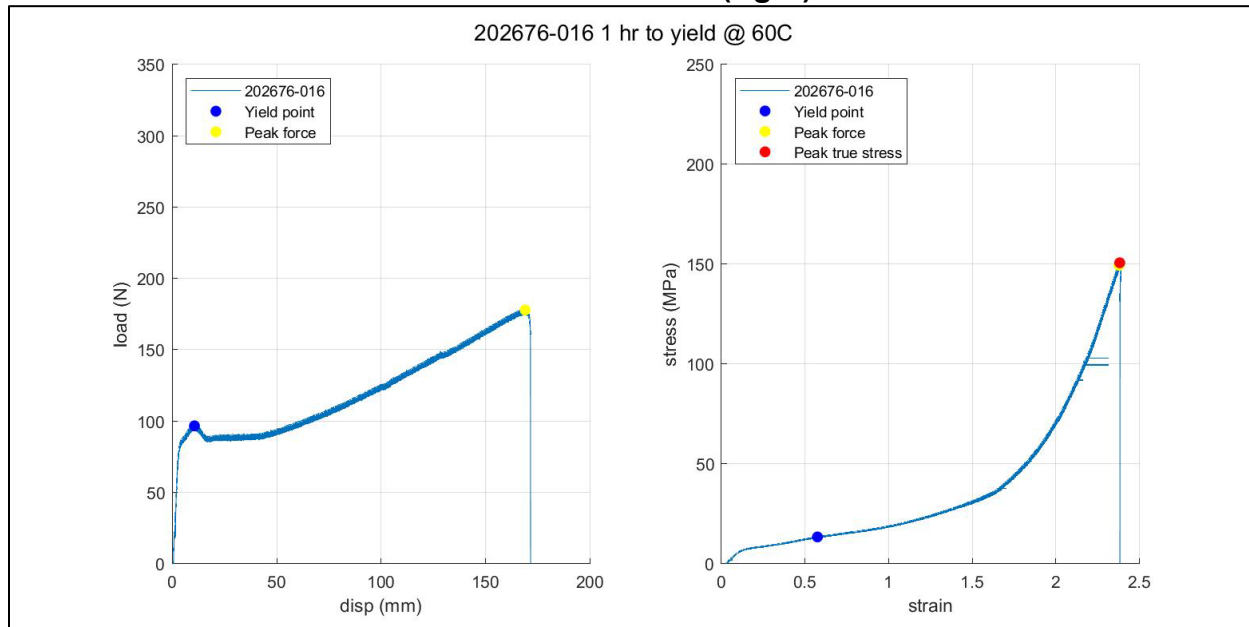
Table 9: Tabulated Tensile Test Results

Specimen ID	Test	Temperature [°C]	Pull rate [mm/min]	Yield stress [MPa]	Displacement at yield [mm]	True stress at peak force [MPa]	Displacement at peak force [mm]	Peak true stress [MPa]	Displacement at peak true stress [mm]	Time-to-Break [h]
202676-001	1 hr to break	23	2.79	18.9	2.96	24.1	158.4	230.3	158.9	0.95
202676-002	1 hr to break	23	2.66	18.8	3.01	20.3	130.8	173.8	132.4	0.83
202676-003	1 hr to break	23	2.44	18.7	2.93	18.5	119.2	149.9	119.4	0.83
202676-004	1 hr to yield	23	0.05	13.8	3.07	17.6	136.5	153.8	138.3	47.03
202676-007	1 hr to break	40	2.58	14.8	3.35	19.3	156.0	177.8	156.7	1.02
202676-008	1 hr to break	40	2.64	14.1	3.46	18.9	151.1	169.9	151.2	0.97
202676-009	1 hr to break	40	2.60	14.4	3.75	20.2	159.8	191.0	160.4	1.04
202676-010	1 hr to yield	40	0.06	9.7	3.10	15.5	150.0	146.1	151.3	45.24
202676-013	1 hr to break	60	3.45	11.1	4.00	17.1	174.4	177.2	176.1	0.85
202676-014	1 hr to break	60	2.95	11.5	3.97	17.0	178.9	184.4	180.5	1.02
202676-015	1 hr to break	60	2.98	11.5	4.49	17.1	176.5	178.3	175.7	1.00
202676-016	1 hr to yield	60	0.07	13.4	10.62	13.9	168.8	149.4	169.3	40.53

UTV Pressure Test Results

Pressure testing was performed on 72 UTV specimens with the goal of obtaining ductile failures at the times shown in Table 10.

Table 10: UTV Planned Failure Times

Temperature [degC]	Target TTF [h]	100% CH4 Replicates	20% H2 / 80% CH4 Replicates
65	500	6	6
65	1000	6	6
65	3000	6	6
40	500	3	3
40	1000	3	3
40	3000	3	3
30	500	3	3
30	1000	3	3
30	3000	3	3

As of the time of writing of this report, UTV specimen failures were only obtained on a portion of specimens. Due to the higher than expected performance of the UTVs, exceeding the target failure times, the pressures were increased on all specimens in an attempt to accelerate ductile rupture failures. After the pressure increases proved insufficient, the temperature was increased on the specimens that were initially set at 30°C and 40°C, which then successfully obtained ductile ruptures.

The non-steady state of the tests that obtained ductile ruptures necessitated the use of the lifetime prediction model (LPM) (Equation 13) in a cumulative damage calculation [85] to iteratively determine the LPMs intercept at 1-hour, at a reference temperature of 23°C. This method captures the variability in individual specimen performance and loading history in a consistent manner. The slope of the LPM in the cumulative damage calculation was set a priori following the development of the constitutive model from tensile tests, as described in section Estimation of the Slope of the Ductile Rupture Curve.

Figure 54 shows the UTV pressure test results as of March 10, 2022. The results thus far show a separation in performance of the UTV specimens tested with methane (CH4)

and hydrogen blend (20% H2). The median performance line of the specimens tested with the hydrogen/methane blend (20% hydrogen by volume) has a time-to-failure performance reduction in the range of 59% versus the median performance line of the UTV specimens tested with methane. The result demonstrates that with the 20% hydrogen blend, the material will rupture in 41% of the time versus no exposure to hydrogen, for a given operating condition (temperature and hoop stress). The failure mode, ductile rupture, was identical for all failed specimens. For general reference, Figure 55 and Figure 56 show photographs of UTV specimens during and after testing, respectively.

The performance of the UTV specimens fell well above the performance of pipe made from the same material (as shown in Figure 54). This is reflective of the difference in manufacturing process: injection molding (UTV) versus extrusion (pipe). The UTV test specimens are thus representative of the PE material's best possible performance, as it is fully described by the drawing portion of a standard tensile test, whereas pipe performance represents the limits of the extrusion process that is best described by the pre-yield creep rates from tensile tests. A full discussion of this behavior is beyond the scope of this project. Regardless of the natural performance differences due to manufacturing process, the effect of hydrogen on UTV performance is applicable to pipe performance as well.

Figure 54: UTV Pressure Test Results as of 3/10/2022
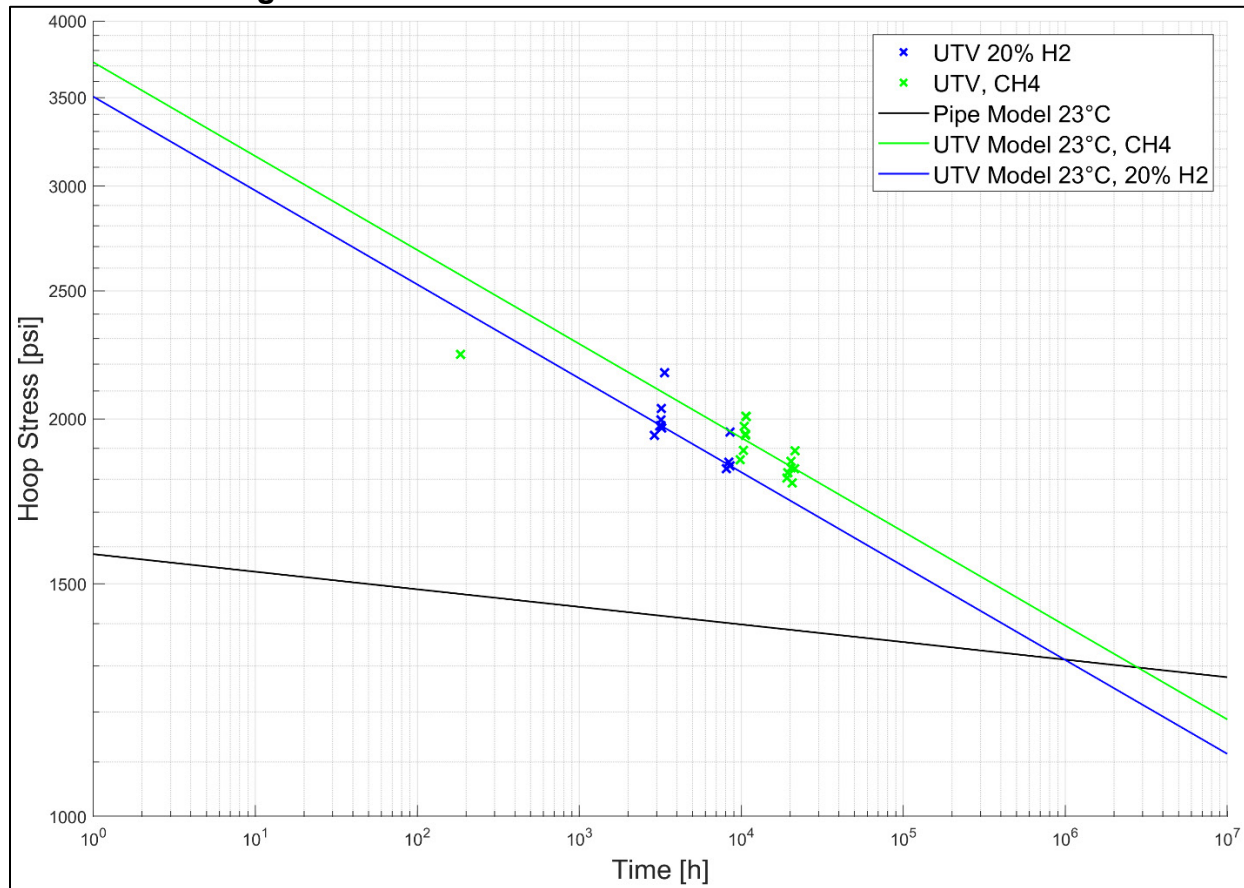
Figure 55: UTV Specimen under Pressure, Exhibiting Significant Distension

Distention under pressure
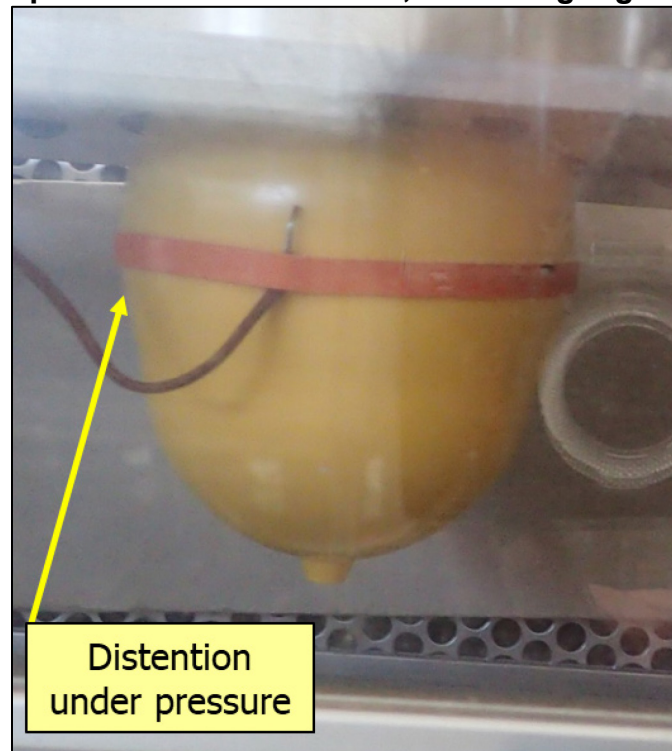
Figure 56: UTV Specimens Showing Ductile Ruptures

Ductile rupture

Ductile rupture

4—1 4—2
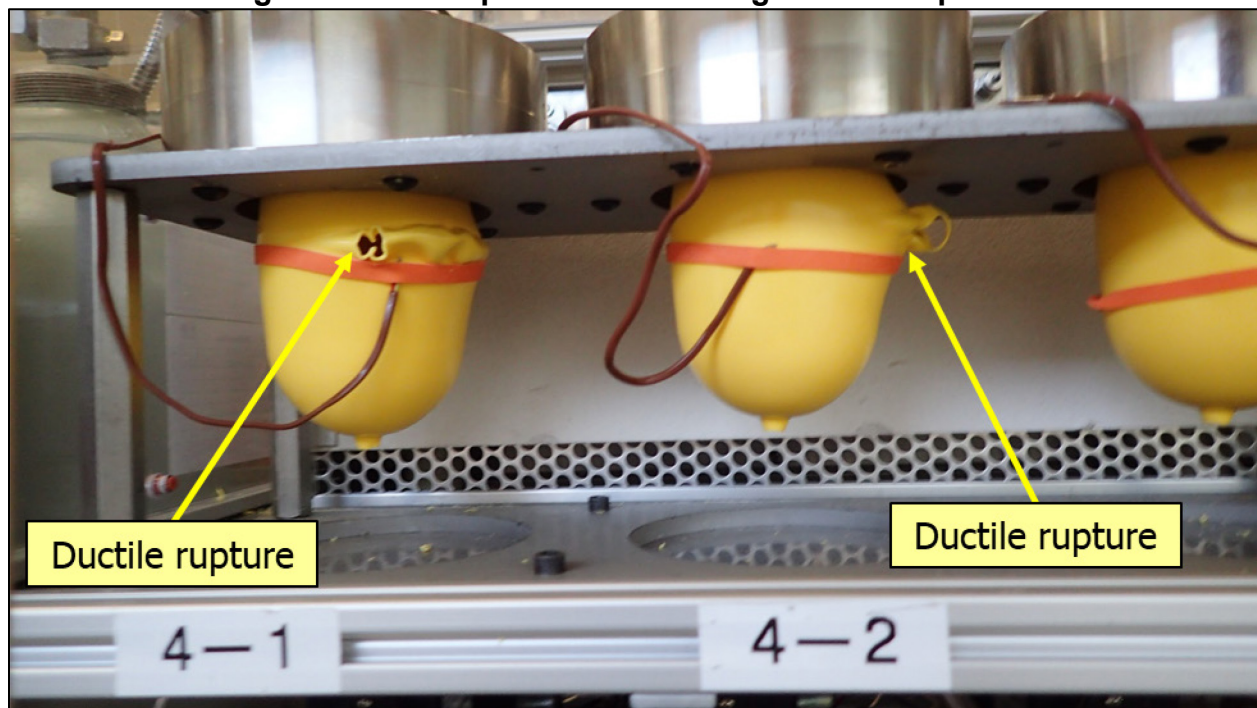
Estimation of the Slope of the Ductile Rupture Curve

The slope of the ductile regression line for the UTV specimens is different from that of pipe (Figure 54). The most likely explanation of this difference in slope is that it is due to the UTVs' injection molding process that does not introduce the same creep rate variance encountered in extruded pipe. Potentially, injection molded specimens provide a better indication of the material's best possible creep performance. The ductile regression line is typically established via times-to-failure from pressure testing, but the apparent slope in obtained from the UTV data is significantly different from the pipe data.

The slope parameter is the creep-rate exponent in the lifetime prediction model (LPM) (see Equation 7) which determines the power-law dependence of the creep rate on stress. This exponent is characteristic to any given PE resin, as exhibited by ductile rupture curves of PE pipes.

Since the creep-rate exponent is characteristic to each PE material, an alternative approach to establishing the slope of the ductile regression line is through fitting a constitutive model to tensile tests performed at different pull rates and temperatures and then virtually simulating creep tests. The simulated temperature, engineering stress, and time to reach a given true strain are then fitted to the LPM to extract a creep-rate exponent. Figure 57 shows the structure of the constitutive model used for simulating creep tests of the UTV material. This viscoelastic-plastic model structure is based on works presented in [86]–[88], which discuss viscoelastic-plastic constitutive modeling of polymers in detail. The model is able to capture the monotonic tensile response of the material up to very high strains, over a wide range of temperatures and strain rates. This ability is key to allowing the model to be used for creep test simulations.

The temperature, engineering stress, and time to reach a given true strain from the simulated creep tests are then fitted to the LPM to extract a creep-rate exponent. Figure 58 shows the predictions of this model, overlaying the actual true stress-strain curves from 23°C, 40°C, and 60°C to which it was calibrated. Figure 59 shows the virtual creep tests predicted from the calibrated constitutive model.

Figure 57: Constitutive Model for MDPE Tensile Response
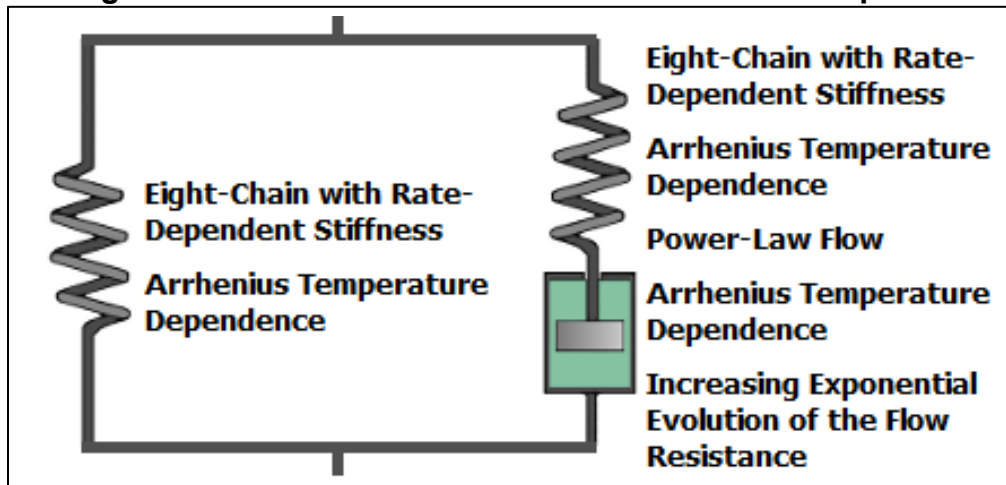
Figure 58: Calibrated Constitutive Model Predictions (blue curves) of Tensile Tests. Green 23°C, orange 40°C, red 60°C.
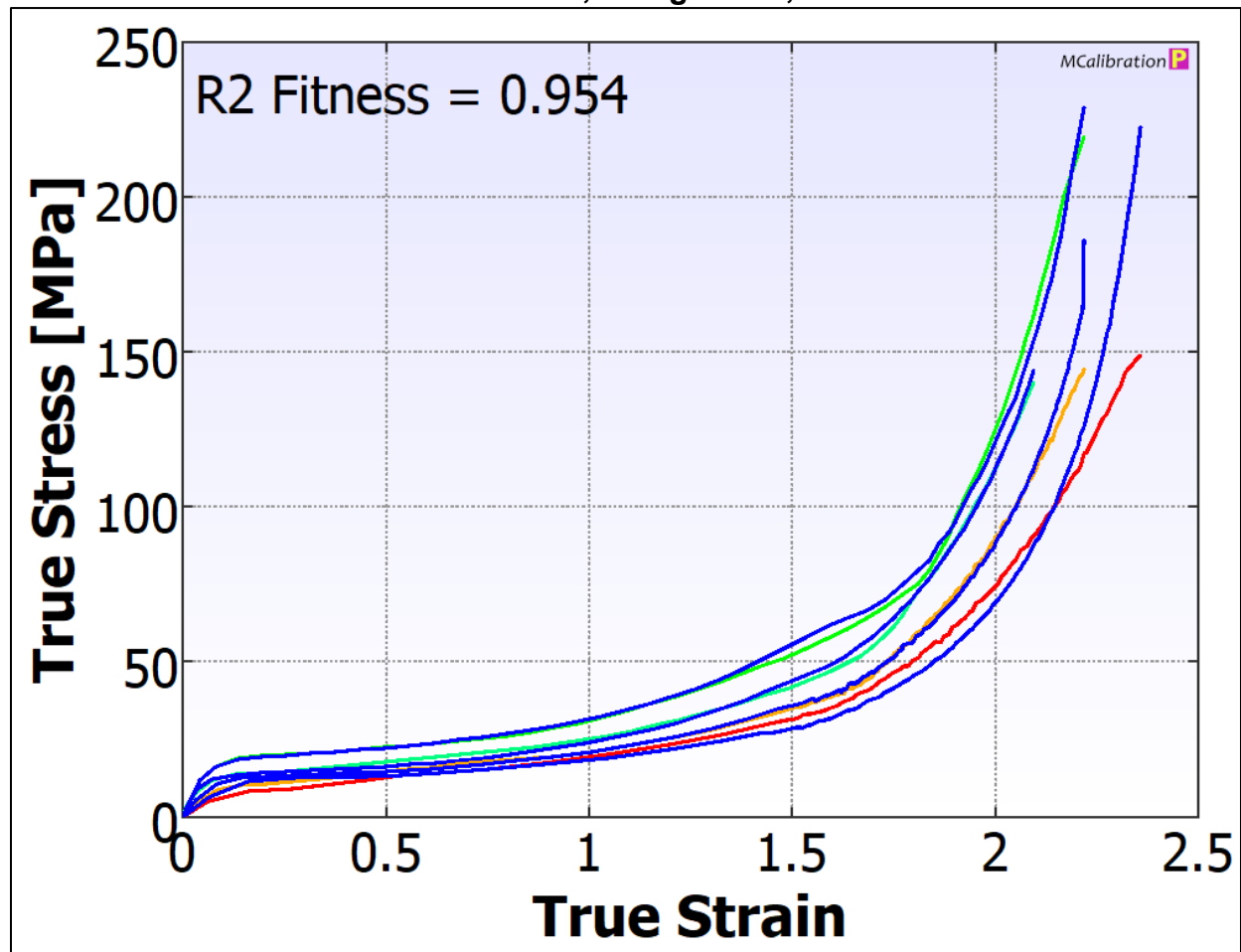
Figure 59: Virtual Creep Test Predictions from the Calibrated Constitutive Model. Green 23°C, orange 40°C, red 60°C.
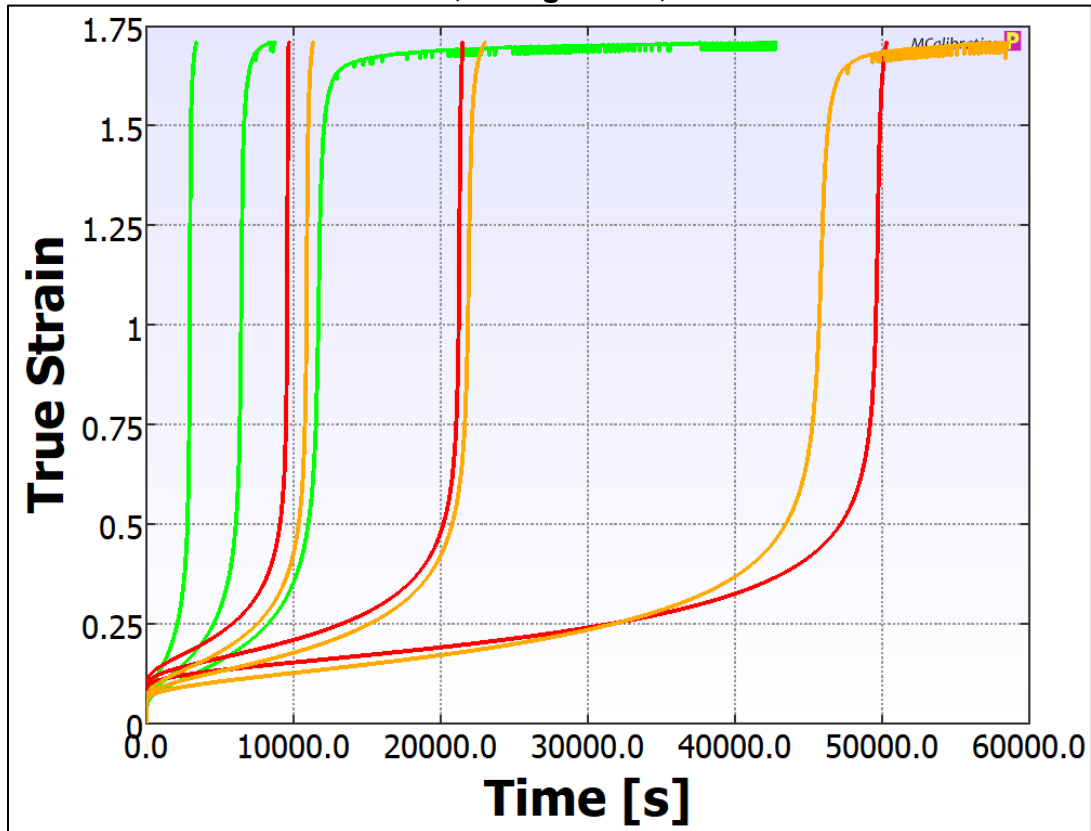
Based on the virtual creep tests, the LPM model formula in Equation 7 was used to extract a creep slope exponent:

$$S = C \cdot exp\left[\frac{E}{R}\left(\frac{1}{T} - \frac{1}{T_{ref}}\right)\right] \cdot t^{-\frac{1}{n}}$$

Equation 7

Where:

t = test time at test temperature, [h]

S = test stress at test temperature, [psi]

T_{ref} = reference temperature, [K]

T = test temperature, [K]

C = stress that will result in a ductile failure in one (1) hour, [psi/h]

n = characteristic creep rate exponent, [unitless]

E = activation energy, [cal/(mol*K)] or [J/(mol*K)]

R = gas constant, 1.9872036 [cal/(mol*K)] or 8.3144598 [J/(mol*K)]

The creep slope of this model changes based on the creep strain that is selected to define the virtual time-to-failure, therefore, the minimum slope was found by scanning through the full range of engineering strains provided by the simulated creep curves. A minimum creep-rate exponent of n=14.08 was obtained, shown in Figure 60. Figure 61 shows the fit of the LPM model to the virtual creep test results that provided the minimum creep slope exponent.

Figure 60: Creep Rate Slope Exponent vs Engineering Strain Creep Target. Minimum slope highlighted in red
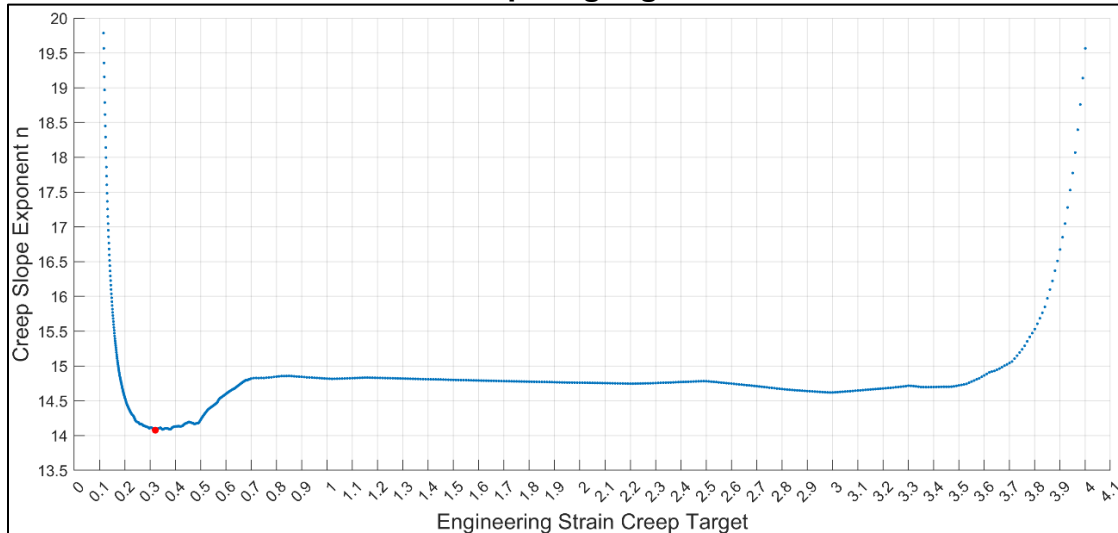
Figure 61: Fitting of Equation 7 to the Simulated Creep Test
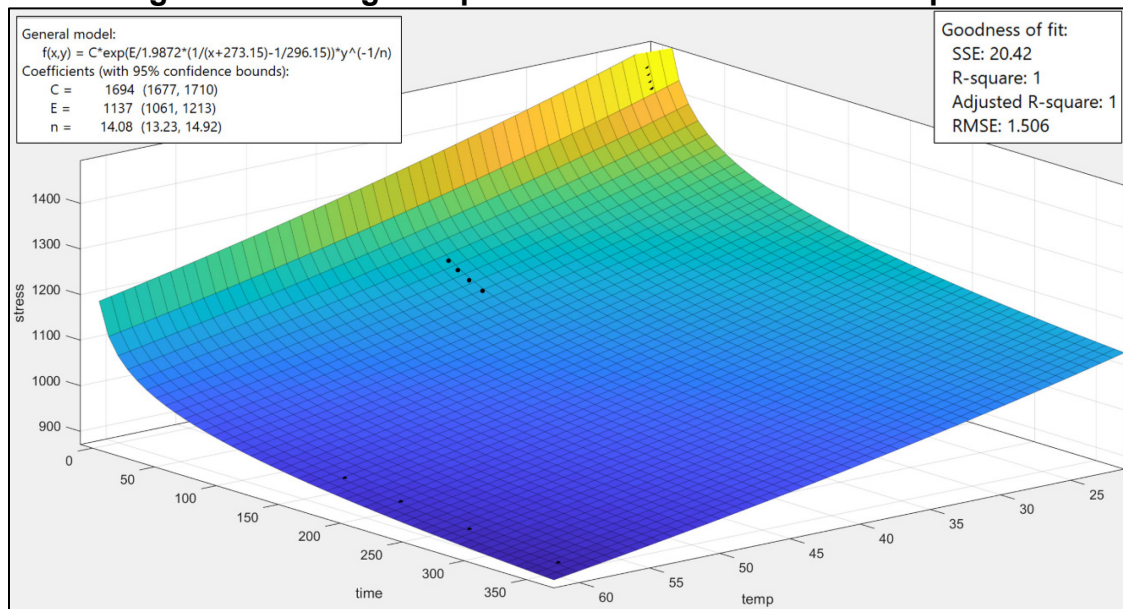
This minimum creep rate exponent fits the UTV data points remarkably well as shown in Figure 54. The UTV specimens under test undergo large scale, uniform expansion (Figure 55 and Figure 56). To undergo this type of expansion a significant amount of

drawing of the specimen needs to take place. This process is described by the constant plateau of creep exponent in Figure 60. This result is extremely interesting as it shows that simple tensile tests, at multiple temperatures and strain rates, provide a constitutive model capable of explaining the behavior of a complex specimen in a complex test like the UTV pressure tests.

In the discussion of UTV test results section UTV Pressure Test Results, the slope of the regression model was set a priori following the development of the constitutive model from tensile tests described above.

Discussion and Conclusions

The UTV failures obtained thus far suggest a reduction in the creep performance of the MDPE. The performance difference between the methane-exposed UTVs and the 20% hydrogen blend-exposed UTVs is an approximately 59% reduction in time-to-failure at a given stress, or, equivalently a 6.2% reduction in stress to reach a given time-to-failure. A brief general overview of how a reduction in PE performance can be viewed is provided in APPENDIX 2 - PE Pipe Performance Safety Factors.

The implications associated with the reduced UTV specimen performance and transferability to operational piping systems are outside of the scope of this project and should be addressed by the applicable standards bodies that establish PE pipe performance standards.

As of March 10, 2022, no conclusions are available regarding the impact of hydrogen on the aging of MDPE or NBR, as the OIT tests are still pending the completion of UTV pressure testing.

Recommendations

The work initiated by this project to evaluate the impact of hydrogen on PE should be extended to include actual pipes to further substantiate any performance reduction. GTI is already working on a project, sponsored by utilities, to test vintage PE pipes with 20% hydrogen/natural gas blend. Performing pressure and aging tests on pipes made from vintage and modern HDPE and MDPE materials will be important for confirming if the impact found on the UTV specimens also manifests in pipes and to what extent. As noted in the preceding section, the implications of a reduction in PE performance due to hydrogen should be address by the applicable standards bodies that establish PE pipe performance standards.

Task 2c - Modeling Assessment of any Impact on Valves, Fittings, Materials, and Welds due to Hydrogen Embrittlement

The effective result of hydrogen embrittlement of steel materials is a reduction of ductility. Stress-strain curves of hydrogen-embrittled steels exhibit a lower break strain at the stress-strain regime beyond the ultimate tensile stress (UTS), while often the stress-strain curve preceding the UTS is identical to the non-embrittled steel [89]. For pipeline steels, the stress-stain regime beyond the UTS is typically where most of the steel's toughness, i.e. its ability to absorb energy, is realized. The reduction in toughness from HE helps explain the accelerated crack growth rates observed in tests utilizing hydrogen containing environments, as well as reduction in Charpy V-Notch impact energies of specimens exposed to hydrogen, as found by test performed by UC-Riverside under this project, presented in section Charpy Impact Toughness Testing.

The modeling approach in this project was synthetic in nature, given the lack of stress-strain curves available for hydrogen-embrittled steels. Steel materials, in general, present material property uncertainties, which operators seek to reduce. In 2021, GTI completed a report for DOT PHMSA titled "Improvements to Pipeline Assessment Methods and Models to Reduce Variance" [90] in which the topic of pipe material property uncertainties and their implications on the pipe's performance envelope was addressed. An excerpt from that report with explanations of GTI's modeling approach is provided in APPENDIX 3 - Excerpt from Reference [82]. GTI's modeling of the impact of hydrogen embrittlement follows the same approach, where hydrogen embrittlement is treated as a parametric adjustment to the true stress-strain curve of a given material, in the same way conventional material uncertainty would be modeled. The concept of adjustment to the true stress-strain curve to account for hydrogen embrittlement (HE) is based on tensile test findings available in literature [24], [91].

In lieu of empirical data, GTI's material models for three different steel – representing low/mid/high toughness of vintage steels – were each artificially embrittled by reducing the respective constitutive model's fracture strain such that they reflect a 50% reduction in toughness, as can be seen in the example in Figure 62. Toughness refers to the integral of the true stress-strain curve, which provides the energy-to-break value. The energy-to-break value is also equivalent to the area under the true stress-strain curve, as illustrated in Figure 63.

Figure 62: True Stress-strain Curve of the Nominal Material and Modified Curve Representing Hydrogen Embrittlement Leading to 50% Reduction in Toughness
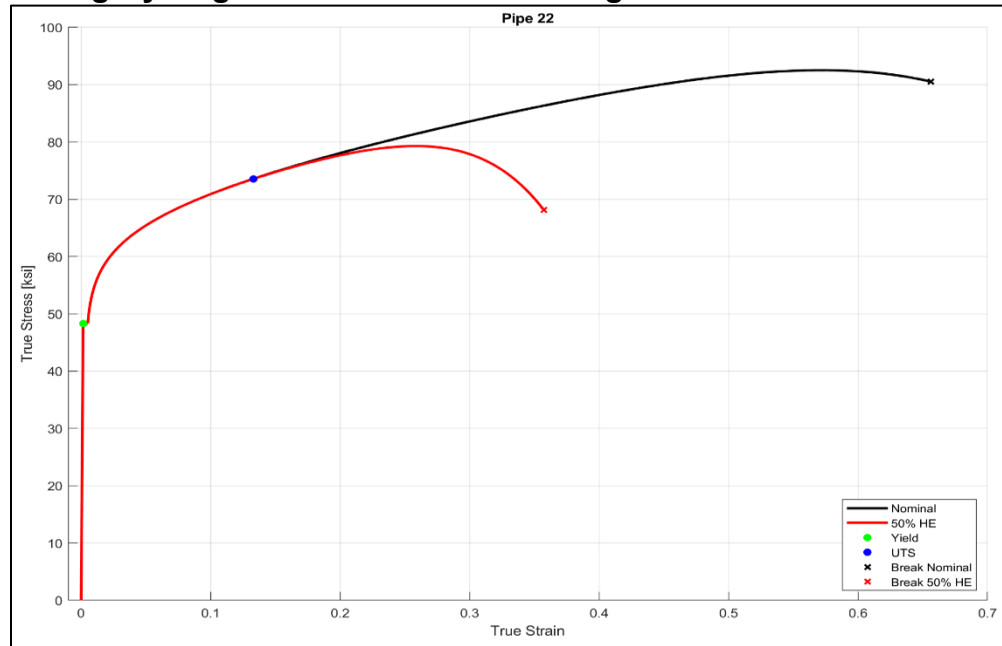
Figure 63: Curves from Figure 61 with their Respective Area under the Curve, Representing the Energy-to-Break (Toughness).
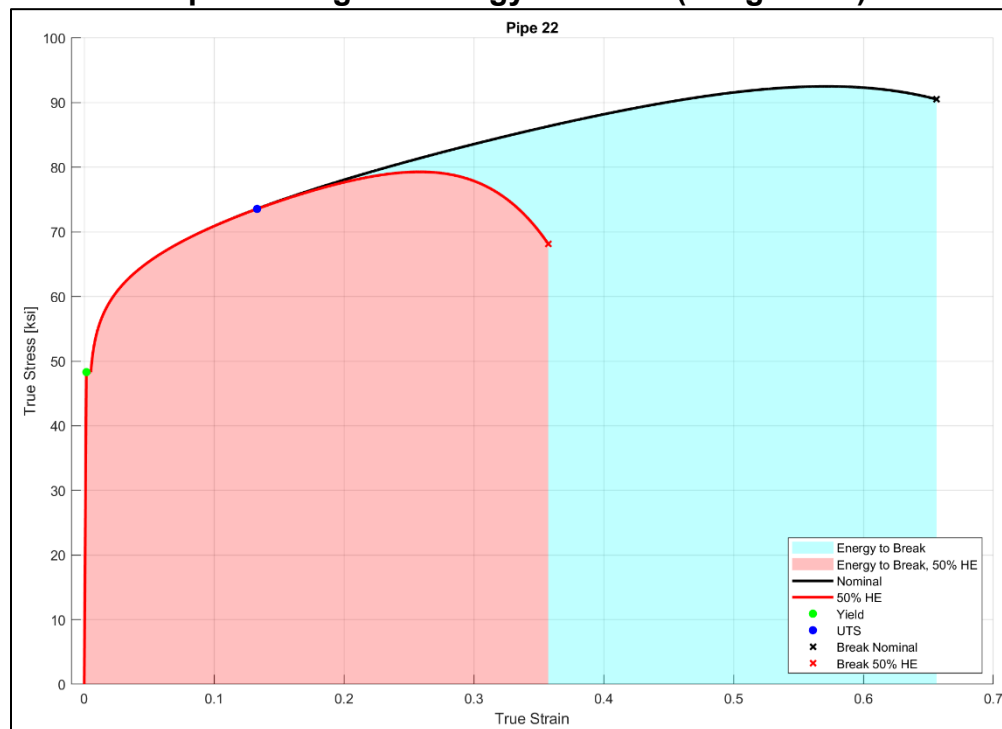
To determine the fitness-for-service (FFS) of a steel component under tensile load (e.g. hoop stress in a pressurized pipe), the material strength is related to application stress via a failure assessment diagram (FAD) [92], [93]. On the horizontal axis, the FAD plots the bulk stress of the load bearing ligament as a ratio (Lr) to the yield stress, and on the vertical axis, the stress intensification factor at the load bearing ligament as a ratio (Kr) to the fracture toughness of the material. The FAD thus allows the assessment of whether a component is safe or not, and in an unsafe case, what the expected damage propagation mode will be – crack propagation or ductile collapse. The material's performance envelope is represented on the FAD by the failure assessment line (FAL), which is obtained from the true stress-strain curve of the material (Figure 64). Specific load cases are plotted on the FAD together with the FAL; load cases that fall below the FAL are considered safe, and load cases that fall above the FAL are considered unsafe. Plastic collapse is assumed if an assessment point falls at or beyond a predetermined maximum Lr value, which is typically the Lr value corresponding to the mean stress between the yield stress and UTS.

Hydrogen embrittlement introduces a reduction in fracture toughness, while the yield stress is typically unchanged. Figure 65 illustrates the shift in assessment when comparing the nominal material to the hydrogen embrittled (HE) material. The blue and red "cones" in Figure 65 represent the range of Level-2 limit-load calculations in ASME FFS-1 [92] applicable to the geometry cases simulated for this task. The limit-load in these calculation is the point where a straight line from the origin intersects the FAL. The slope of the line is dependent on the geometry of the component and crack-like flaw and the fracture toughness of the material.

As can be seen in Figure 65, the red cone, representing the embrittled material, is rotated upwards from the nominal material's cone, thus lowering the range of Lr values corresponding to the point where the cone lines intersect the FAL. In this case, this reduction in Lr represents a reduction in the maximum safe pressure for the hydrogen-embrittled pipe. Again, it is important to note that the determination of a reduced operating envelope would not be reached based upon yield stress alone.

Figure 64: Failure Assessment lines Obtained from the True Stress-strain Curves in Figure 61.
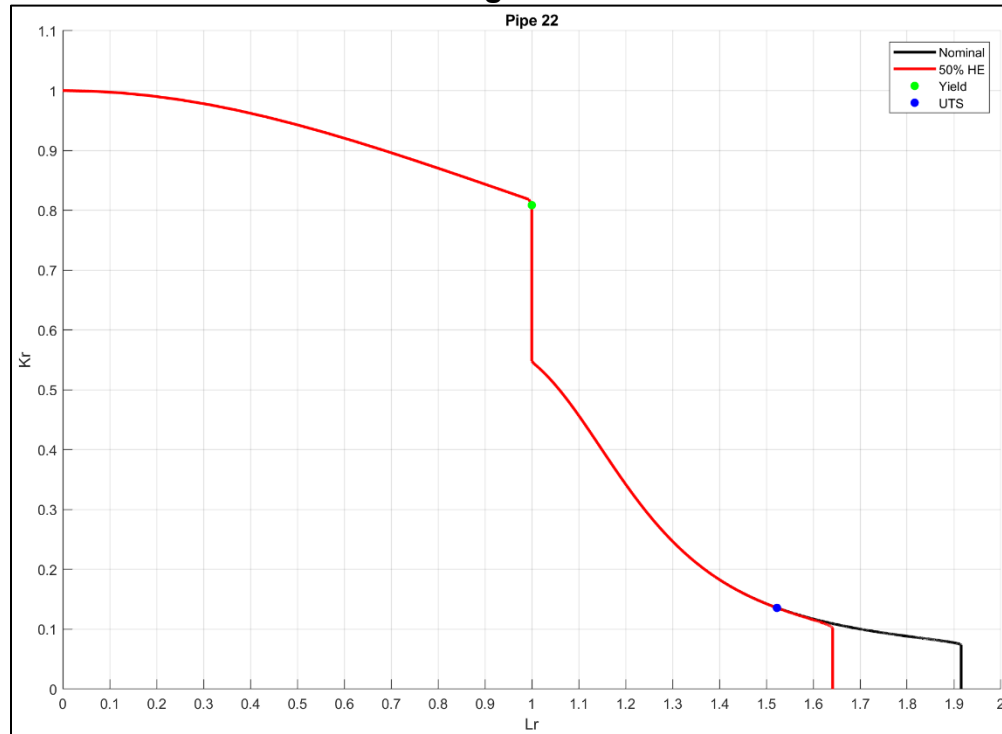
Yield point and UTS point are shown for reference.

Figure 65: FAD Showing the Shift in Material Performance based on Level-2 Calculations in ASME FFS-1 Applicable to the Geometry Cases Simulated in FEA.
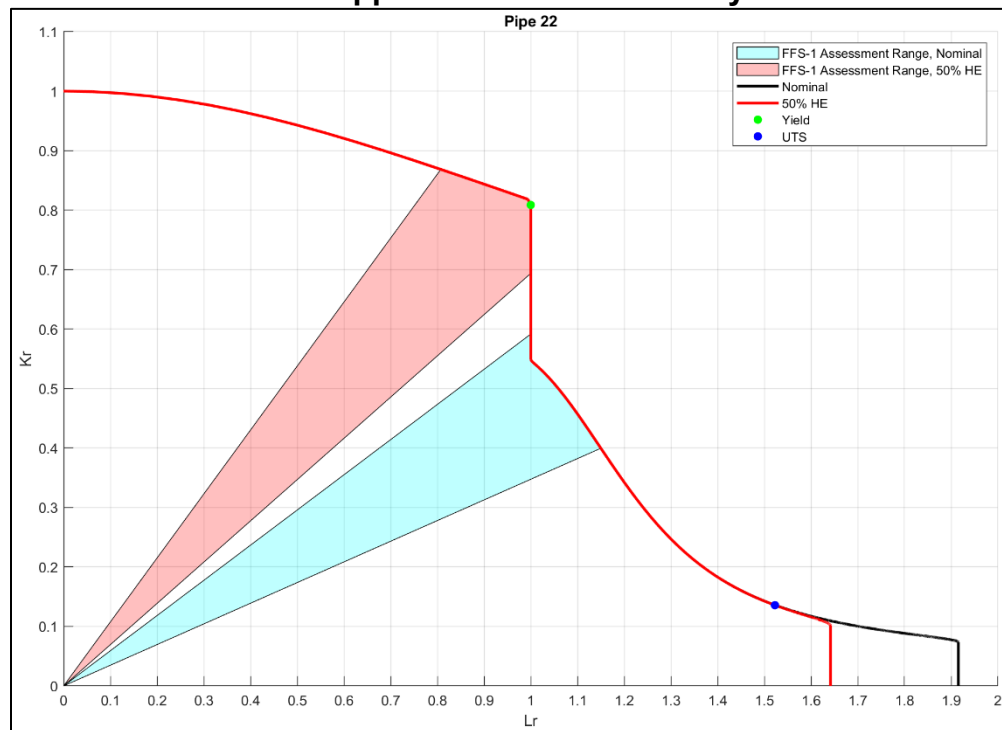
Finite Element Model

To provide a conceptual demonstration of how hydrogen embrittlement would affect fitness-for-service assessments, a model of a pipe with an internal axial crack was selected. An internal axial crack case was selected since it represents a flaw that is perpendicular to the hoop stress, which is the primary stress in a pressurized pipe. A pipe size of 2" IPS was used in all simulations, as this represents a pipe size that is used in gas distribution systems. In all cases the wall thickness of the pipe was set to 0.154" and crack depth was 50% of the wall thickness. A set of different axial crack lengths were then simulated with the embrittled and nominal material models. The normalized crack lengths used for the simulations, in terms of $C=L/sqrt(Rt)$, were: $C = 0.27, 0.4, 0.6, 0.8, 1, 1.5, 2, 3, 6,$ and 10; where L is the actual crack length; R is the pipe outer radius; and t is the wall thickness.

The simulations were run using a quasi-static study with first order elements and an implicit solver. The material model was elastic-plastic, with plastic strain-based damage. Figure 66 through Figure 69 show an example of the geometry and mesh of the model. The boundary conditions were fixed pipe ends and pressure applied to the inner diameter of the pipe and the axial crack's faces. The FEM model used here was developed under a GTI project for DOT PHMSA [90] and further details about it can be found in its publicly available final report.

Figure 66: FEM Model Geometry
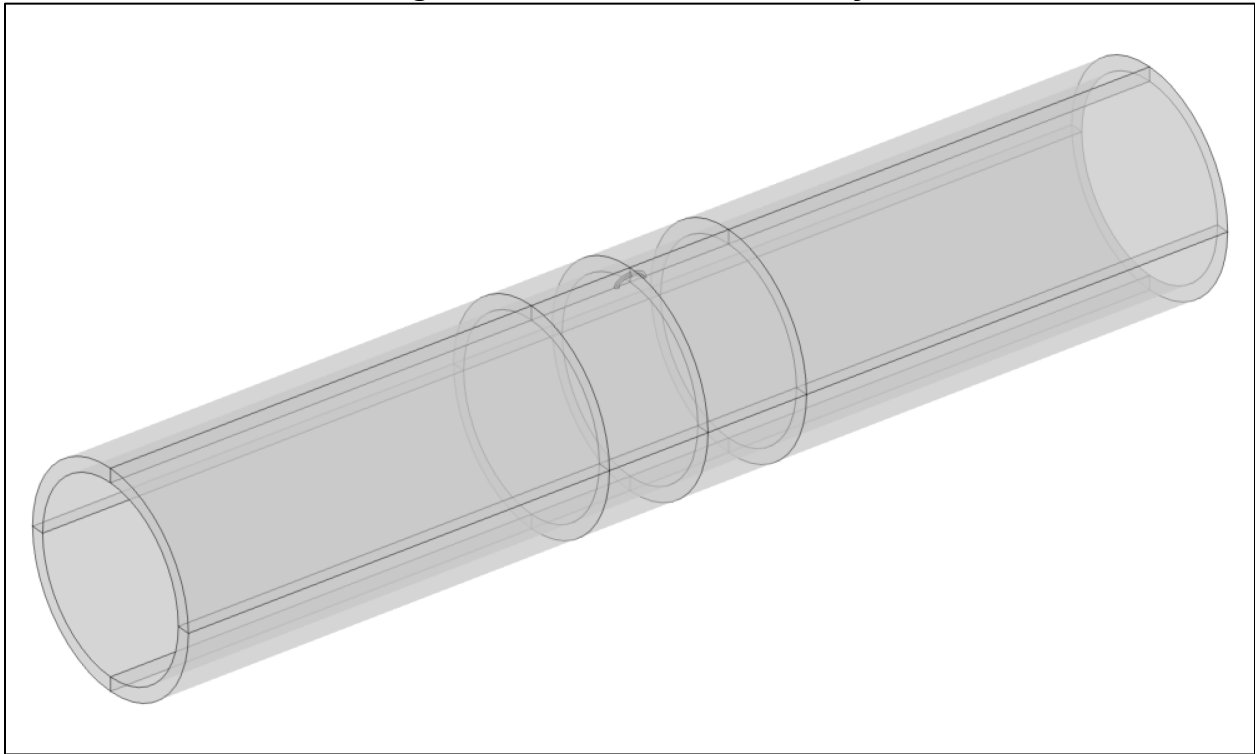
Figure 67: FEM Model Showing Crack Geometry Detail
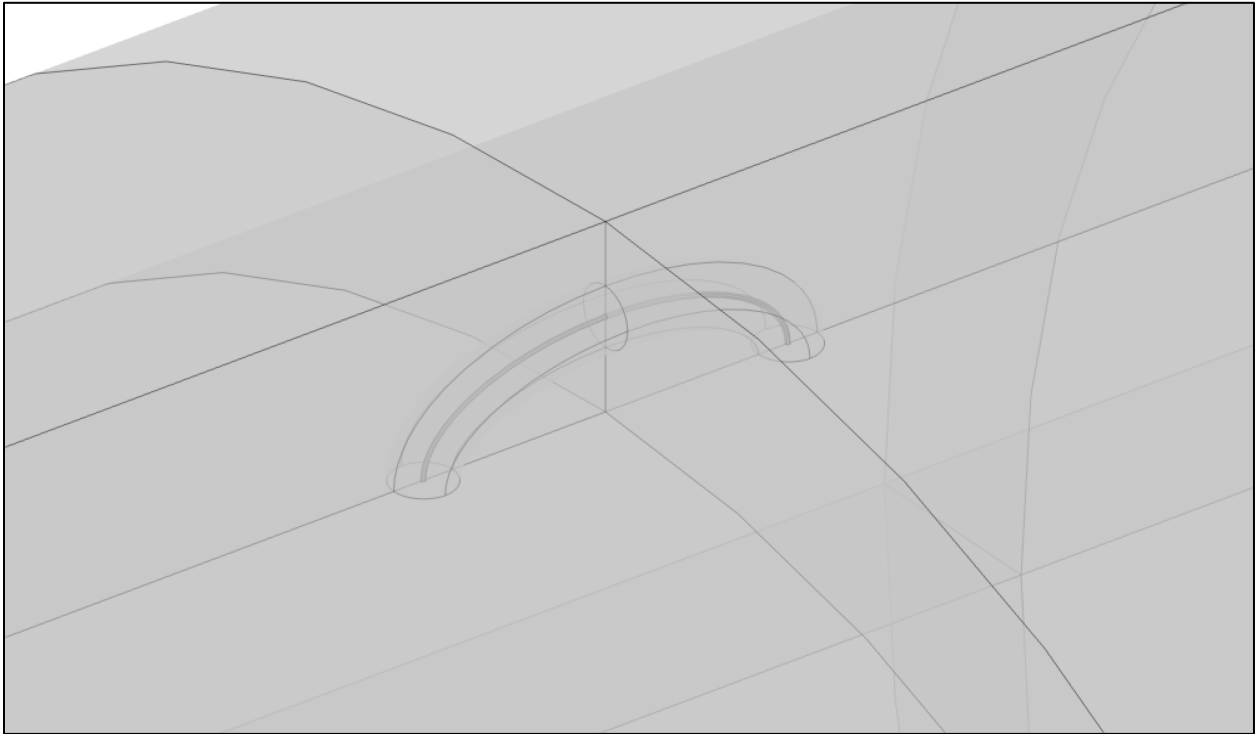
Figure 68: FEM Model Mesh
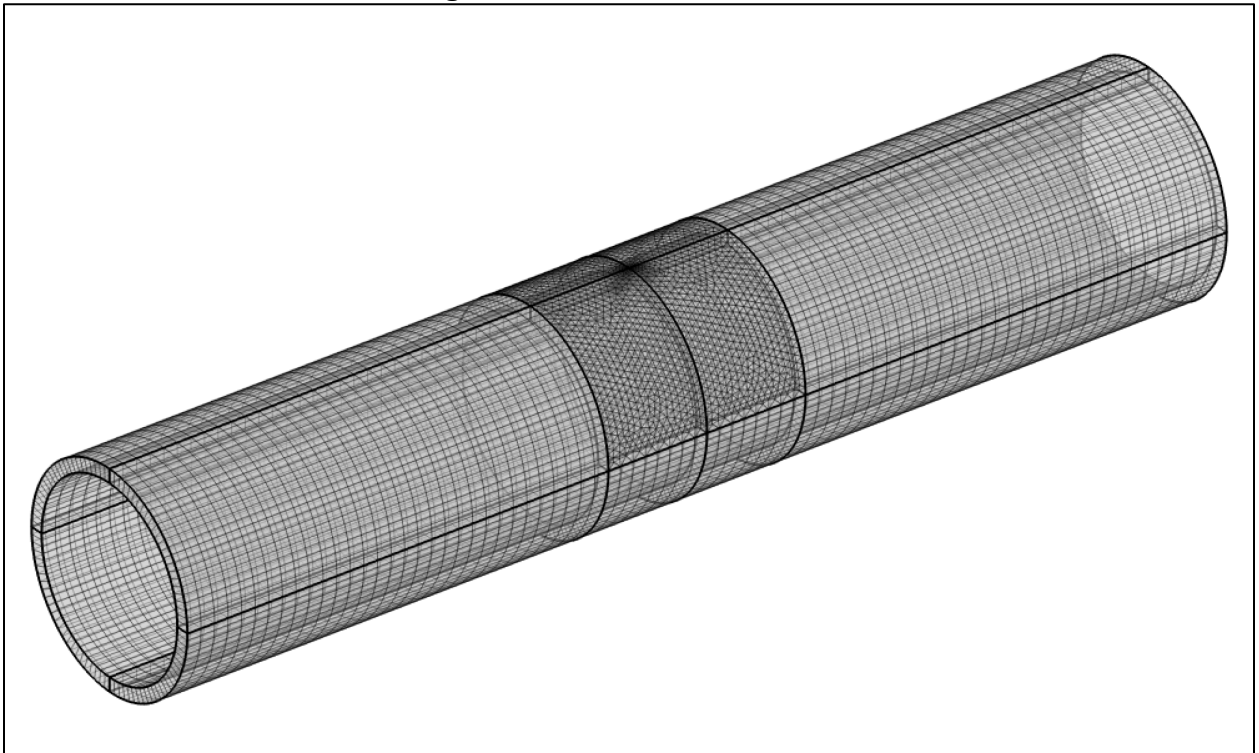
Figure 69: FEM Model Showing Crack Mesh Detail
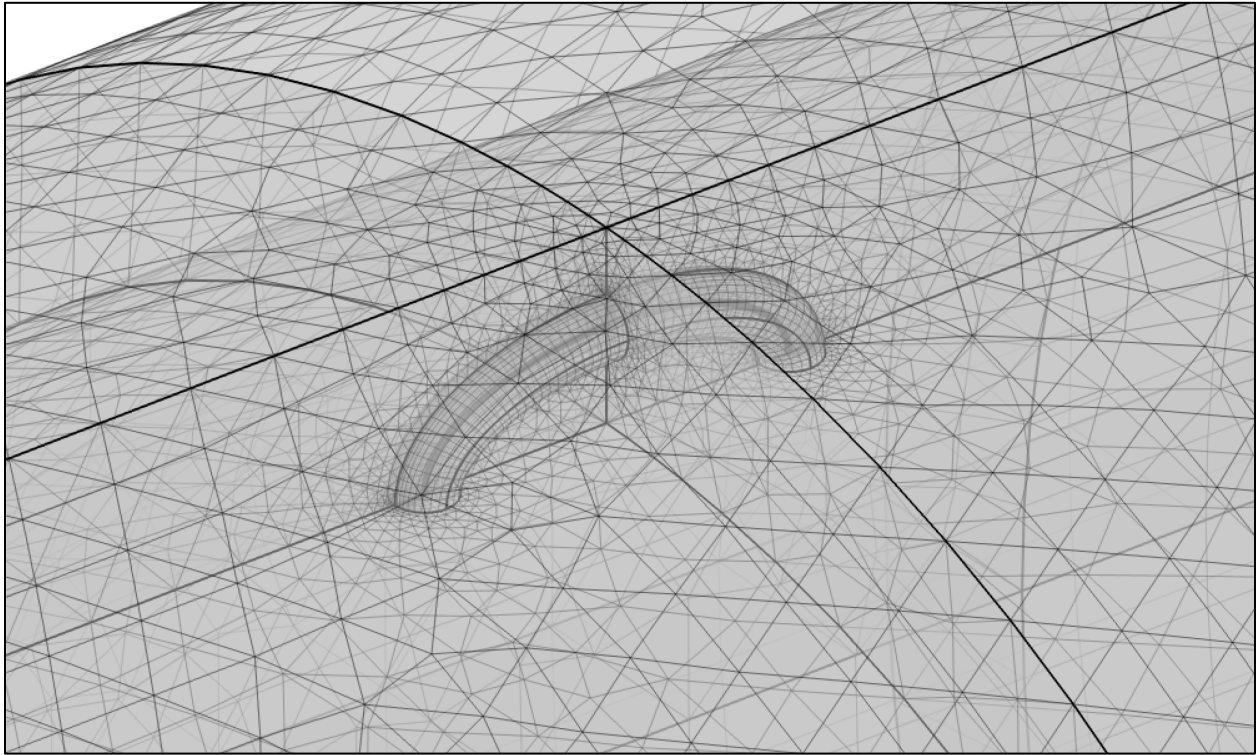
FEM Simulation Results

The results of the simulations are shown in Figure 70, which provides a comparison of the critical pressure from the finite element analysis (FEA) and FFS-1 Level-2 assessment calculations for a pipe with an internal axial surface crack. Critical pressure in this context is defined as the pressure at which damage will propagate the axial crack in the pipe, in other words, the pressure at which the crack is expected to grow in length, depth, or both. As can be seen in Figure 70, the FEA results provide a more conservative prediction, and both the FEA and FFS-1 predictions exhibit a reduction in the performance envelope due to HE, as expected.

Figure 70: FEA Predicted Critical Pressure vs. FFS-1 Predicted Critical Pressure.
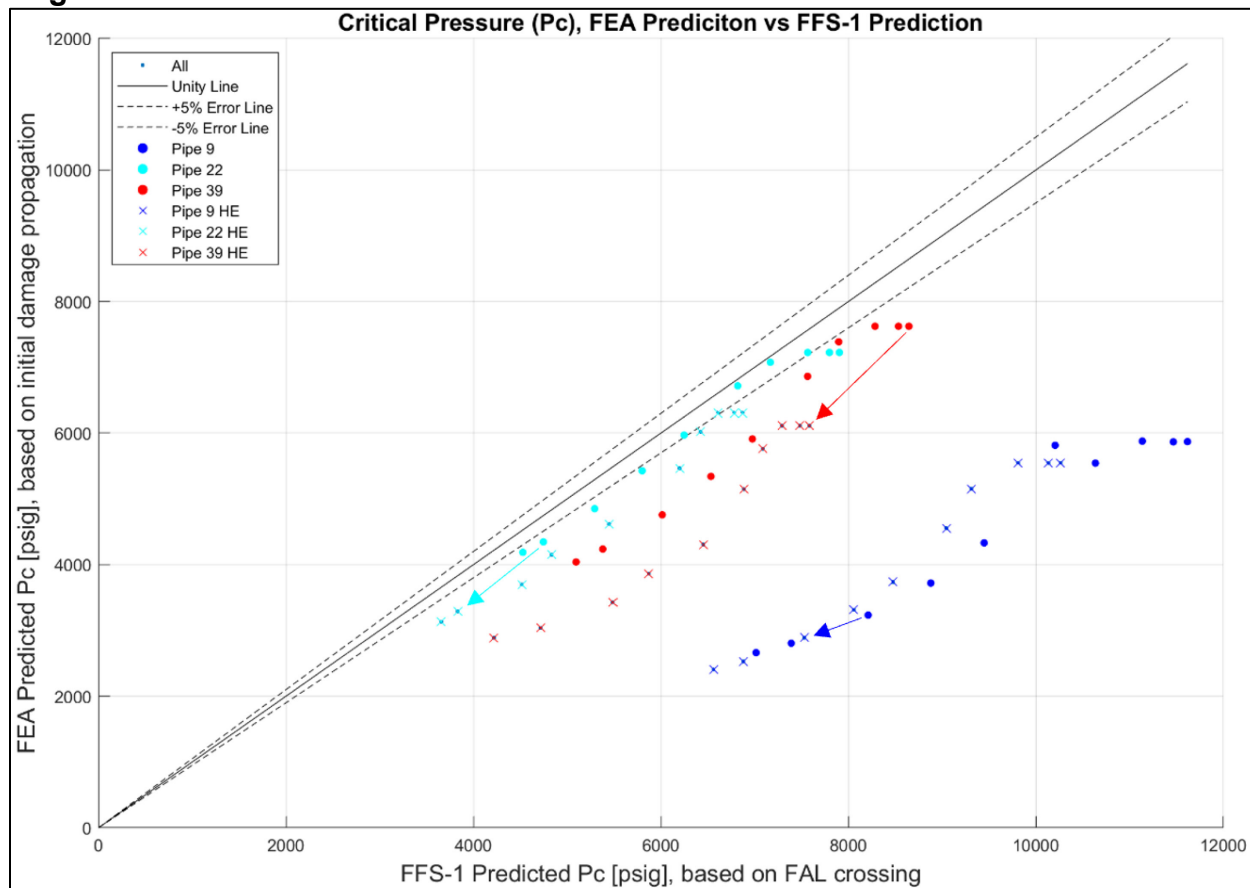
Arrows indicate the hydrogen embrittlement induced reduction in critical pressure

Discussion and Conclusions

Recent presentations provided be the Sandia National Laboratory (SNL) teams conducting research under the DOE HyBlend project [94], discussed the following findings about pipeline steels in gaseous hydrogen environments:

- Fatigue is accelerated by >10x.

- Fracture resistance is reduced by >50%.

- Even small amounts (1% by vol) of hydrogen have large effects.

- Welds (of comparable strength) have similar performance to base metals when residual stresses are accounted for.

The reduction in performance envelope due to hydrogen embrittlement needs to be understood in the context of fitness-for-services (FFS), which is to say, under what circumstances will the component maintain its integrity or fail. Piping systems are designed according to the yield strength and the ultimate tensile strength of a steel,

and given that these parameters are typically not significantly affected by hydrogen embrittlement [24], [91], it may seem that the existing natural gas infrastructure can readily accommodate hydrogen blends. However, it is important to consider hydrogen-embrittled steels' increased crack growth rates and reduced impact toughness. The order-of-magnitude increased crack growth rate and approximately 50% reduction in toughness suggest the need for the following:

- Increased inspection intervals,
- Increased resolution of flaw detection,
- Avoidance of upset loadings, e.g. 3rd-party damage, sudden soil loads/unloads, large soil displacement,
- Awareness of any increase in the ductile-to-brittle transition temperature,
- Awareness of the change in the leak/rupture boundary of the embrittled steel.

To summarize, hydrogen embrittlement may appear to have no effect on the static loading capacity of steels when considering only yield stress and ultimate tensile stress, however, both FEM simulations and ASME FFS-1 calculations predict a reduction in static pressure threshold to initiate damage propagation when crack-like flaws are present. Fatigue testing has thus far indicated significantly accelerated crack growth under hydrogen environments, which will apply to any existing flaws. Moreover, hydrogen embrittlement introduces an increased risk of failure under dynamic/impact loading, which will require appropriate updates to monitoring, maintenance, and damage mitigation procedures.

Recommendations

Research into the impact of hydrogen on metallic pipes and components can be further extended by applying the material data obtained by completed hydrogen impact projects, such as this project and SNL's H-Mat and HyBlend projects, into established FFS assessment calculations. Further material testing under pressure, stress, and hydrogen concentration(s) applicable to gas pipelines is also of interest. The performance reduction from hydrogen embrittlement that is obtained from material testing can be overlaid on performance envelope charts, such as the one shown in Figure 71 (taken from [90]) to help determine operating pressure and factors of safety. An explanation of the information presented Figure 71 is provided in APPENDIX 3 - Excerpt from Reference [82].

Figure 71: Maxey/Folias Critical Pressure vs. FFS-1 Critical Pressure, Data Points from FEM Simulations of Various Pipe Materials, Pipe Sizes, and Flaw Sizes.
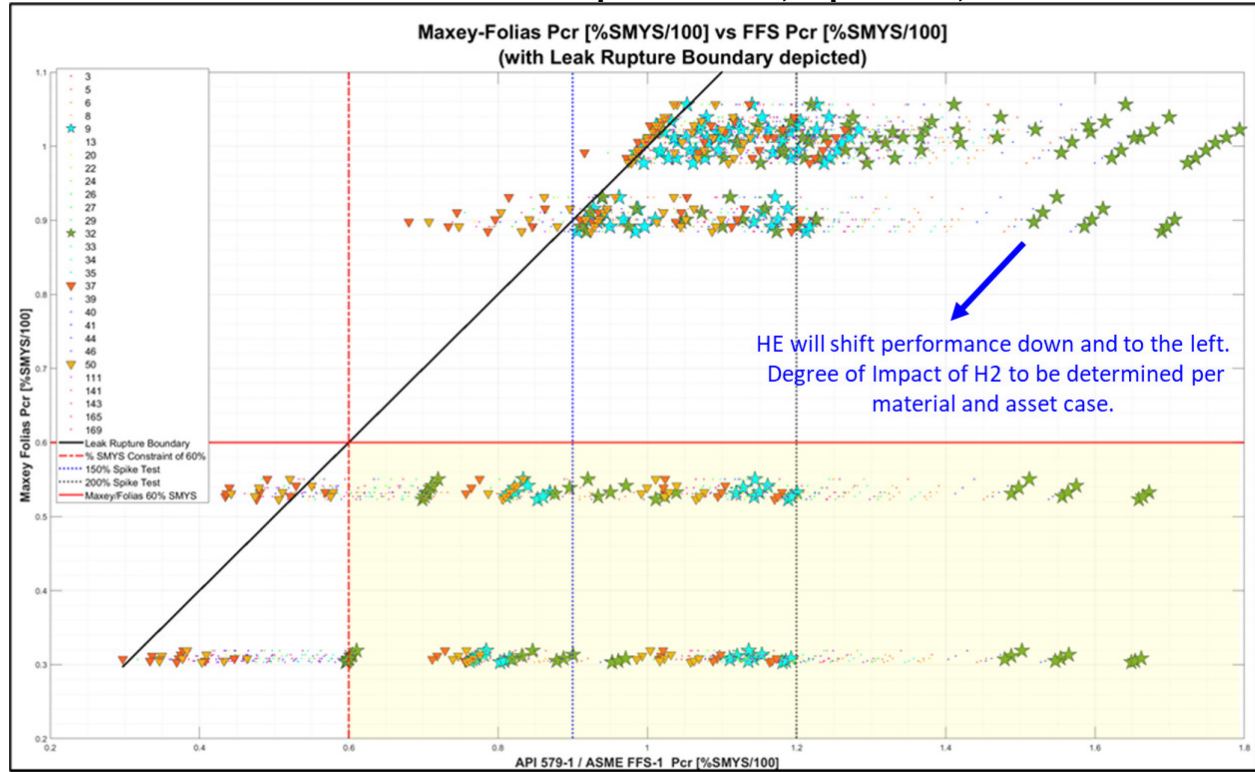
Task 2d - Degradation Analysis

Introduction

One of the major concerns with the introduction of hydrogen gas in the natural gas pipeline system is the impact of hydrogen embrittlement on the broad range of materials making up the current infrastructure. It has been demonstrated that mechanical properties of metals, primarily steels, have been adversely impacted by exposure to hydrogen gas. The resulting increased crack growth rate, reduced ductility, and reduced toughness in steels, have been attributed to hydrogen embrittlement [22]–[25].

In the case of metal exposure to hydrogen gas, adsorbed hydrogen molecules on the metal surface dissociate into hydrogen atoms, followed by absorption of hydrogen atoms in the bulk material, and ultimately solution and diffusion of hydrogen atoms through the material. The transport properties of hydrogen though a given material are influenced greatly by the crystal microstructure of the material. For example, the hydrogen diffusivity in body-centered cubic (BCC) crystallographic microstructures, such as ferritic steels, is several orders of magnitude higher than diffusivity in face-centered cubic (FCC) microstructures, such as austenitic stainless steels, as demonstrated by Figure 72. On the other hand, solubility of hydrogen in FCC microstructures is greater than hydrogen solubility in BCC microstructures, shown in Figure 73.

Figure 72: Hydrogen Diffusivity in Ferritic and Austenitic Steels
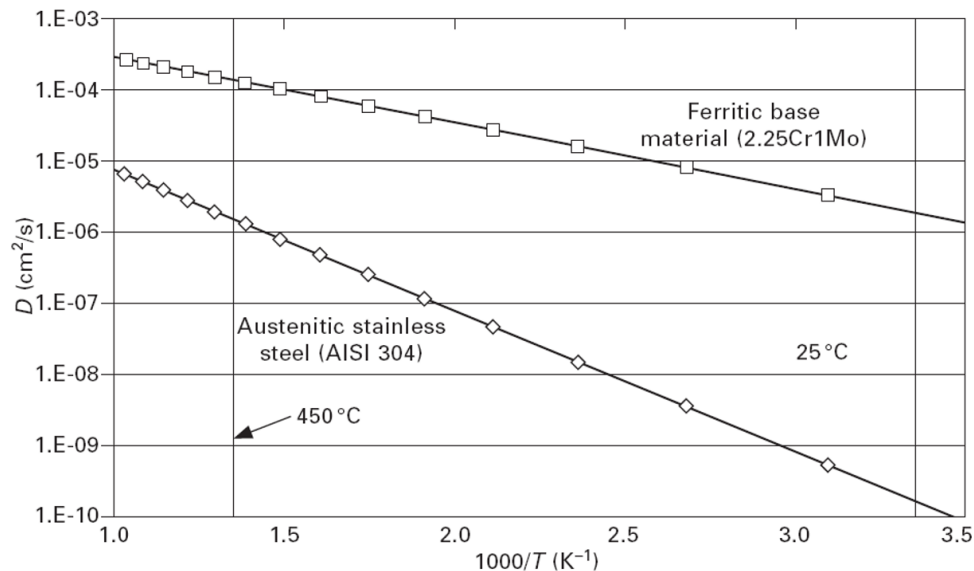
Source: Gaseous Hydrogen Embrittlement of Materials in Energy Technologies, Vol 1: The Problem, its Characterization and Effects on Particular Alloy Classes. (ed. Gangloff, RP and Somerday, BP) (2012).

Figure 73: Hydrogen Solubility in Ferritic and Austenitic Steels
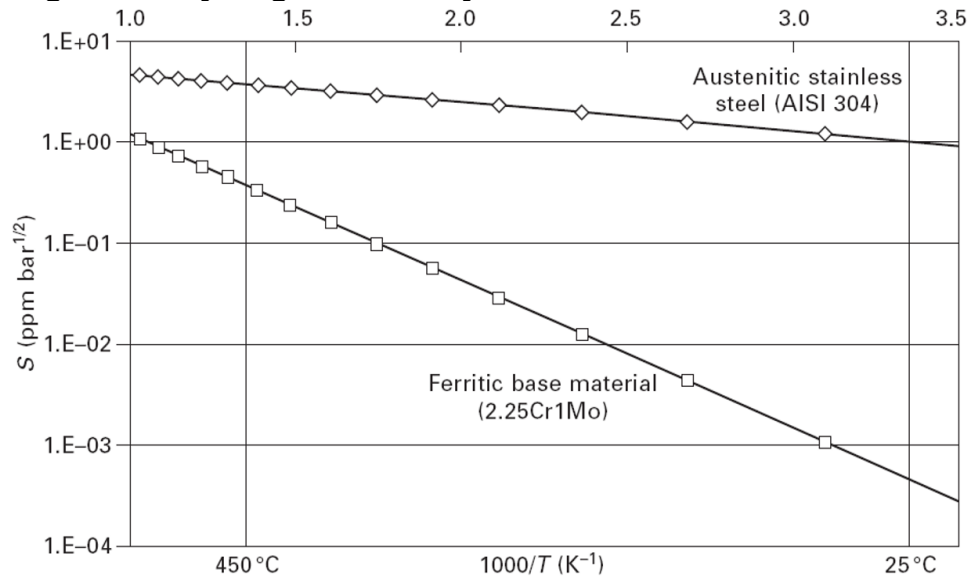
Source: Gaseous Hydrogen Embrittlement of Materials in Energy Technologies, Vol 1: The Problem, its Characterization and Effects on Particular Alloy Classes. (ed. Gangloff, RP and Somerday, BP) (2012).

Hydrogen diffusion depends greatly on temperature and can be expressed by an Arrhenius law as shown by Equation 8, where D_o is a constant used to fit the model, E is migration enthalpy, R is the universal gas constant, and T is temperature. The unit of measurement is expressed in terms of distance squared over time.

$$D = D_o \exp\left(-E/RT\right) \quad\quad \text{Equation 8}$$

The solubility of hydrogen, given by Equation 9, can also be expressed by an Arrhenius law, where S_o is a constant and ΔH is dissolution enthalpy. The unit of measurement is expressed in terms of concentration (ppm) over square root of pressure.

$$S(T) = S_o \exp(-\Delta H/RT) \quad\quad \text{Equation 9}$$

The diffusion distance or depth (x) in a material over time, can be expressed by Equation 10, where D is hydrogen diffusivity and t is time.

$$x = 2\sqrt{D \cdot t} \quad\quad \text{Equation 10}$$

Maximum hydrogen concentration (ppm) in the material can be expressed as the product of its solubility times the square root of hydrogen fugacity. At pressures below 3,600 psi and temperatures above ambient, fugacity can be replaced with the hydrogen partial pressure, as shown by Equation 11 [9].

$$C_H = S(T) \cdot P^{1/2} \quad\quad \text{Equation 11}$$

In addition to the type of crystallographic microstructure of the material, the existence of microstructural trap sites for hydrogen, including grain boundaries, phase

boundaries, dislocations, and vacancies can greatly impact the diffusion of hydrogen through the bulk of the material. Diffusion of hydrogen in the presence of microstructural trap sites, is slower compared to interstitial lattice diffusion, due to longer residence of hydrogen atoms in the trap sites. Furthermore, in some cases hydrogen trapping is an irreversible process for a given temperature, thus some trap sites can permanently trap hydrogen atoms in the material.

The presence of surface oxides can also result in slower hydrogen diffusion rate through the bulk material compared to lattice diffusion rates, as it becomes the limiting factor for the amount of hydrogen atoms absorbed in the material.

A summary by Völkl and Alefeld [95], of literature data on the diffusivity of hydrogen in alpha iron (α-Fe) with a BCC crystalline microstructure is shown in Figure 74. While the majority of data points follow the Arrhenius law at temperatures above 150° C, there is significant scatter in the data at lower temperatures. This scatter in the reported data has been attributed to surface effects and trapping of hydrogen at lattice defects such as dislocations, grain boundaries, and vacancies. Thus the cluster of data points with slowest hydrogen diffusion rates, can be attributed to surface effects, while the cluster of data points directly above it can be attributed to hydrogen trap sites [96].

Figure 74: Diffusivity of Hydrogen in α-Fe based on Various Reports
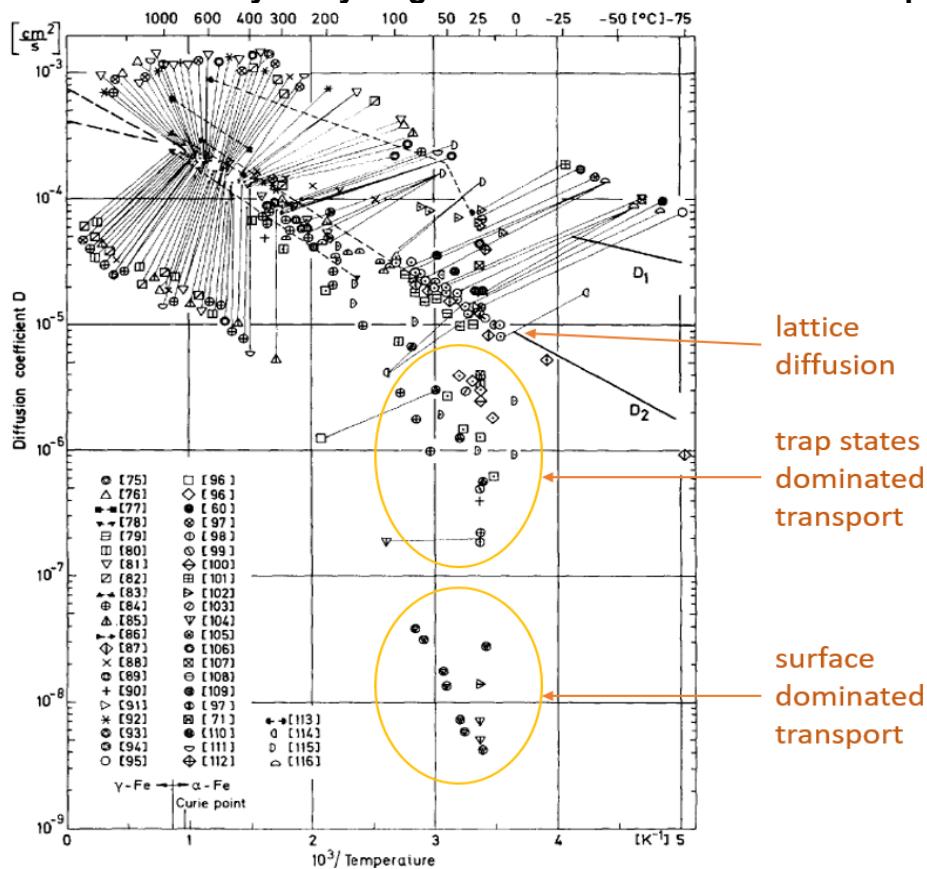
Source: Völkl, J. & Alefeld, G. Diffusion of hydrogen in metals. in Hydrogen in metals I 321–348 (Springer, 1978).

The API 5L X42 and X52 steels are widely used pipe materials in the natural gas infrastructure both in transmission and distribution side. Therefore, most of hydrogen impact studies on pipeline material are focused on API 5L grade steels, particularly X42 and X52. As reported in the literature, mechanical resistance reduction is a common consequence of hydrogen embrittlement in the steel materials based on the literature [97]. The ductility loss and increased embrittled area in the fracture surface have been observed in scanning electron microscopy (SEM) fractographic analyses. To date, most of the state-of-the-art research is heavily focused on the tensile strength of API 5L grade steels. Electrochemical hydrogen charging can be used as a time- and cost-effective manner to accelerate the hydrogen charging and conduct a first-order analysis on the effect of hydrogen with respect to material's properties (tensile strength, toughness, etc.) [98], [99]. The electrochemical hydrogen charging is the most widely used method to study of hydrogen corrosion of metals, although it does not represent the in-service conditions, and quantitative relationship to the hydrogen-blended pipeline conditions needs to be developed [100]. In the literature, results of hydrogen impact on the materials in the natural gas infrastructure such as API 5L grade steels, and stainless-steels under various experimental conditions in terms of the composition and pH of the electrolytes, and applied potential and current are reported [101]–[107].

The majority of the state-of-the-art research is heavily focused on the tensile strength of API 5L grade steels in the transmission network of the natural gas infrastructure, while the materials in the distribution network are being relatively neglected [108]. At the transmission level mostly API 5L grade steels are used, but at the distribution network there is a more diverse range of materials due to components such as meters, joints, valves, and hoses. Therefore, a comprehensive hydrogen impact study on materials including stainless-steel, cast iron, brass, Cu alloy, and Al alloy is required.

The objectives of the degradation analysis with respect to electrochemical hydrogen charging are to:

1) to establish an electrochemical hydrogen charging system as an alternative method to the pressurized gaseous hydrogen charging.
2) to confirm the charging effectiveness and hydrogen concentration after charging in the diverse steels and non-steel materials.
3) to test the mechanical properties of the materials in the natural gas pipeline infrastructure before and after the hydrogen exposure.
4) to analyze the hydrogen impact and mechanism on the materials.

In this section, we utilized a multi-channel potentiostat to create a reliable and stable power source to electrochemically generate the hydrogen from aqueous electrolyte solution with 2-electrode configuration under the galvanostatic environment. Table 11 shows list of materials in the natural gas infrastructure [109] (bolds are the materials tested in this project). To utilize the electrochemical approach on the hydrogen exposure, we chose the electrically conductive materials among the listed materials in

the natural gas infrastructure. Hydrogen concentration after electrochemical charging was confirmed by elemental analysis to quantify the elemental composition of the charged materials.

Table 11: List of Materials in the Natural Gas Infrastructure

Materials	Area of Use	Material	Area of Use
MDPE PE80	Pipeline	Tin-copper and lead solders	Pipe joints
API 5L steels	Pipeline, risers	Elastomers	O-ring, diaphragms
Cast iron	Valves, appliances	Rubber hoses	In-home connections
Copper	In-building pipelines	Nylon	Meters
Brass	Pipe joints	Epoxy	Meters, regulators, pipeline repairs
Aluminum	Valves, appliances	**Stainless-steel**	Hydrogen injection and mixing units

Source: Reference [109]

Tensile Testing

Tensile strength is one of the major mechanical properties in the specifications of steel pipeline materials and is commonly tested in the study of hydrogen embrittlement on these materials. In the literature, both pressurized gaseous hydrogen charging and electrochemical charging have been conducted to study changes in the tensile strength and fracture strain before and after hydrogen charging. The API 5L grade steel materials show a reduction of the fracture strain due to hydrogen effect, as shown in Table 12.

Table 12: Mechanical Properties Change After Hydrogen Charging in Literature

Grade	Charging method	Ultimate strength (before/after) (MPa)	Fracture strain (before/after) (%)	Ref #
X42	Electrochemical	483 / 493	46.0 / 31.1	[101]
X70	Electrochemical	602 / 613	15.2 / 12.8	[110]
X70	Electrochemical	557 / 557	13.8 / 10.9	[111]
X80	Electrochemical	692 / 699	14.6 / 12.5	[110]
X100	Electrochemical	756 / 762	12.4 / 9.6	[110]
X100	Electrochemical	793 / 729	5.8 / 1.6	[112]
X52	Gaseous	510 / 510	32.2 / 25.1	[113]
X60	Gaseous	532 / 530	21.1 / 16.3	[114]
X70	Gaseous	636 / 631	22.9 / 14.1	[115]
X100	Gaseous	796 / 812	20.9 / 10.8	[113]

Source: Reference [101], [110]–[115]

Figure 75 shows a typical tensile testing result and the interpretation of the strain-stress curve. In the early stage of tensile testing, the stress-strain curve shows a linear relationship, representative of the specimen undergoing elastic deformation, under which the specimen will recover its original state immediately if the external force is removed. The end point of the linear region is the elastic limit, where the stress at this point is the maximum yield strength of the material. Beyond the elastic limit, the specimen shows plastic deformation with an irregular stress-strain pattern, and the material cannot fully recover any longer, even if the external force is removed. Under continued external stress, dislocation activity in the crystal lattice starts to occur resulting in the hardening of the material until it reaches the maximum stress point, which represents the ultimate tensile strength of the specimen. If external strain is continued to be applied, necking occurs at the weakest point with the specimen reducing its cross-sectional area and forming void or cavities inside.

Figure 75: Interpretation of the Tensile Testing Results
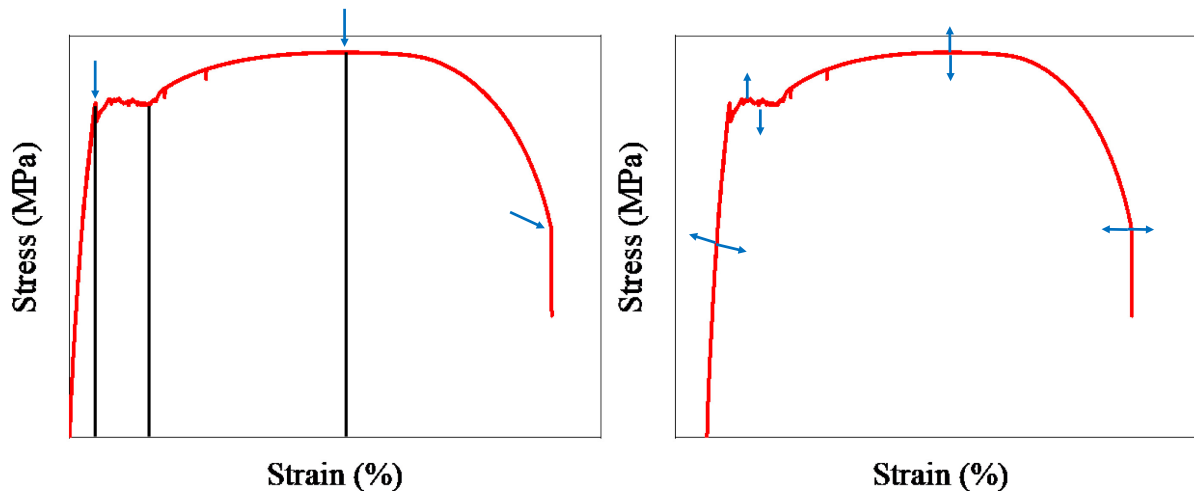
The tensile testing results show diverse aspects of the specimen's mechanical properties. In the elastic deformation region, the slope is the Young's modulus, which represents the stiffness or elasticity of the materials. The maximum stress in the elastic deformation region shows the range of stress under which the material fully recovers if the external force is removed. In the plastic deformation region, the maximum stress, or ultimate tensile strength, shows the stress that the material can endure until necking or tearing occurs. The fracture strain in this region is closely related to the brittleness of the material. The selected tensile testing results before and after the hydrogen charging listed in Table 10 show no significant changes in the tensile strengths, while the fracture strain reduces significantly from the hydrogen impact.

The fractured surface obtained from the tensile strength testing can be utilized for the fractographic analysis to study the cross-sectional area reduction, local brittleness, and crack growth mechanism. The SEM fractographic images in Figure 76 show the change in fracture morphology before (left) and after (right) hydrogen exposure of API 5L X65 steel. The typical plastic deformation of ductile material leaves porous dimple pattern due to microvoid coalescence [105]. In contrast, the hydrogen-exposed steel shows the absence of dimples in the fracture surface, which suggests a brittle fracture induced by hydrogen [116].

Figure 76: SEM Fractographic Images of before (left) and after (right) Hydrogen Exposure of API 5L X65 Steel
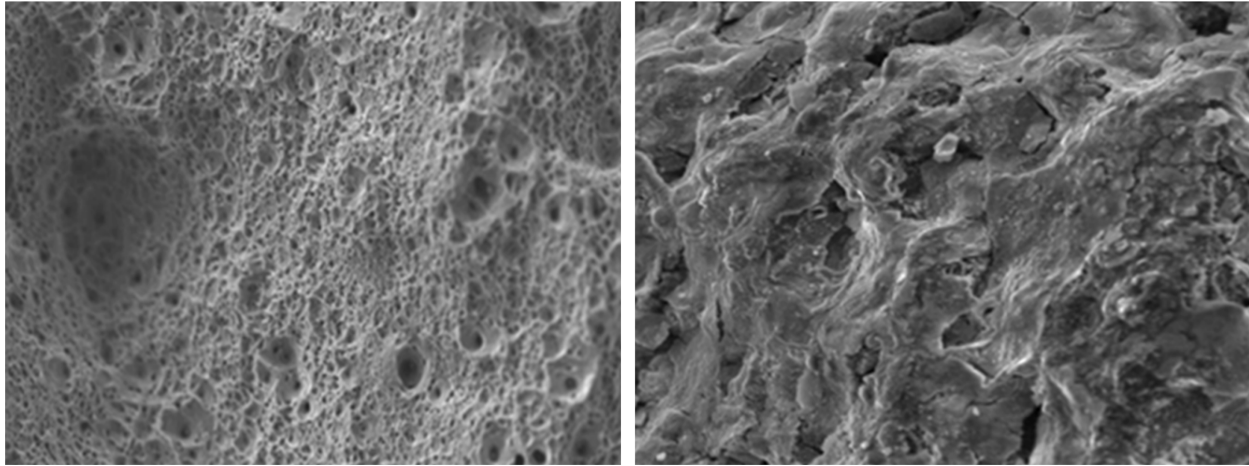
Source: Reference [116]

Charpy Impact Toughness Testing

Impact resiliency is another important mechanical property for natural gas pipeline materials. According to a report from NREL, the highest expected risk by natural gas utility companies for pipeline failure is damage from mechanical impact e.g. excavating [2]. Table 13 shows a list of operator perceptions on threat significance. The external mechanical force-related threats to steel pipeline are bolded. The two highest threats are related to the physical and mechanical damage of the pipes, with 49% of the respondent answering that outside force on the steel pipe is also a significant threat.

The statistics on failure causes for years 2008-2015 are shown in Figure 77. The mechanical damage-related causes are presented separately for transmission (left) and distribution (right) gas pipelines. The statistical data shows that excavation damage is the highest failure cause for both transmission and distribution pipelines. Particularly, mechanical-related damage including excavation damage, other outside forces, and natural forces accounts for 58% of the total failure causes in the gas distribution pipeline [117].

Table 13: Operator Perceptions on Threat Significance

Threat Priority	Threat	% of Respondent
1	**Outside Force / Weather Cast Iron Pipe**	90
2	**Excavation / Mechanical Damage**	87
3	External Corrosion Bare Steel Pipe	86
4	External Corrosion (Graphitization) Cast Iron Pipe)	71
5	External corrosion Coated & Wrapped Pipe	69
6	Construction-Related Defects Plastic Pipe	57
7	**Outside Force / Weather Steel Pipe**	49
8	Construction-Related Defects Steel Pipe	48
9	Incorrect Operations & Operator Error	35
10	Equipment Malfunction	35
11	Manufacture-Related Defects Plastic Pipe	30
12	Outside Force / Weather Plastic Pipe	26
13	Internal Corrosion	22
14	Manufacture-Related Defects Plastic Pipe	22

Source: Reference [2]

Figure 77: Pipeline Failure Causes
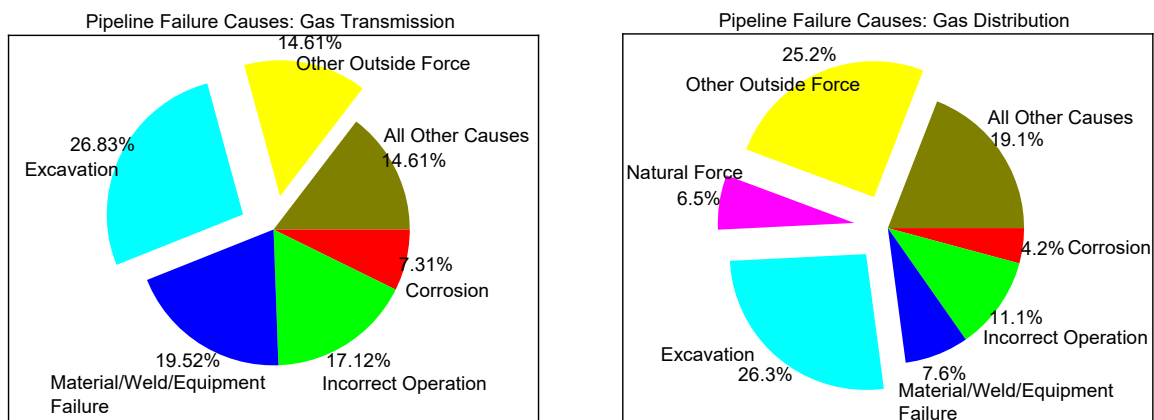
Source: U.S. DOT Pipeline and Hazardous Materials Safety Administration (PHMSA)

Charpy impact toughness of API 5L grade steels and other natural gas pipeline materials before and after electrochemical hydrogen charging were conducted in this project to investigate the hydrogen impact on materials present in the distribution side of the natural gas pipeline (see section Charpy Impact Toughness Testing). The V-notch Charpy test is the most common method to measure the impact resiliency, failure behavior, and ductile-to-brittle transition of metal and alloy materials. In general, the

96

Charpy impact test is employed for the qualitative analysis of the toughness of materials. Current research efforts are trying to develop a quantitative relationship with the mechanical properties of materials [102], [118].

Ductile-to-brittle transition temperature (DBTT) is the temperature where the metal and alloy material changes from ductile to brittle state when the temperature is decreased [119]. The impact toughness and failure mechanism show significant change before and after the DBTT as shown in Figure 78. The ductility and brittleness of the specimen in the Charpy testing is characterized by the morphology of the fracture

Figure 78: Ductile to Brittle Transition
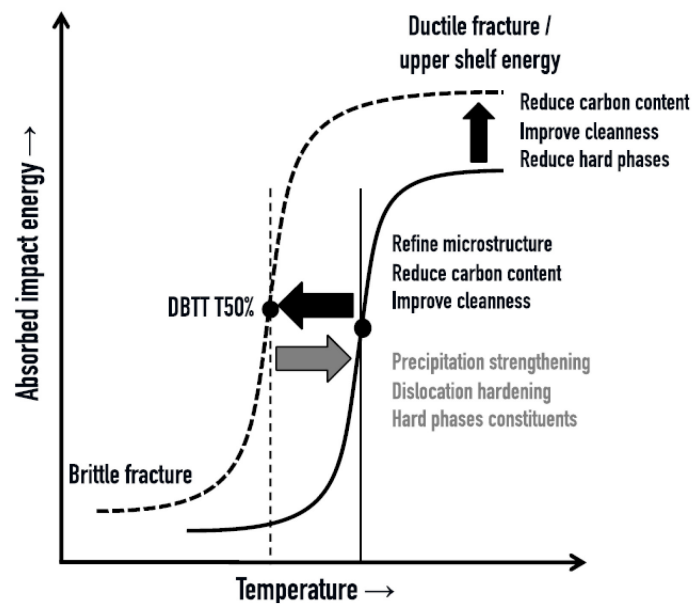
Source: Reference [119]

surface and specimen breakage during the testing. Figure 79 shows the photograph of Charpy toughness testing performed on 316L stainless-steel (SS) samples. The specimens show different break angles and fracture morphologies from the different temperature and hydrogen impact [120].

Figure 79: Photograph of Charpy Tested Specimens
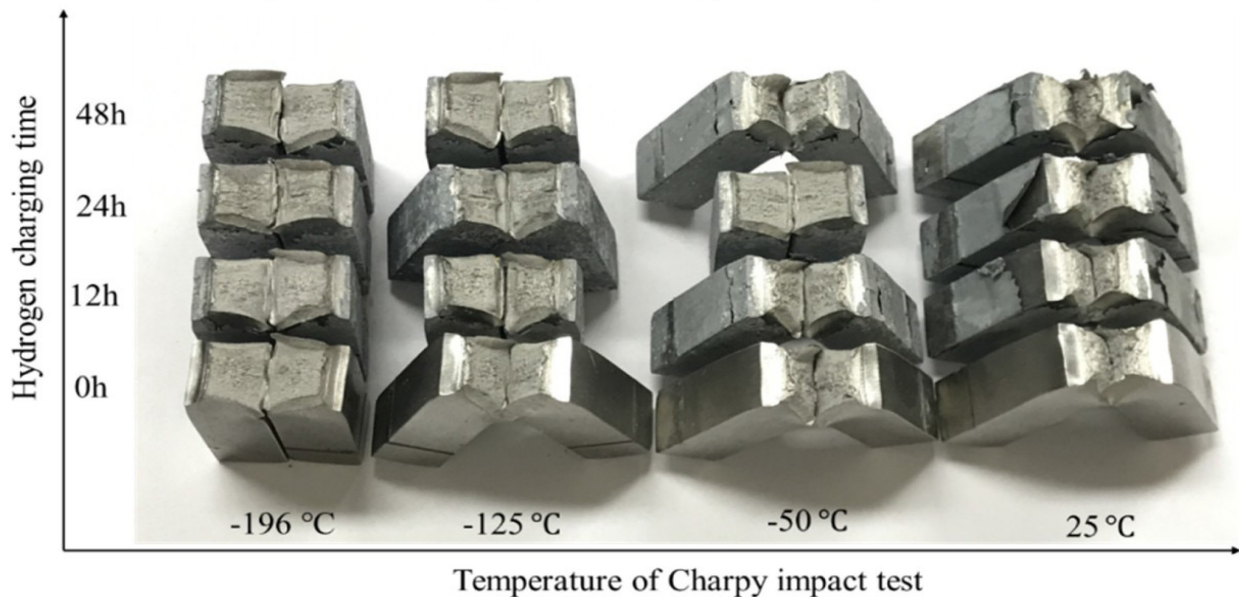
Source: Reference [120]

97

Experimental Approach

Two different approaches were employed for charging material samples with hydrogen, to evaluate their susceptibility to hydrogen embrittlement. The first approach, involved hydrogen charging of metal samples by an electrochemical method, which is a well-established method described in ASTM G-148 for evaluating hydrogen uptake, permeation and transport. The advantages of this method include relatively quick turn-around, lower instrumentation cost, lower risk of fire due to smaller hydrogen gas volume. A noticeable limitation in the electrochemical approach is the effect of the hydrogen can be overestimated due to the higher charging level. The second approach used, involved exposing test samples to hydrogen gas in a pressure vessel, performed at elevated pressure and temperature to increase hydrogen diffusion and solubility. Although the latter method more accurately emulates exposure of material to hydrogen under more realistic conditions, the increased fire hazard associated with high pressure hydrogen gas at elevated temperatures, required the incorporation of multiple safety layers in the experimental setup and imposed safety limits in pressure and temperature.

Electrochemical Hydrogen Charging

The basic electrochemical hydrogen charging setup composed of an electric power source, counter electrode, reference electrode, and wiring, is shown in Figure 80 (left). Using a potentiostat allows for the precise control the hydrogen generation rate. The Biologic VMP-3e potentiostat (right) used for the electrochemical charging is capable of galvanostatic hydrogen generation at a constant hydrogen generation rate.

Figure 80: Electrochemical Hydrogen Charging Setup with a Power Supply (left) and a Potentiostat (right)
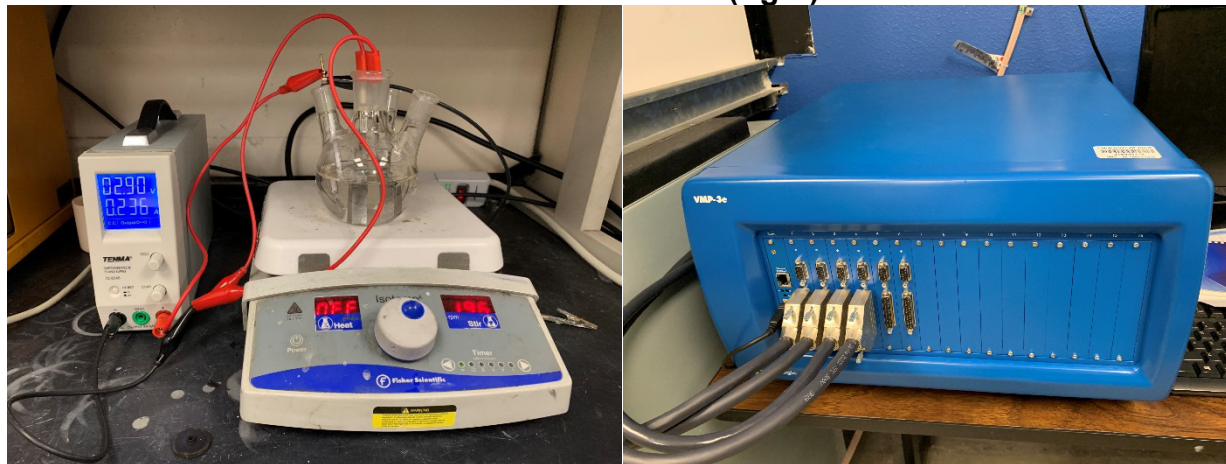
Table 14: Detailed Experimental Parameters and Conditions for the Electrochemical Hydrogen Charging Experiment

Experimental Parameter	Condition	Experimental Parameter	Condition
Charging mode	Galvanostatic	Current density	-5 mA/cm^2
Surface area	21-24 cm^2	Charging duration	12-24 hours
Electrolyte pH	0	Counter electrode	Pt plate
Electrolyte composition	0.5 M H_2SO_4 0.25 g/L As_2O_3	Electrode configuration	2-electrodes

Gaseous Hydrogen Charging

Figure 81 shows the design diagram of the setup used for hydrogen charging of test samples. The system consists of a stainless steel chamber, heating element on the surface of the chamber, pressure transducer reporting pressure in the chamber, thermocouples measuring temperature of the gas in the chamber and the heating element, solenoid valves, H_2 gas detector, H_2 flame detector, H_2 supply gas used to charge test samples, and N_2 gas used for purging the system. Monitoring and control of the system instrumentation is accomplished through LabVIEW software application.

Figure 81: P&ID of Gaseous Hydrogen Charging Instrumentation Setup
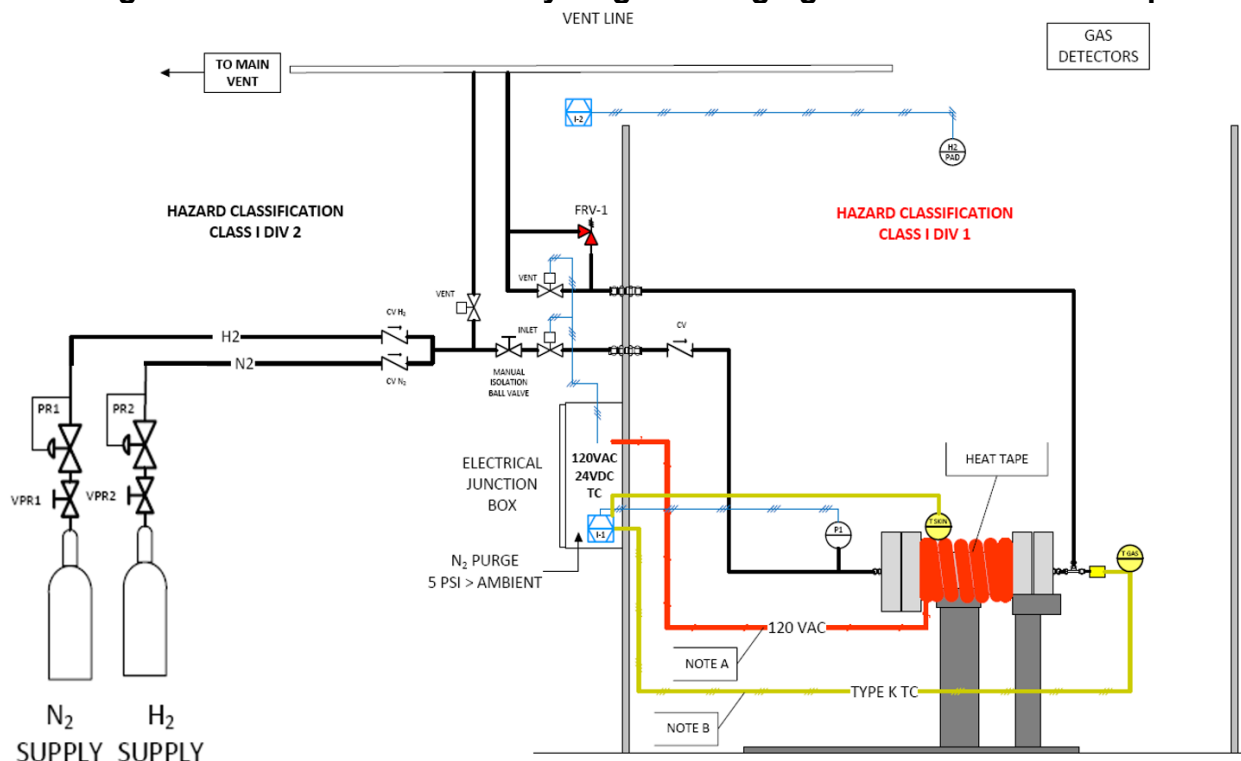
Figure 82: External View of Gaseous Hydrogen Charging Chamber (left), Test Samples Loaded in the Chamber (right)

Figure 83: View of Test Chamber with Heating Element and Thermal Insulation
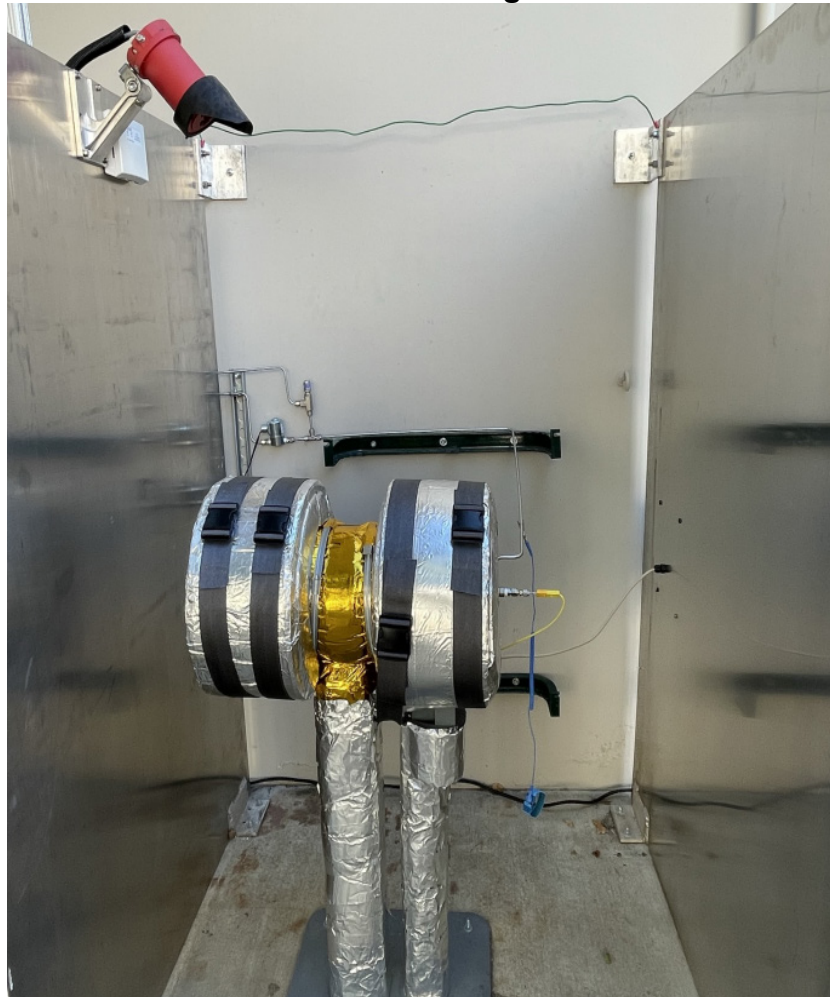
Figure 82 shows the hydrogen test chamber, built using a schedule 80 316 stainless steel pipe section with 6" diameter, and class 600 316 stainless steel flanges welded on both ends. The chamber is capable of operating pressure of up to 1,500 psi. Figure 83 shows test chamber area is enclosed by ¼" aluminum sheet wall, and monitored with gas leak and flame detectors. A 600 W power silicone heating tape, capable of operating at temperatures of up to 450° F, is wrapped around the surface of the chamber. The heating elements and remaining parts of the chamber are covered by layers of thermal insulation.

Figure 84 shows the LabVIEW software application used to regulate the heating element to achieve the target temperature of the gas inside the test chamber. The application uses temperature readings from the heating element and the gas in the chamber, and PID control loop to manage the output power of the heating element by pulse width modulation. The system also receives input from the hydrogen gas and flame detectors. The temperature inside the chamber was maintained at 250° F, while the hydrogen pressure in the chamber was 1,042 psig, during the duration of the experiment (15 days).

Figure 84: LabVIEW Control Panel of Gaseous Hydrogen Charging Chamber

Elemental Analysis

To quantify the concentration of hydrogen in uncharged and hydrogen charged metal samples, elemental analysis was performed by an ONH Elementrac analyzer using fusion process. The instrument is equipped with a TCD detector and can detect hydrogen concentrations between 0.1 to 1,000 ppm on 1 g samples. Four samples with

nominal weight of 1 g, were used for each metal type and charging condition. Figure 85 demonstrates the process of loading a test sample in the instrument for analysis.

Figure 85: Operation of the Elementrac ONH Elemental Analyzer

Tensile Testing

Figure 86 (a) shows the Instron 5969 dual column mechanical testing system. A dogbone shape specimen is mounted on the Instron mechanical tester (Figure 86 (b)) and extended at a constant rate to observe the strain against the mechanical stress until it breaks. During tensile testing, the specimen shows necking beyond the ultimate tensile strength and starts to deform (Figure 86 (c)). Figure 86 (d) shows the specimen dimension following ASTM E8/E8M standards. The tensile strength of the specimen before and after the hydrogen charging were tested in different extension rates (0.24 mm/min to 10 mm/min).

Figure 86: Tensile Testing System
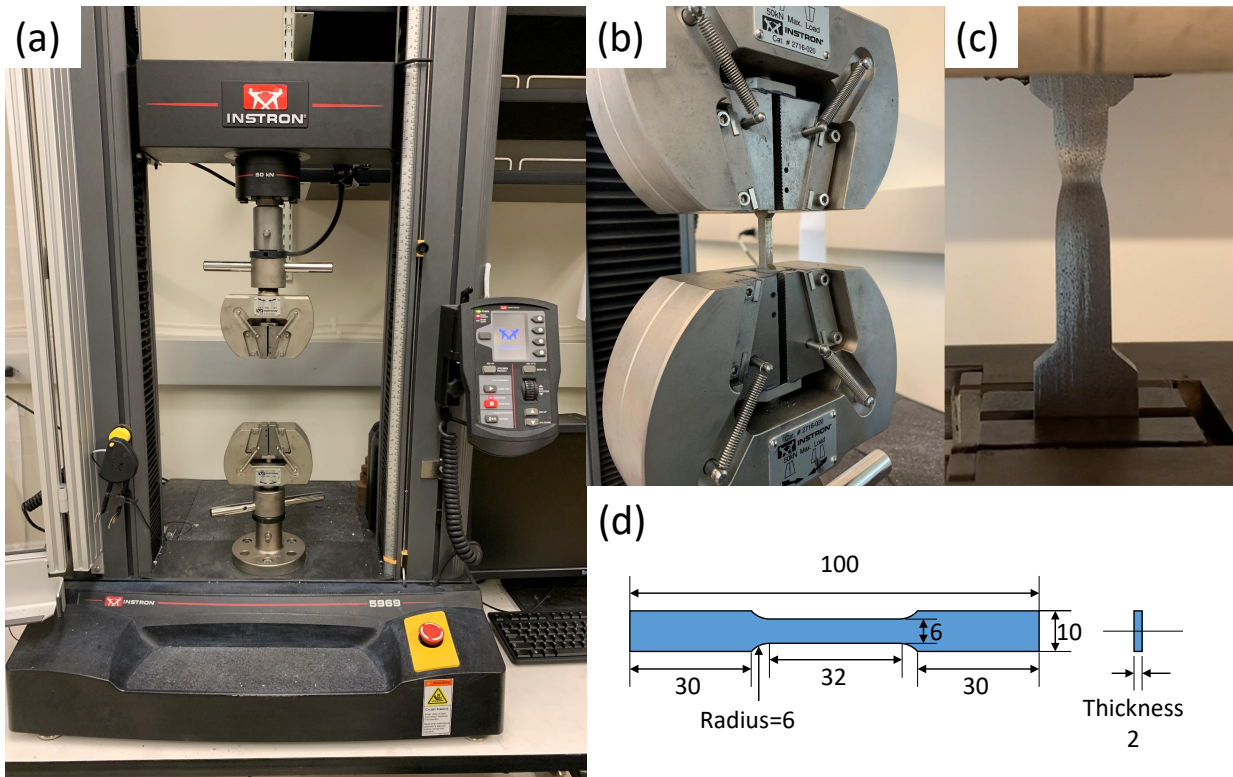
a) Instron 5969 mechanical tester, b) Mounted specimen, c) Necking of the specimen, and d) Dimension of the specimen in ASTM E8/E8M

As a preliminary test, specimens of uncharged cold-roll 1018 carbon steel (CR 1018) and API 5L X65 steel (X65) were tested under different strain rates ranging from 0.24 mm/min and 10 mm/min, as shown in Figure 87.

The results show deviated results under the different strain rates without a clear trend or relationship between the strain rate and testing results including ultimate tensile strength and fracture strain. The observed deviation in the measurements are inherent experimental error, and the strain rate effect in the range between 0.24 mm/min and 10 mm/min is relatively small [121], [122].

Figure 87: CR 1018 (left) and X65 (right) Tensile Testing under Different Strain Rate
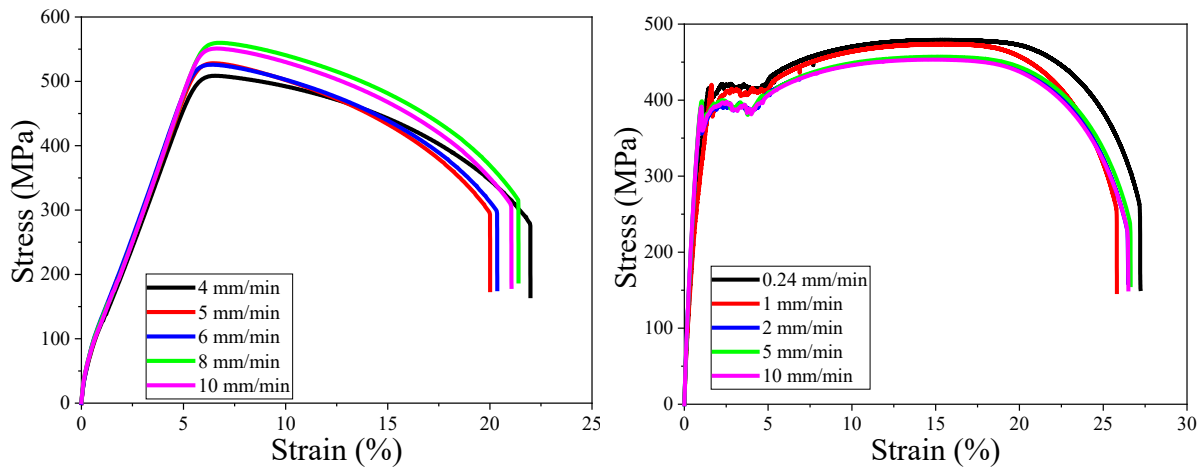
The fracture surface resulting from the tensile testing was characterized by SEM to analyze the ductility or brittleness of the specimen, as shown in Figure 88. The CR 1018 specimen fractured in the form of cup and cone and microvoid coalescence (MVC) was observed throughout the entire fracture surface. MVC is a characteristic fracture mechanism observed in ductile materials, which is expected in steels unaffected by the hydrogen.

Figure 88: SEM Fractographic Images of the Tensile Tested CR 1018
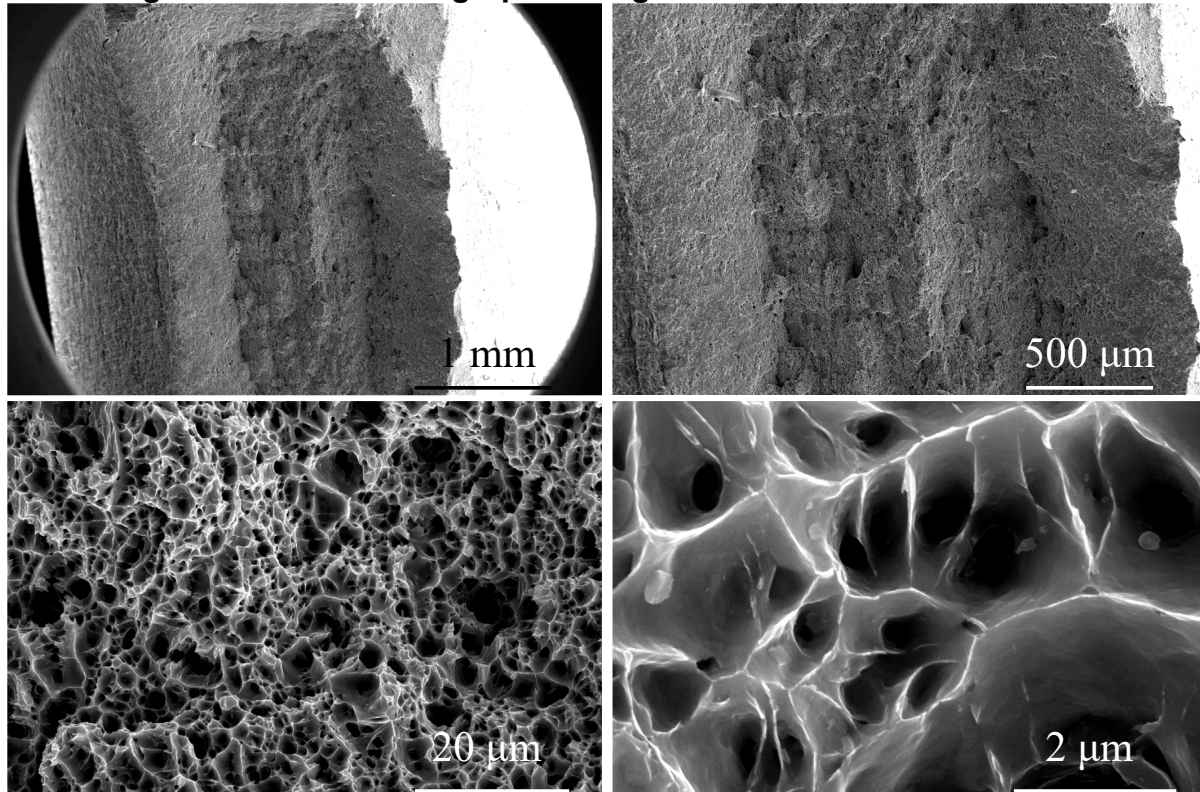
Charpy Impact Toughness Testing

Figure 89 shows the Charpy impact toughness testing system used in this project. Figure 89 (a) is the photo of the Charpy impact tester. To measure the absorbed energy by the specimen, the hammer is loaded (Figure 89 (b) and (c)) and the back side of the v-notched specimen is hit as illustrated in Figure 89 (d). The mechanical energy of the hammer is partially absorbed while it breaks the specimen, so that the final height of the hammer after the measurement is lower than the initial height. The difference of the height indicates the absorbed energy within a range of 0 to 405 J.

Figure 89: Charpy Impact Toughness Testing System
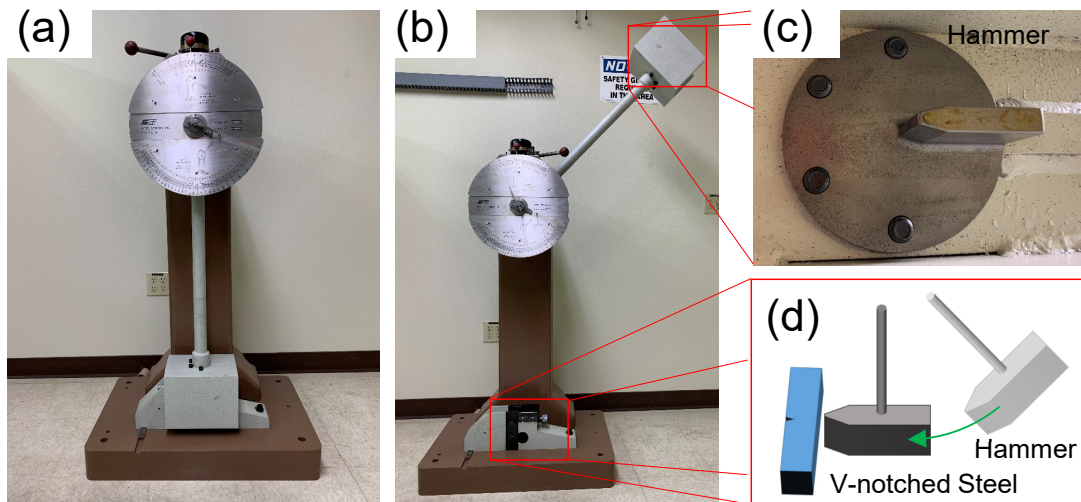
(a) Charpy impact tester, (b) Hammer loaded, (c) photo of the hammer, and (d) schematic drawing for the impact test on the v-notched specimen

Preliminary Charpy toughness testing results on 18-8 and 316 SS specimens show reduced absorbed Charpy energy, as shown in Figure 90. The reduction in Charpy absorbed energy indicates that the specimens lose ductility after being electrochemically charged for 12 hours, requiring less energy to cleave the v-notched specimen. In the case of 18-8 SS (black squares), the Charpy absorbed energy in the pristine specimen was 258 J. After hydrogen charging, the Charpy energy was reduced to 220 J for a reduction in the absorbed energy of 38 J.

The same trend was observed in the 316 SS (red circles). The Charpy absorbed energy was reduced from 231 J to 184 J after electrochemical hydrogen charging. The Charpy energy difference in 316 SS of 47 J is greater than that of 18-8 SS. These results indicate that 316 SS is relatively more susceptible to hydrogen exposure.

In addition to testing the Charpy impact energy under ambient temperature, testing in the temperature range of -50 °C to 50 °C (-58 °F to 122 °F) was also conducted.

Figure 91 shows the detailed cooling and temperature recording setup used during the Charpy testing. A Fluke 1586A temperature scanner was used to monitor the real-time temperature of the specimen during cooling and Charpy testing. A thermocouple was prepared as a square ring to enlarge the interfacial area with the specimen for higher precision temperature sensing (Figure 91 (a)). The ring was connected to the V-notch Charpy specimen (Figure 91 (b)),

Figure 90: Charpy Toughness Testing Result before and after 12 Hour Hydrogen Charging on 18-8 and 316 Stainless-Steel

and the specimen along with the temperature probe was put into the dry ice stainless-steel dewar (Figure 91 (c)). After the specimen reaches the targeted cold temperature, it is loaded on the Charpy tester with the temperature probe attached (Figure 91 (d) and (e)).
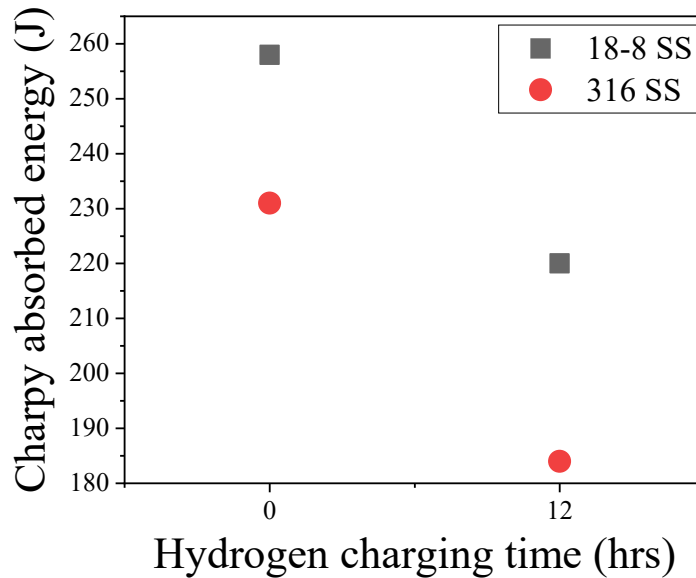
Figure 91: Low-Temperature Charpy Testing and Temperature Measurement System
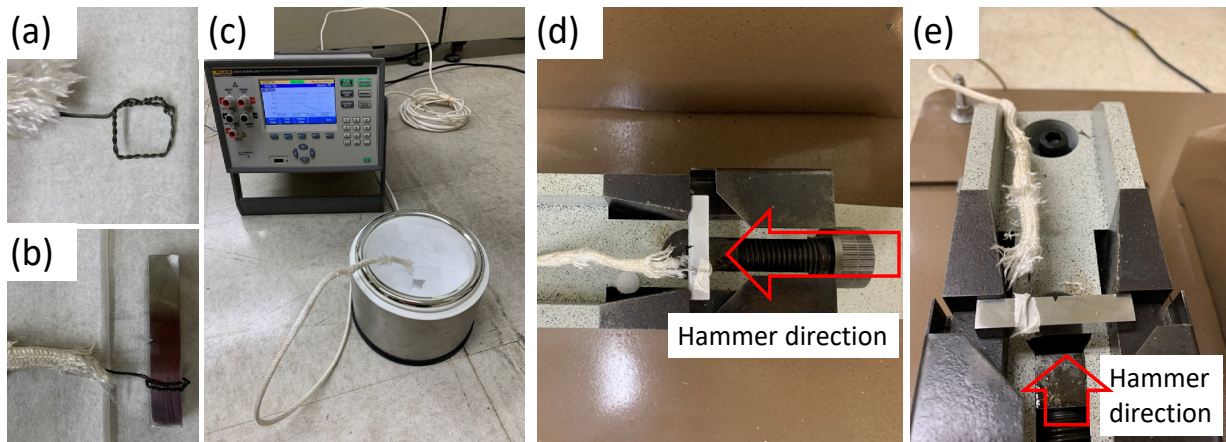
Experimental Results and Discussion

Electrochemical Hydrogen Charging

Figure 92 shows the electrochemical hydrogen generation setup with a CR 1018 specimen as the working electrode. The negative potential on the CR 1018 steel drives the hydrogen generation reaction from the electrolysis of water. The generated hydrogen either diffuses into the steel or escapes out of the solution in the form of bubbles. The hydrogen content in the specimen is dependent on the solubility of the material. After 24 hours, the hydrogen diffusion in the steel reaches equilibrium, at which point no further net charging or discharging is observed.

Figure 92: Photo of Electrochemical Hydrogen Generation

The amount of charged hydrogen was measured in two different ways. Firstly, the amount of hydrogen diffused out from the steel is electrochemically measured, and the result is shown in Figure 93. The plot on the left is the comparison between an uncharged and a 24-hour charged CR 1018 steel specimen. The curves represent the responsive current under a mild positive potential (+177 mV vs Ag/AgCl) in 0.2 M NaOH (pH 13.3) solution measured by the potentiostat. To quantify the hydrogen diffused out of the specimen over a period of 30 minutes, the current was converted to the mole number using Equation 12.

$$mole\ H_2 = I \times t \div 6.02 \times 10^{23} \div 1.60^{-19} \div 2$$

Equation 12

Where I is current measured in Coulombs per second, t is time measured in seconds, 6.02×10^{23} is Avogadro's number, and 1.60^{-19} is the electron charge in Coulombs.

The plot on the right of Figure 93 shows the mole number of detected diffusive hydrogen gas over time. Integration of the difference of the hydrogen molecules between uncharged and charged is used to calculate the total mole number of hydrogen gas=2.29 x 10^{-5} mol, which is 4.57 x 10^{-5} g. The calculated hydrogen content in the specimen is 1.06 ppm, and it is in the range of reported hydrogen content in steel materials (0.6 ppm to 2.0 ppm) [102], [123]. However, the electrochemically detected hydrogen only quantifies the shallow-trapped diffusive hydrogen, and the deep-trapped hydrogen with high bounding energy cannot be detected. Therefore, the hot melting extraction by the elemental analyzer was employed to quantify the hydrogen content in a diverse number of steel and non-steel alloy materials.

Figure 93: Electrochemical Decharging of the Hydrogen in CR 1018 (left) and Differential (right) to Calculate the Hydrogen Charging Concentration
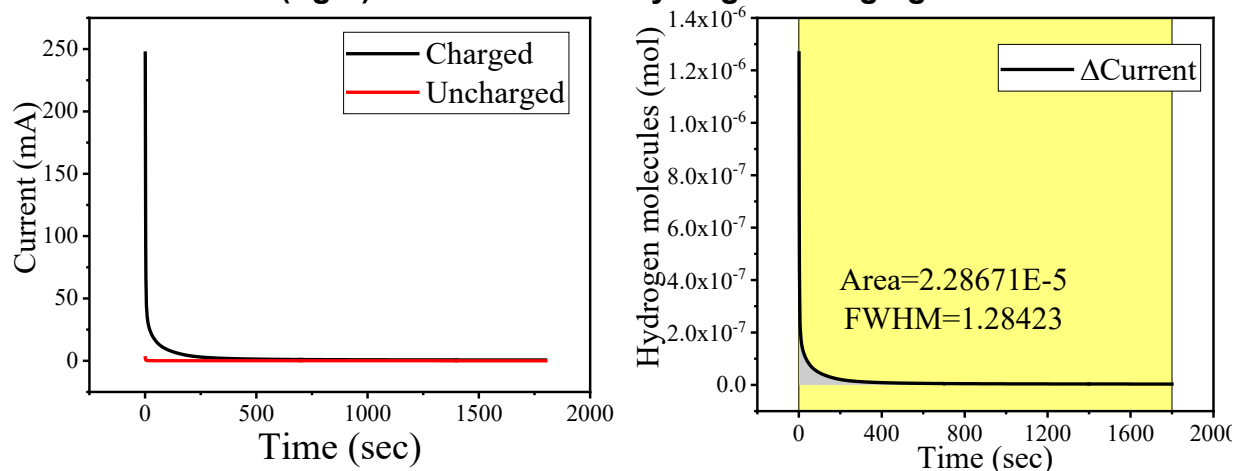
Figure 94 shows the hot melting extraction elemental analysis results on API 5L X42, X52, and X65 steel specimens. The X42, X52, and X65 are represented as a square, circle, and triangle, respectively. The uncharged, electrochemically charged (EC), and gaseous hydrogen (GH) charged samples are colored as black, red, and blue, respectively. The uncharged steels show low concentrations up to about 0.5 ppm. After 24 hours of electrochemical hydrogen charging, hydrogen content was significantly increased up to 1.7 ppm, 2.1 ppm, and 4.3 ppm in X42, X52, and X65, respectively. The hydrogen content by the electrochemical charging is dependent on the material's hydrogen solubility. After 24 hours electrochemical charging reached its equilibrium state. Hydrogen solubility in API 5L steels was confirmed via elemental analysis to increase with the yield strength of the electrochemically charged specimens analyzed. However, in the case of gaseous hydrogen charging, the hydrogen content decreased with the increase of the tensile strength of the specimens analyzed. This result suggests that the hydrogen content in a dynamic condition (pressurized gas) is affected by other factors such as the diffusion rate near the surface and body of specimens. Detailed experimental research to establish the models and relationships among hydrogen concentration, microstructure, and mechanical behavior will be needed in future work for a better understanding and interpretation of the results.

Figure 94: Elemental Analysis on API 5L X42, X52, and X65 Steels
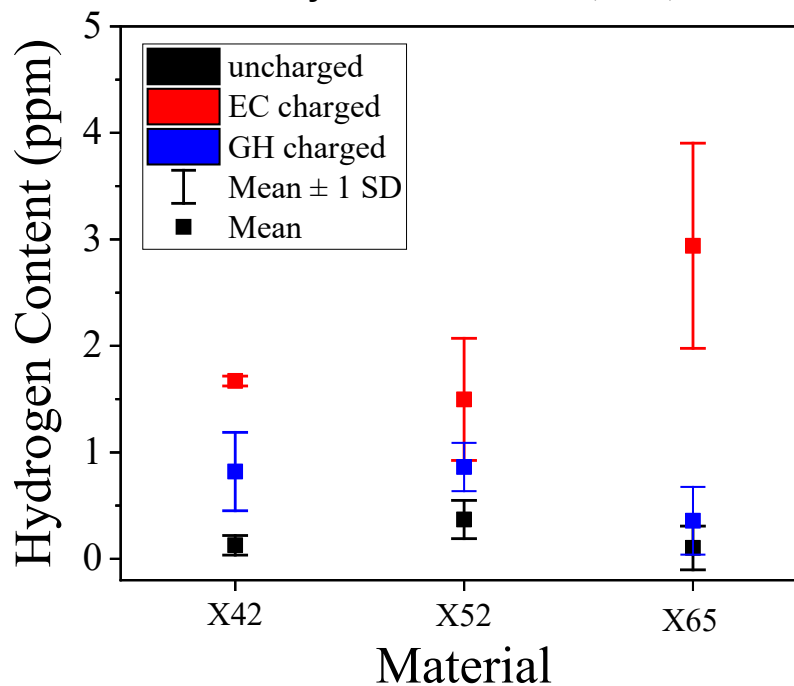
Figure 95 shows the elemental analysis results on stainless-steel 304 (SS304), cast iron (CI), and ductile iron (DI) comparing uncharged versus EC- and GH-charged specimens. Uncharged SS304 shows low hydrogen concentration similar to API 5L steels. After both EC and GH charging, the hydrogen content in SS304 is significantly higher than API 5L steels. CI and DI show higher hydrogen content in the uncharged specimen up to 4.4 ppm. The hydrogen content in ductile iron after charging is much higher than cast iron, which supports the thesis that the microstructure and elemental composition of the base material plays an important role in the solubility of hydrogen. The same trend, in which EC-charged specimens show higher hydrogen content compared to GH-charged specimens, also applied to this set of materials.

Figure 96 shows the elemental analysis results on brass, copper alloy (CA), and aluminum alloy (AA). While brass and copper alloy show similar hydrogen contents before and after charging to those of API 5L steels, aluminum alloy show larger deviation in each repeated measurement and decreased hydrogen content after charging. Further investigation is needed to interpret these results on the aluminum alloy in the future work to properly analyze and validate these results.

Figure 95: Elemental Analysis on SS304, Cast Iron, and Ductile Iron
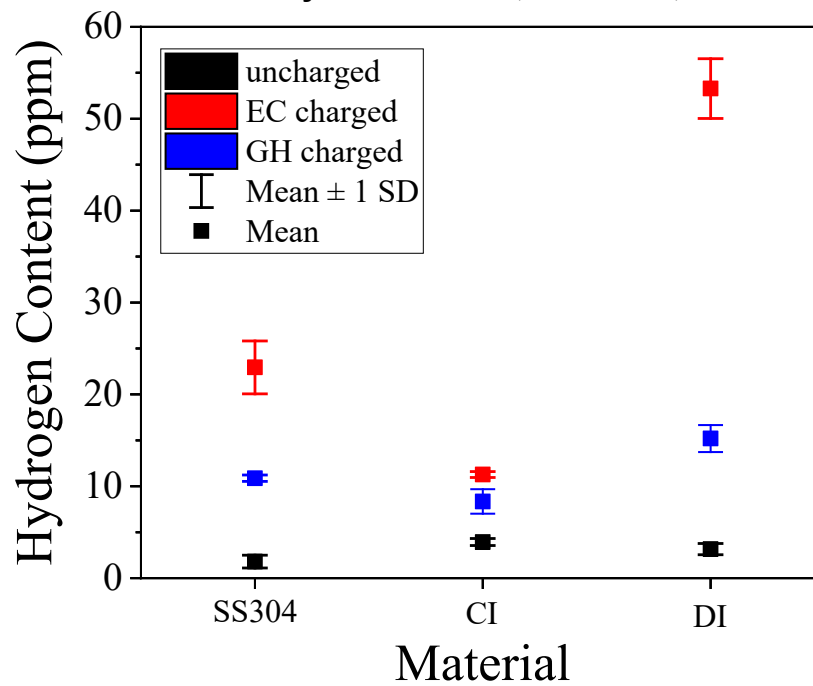
Figure 96 Elemental Analysis on Brass, Copper Alloy, and Aluminum Alloy
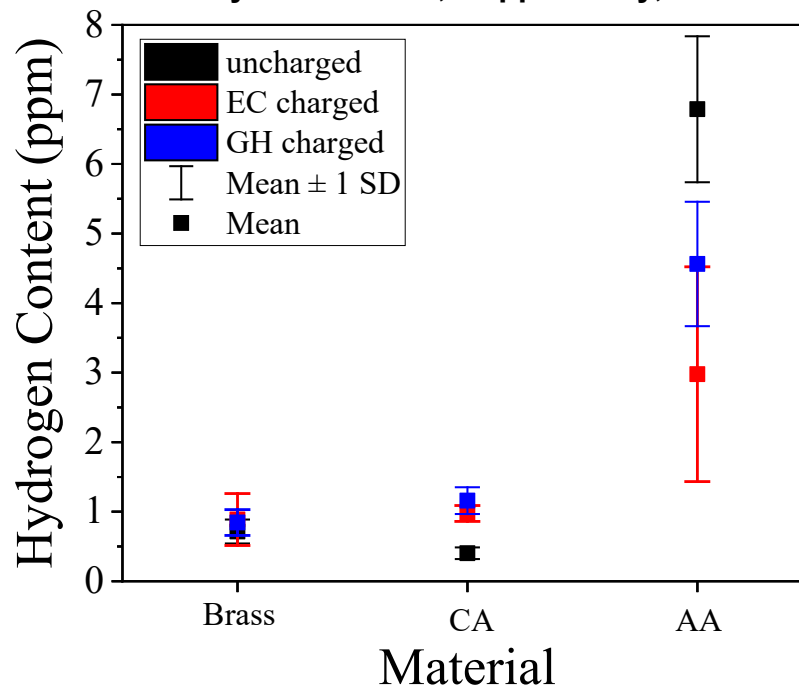
Tensile Testing

Figure 97 (left) shows the tensile testing result before and after hydrogen charging of X65 specimens, using an Instron 5969 mechanical tester. The uncharged samples (solid lines) show similar results under the different strain rates from 2 mm/min to 10 mm/min. After 24 hours of electrochemical hydrogen charging, all three results show hardened behavior and increased yield and ultimate tensile strength. The hardening of the specimen after the hydrogen charging is matched with the results in literature [124]. In terms of brittleness, the results under slow strain rates (2 and 5 mm/min) showed clear hydrogen impact, while the result under fast strain rate (10 mm/min) showed less impact on the embrittlement. This result means there was insufficient time for hydrogen embrittlement to affect when the strain rate is too fast [125]. Therefore, the strain rate has to be chosen properly to observe the hydrogen impact in the tensile strength testing.

Figure 97 (right) shows the photograph of the fracture surface after tensile testing. The uncharged specimens show a reduced cross-sectional area due to necking during the testing with uniform dark gray color inside the specimen. In contrast, the charged specimens show a larger cross-sectional area, indicative that the specimen broke earlier than the uncharged specimens due to the embrittlement of the material. The visual signs of embrittlement in the charged specimen support the tensile testing results. More importantly, the fracture surface of the charged specimens shows irregular circular light gray patterns, representative of localized embrittlement. The detailed fractographic analysis of electrochemically charged X65 steel for 12 hours was conducted with the SEM analysis shown in Figure 98.

Figure 97: X65 Tensile Testing Before/After Hydrogen Charging
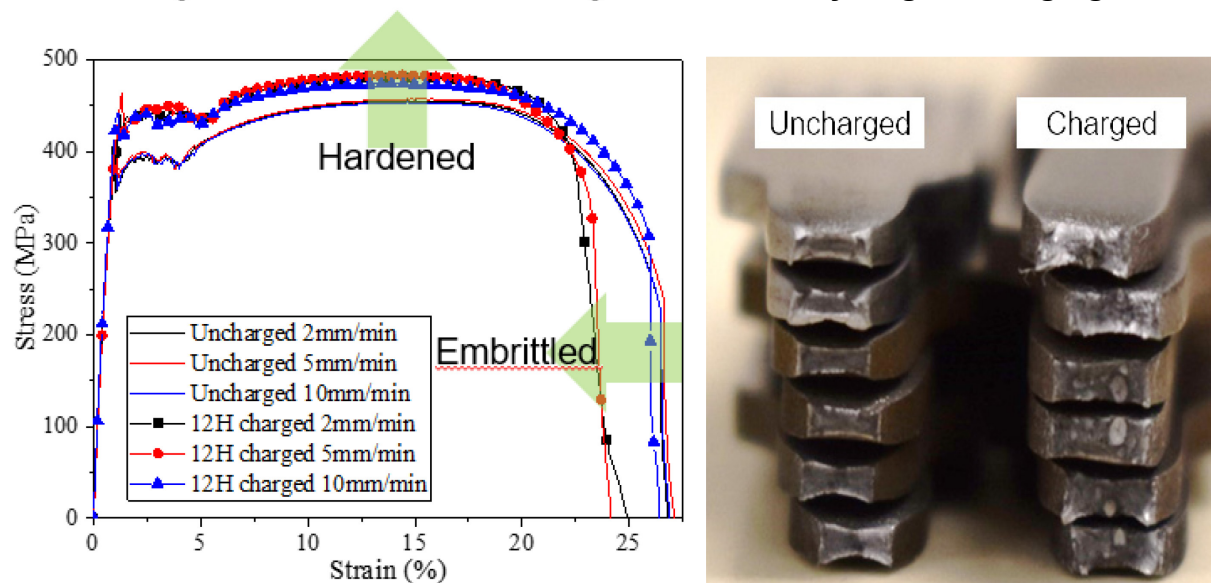
Figure 98 SEM Fractographic Analysis of Uncharged (top) and Charged (bottom) X-65 Steel

A_1=3.062 mm²
L1=8.42 mm
Area reduction=0.75
Elongation=0.26

A_2=5.016 mm²
L1=7.35 mm
Area reduction=0.42
Elongation=0.23
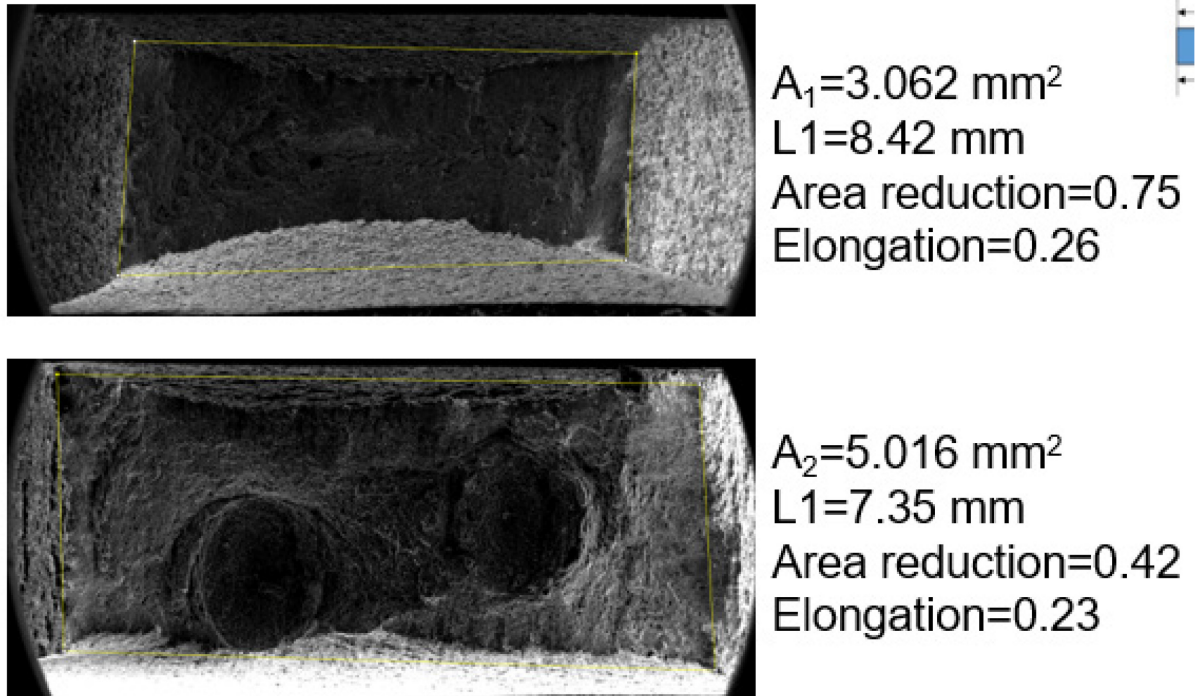
The cross-sectional area before the hydrogen charging was decreased from 12 mm² (6 mm width and 2 mm thickness) to 3.062 mm², a 75% reduction in area. The hydrogen charged specimen showed a 5.016 mm² surface area, a 42% area reduction. In addition, the hydrogen charged specimen shows circular patterns as observed in Figure 97 (left).

Figure 99 shows the detailed fractographic analysis on the uncharged specimen under different magnifications. The fracture surface shows microvoid coalescence uniformly on the entire fracture surface. This result is expected to the mid-strength steel materials.

Figure 99: SEM Micrographs on the Uncharged X65 Steel
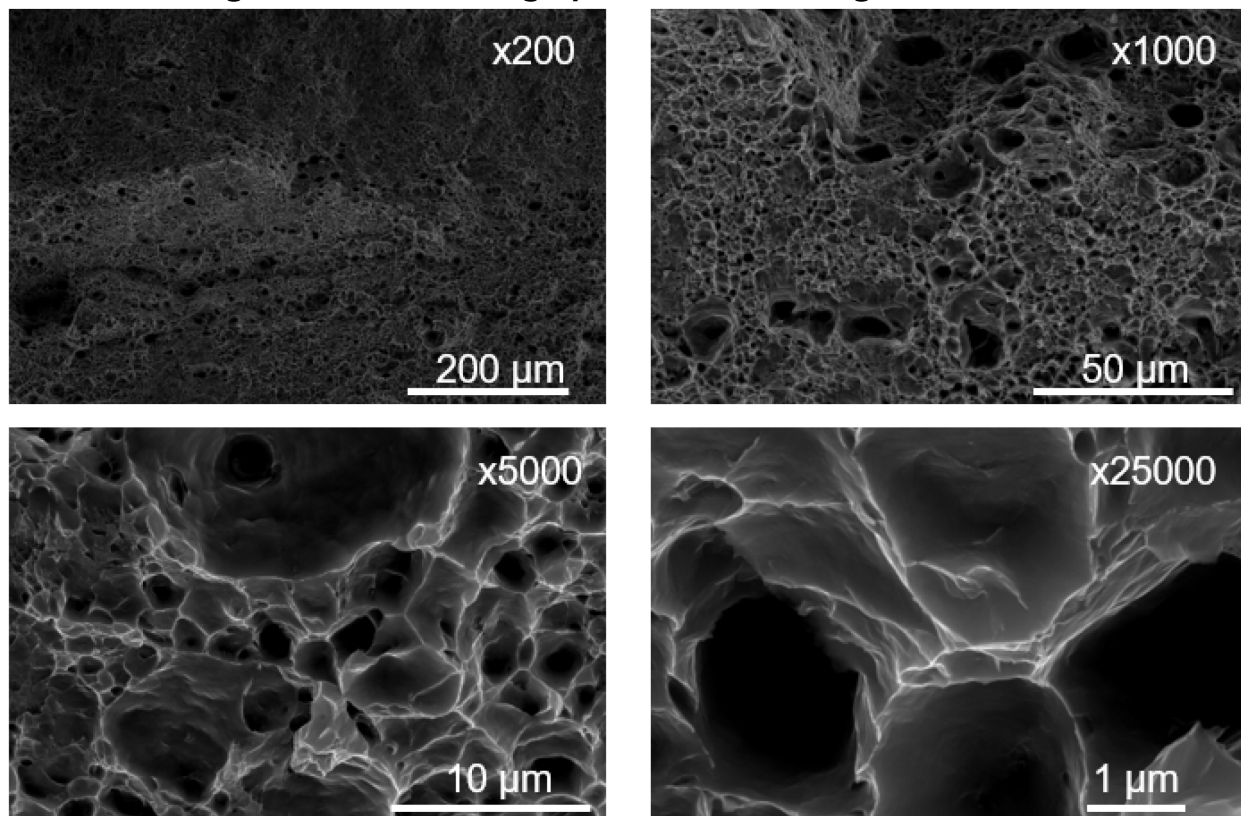
In the hydrogen charged specimen, there are two different regions: outside the circular pattern, and inside the circular pattern. Figure 100 shows the SEM micrographs obtained outside the circular pattern. The results at all magnifications are similar to the uncharged specimen, indicating that these areas outside the circles remained ductile. In contrast, Figure 101 shows the SEM micrographs obtained inside the circular pattern, which show clearly a different morphology to the uncharged specimen. No trace of microvoid coalescence was observed, but the intergranular failure was observed throughout the circles. The fact that the hydrogen affected the mechanical behavior of the material locally suggests that there are more susceptible areas in the materials. The detailed investigation in regards to microstructure, local elemental composition, and crystallographic properties needs to be address in future work.

Figure 100: SEM Micrographs outside the Circles on the Charged X65 Steel
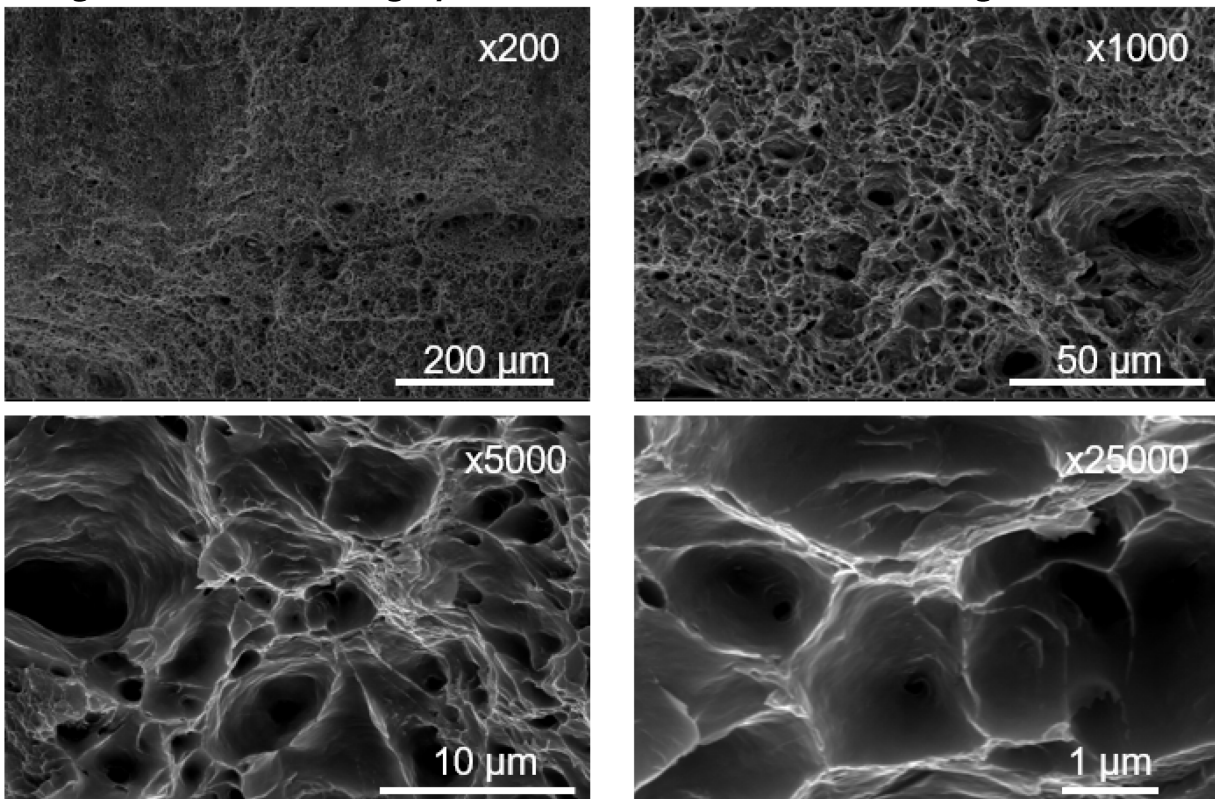
Figure 101: SEM Micrographs inside the Circles on the Charged X65 steel
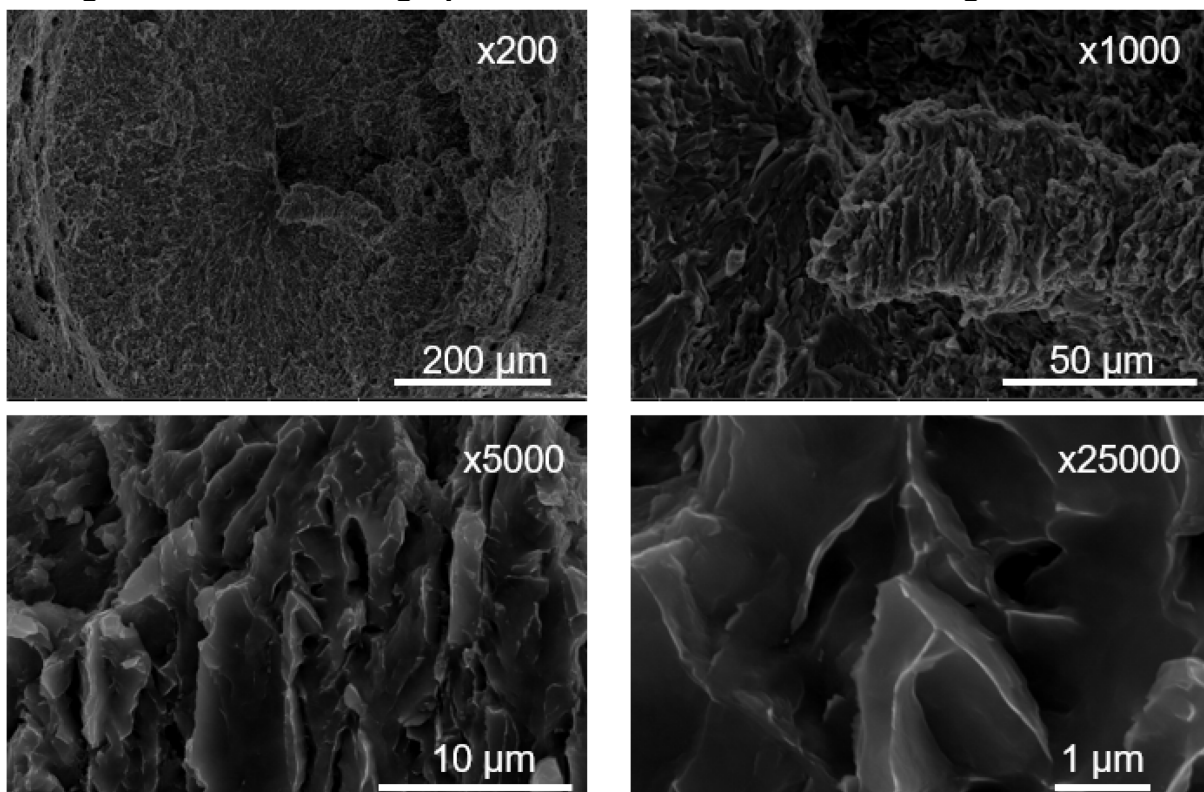
Charpy Impact Toughness Testing

Figure 102 shows the Charpy absorbed energy of API 5L X42 steel uncharged and EC-charged at different resting states. The uncharged X42 shows 375 J Charpy energy, and it is significantly decreased to 231 J after the 24 hours of hydrogen EC charging. The reduced Charpy absorbed energy shows that it requires less energy to cleave the v-notched specimen. The charged specimen becomes more susceptible to external mechanical forces e.g., excavation. Repeating the Charpy test after a recovery period shows that the EC-charged material recovers over time, with the recovering rate decreasing over time. The 1 hour and 3 hour rested specimen showed 294 J, and 338 J, respectively, and eventually it fully recovered after 2 days resting. This observation suggests that the hydrogen impact does not leave a permanent degradation on the steels in terms of the resiliency against the external mechanical force.

Figure 102: Charpy Energy of X42 Steel at Different Resting Conditions
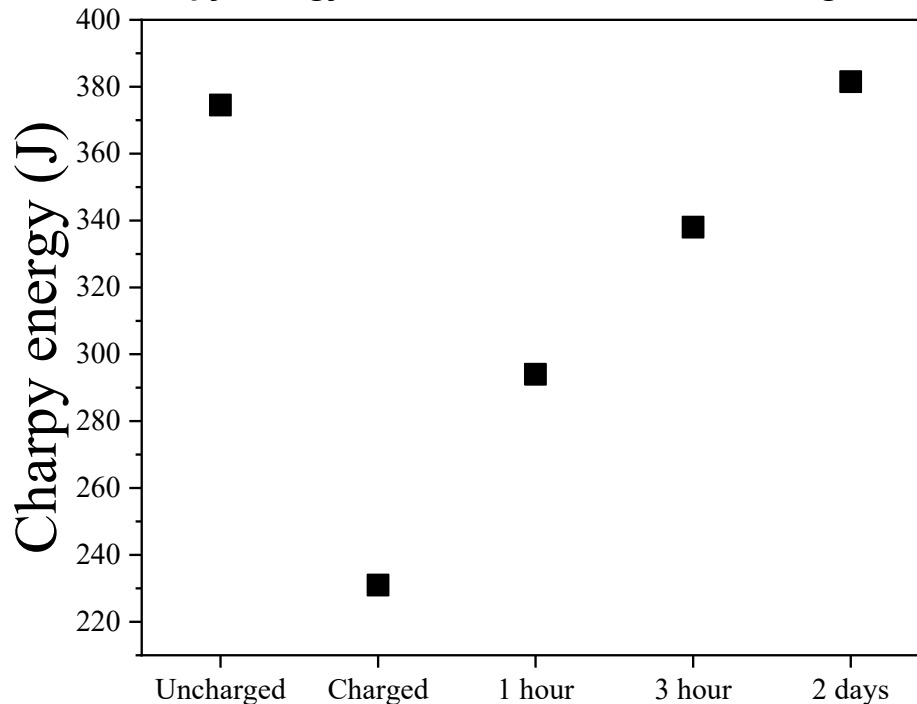
Figure 103 shows the photographs of the Charpy impact tested specimens. The uncharged, 3 hours rested, and 2 days rested specimens are still connected to each other, while the charged and 1 hour rested specimens are completely cleaved. The cleavage of the V-notch specimen is further evidence of the reduced ductility of the X42 specimen after hydrogen charging and slow recovery of the specimen, required more than one hour of recovery time under ambient conditions.

Figure 103: Charpy Tested X42 Steel Samples under the Different Charging and Resting Conditions

Uncharged	Charged	Rest 1 H	Rest 3 H	Rest 48 H
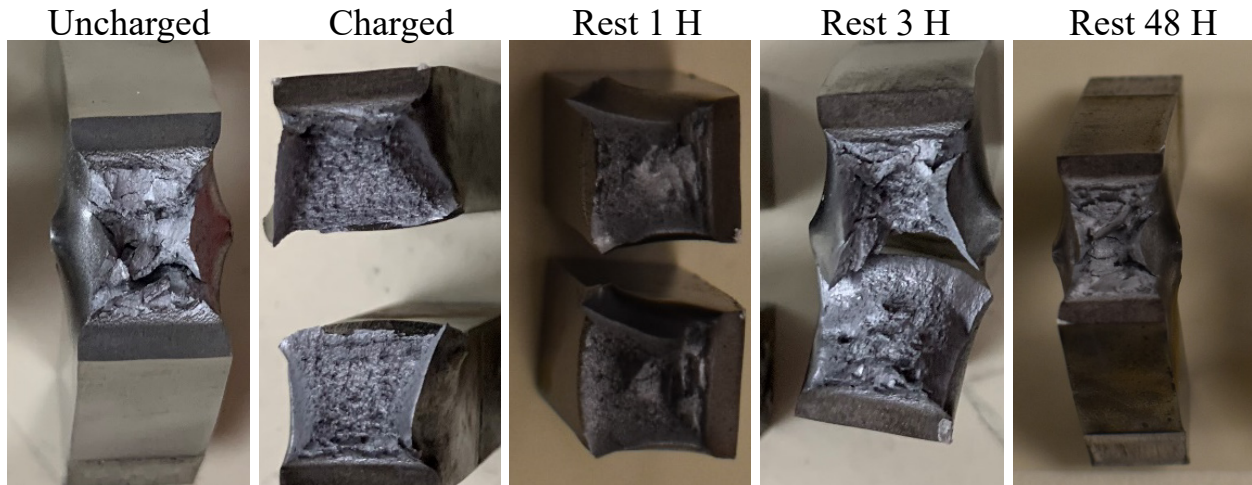
To investigate the Charpy energy dependency on temperature, low-temperature Charpy testing with in-situ temperature monitoring testing was performed. The real-time temperature during the Charpy testing on the X42 specimen is shown in Figure 104. The charged/uncharged X42 Charpy specimen was connected to a temperature sensor and cooled with dry ice in a stainless-steel dewar until it reached equilibrium at the targeted temperature set with the dry ice bath. Once the specimen reached the target temperature, it was loaded onto the Charpy tester. After removal from the dry ice bath, the temperature increased at a high rate, slowing down from -0.21 to -0.23 °C/s due to the insulating layer formed on top of the surface of the specimen. The specimen was tested when the reading temperature reached -50 °C (left) and -25 °C (right).

Figure 104: Temperature Profiles in the Low-Temperature Charpy Testing on X42
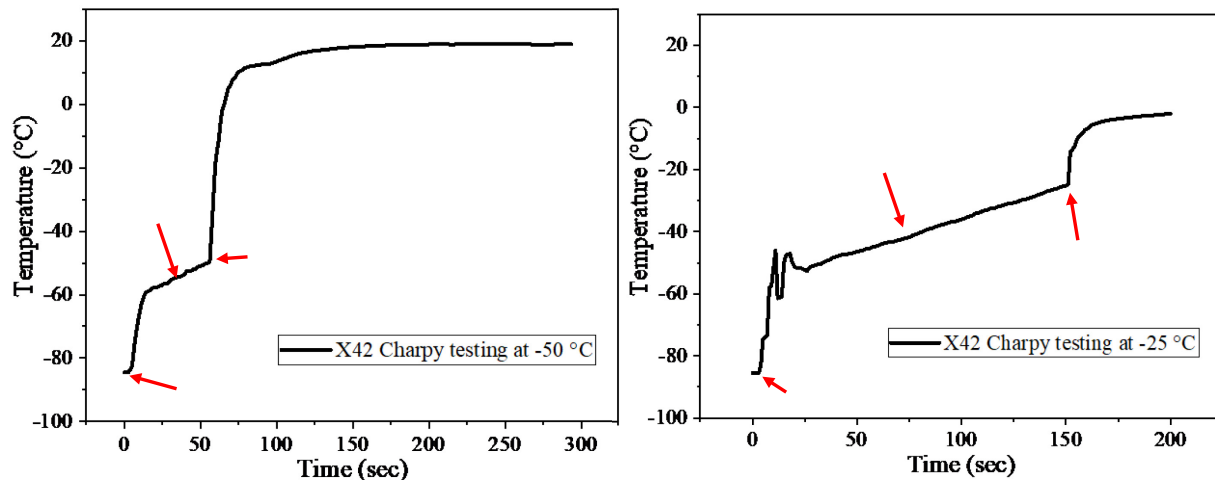
Figure 105 shows the X42 Charpy testing results under different temperatures before and after EC hydrogen charging. The uncharged X42 shows reduced trend on Charpy energy as the temperature is decreased, and is significantly decreased at -50 °C. The hydrogen charged X42 specimens also show reduced Charpy energy due to the

116

hydrogen impact, in addition to the temperature effect. The difference on the Charpy energy before and after charging is significant when the temperature is ambient or higher. However, the difference is reduced when the temperature is decreased. The hydrogen charged and uncharged specimens show similar Charpy energy at -50 °C. These results suggest that the API 5L X42 steel is impacted by both the hydrogen and low-temperature effects, with the temperature effect being dominant under the low-temperature conditions.

Figure 105: Charpy Test Results of X42 Steel under Different Temperature
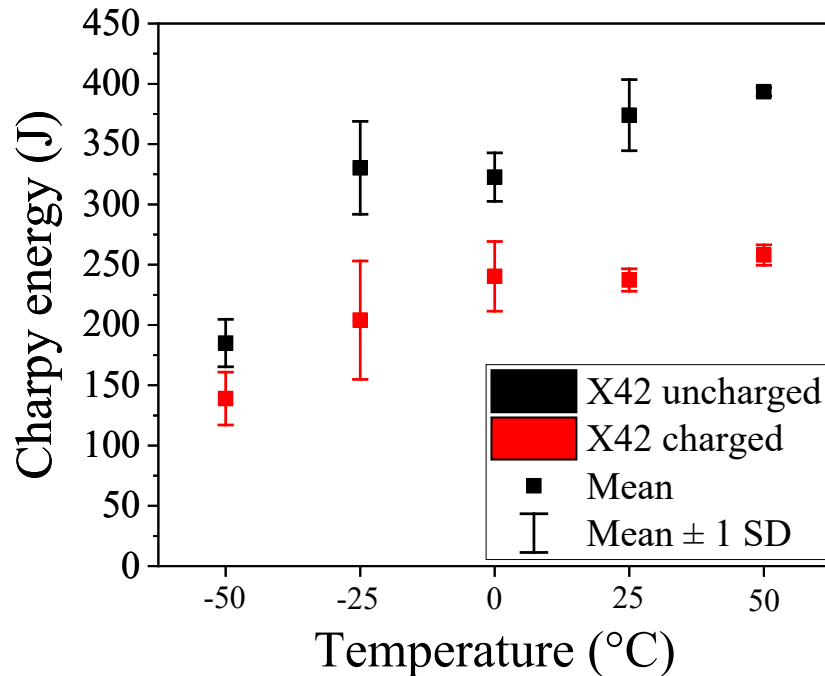
The API 5L X52 shows the same trend in the Charpy toughness testing under different temperatures as shown in Figure 106. The difference before and after hydrogen charging is large in higher temperatures but significantly lower under the low temperature conditions. These results also suggest that the embrittlement is originated from both the hydrogen and temperature effect, but the temperature effect is dominant and the hydrogen impact is relatively negligible under the low-temperature environment.

SS304 shows a different trend in the Charpy toughness testing as shown in Figure 107. Even though the elemental analysis results showed that the SS304 specimen contains hydrogen up to 25 ppm (Figure 95), there is no noticeable difference between the charged and uncharged SS304 specimens in the Charpy results. Moreover, SS304 does not show a clear Charpy energy reduction under the low-temperature condition but the deviation is reduced when the temperature is decreased. These results show that SS304

is not susceptible to the hydrogen impact. The detailed mechanism needs to be studied with the microstructure, elemental, and crystal structure analysis in the future work.

Figure 106: Charpy Test Results of X52 Steel under Different Temperature
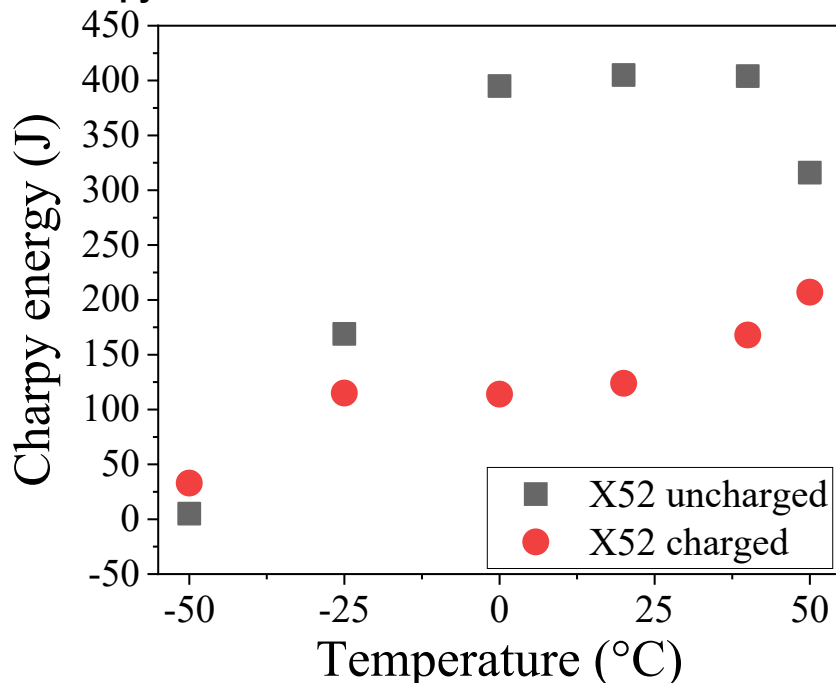
Figure 107: Charpy Test Results of SS304 Steel under Different Temperatures
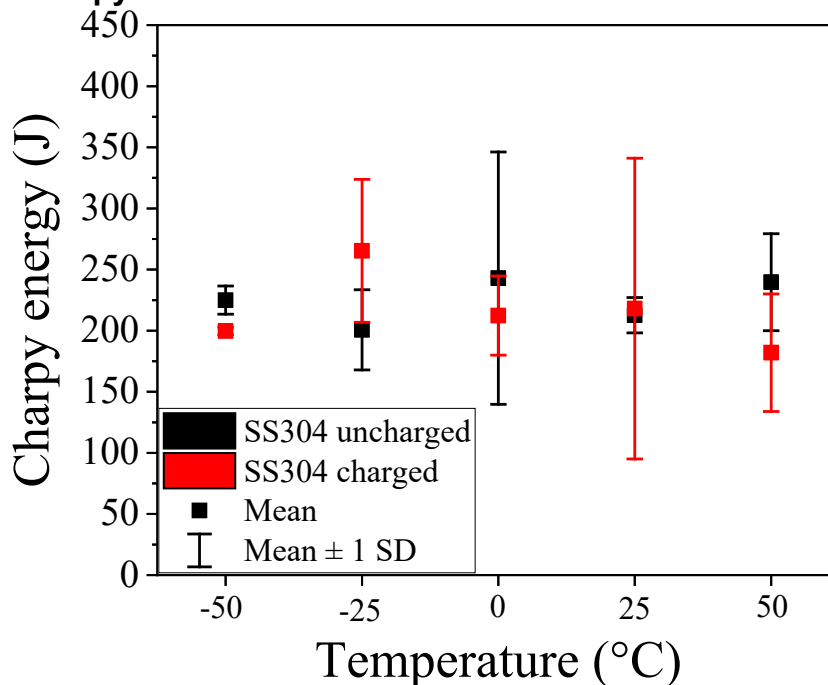
Other non-steel materials in the natural gas infrastructure were Charpy tested as shown in Figure 108. However, those materials showed much less Charpy energy than the API

5L steels and stainless-steel. The Charpy energy after charging is not significantly different from the uncharged specimen and within the experimental error range. In future work, other techniques or a specialized setup for testing these materials with a smaller Charpy energy needs to be done to investigate the effects of the hydrogen and temperature on these materials.

Figure 108: Charpy Test Results from other Non-Steel Metals (Al Alloy, Brass, Cast Iron, and Ductile Iron)
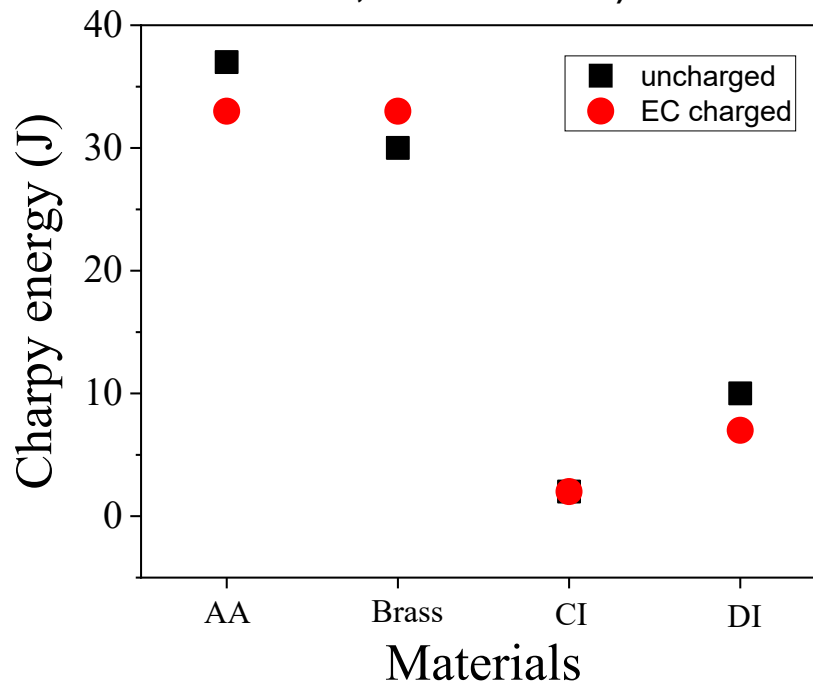
The Cu alloy showed different behavior in the Charpy toughness testing due to the softness of the material. Figure 109 shows the Charpy tested Cu alloy specimen which was deformed by the Charpy hammer rather than breaking at the V-notch. This result is unreliable due to the inaccurate energy measured during the testing. Most of the Charpy results were observed in between 155 and 190 J irrespective of charging and temperature conditions except for the charged Cu at -50 °C (Figure 110). As shown in the previous Charpy results for other materials, both the hydrogen and temperature can affect the ductility and brittleness of the material. It is possible that the reduced ductility in Cu alloy is caused by both the hydrogen and low temperature effects.

Figure 109: Photo of Charpy Tested Cu Alloy

Figure 110: Charpy Test Results of Cu Alloy under Different Temperatures
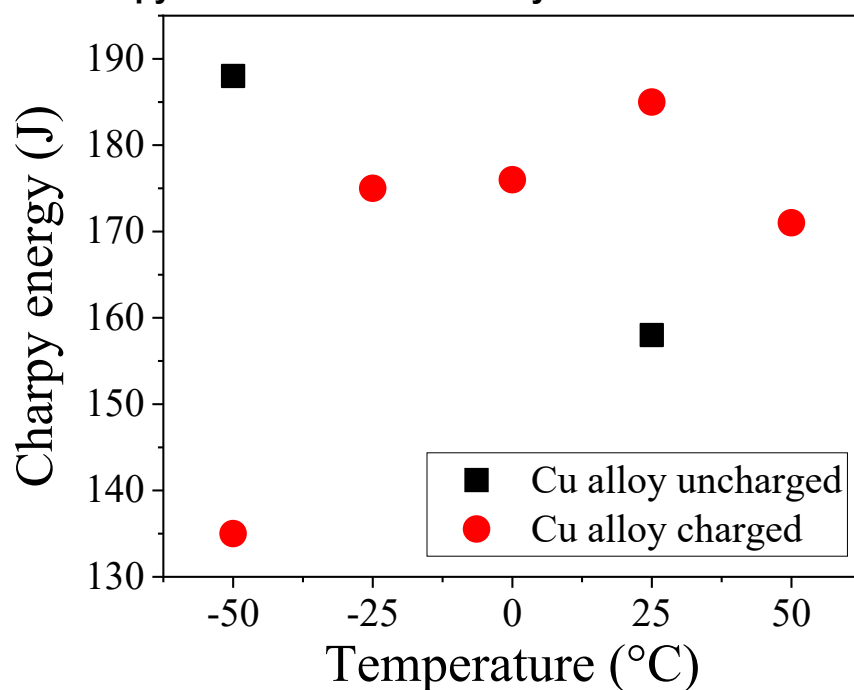
The X42, X52, and SS304 were charged by gaseous hydrogen in a pressure chamber to examine the impact of hydrogen under the presence of gaseous hydrogen. The charged specimens are Charpy impact tested as shown in Figure 111. The gaseous hydrogen charged specimens do not show a noticeable change in the Charpy toughness even though the elemental analysis results (Figure 94 and Figure 95) show the materials were gaseous hydrogen charged. The gaseous hydrogen charging is less effective in the larger samples like Charpy specimen. These results suggest that the Charpy specimens were not effectively charged in the hydrogen gas environment due to the slow diffusion rates.

Figure 111: Charpy Test Results of Gaseous Hydrogen Charged X42, X52, and SS304 Steels
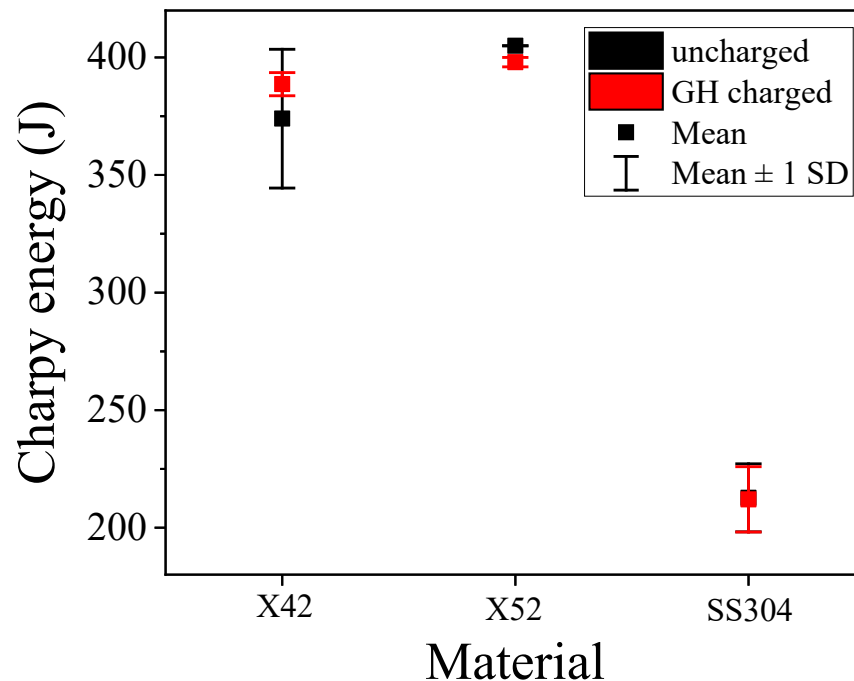
Figure 112 shows the SEM fractography on the Charpy tested X52 specimens under 25 °C and -50 °C. The uncharged X52 under 25 °C shows the pores and spikes on the fracture surface, which is a trace of the ductility of the material. In contrast, the rest of the fractographic images show a brittle fracture with a smooth surface and granular boundaries. The embrittlement behavior of X52 steel is observed either from the existence of hydrogen or lowered temperature as expected from the Charpy results.

In contrast to the X52 steel, the SS304 (Figure 113) shows the consistent fractographic morphologies in uncharged and charged under different temperatures. The morphology of the SS304 has the pores and spikes from the ductility of the material. These results suggest that the SS304 is not susceptible to the hydrogen impact or the low-temperature effect down to -50 °C.

Figure 112: SEM of Charpy Tested X52 Samples under Different Temperatures
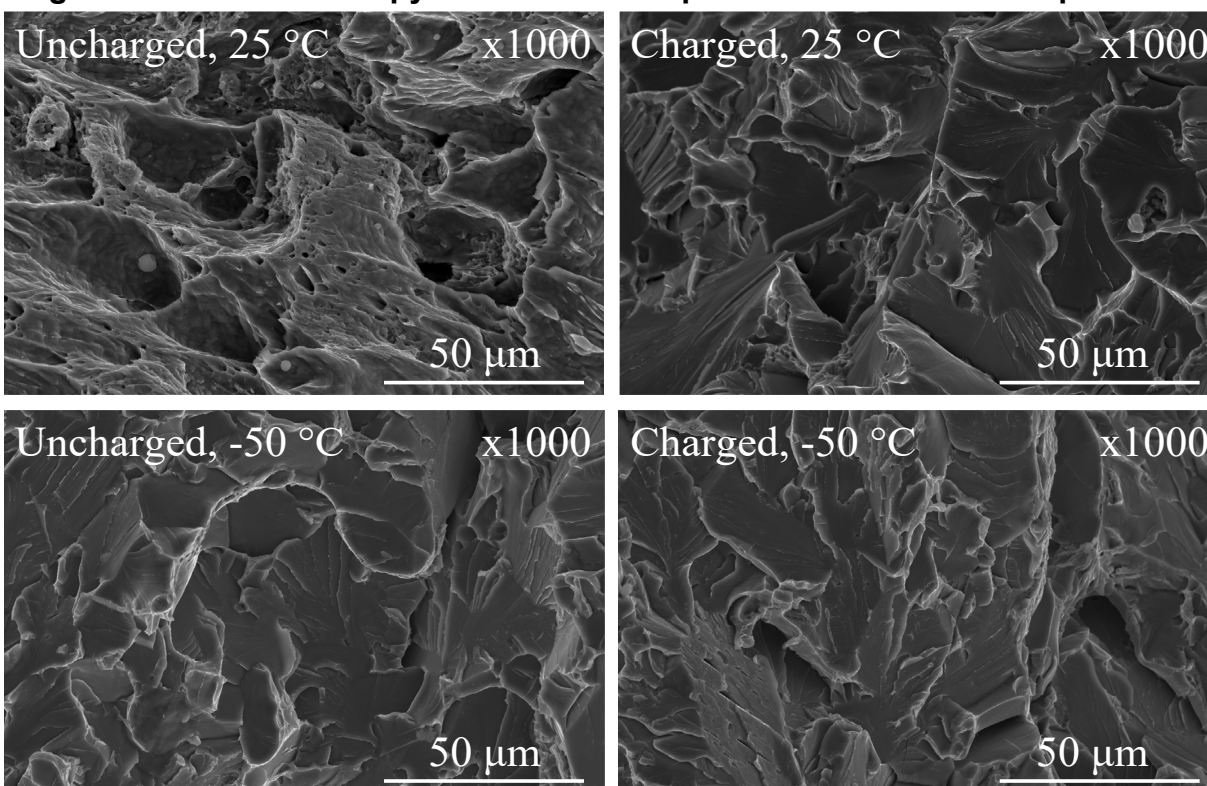
Figure 113: SEM of Charpy Tested SS304 Samples under Different Temperatures
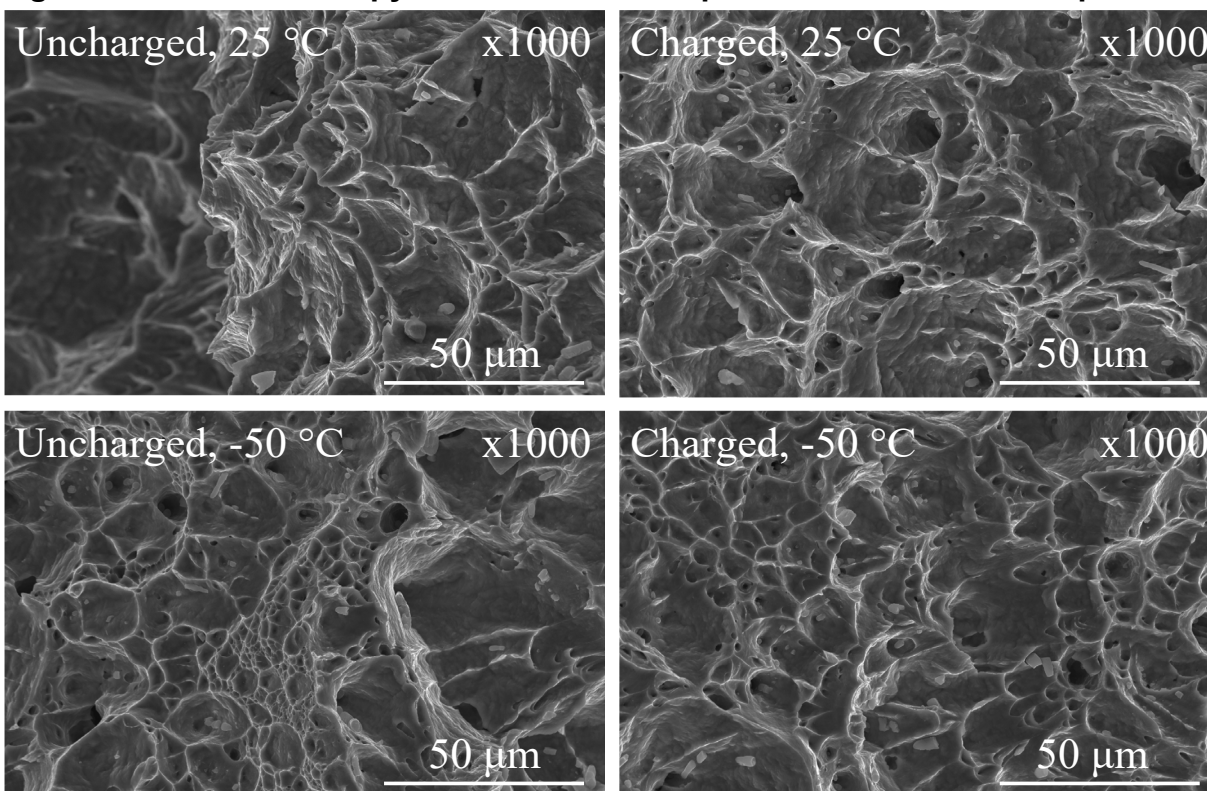
Conclusions

Electrochemical hydrogen charging is an alternative way to test the hydrogen impact on metal and metal alloy materials because it is cost-effective, efficient, and safer. The EC charged steel samples show 103 % increase in hydrogen concentration in API 5L X42, and 73.6 % in X52 steels.

The tensile strength testing results showed that the charged steel samples presented a 12.4 % reduction in fracture strain, while increased 6.2 % and 16.6% in their ultimate tensile strength and yield strength, respectively. The steels showed characteristics of embrittlement, but still exhibit ductile fracture behavior with higher pressure resistance.

Cast iron, ductile iron, aluminum alloy and brass showed relatively low hydrogen impact in regular Charpy testing even though hydrogen charging was confirmed by elemental analysis. X42 and X52 steel samples showed reduced Charpy toughness after hydrogen charging. The difference before and after charging is less significant under the low temperature (-50 °C (-58 °F)). SS304 and brass samples showed no significant difference before and after charging in the Charpy toughness testing.

Elemental analysis was used to measure the hydrogen content (ppm) on both electrochemically and gaseous hydrogen charged test specimens. The elemental analysis results showed hydrogen concentration in gaseous charged samples was lower compared to electrochemically charged samples, likely due to the slower diffusion rates in gaseous hydrogen charging. The elemental analysis can be further utilized to develop a relationship between electrochemical hydrogen charging and gaseous charging methods.

Recommendations

Electrochemical hydrogen charging has a limitation because it cannot reproduce charging under hydrogen gas environment, but the amount of generated hydrogen can be controlled by adjusting experimental parameters such as pH of the electrolyte and applied current. A detailed electrochemical charging study is needed to develop a systematic methodology for electrochemical charging to be used as an effective alternative method to gaseous hydrogen charging.

To investigate the impact on tensile strength in hydrogen charged materials, detailed assessment criteria, in terms of the mechanical properties and permeation rate need to be developed.

Future experimental work needs to be conducted with more sensitive mechanical testing methods and instruments, for the cast iron and ductile irons, due to their relatively low Charpy impact toughness. Further investigation to establish a relationship between gaseous and electrochemical hydrogen charging is needed, specifically the detailed EC charging parameters needed to simulate the diverse concentrations of hydrogen in the gas mixture. This relationship can be developed with elemental analysis and mechanical testing.

Task 3: Maximum Blending Potential

Blending of hydrogen into the existing natural gas pipeline network has been proposed as a way forward towards developing a hydrogen economy, decarbonizing the grid and reducing greenhouse gas emissions. This strategy raises the natural question: What is hydrogen's maximum blending potential? The answer to this question must consider two different possibilities:

1) What is the maximum hydrogen percentage at which 'no' or 'minor' modifications are needed?
2) What modifications may be required for higher percentages of hydrogen?

Answers to these questions must consider foremost safety. In addition to safety, a recent study identified six additional key discussion topics related to hydrogen injection and blending into natural gas pipeline networks [2], specifically: 1) benefits of blending, 2) extent of the U.S. natural gas pipeline network, 3) impact on end-use systems, 4) material durability and integrity management, 5) leakage, and 6) downstream extraction.

An additional study recently performed a detailed State-of-the-art and Gap analysis that considered eight specific impacts areas of importance to transmission/distribution network operators and end-users [126]. The impacts areas were: 1) pipeline integrity, 2) safety, 3) end-use, 4) metering & gas quality, 5) network management & compression, 6) maintenance & inspection, 7) hydrogen-natural gas separation, and 8) underground gas storage.

A primary concern with hydrogen blending is the impact on the integrity of natural gas infrastructure, due to hydrogen embrittlement in metals and other potential detrimental impacts of hydrogen gas on polymers. The majority (99%) of materials employed in the transmission natural gas pipeline system in California is comprised of cathodically protected externally coated steel. Other metals commonly used in the natural gas distribution and service systems include stainless steels, copper, aluminum, brass, cast and ductile iron. More than half of the pipe materials used in distribution pipelines are plastics (predominantly MDPE and HDPE). Other less commonly used plastic materials include PVC and ABS. A variety of elastomer materials are used in the natural gas pipeline system as coupling seals and gaskets, meter and regulator diaphragms, o-rings, seals, and valve seats.

This project conducted by UCR and GTI focused primarily on investigating the potential impacts on the integrity and durability of polymers (MDPE, NBR) and low-, medium-strength steels used in the existing natural gas pipeline network, as well as leak rates throughout controlled leaks (orifices) and components.

Task 3a - Maximum Hydrogen Percentage at Which No or Minor Modifications Are Needed

Introduction

The body of literature reports that in relatively low hydrogen concentration (1-5% by volume) this approach seems to be viable without significantly increasing risk factors in the storage, transmission, and utilization of hydrogen blends [126]. Up to 20% hydrogen blending has been studied and demonstrated in a limited fashion throughout the world without significant incidents (U.S., Europe, Australia) [2], [127]. Ongoing studies and demonstration projects are investigating >50% hydrogen blends to provide additional experimental and real-world results that will advance the current state of the art [126].

The specific blend concentration for a particular pipeline network must be studied carefully given the intricacies of vintage pipes, natural gas composition, and operational conditions that are specific to each section of the natural gas network (transmission, distribution, service lines). Hydrogen injection and blending will necessitate the study of the modifications needed to existing pipeline networks monitoring, maintenance, and replacement, to maintain safety and delivery of gas products to customers.

Conclusions

Relative to injecting and blending hydrogen into the natural gas pipeline, leaks and losses of hydrogen gas are two important considerations. Leaks are of high importance for safety reasons particularly in confined spaces, while losses are more relevant to storage and economics. Leaks in the distribution natural gas system, comprised of plastic pipelines are expected to occur primarily by hydrogen permeation, while the majority of leaks in the transmission system and distribution system comprised of metal pipelines are expected to occur through cracks, joints, seals, or threads [2]. The findings of the experimental work conducted by this project on controlled leaks through orifices, suggest that volumetric gas blend leak flow rate increases with increase in concentration of hydrogen gas in the blend (see Task 2a - Modeling and/or Experimental Assessment of Potential Impact on Natural Gas Pipeline Leakage Rates) Therefore it is important to understand the safety-related properties of different blends, identify methods and strategies (e.g. use of odorants) for prompt detection, and to develop effective safety procedures for the monitoring, identification and repair of leaks to reduce safety risks.

Based on a recently published report, there is literature available for the lower blending percentage (1-2% per volume). Beyond 2%, the literature starts to show gaps in areas such as 'inspection and maintenance' and 'underground gas storage'. Particularly, beyond 10% the knowledge gap extends to 'network management & compression'. Some knowledge and deployments exit for blending hydrogen up to 30% and is mostly

limited to the distribution, safety and end-use equipment. The amount of knowledge gap beyond 50% becomes very significant, with limited reports or projects [126].

Providing that the hydrogen blend is homogeneous, it was reported that the addition of 10% hydrogen to a typical natural gas blend, does not impose significant impacts to the gas quality, materials, network capacity, safety or risk aspects [127].

The experimental work conducted by GTI on MDPE, comparing methane-exposed UTVs and the 20% hydrogen-methane blend-exposed UTVs, suggests a reduction in the creep performance of the MDPE associated with the 20% hydrogen blend (see Task 2b - Experimental Assessment of the Impacts, Including Degradation, on Durability/Integrity of the Existing Natural Gas Pipeline System and the Effects of Transient/Non-homogeneous Gas Compositions). Performing future pressure and aging tests on pipes made from vintage and modern HDPE and MDPE materials will be important for confirming if the impact found on the UTV specimens similarly manifests in pipes and to what degree.

Experiments conducted on API 5L X42 and X52 steel samples showed reduced Charpy toughness after electrochemical hydrogen charging (see Task 2d - Degradation Analysis). However, in order to determine if similar effect would occur in API 5L steel pipelines exposed to hydrogen-natural gas blends, further investigation to establish a relationship between gaseous and electrochemical hydrogen charging is needed.

Recommendations

It is necessary to conduct case-by-case studies to determine the appropriate blend percentage suitable to mitigate operational risks, public safety, durability and integrity of the network and prevent negative impacts to appliances.

Existing standards applicable to the natural gas transmission and distribution network, including Title 49 Code of Federal Regulations Part 191 and 192 [6], California General Orders No. 58-A, No, 58-B, and No. 112-F, may need to be updated to reflect the forthcoming use of hydrogen to identify knowledge gaps in materials and safety operating under possibly higher network pressures that may be needed to maintain gas quality. Other standards that may be indirectly impacted by the injection of hydrogen in the natural gas infrastructure include California Residential Code, California Plumbing Code, California Fire Code, and California Building Energy Efficiency Standards.

Task 3b - Modifications That May Be Required for Higher Percentages of Hydrogen

Introduction

Currently, a wide knowledge gap exists in the literature for blends with >50% hydrogen, due to the lack of results and data regarding the long-term use and demonstration of high hydrogen content blends. In general, a portion of the study of blends with >50% hydrogen has been focused on end-use equipment and appliances.

In this respect, the overall strategy thus far has been to perform extensive analysis on a case-by-case basis to determine the safety threshold needed for making modifications to the design (upgrading burner) and developing control methods (additives, catalysts) and/or mitigation strategies (fuel gas recirculation) [126].

Conclusions

Because of the lower energy content of hydrogen compared to natural gas at higher percentages of hydrogen (>50%), operational pressures may need to be increased by 2-3 times, which would require the close evaluation of impacts in the natural gas pipeline network under higher pressures. Conversely, the results of this study and prior studies indicate that increased pressures of hydrogen blends demonstrate increased risk relative to embrittlement, fatigue crack growth, and failure in high strength steels. Similarly, poorer creep performance in polymers has been demonstrated for a 20% hydrogen blend. These conflicting characteristics of reduced energy density and increased risk with high pressures creates a significant challenge for pipeline operators.

Recommendations

Further research and development is required that considers the system integrity and durability at all levels of steels (low-, medium-, high-strength), distribution-level polymer pipes, and all components, valves & sealants used throughout the different network levels. The impact of integrity and durability on safety as the blending percent and pressure increase requires an in-depth study of leak detection, odorization, gas build-up, dispersion dynamics, and safety zones to account for changes in flammability, ignition, and explosivity.

Task 3c - Standardization and Certifications Requirements and Potential Mitigation Methods

Introduction

Standardization and certifications with respect to integrity, durability, and safety requirements will be needed to facilitate the regulation of hydrogen injection and blending into the natural gas pipeline. Particularly, the blend percentage will be a critical factor to consider in guiding and informing regulatory bodies towards developing and/or updating regulations, codes, safety standards, and safety zones.

Currently, projects utilizing up to 20% hydrogen blending use the standard odorization for natural gas [126]. One important factor to consider is the dispersion dynamics that may take place that lead to a separation of hydrogen from natural gas, turning the odorant potentially ineffective if it is unable to stay with the hydrogen gas as it disperses.

Considering that some end-use equipment at the residential and industrial levels may be sensitive to hydrogen blending, the assessment and understanding of the limits of

existing equipment, appliances, and industrial processes is an important aspect to further investigate.

Additionally, certifications of meters are needed to accurately measure calorific value for natural gas/hydrogen blends (>10% by volume), by developing appropriate gas standards for the accurate transaction, accounting and billing on hydrogen blends.

Conclusions

Investigation of the technical, safety, and operational impacts of hydrogen injection and blending into the natural gas pipeline is needed to produce the data and information required by regulatory and certification bodies for the development of a technical regulatory framework for gas distribution networks operating with hydrogen blends.

Furthermore, knowledge is needed to understand the impact of hydrogen blending on the heat transfer mechanism taking place in residential and industrial applications for the development of certification guidelines and criteria.

Recommendations

In addition to working on the development of standards and certifications, it is recommended that the work by other international stakeholders is reviewed and adopted to the extent that is practical and relevant, such as the EIGA standard on hydrogen pipeline systems, which allows for lower strength steels such as ASTM A106 B and API 5L X52 to be used with hydrogen based on historical hydrogen use in the gas service lines without reported issues [21]. Materials that have identified as being compatible with hydrogen should be tested in real-world setups to further confirm their suitability.

Summary and Recommendations

Blending hydrogen into the natural gas pipeline networks is an important approach towards decarbonizing the grid, lowering greenhouse gas emissions, and advancing the development of a hydrogen economy. Utilizing the existing natural gas infrastructure to transition to green hydrogen use can avoid significant capital expenses and time delays that would be associated with building a new hydrogen storage and transportation network. Thus, this approach has the potential to increase the output from renewable energy facilities, increase the share of green hydrogen in the energy mix, and provide the means for the delivery of hydrogen for power and transportation applications.

Projects integrating hydrogen within existing infrastructure must carefully consider potential impacts to the integrity, durability, and safety of the entire natural gas infrastructure as the percentage of hydrogen in the blend increases over time. Varied concentrations of hydrogen will have different implications at the transmission, distribution and service lines, storage facilities, and end-use equipment and appliances.

This report evaluates three different aspects that are important towards developing a better understanding of the potential impacts of hydrogen on metal alloys and polymer materials that are commonly used throughout various sections of existing California natural gas pipeline networks. A combination of literature review, modeling, and experimental work was performed in three main areas:

1) Leakage rates of methane and hydrogen blends compared to pure methane,

2) Hydrogen impacts on polymeric materials, and

3) Hydrogen impacts on metals and alloys

Safety and performance concerns associated with injecting hydrogen into the existing natural gas pipeline system at various percentages were assessed in order to develop recommendations on allowable hydrogen blending percentages and the next steps. UCR, and the subcontractor, GTI, have conducted experimental and modeling analysis on the following topics:

- Assessment of components and systems – evaluation of hydrogen impacts on components, systems, leakage rates, degradation, durability, and embrittlement. The project team conducted a review of relevant literature and information from ongoing efforts to identify materials, applications, and components requiring further investigation. These findings were summarized in the literature review and were used to develop experimental and modeling tasks assessing specific considerations.

The tasks were designed to focus on the materials, components, and system conditions benefitting from further analysis.

- Hydrogen blend leakage analysis – comparison and analysis of methane and hydrogen blend leakage rates under varying system conditions. The project team evaluated methane and hydrogen blend leakage rates using modeling and experimental techniques under varying hydrogen percentages, flow rates and system pressures. The results were compared against 100% methane leakage rates to represent deviations from natural gas leakage rates. The results show that blends with higher hydrogen percentages leak faster compared to methane, although hydrogen does not leak preferentially through orifices.

- Hydrogen impacts in metals and alloys – the project team exposed select metals and alloys used in the natural gas transmission systems to hydrogen through gaseous exposure and electrochemical charging. The exposed metal samples were then subjected to tensile strength tests, and impact tests to assess material toughness followed by characterization of the samples using a number of techniques. The results show that charged steel samples showed characteristics of hydrogen embrittlement which affects the material's strength and toughness.

- Dynamic thermo-mechanical analysis – Dynamic thermo-mechanical analysis (DTMA) testing was performed on the MDPE material to obtain the shift-factors that allow translation of pressure test results obtained under elevated temperatures to equivalent performance under a reference (operating) temperature. The results suggest a reduction in the creep performance of the MDPE. Failure assessment to identify failure vs. safe condition for pipe system in the hydrogen environment was developed. The polymeric material results identify limitations in material integrity for mixtures of 20% hydrogen. The results also indicate that the pipe formation process may influence the susceptibility of polymeric materials and requires further investigation.

- Morphology and elemental analysis – the team performed morphological and elemental analysis to characterize hydrogen impacts on pipeline materials and components. Exposed materials and components were analyzed by optical microscopy and scanning electron microscopy. Surface, cross-sectional, and physically/mechanically damaged analysis areas were analyzed for impacts resulting from hydrogen exposure. The Team identified and characterized the impacts of hydrogen embrittlement of various materials. Elemental analysis using electron beam was conducted to understand and explore the degradation

process and further characterize the influence of hydrogen/methane blends on exposed materials.

Based on the literature review conducted and the modeling and experimental work performed in this project, we make the following recommendations towards further closing the existing knowledge gap on the potential effects of hydrogen blending into existing natural gas pipeline systems:

- Conduct research to address knowledge gaps in specific leak mechanisms through joints, threads, cracks, and pinhole defects to accurately predict the leak flow rates with gas blends with varying concentration of hydrogen.

- Conduct research to address knowledge gaps in hydrogen diffusion and embrittlement processes in metals, alloys, and other materials used in the natural gas infrastructure.

- Study elastomers in the form-factors in which they are used and under the real operational conditions to investigate the long-term performance and to generate the data needed for developing appropriate system management strategies.

- Evaluate the impact of hydrogen on polyethylene pipes to further substantiate if the performance reduction observed in injection molded pressure vessels manifests in pipes, and to what extent it does, as a way to guide the revision of applicable performance standards.

- Research the impact on metallic pipes and components under pressure, stress, and hydrogen concentrations that are of interest but are lacking experimental results that can be used in established Fit For Service assessment calculations to determine appropriate operating pressure and factors of safety.

- Conduct an in-depth electrochemical charging study to develop a systematic methodology for electrochemical charging to be used as a more effective alternative method to pressurized gaseous hydrogen charging.

- Establish a relationship between gaseous and electrochemical charging to enable higher fidelity simulations of exposure to different hydrogen concentration blends.

- Evaluate blending technologies and strategies to ensure uniform blending and gas compositions throughout the system.

- Evaluate strategies and technologies (ex.: coatings to mitigate hydrogen diffusion, propane blending to meet Wobbe index requirements, etc.) and eliminate or

mitigate the impacts of hydrogen on safety and performance of materials and components.

- Conduct case-by-case studies of key components, equipment and facilities to determine the appropriate blend percentage suitable to mitigate operational risks, public safety, durability and integrity of the network and prevent negative impacts to appliances.

- Perform an in-depth study of leak detection, odorization, gas build-up, dispersion dynamics, and safety zones to account for changes in flammability, ignition, and explosivity to identify potential impacts on the integrity, durability, and safety at various hydrogen blending percentages.

- Conduct experimental and modeling work and analysis to develop strategies to mitigate or avoid known hydrogen impacts including underground storage facilities other than salt caverns, end use equipment with specific restrictions, etc.

- Evaluate strategies that can accelerate hydrogen use and blending into the natural gas infrastructure including above ground storage, distributed production and use with the ability to connect to the pipeline, and integration with the electric grid.

- Update existing inspection, leak detection, maintenance and repair procedures to mitigate the potential risk factors due to hydrogen's broader flammability range, low ignition energy, and high flame velocity.

- Evaluate impacts on gas compression, quality, metering accuracy and integrity using experimental and modeling analysis.

- Review and adopt work by other international stakeholders to the extent that is practical and relevant based on historical and ongoing hydrogen use in gas production, storage, transmission, distribution, and end-use systems.

Hydrogen blending into California's natural gas pipeline infrastructure can help accelerate the transition towards the use of clean hydrogen as a fuel and energy storage medium, and help the state meet a number of climate and air quality goals. However, the hydrogen blending must be carefully planned and conducted in stages to address the effect of hydrogen on materials, components, facilities, and equipment. As there are knowledge gaps in several areas, including those that cannot be addressed through modeling or laboratory scale experimental work, it is critical to conduct real world demonstration of hydrogen blending under safe and controlled conditions. Based on data from the literature and ongoing research and demonstration efforts, we make the following recommendations on the next steps. A three year timeline is proposed to complete these activities and the adopt a hydrogen blending standard.

	Year 1	Year 2	Year 3
A. Large Scale Demonstration		Lead: Utilities	
B. Laboratory R&D	Lead: R&D Organizations		
C. Planning Activities	Lead: State Agencies		
D. Stakeholder Engagement	Lead: State Agencies/Community Organizations		

Key Activities:

A. Demonstrations: Blending under real world conditions over extended periods, develop and demonstrate mitigation strategies to address safety and performance issues

B. R&D: Address knowledge gaps and assess higher hydrogen percentages blending, mitigation strategies, support demonstration activity

C. Planning: Develop inventories, update and develop specifications, safety/maintenance protocols, workforce development

D. Engagement: Understand priorities and concerns, outreach and consensus building

A discussion of the activities is provided below.

- Conduct demonstration of hydrogen blending in a section of the infrastructure that is isolated or is custom-built to include the commonly present materials, vintages, facilities, and equipment of the generic California natural gas infrastructure with appropriate maintenance, monitoring and safety protocols over extended periods. The recommended hydrogen percentages for this demonstration are 5 to 20%. Such demonstration projects will allow critical knowledge gaps to be filled, including the effect of parameters such as weather induced temperature changes, pressure cycling, length of exposure, effect of natural gas components and contaminants, and potential mitigation techniques.

- Conduct laboratory scale research and analysis to address critical technological and scientific issues and unknowns to provide support to the demonstration and deployment projects, with a specific focus on higher hydrogen percentage blends. The immediate focus should be on 0-20% and 20-50% hydrogen with longer term research focused on blends with higher than 50% hydrogen. The analysis should include the development of a comprehensive inventory of materials and equipment in the California natural gas infrastructure, along with available information on vintages, operational data, hydrogen tolerance levels and potential impacts. This inventory can be used to identify materials with known hydrogen related safety and performance concerns and materials that

have not been assessed from a hydrogen blending perspective. Further research and analysis should be conducted to specifically evaluate potential impacts and mitigation strategies, maintenance procedures, and replacement timelines. Working groups consisting of different stakeholder sectors, including domestic and international entities involved in ongoing major research and demonstration efforts should be created to develop a hydrogen blending blueprint that creates a recommended timeline for injection standards; policies and procedures necessary to enable safe and planned hydrogen blending, potential hydrogen sources, and costs. The direct and indirect costs associated with the transition, including cost savings, environmental and public health benefits should be better understood.

- Engage the gas utilities, material and equipment manufacturers, suppliers, and regulatory agencies to anticipate hydrogen injection over a predetermined timeframe. The core activities would include updating existing manufacturing, procurement, installation, maintenance, and safety procedures, developing new procedures and protocols as needed; and developing and updating material and equipment specifications as needed. The group would also develop alternate strategies for portions of the infrastructure where hydrogen blending is not recommended in the near term (ex., select storage facilities and end use sectors). Activities will include workforce training and education.

- Engage stakeholder groups including community and environmental organizations, industry, government, academia, and the general public to provide perspectives on hydrogen blending, conduct outreach to address technological, societal, economic, and safety concerns and to build consensus on hydrogen production, storage, transport, and use including blending into the natural gas infrastructure.

LIST OF ACRONYMS

Term	Definition
API	American Petroleum Institute
ASME	American Society of Mechanical Engineers
ASTM	American Society for Testing and Materials
CARB	California Air Resource Board
CI	Cast Iron
CPUC	California Public Utilities Commission
DBTT	Ductile-to-Brittle Transition Temperature
DF	Design Factor
DI	Ductile Iron
DOE	Department of Energy
DOT	Department of Transportation
DR	Dimension Ratio
DTMA	Dynamic Thermo-Mechanical Analysis
EC	Electrochemical
EPA	Environmental Protection Agency
FAD	Failure Assessment Diagram
FAL	Failure Assessment Line
FEA	Finite Element Analysis
FEM	Finite Element Method
FFS	Fitness For Service
FID	Flame Ionization Detector
FS	Factor of Safety
GC	Gas Chromatography
GH	Gaseous Hydrogen
GTI	Gas Technology Institute
HDB	Hydrostatic Design Basis

Term	Definition
HDPE	High Density Polyethylene
HE	Hydrogen Embrittlement
IPS	Iron Pipe Size
IR	Infrared
LFM	Laminar Flow Element
LPM	Lifetime Prediction Model
MDPE	Medium Density Polyethylene
MMSCF	Million Standard Cubic Feet
MMT	Million Metric Ton
MVC	Microvoid Coalescence
NBR	Nitrile Butadiene Rubber
NI	National Instruments
NIST	National Institute for Standards and Technology
OD	Outside Diameter
P&ID	Piping and Instrumentation Diagram
PE	Polyethylene
PG&E	Pacific Gas and Electric
PHMSA	Pipeline and Hazardous Materials Safety Administration
PPI	Plastics Pipe Institute
PPM	Part per Million
PSIA	Pounds per Square Inch Absolute
PSIG	Pounds per Square Inch Gauge
PTFE	Polytetrafluoroethylene
PVC	Polyvinyl Chloride
REFPROP	Reference Fluid Thermodynamic and Transport Properties
RPM	Rate Process Method
SCCM	Standard Cubic Centimeters per Minute

Term	Definition
SCCS	Standard Cubic Centimeter per Second
SCFH	Standard Cubic Feet per Hour
SCG	Slow Crack Growth
SDG&E	San Diego Gas and Electric
SEM	Scanning Electron Microscopy
SLM	Standard Liter per Minute
SNL	Sandia National Laboratory
SoCalGas	Southern California Gas Company
SS	Stainless Steel
TCD	Thermal Conductivity Detector
TTF	Time-to-Failure
UTS	Ultimate Tensile Stress
UTV	Universal Test Vessel
UV	Ultraviolet

REFERENCES

[1] J. Leicher *et al.*, "The Impact of Hydrogen Admixture into Natural Gas on Residential and Commercial Gas Appliances," *Energies*, vol. 15, no. 3, 2022, doi: 10.3390/en15030777.

[2] M. Melaina, O. Antonia, and M. Penev, "Blending Hydrogen into Natural Gas Pipeline Networks: A Review of Key Issues," *Contract*, vol. 303, no. December, pp. 275–3000, 2013, doi: 10.2172/1068610.

[3] J. R. Anstrom and K. Collier, "Blended hydrogen–natural gas-fueled internal combustion engines and fueling infrastructure," in *Compendium of Hydrogen Energy*, Elsevier, 2016, pp. 219–232.

[4] "Eccleston, D.B., Fleming, R.D., 1972. Clean Automotive Fuel. Technical Progress Report 48. US Bureau of Mines Automotive Exhaust Emissions Program, February 1972."

[5] A. Genovese, N. Contrisciani, F. Ortenzi, and V. Cazzola, "On road experimental tests of hydrogen/natural gas blends on transit buses," *Int. J. Hydrogen Energy*, vol. 36, no. 2, pp. 1775–1783, Jan. 2011, doi: 10.1016/j.ijhydene.2010.10.092.

[6] D. of Transportation, "CFR 49 PART 192 – TRANSPORTATION OF NATURAL AND OTHER GAS BY PIPELINE: MINIMUM FEDERAL SAFETY STANDARDS." https://www.phmsa.dot.gov/pipeline/annotated-regulations/49-cfr-192.

[7] T. H. E. United and S. Of, "ASME B31.8: Gas Transmission and Distribution Piping Systems," *ASTM E695Standard Method Meas. Relat. Resist. Wall, Floor, Roof Constr. to Impact Load.*, vol. 552, no. 1, p. 203, 2004.

[8] B. Meng *et al.*, "Hydrogen effects on X80 pipeline steel in high-pressure natural gas/hydrogen mixtures," *Int. J. Hydrogen Energy*, vol. 42, no. 11, pp. 7404–7412, 2017, doi: 10.1016/j.ijhydene.2016.05.145.

[9] R. Gangloff and B. Somerday, "Gaseous Hydrogen Embrittlement of Materials in Energy Technologies, Vol 1: The Problem, its Characterisation and Effects on Particular Alloy Classes," 2012, pp. 1–840.

[10] R. A. Oriani and P. H. Josephic, "Equilibrium aspects of hydrogen-induced cracking of steels," *Acta Metall.*, vol. 22, no. 9, pp. 1065–1074, 1974, doi: 10.1016/0001-6160(74)90061-3.

[11] D. Delafosse and T. Magnin, "Hydrogen induced plasticity in stress corrosion cracking of engineering systems," *Eng. Fract. Mech.*, vol. 68, no. 6, pp. 693–729, Mar. 2001, doi: 10.1016/S0013-7944(00)00121-1.

[12] W. W. Gerberich, P. G. Marsh, and J. W. Hoehn, "Hydrogen Induced Cracking Mechanisms - Are There Critical Experiments?," in *Hydrogen Effects in Materials*, Hoboken, NJ, USA: John Wiley & Sons, Inc., 2013, pp. 539–554.

[13] H. K. BIRNBAUM and P. SOFRONIS, "HYDROGEN-ENHANCED LOCALIZED PLASTICITY - A MECHANISM FOR HYDROGEN-RELATED FRACTURE," *Mater. Sci. Eng. A-STRUCTURAL Mater. Prop. Microstruct. Process.*, vol. 176, no. 1–2, pp. 191–202, Mar. 1994, doi: 10.1016/0921-5093(94)90975-X.

[14] M. L. Martin, M. Dadfarnia, A. Nagao, S. Wang, and P. Sofronis, "Enumeration of the hydrogen-enhanced localized plasticity mechanism for hydrogen embrittlement in structural materials," *Acta Materialia*, vol. 165. Acta Materialia Inc, pp. 734–750, Feb. 15, 2019, doi: 10.1016/j.actamat.2018.12.014.

[15] I. M. Robertson, "The effect of hydrogen on dislocation dynamics," *Eng. Fract. Mech.*, vol. 68, no. 6, pp. 671–692, Apr. 2001, doi: 10.1016/S0013-7944(01)00011-X.

[16] S. P. LYNCH, "METALLOGRAPHIC CONTRIBUTIONS TO UNDERSTANDING MECHANISMS OF ENVIRONMENTALLY ASSISTED CRACKING," *METALLOGRAPHY*, vol. 23, no. 2, pp. 147–171, Sep. 1989, doi: 10.1016/0026-0800(89)90016-5.

[17] S. P. LYNCH, "ENVIRONMENTALLY ASSISTED CRACKING - OVERVIEW OF EVIDENCE FOR AN ADSORPTION-INDUCED LOCALIZED-SLIP PROCESS," *ACTA Metall.*, vol. 36, no. 10, pp. 2639–2661, Oct. 1988, doi: 10.1016/0001-6160(88)90113-7.

[18] L. Blanchard and L. Briottet, "Testing Hydrogen admixture for Gas Applications - Non-combustion related impact of hydrogen admixture - material compatibility," 2020.

[19] H. Barthélémy, "Compatability of Metallic Materials with Hydrogen - Review of the Present Knowledge," 2006.

[20] I. M. Robertson *et al.*, "Hydrogen Embrittlement Understood," *Metall. Mater. Trans. B Process Metall. Mater. Process. Sci.*, vol. 46, no. 3, pp. 1085–1103, 2015, doi: 10.1007/s11663-015-0325-y.

[21] "Hydrogen Pipeline Systems," 2014.

[22] D. Stalheim *et al.*, "Microstructure and Mechanical Property Performance of Commercial Grade API Pipeline Steels in High Pressure Gaseous Hydrogen," 2010, vol. 2010 8th I, pp. 529–537, doi: 10.1115/IPC2010-31301.

[23] C. San Marchi, B. P. Somerday, K. A. Nibur, D. G. Stalheim, T. Boggess, and S. Jansto, "Fracture and fatigue of commercial grade API pipeline steels in gaseous hydrogen," in *Pressure Vessels and Piping Conference*, 2010, vol. 49255, pp. 939–948.

[24] L. Briottet, I. Moro, and P. Lemoine, "Quantifying the hydrogen embrittlement of pipeline steels for safety considerations," *Int. J. Hydrogen Energy*, vol. 37, no. 22, pp. 17616–17623, 2012, doi: 10.1016/j.ijhydene.2012.05.143.

[25] I. Moro, L. Briottet, P. Lemoine, E. Andrieu, C. Blanc, and G. Odemer, "Hydrogen

embrittlement susceptibility of a high strength steel X80," *Mater. Sci. Eng. A*, vol. 527, no. 27–28, pp. 7252–7260, Oct. 2010, doi: 10.1016/j.msea.2010.07.027.

[26] American Society of Mechanical Engineers., "Hydrogen piping and pipelines : ASME code for pressure piping, B31," vol. 2011, p. 242, 2014, [Online]. Available: https://www.asme.org/products/codes-standards/b3112-2014-hydrogen-piping-pipelines-(1).

[27] I. Alliat and J. Heerings, "Assessing the durability and integrity of natural gas infrastructures for transporting and distributing mixtures of hydrogen and natural gas," pp. 1–8, 2004.

[28] A. Hormaza Mejia, J. Brouwer, and M. Mac Kinnon, "Hydrogen leaks at the same rate as natural gas in typical low-pressure gas infrastructure," *Int. J. Hydrogen Energy*, vol. 45, no. 15, pp. 8810–8826, 2020, doi: 10.1016/j.ijhydene.2019.12.159.

[29] X. Ge and W. H. Sutton, "Analysis and test of compressed hydrogen interface leakage by commercial stainless steel (NPT) fittings," *SAE Tech. Pap.*, vol. 2006, no. 724, 2006, doi: 10.4271/2006-01-0130.

[30] M. R. Swain and M. N. Swain, "A comparison of H2, CH4 and C3H8 fuel leakage in residential settings," *Int. J. Hydrogen Energy*, vol. 17, no. 10, pp. 807–815, Oct. 1992, doi: 10.1016/0360-3199(92)90025-R.

[31] O. Florisson, A. Isabelle, L. Barbara, and G. Hankinson, "The value of the existing natural gas system for hydrogen, the sustainable future energy carrier (process obtained in the NATURALHY project)."

[32] PG&E, "Whitepaper: Pipeline Hydrogen," 2018.

[33] J. Hodges, W. Geary, S. Graham, P. Hooker, and R. Goff, "Injecting hydrogen into the gas network – a literature search," *Heal. Saf. Lab.*, pp. 1–53, 2015.

[34] A. S. O. Aweimer and A. H. Bouzid, "Experimental investigation of interfacial and permeation leak rates in sheet gaskets and valve stem packing," in *American Society of Mechanical Engineers, Pressure Vessels and Piping Division (Publication) PVP*, Oct. 2018, vol. 2, doi: 10.1115/PVP2018-85112.

[35] W. J. Jasionowski and H. D. Huangt, "Gas Distribution Equipment in Hydrogen Service — Phase II," *J. Energy*, vol. 5, no. 5, pp. 298–301, 1981.

[36] W. J. Jasionowski, D. G. Johnson, and J. B. Pangborn, "Gas Distribution Equipment in Hydrogen Service," *Int. J. Hydrog. Energy*, vol. 5, pp. 323–336, 1979.

[37] C. S. Marchi and B. P. Somerday, "Technical Reference for Hydrogen Compatibility of Materials." [Online]. Available: https://www.sandia.gov/matlstechref/.

[38] C. S. Marchi and B. P. Somerday, "Technical Reference on Hydrogen Compatibility of Materials - Copper Alloys: Pure Copper." [Online]. Available:

https://www.sandia.gov/app/uploads/sites/158/2021/12/4001TechRef_Cu.pdf.

[39] C. S. Marchi and B. P. Somerday, "Technical Reference on Hydrogen Compatibility of Materials - Aluminum Alloys: Pure Aluminum." [Online]. Available: https://www.sandia.gov/app/uploads/sites/158/2021/12/3101TechRef_pureAlumi num.pdf.

[40] K. Altfeld and D. Pinchbeck, "Admissible hydrogen concentrations in natural gas systems," *Gas Energy*, vol. March/2013, pp. 1–16, 2013, doi: ISSN 2192-158X.

[41] N. Menon, A. Kruizenga, K. Alvine, C. San Marchi, A. Nissen, and K. Brooks, "Behaviour of Polymers in High Pressure Environments as Applicable to the Hydrogen Infrastructure," in *Pressure Vessels and Piping Conference*, 2016, p. V06BT06A037, doi: 10.1115/PVP2016-63713.

[42] E. R. Duranty *et al.*, "An in situ tribometer for measuring friction and wear of polymers in a high pressure hydrogen environment," *Rev. Sci. Instrum.*, vol. 88, no. 9, p. 95114, 2017.

[43] M. Panfilov, "Underground and pipeline hydrogen storage," in *Compendium of hydrogen energy*, Elsevier, 2016, pp. 91–115.

[44] R. Judd and D. Pinchbeck, "Hydrogen admixture to the natural gas grid," *Compend. Hydrog. Energy*, pp. 165–192, 2016, doi: 10.1016/b978-1-78242-364-5.00008-7.

[45] "Communication with SoCalGas (Kwan May)." 2021.

[46] O. Abootalebi, A. Kermanpur, M. R. Shishesaz, and M. A. Golozar, "Optimizing the electrode position in sacrificial anode cathodic protection systems using boundary element method," *Corros. Sci.*, vol. 52, no. 3, pp. 678–687, 2010, doi: 10.1016/j.corsci.2009.10.025.

[47] U. M. Angst, "A critical review of the science and engineering of cathodic protection of steel in soil and concrete," *Corrosion*, vol. 75, no. 12, pp. 1420–1433, 2019, doi: 10.5006/3355.

[48] E. S. Ameh and S. C. Ikpeseni, "Pipelines cathodic protection design methodologies for impressed current and sacrificial anode systems," *Niger. J. Technol.*, vol. 36, no. 4, p. 1072, 2018, doi: 10.4314/njt.v36i4.12.

[49] M. Alexander Stopher and P. E. J. Rivera-Diaz-del-Castillo, "Hydrogen embrittlement in bearing steels," *Mater. Sci. Technol. (United Kingdom)*, vol. 32, no. 11, pp. 1184–1193, 2016, doi: 10.1080/02670836.2016.1156810.

[50] S. J. Kim, S. K. Jang, and J. Il Kim, "Electrochemical study of hydrogen embrittlement and optimum cathodic protection potential of welded high strength steel," *Met. Mater. Int.*, vol. 11, no. 1, pp. 63–69, 2005, doi: 10.1007/BF03027486.

[51] V. Olden, C. Thaulow, R. Johnsen, E. Østby, and T. Berstad, "Influence of

hydrogen from cathodic protection on the fracture susceptibility of 25%Cr duplex stainless steel - Constant load SENT testing and FE-modelling using hydrogen influenced cohesive zone elements," *Eng. Fract. Mech.*, vol. 76, no. 7, pp. 827–844, 2009, doi: 10.1016/j.engfracmech.2008.11.011.

[52] H. Hayatdavoudi and M. Rahsepar, "A mechanistic study of the enhanced cathodic protection performance of graphene-reinforced zinc rich nanocomposite coating for corrosion protection of carbon steel substrate," *J. Alloys Compd.*, vol. 727, pp. 1148–1156, 2017, doi: 10.1016/j.jallcom.2017.08.250.

[53] E. Shekari, M. r. Shishesaz, G. Rashed, M. Farzam, and E. Khayer, "Failure Investigation of Hydrogen Blistering on Low-strength Carbon Steel," *Iran. J. Oil Gas Sci. Technol.*, vol. 2, no. 2, pp. 65–76, 2013, [Online]. Available: http://ijogst.put.ac.ir/article_3538_0.html.

[54] Hawaiʻi Gas, "Decarbonization and Energy Innovation." https://www.hawaiigas.com/clean-energy/decarbonization (accessed Mar. 15, 2022).

[55] S. Bauer, "Underground Sun Storage Final report," 2017. [Online]. Available: https://www.underground-sun-storage.at/fileadmin/bilder/03_NEU_SUNSTORAGE/Downloads/Underground_Sun.Storage_Publizierbarer_Endbericht_English.pdf.

[56] J. Bruun, "Energy storage - Hydrogen injected into the gas grid via electrolysis field test Final report," 2014. [Online]. Available: https://energinet.dk/-/media/05ED24206FC04069817A3860DF56C3F7.pdf.

[57] ENGIE, "The GRHYD demonstration project." https://www.engie.com/en/businesses/gas/hydrogen/power-to-gas/the-grhyd-demonstration-project (accessed Mar. 26, 2022).

[58] GRTgaz, "Jupiter 1000 - First industrial demonstrator of power to gas in France." https://www.jupiter1000.eu/english (accessed Mar. 01, 2022).

[59] SGN, "Aberdeen Vision Project Final Report," 2020. [Online]. Available: https://www.sgn.co.uk/sites/default/files/media-entities/documents/2020-11/SGN-Aberdeen-Vision-Project_Final-Report_0520.pdf.

[60] "SNAM: Hydrogen Blend Doubled to 10% in Contursi Trial." https://www.snam.it/en/Media/news_events/2020/Snam_hydrogen_blend_doubled_in_Contursi_trial.html#:~:text=Snam%3A hydrogen blend doubled to 10%25 in Contursi trial,-08&text=On 16th December%2C Snam doubled,Salerno)%2C to 10%25. (accessed Feb. 06, 2022).

[61] "Blended Gas," *Australian Gas Infrastructure Group*. Accessed: Apr. 08, 2022. [Online]. Available: https://blendedgas.agn.com.au/about-the-project.

[62] T. Isaac, "HyDeploy: The UK's First Hydrogen Blending Deployment Project," *Clean Energy*, vol. 3, May 2019, doi: 10.1093/ce/zkz006.

[63] "Pipeline and Hazardous Materials Safety Administration." .

[64] "USA DOT PHMSA Annual Report for Gas Transmission and Gathering Pipeline Systems – 2019."

[65] "USA DOT PHMSA Annual Report for Gas Distribution Pipeline System - 2019."

[66] EPA, "Draft Inventory of U.S. Greenhouse Gas Emissions and Sinks: 1990-2020. U.S. Environmental Protection Agency," *EPA 430-P-22-001*, 2022. https://www.epa.gov/ghgemissions/draft-inventory-us-greenhouse-gas-emissions-and-sinks-1990-2020.

[67] G. Plant, E. A. Kort, C. Floerchinger, A. Gvakharia, I. Vimont, and C. Sweeney, "Large Fugitive Methane Emissions From Urban Centers Along the U.S. East Coast," *Geophys. Res. Lett.*, vol. 46, no. 14, pp. 8500–8507, 2019, doi: https://doi.org/10.1029/2019GL082635.

[68] T. Lauvaux *et al.*, "Global assessment of oil and gas methane ultra-emitters," *Science (80-.).*, vol. 375, no. 6580, pp. 557–561, 2022, doi: 10.1126/science.abj4351.

[69] "Analysis of the Gas Natural Gas Leak and Emission Reports," *Joint Staff Report California Public Utilities commission California Air Resource Board*, 2022. https://www.cpuc.ca.gov/-/media/cpuc-website/divisions/safety-policy-division/reports/final-2021-ngla-joint-report_012122.pdf.

[70] D. Ersoy, M. Adamo, and K. Wiley, "Quantifying Methane Emissions from Distribution Pipelines in California," 2021. [Online]. Available: https://ww2.arb.ca.gov/sites/default/files/2021-01/Final_CARB_Pipeline Study_1-14-21.pdf.

[71] *Measurement of Fluid Flow in Pipes Using Orifice, Nozzle, and Venturi*. The American Society of Mechanical Engineers, 2004.

[72] "NIST Reference Fluid Thermodynamic and Transport Properties Database (REFPROP): Version 10." https://www.nist.gov/srd/refprop.

[73] K. Simmons, K. Bhamidipaty, N. Menon, B. Smith, A. Naskar, and M. Veenstra, "Compatibility of polymeric materials used in the hydrogen infrastructure," *Pacific Northwest Natl. Lab. DOE Annu. Merit Rev.*, 2017.

[74] M. C. Celina, "Review of polymer oxidation and its relationship with materials performance and lifetime prediction," *Polym. Degrad. Stab.*, vol. 98, no. 12, pp. 2419–2429, 2013.

[75] A. S. Wineman and K. R. Rajagopal, *Mechanical response of polymers: an introduction*. Cambridge University Press, 2000.

[76] C. G. Bragaw, "Service rating of polyethylene piping systems by the rate process method," in *Proceedings Eighth Plastic Fuel Gas Pipe Symposium*, 1983, pp. 40–47.

[77] C. G. Bragaw, "The Forecast of Polyethylene Pipe and Fitting Burst Life Using Rate Process Theory," in *5th International Conference on Plastic Pipes, York UK*, 1982.

[78] E. Lever, U. S. D. of T. PHMSA, and U. S. D. of T. PHMSA, "Slow Crack Growth Evaluation of Vintage Polyethylene Pipes, DOT PHMSA research project DTPH5615T00007 Project# 643," US DOT PHMSA, Washington DC, USA, 2017.

[79] C. F. Popelar, C. H. Popelar, and V. H. Kenner, "Viscoelastic material characterization and modeling for polyethylene," *Polym. Eng. Sci.*, vol. 30, no. 10, pp. 577–586, 1990.

[80] C. H. Popelar, V. H. Kenner, and J. P. Wooster, "An Accelerated Method for Establishing the Long Term Performance of Polyethylene Gas Pipe Materials," *Polym. Eng. Sci.*, vol. 31, no. 24, pp. 1693–1700, 1991.

[81] H. Mavridis and R. N. Shroff, "Temperature dependence of polyolefin melt rheology," *Polym. Eng. Sci.*, vol. 32, no. 23, pp. 1778–1791, 1992.

[82] ASTM, "D638-14 Standard Test Method for Tensile Properties of Plastics," *D638-14*. American Society for Testing and Material, Philadelphia, PA, 2014.

[83] ISO, "ISO 11357-6:2018(en) Plastics — Differential scanning calorimetry (DSC) — Part 6: Determination of oxidation induction time (isothermal OIT) and oxidation induction temperature (dynamic OIT)." International Organization for Standardization, 2018.

[84] E. Lever, "Bi-Directional Shift Factors Revisited," *Plastic Pipes XVII*. Chicago, IL, 2014.

[85] ISO, "13760-98 Plastics pipes for the conveyance of fluids under pressure - Miner's rule - Calculation method for cumulative damage." International Standization Organization, 1998.

[86] G. R. Strobl, *The Physics of Polymers: Concepts for Understanding Their Structures and Behavior*. Springer Berlin Heidelberg, 2013.

[87] K. Hong, A. Rastogi, and G. Strobl, "A model treating tensile deformation of semicrystalline polymers: Quasi-static stress− strain relationship and viscous stress determined for a sample of polyethylene," *Macromolecules*, vol. 37, no. 26, pp. 10165–10173, 2004.

[88] J. S. Bergstrom, *Mechanics of Solid Polymers: Theory and Computational Modeling*. Elsevier Science, 2015.

[89] N. E. Nanninga, Y. S. Levy, E. S. Drexler, R. T. Condon, A. E. Stevenson, and A. J. Slifka, "Comparison of hydrogen embrittlement in three pipeline steels in high pressure gaseous hydrogen environments," *Corros. Sci.*, vol. 59, 2012.

[90] E. Lever and D. O. T. PHMSA, "Improvements to Pipeline Assessment Methods and Models to Reduce Variance," Gas Technology Institute, DOT PHMSA Public Website, 2021. [Online]. Available:

https://primis.phmsa.dot.gov/matrix/PrjHome.rdm?prj=727.

[91] I. Moro, L. Briottet, P. Lemoine, E. Andrieu, C. Blanc, and G. Odemer, "Hydrogen embrittlement susceptibility of a high strength steel X80," *Mater. Sci. Eng. A*, vol. 527, no. 27–28, pp. 7252–7260, 2010, doi: 10.1016/j.msea.2010.07.027.

[92] API, "API579-1/ASME FFS-1: Fitness for Service." API, American Petroleum Institute, United States.

[93] T. L. Anderson, *Fracture mechanics: fundamentals and applications*. CRC press, 2005.

[94] J. A. Ronevich & San Marchi, C., "Materials Compatibility Concerns for Hydrogen Blended Into Natural Gas," in *ASME Proceedings of the . Volume 4: Materials and Fabrication*, 2021, vol. 4, doi: https://doi.org/10.1115/PVP2021-62045.

[95] J. Völkl and G. Alefeld, "Diffusion of hydrogen in metals," in *Hydrogen in metals I*, Springer, 1978, pp. 321–348.

[96] Z. Feng, L. Anovitz, P. Sofronis, P. Kironko, A. Duncan, and T. Adams, "Permeation, Diffusion, Solubility Measurements: Results and Issues," 2007. [Online]. Available: https://www.energy.gov/sites/prod/files/2014/03/f10/pipeline_group_feng_ms.pdf.

[97] H. Boukortt *et al.*, "Hydrogen embrittlement effect on the structural integrity of API 5L X52 steel pipeline," *Int. J. Hydrogen Energy*, vol. 43, no. 42, pp. 19615–19624, 2018, doi: 10.1016/j.ijhydene.2018.08.149.

[98] Ming Au, "Mechanical Behavior and Fractography of 304 Stainless Steel with High Hydrogen Concentration," *WSRC-TR-2002-00558*, 2003.

[99] H. Hortlund, "Study of the hydrogen diffusion out of press hardened boron steel," *Luleå Univ. Technol.*, 2009.

[100] X. Wu, H. Zhang, M. Yang, W. Jia, Y. Qiu, and L. Lan, "From the perspective of new technology of blending hydrogen into natural gas pipelines transmission: Mechanism, experimental study, and suggestions for further work of hydrogen embrittlement in high-strength pipeline steels," *Int. J. Hydrogen Energy*, vol. 47, no. 12, pp. 8071–8090, 2022, doi: 10.1016/j.ijhydene.2021.12.108.

[101] G. Bai, Q. Wang, Y. Song, H. Deng, D. Li, and Y. Li, "Study on hydrogen resistance of x42 pipeline steel under electrochemical hydrogen charging condition," *Am. Soc. Mech. Eng. Press. Vessel. Pip. Div. PVP*, vol. 6, 2020, doi: 10.1115/PVP2020-21007.

[102] S. M. Beden, "Reliability of the Installation and Operation of Pipeline Systems," vol. 16, no. 2, pp. 108–112, 2016.

[103] Y. F. Cheng and L. Niu, "Mechanism for hydrogen evolution reaction on pipeline steel in near-neutral pH solution," *Electrochem. commun.*, vol. 9, no. 4, pp. 558–

562, 2007, doi: 10.1016/j.elecom.2006.10.035.

[104] T. A. Jack, R. Pourazizi, E. Ohaeri, J. Szpunar, J. Zhang, and J. Qu, "Investigation of the hydrogen induced cracking behaviour of API 5L X65 pipeline steel," *Int. J. Hydrogen Energy*, vol. 45, no. 35, pp. 17671–17684, 2020, doi: 10.1016/j.ijhydene.2020.04.211.

[105] S. Hassanzadeh, I. Danaee, E. Saebnoori, O. Chocholatý, A. Kříž, and H. Eskandari, "Investigation of the Effect of pH on Stress Corrosion Cracking of API 5L X65 Steel by Impedance Spectroscopy and Slow Strain Rate Tensile Test," *J. Mater. Eng. Perform.*, vol. 30, no. 8, pp. 5633–5651, 2021, doi: 10.1007/s11665-021-05826-w.

[106] R. Khatib Zadeh Davani, R. Miresmaeili, and M. Soltanmohammadi, "Effect of thermomechanical parameters on mechanical properties of base metal and heat affected zone of X65 pipeline steel weld in the presence of hydrogen," *Mater. Sci. Eng. A*, vol. 718, no. November 2017, pp. 135–146, 2018, doi: 10.1016/j.msea.2018.01.101.

[107] L. Cai, G. Bai, X. Gao, Y. Li, and Y. Hou, "Experimental investigation on the hydrogen embrittlement characteristics and mechanism of natural gas-hydrogen transportation pipeline steels," *Mater. Res. Express*, vol. 9, no. 4, 2022, doi: 10.1088/2053-1591/ac6654.

[108] C. San and M. B. P. Somerday, "SANDIA REPORT Technical Reference for Hydrogen Compatibility of Materials," 2012.

[109] K. Birkitt, M. Loo-Morrey, C. Sanchez, and L. O'Sullivan, "Materials aspects associated with the addition of up to 20 mol% hydrogen into an existing natural gas distribution network," *Int. J. Hydrogen Energy*, vol. 46, no. 23, pp. 12290–12299, 2021, doi: 10.1016/j.ijhydene.2020.09.061.

[110] T. Zhang *et al.*, "Comparison of hydrogen embrittlement susceptibility of three cathodic protected subsea pipeline steels from a point of view of hydrogen permeation," *Corros. Sci.*, vol. 131, no. November 2017, pp. 104–115, 2018, doi: 10.1016/j.corsci.2017.11.013.

[111] W. Wu, Y. Pan, Z. Liu, C. Du, and X. Li, "Electrochemical and stress corrosion mechanism of submarine pipeline in simulated seawater in presence of different alternating current densities," *Materials (Basel).*, vol. 11, no. 7, 2018, doi: 10.3390/ma11071074.

[112] C. F. Dong, Z. Y. Liu, X. G. Li, and Y. F. Cheng, "Effects of hydrogen-charging on the susceptibility of X100 pipeline steel to hydrogen-induced cracking," *Int. J. Hydrogen Energy*, vol. 34, no. 24, pp. 9879–9884, 2009, doi: 10.1016/j.ijhydene.2009.09.090.

[113] R. L. Amaro, E. S. Drexler, and A. J. Slifka, "Fatigue crack growth modeling of pipeline steels in high pressure gaseous hydrogen," *Int. J. Fatigue*, vol. 62, pp.

249–257, 2014, doi: 10.1016/j.ijfatigue.2013.10.013.

[114] T. Boot, T. A. C. Riemslag, E. T. E. Reinton, P. Liu, C. L. Walters, and V. Popovich, "In-situ hollow sample setup design for mechanical characterisation of gaseous hydrogen embrittlement of pipeline steels and welds," *Metals (Basel).*, vol. 11, no. 8, 2021, doi: 10.3390/met11081242.

[115] U. B. Baek, H. M. Lee, S. W. Baek, and S. H. Nahm, "Hydrogen embrittlement for X-70 pipeline steel in high pressure hydrogen gas," *Am. Soc. Mech. Eng. Press. Vessel. Pip. Div. PVP*, vol. 6B-2015, pp. 1–7, 2015, doi: 10.1115/PVP201545475.

[116] S. C. Silva, A. B. Silva, and J. A. C. Ponciano Gomes, "Hydrogen embrittlement of API 5L X65 pipeline steel in CO2 containing low H2S concentration environment," *Eng. Fail. Anal.*, vol. 120, no. June 2020, p. 105081, 2021, doi: 10.1016/j.engfailanal.2020.105081.

[117] M. Matters, "Serious Incident Cause Breakdown 10 Year Average (2008-2015)." .

[118] M. S. Joo, P. H. K. D. H. Bhadeshia, and P. D.-W. Suh, "Anisotropy of Charpy Properties in Linepipe Steels," *Grad. Inst. Ferr. Technol.*, vol. Ph.D., 2012.

[119] H. Mohrbacher, "Metallurgical effects of niobium and molybdenum on heat-affected zone toughness in low-carbon steel," *Appl. Sci.*, vol. 9, no. 9, pp. 1–17, 2019, doi: 10.3390/app9091847.

[120] L. T. H. Nguyen, J. S. Hwang, M. S. Kim, J. H. Kim, S. K. Kim, and J. M. Lee, "Charpy impact properties of hydrogen-exposed 316l stainless steel at ambient and cryogenic temperatures," *Metals (Basel).*, vol. 9, no. 6, 2019, doi: 10.3390/met9060625.

[121] S. H. Cho, Y. Ogata, and K. Kaneko, "Strain-rate dependency of the dynamic tensile strength of rock," *Int. J. Rock Mech. Min. Sci.*, vol. 40, no. 5, pp. 763–777, 2003, doi: 10.1016/S1365-1609(03)00072-8.

[122] O. Fatoba and R. Akid, "Uniaxial cyclic elasto-plastic deformation and fatigue failure of API-5L X65 steel under various loading conditions," *Theor. Appl. Fract. Mech.*, vol. 94, no. January, pp. 147–159, 2018, doi: 10.1016/j.tafmec.2018.01.015.

[123] P. Fassina, F. Bolzoni, G. Fumagalli, L. Lazzari, L. Vergani, and A. Sciuccati, "Influence of Hydrogen and Low Temperature on Pipeline Steels Mechanical Behaviour," *Procedia Eng.*, vol. 10, pp. 3226–3234, 2011, doi: https://doi.org/10.1016/j.proeng.2011.04.533.

[124] R. Pourazizi, M. A. Mohtadi-Bonab, R. K. Zadeh Davani, and J. A. Szpunar, "Effect of thermo-mechanical controlled process on microstructural texture and hydrogen embrittlement resistance of API 5L X70 pipeline steels in sour environments," *Int. J. Press. Vessel. Pip.*, vol. 194, no. PA, p. 104491, 2021, doi: 10.1016/j.ijpvp.2021.104491.

[125] M. Kappes, M. Iannuzzi, R. B. Rebak, and R. M. Carranza, "Sulfide stress cracking of nickel-containing low-alloy steels," *Corros. Rev.*, vol. 32, no. 3–4, pp. 101–128, 2014, doi: 10.1515/corrrev-2014-0027.

[126] K. Domptail *et al.*, "Emerging fuels – Hydrogen SOTA , Gap Analysis , Future Project Roadmap," 2020.

[127] D. Krosch and B. O'Shea, "Hydrogen in the Gas Distribution Networks," 2019.

[128] PPI, "TR-3/2021 HDB/HDS/PDB/SDB/MRS/CRS Policies," *TR-3*. Plastics Pipe Institute, 2021.

APPENDIX 1 - Lifetime of PE Pipe

The following slides, taken from a GTI presentation given to the CPUC on December 15, 2021, provide a brief introduction to the topic of the lifetime of PE pipe.

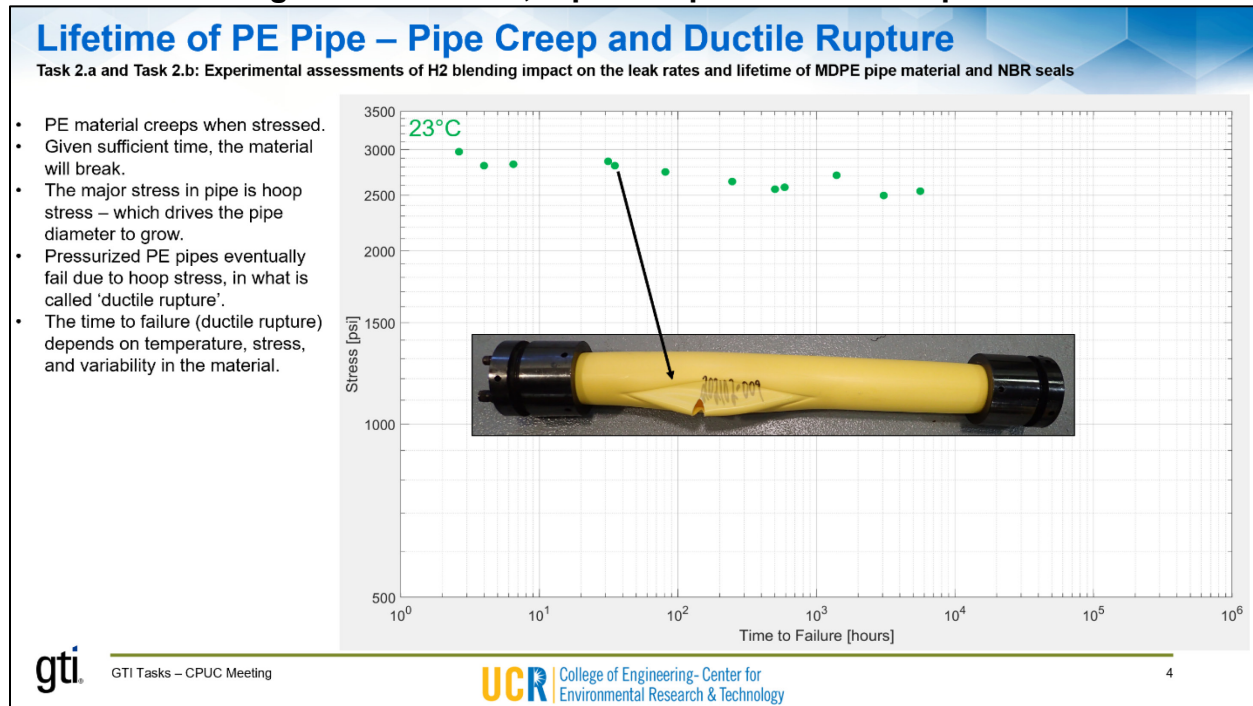**Figure 114: Slide 4, Pipe Creep and Ductile Rupture**

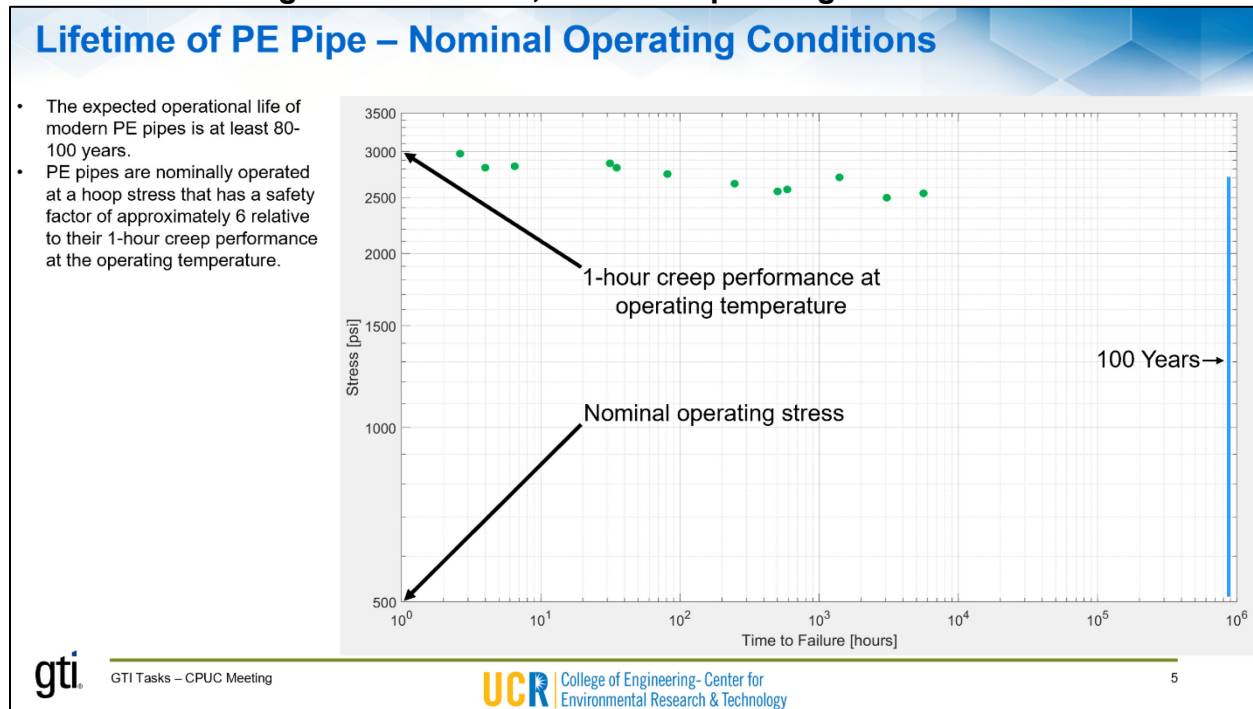**Figure 115: Slide 5, Nominal Operating Conditions**

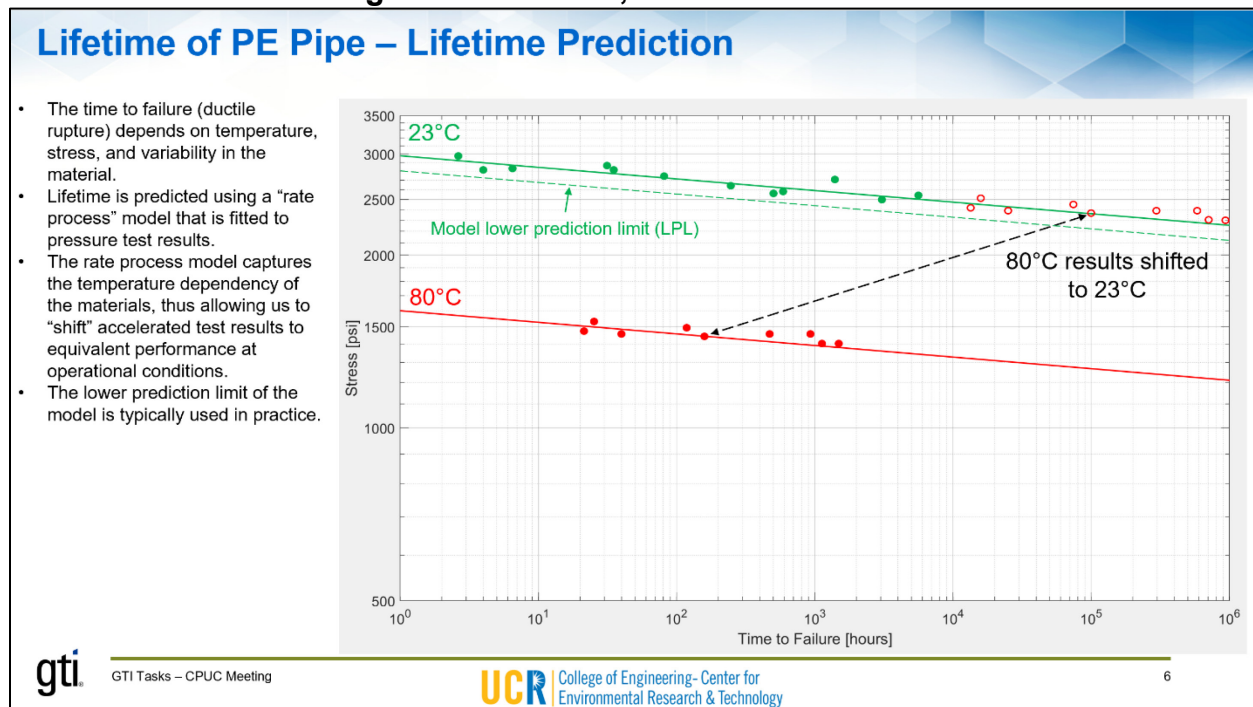**Figure 116: Slide 6, Lifetime Prediction**
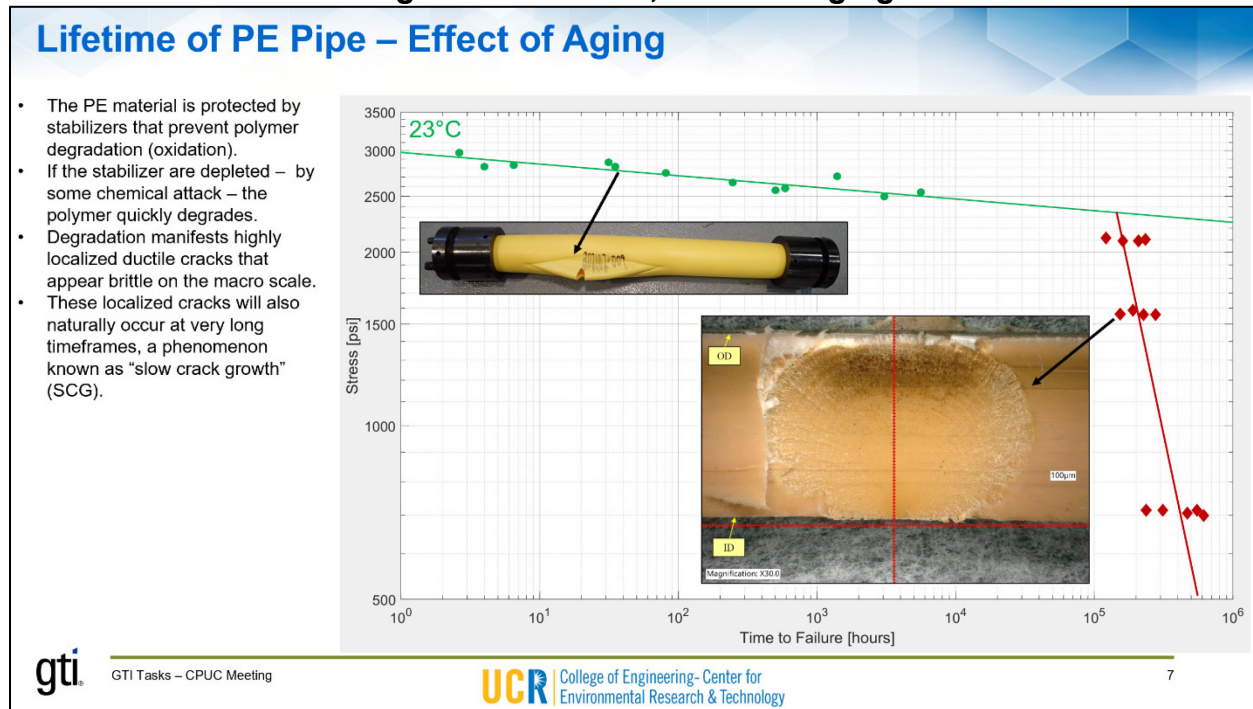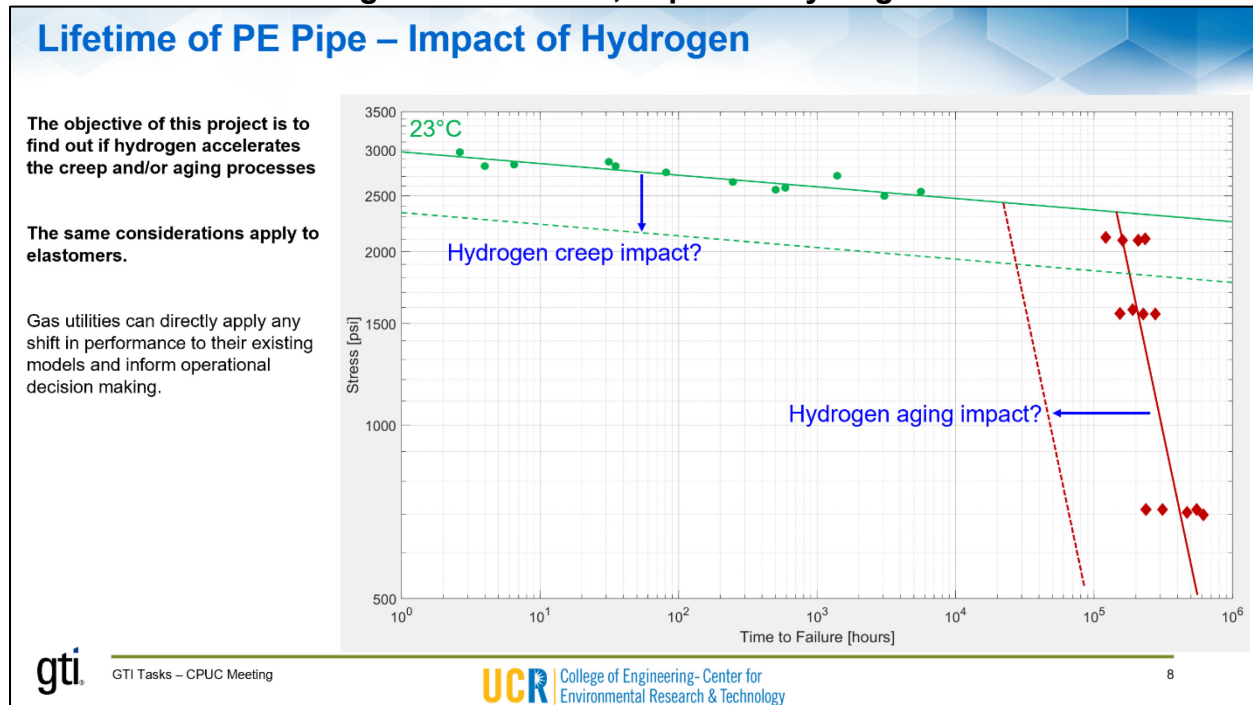
Figure 117: Slide 7, Effect of Aging

Figure 118: Slide 8, Impact of Hydrogen

APPENDIX 2 - PE Pipe Performance Safety Factors

A reduction in PE pipe performance needs to be addressed in context of allowable operational stresses. Operational stresses are much lower than the material capacity due to the application of industry accepted design factors [128]. To put this in context the allowable pipe hoop stress for PE2708 MDPE is derived as follows:

1. *Hydrostatic design basis (HDB) = hoop stress to reach 100,000h @ 73°F = 1,250 psi*
2. *Allowable stress = HDB * (Design Factor) = 1250 x 0.4 = 500 psi*
3. *Allowable pressure = Allowable Stress x 2 / (DR-1) = 500 x 2 / (11-1) = 100 psig*
4. *Yield stress @ 73°F ≈ HDB x 2 = 1250 x 2 = 2,500 psi*

The design factor (DF) for natural gas piping applications with modern PE materials is 0.4. Given that MDPE pipes are typically operated at 60 psig or less on a DR 11 pipe, there is, in effect, a safety factor of 2.5 relative to the HDB of PE2708, and an effective instantaneous safety factor of approximately 5 relative to the yield stress of PE2708. A reduction in performance manifests in a downward vertical shift of the lifetime prediction model's (LPM) regression line. This vertical shift is a linear factor multiplier on the C parameter in the LPM shown in Equation 13 and Equation 14, where the C parameter represents the hoop stress required to reach a failure in 1-hour at the reference temperature, which is typically 73°F (23°C). The linear multiplier on the C parameter can be directly applied to any stress-based safety factor to obtain the applicable reduction in performance from a stress-based perspective.

The stress-based safety factors above can be also translated into time-based performance reduction in order to evaluate how pipe lifetime is reduced if operational stresses remain unchanged. This is done by rearranging the lifetime prediction model from Equation 13 to Equation 14 to get lifetime as a function of hoop stress:

$$S = C \cdot exp\left[\frac{V + \frac{H}{n}}{R}\left(\frac{1}{T} - \frac{1}{T_{ref}}\right)\right] \cdot t^{-\frac{1}{n}} \qquad \text{Equation 13}$$

$$t = \left(\frac{S}{C \cdot exp\left[\left(\frac{V + \frac{H}{n}}{R}\right)\left(\frac{1}{T} - \frac{1}{T_{ref}}\right)\right]} \right)^{-n}$$

Equation 14

Where:

t = test time at test temperature, [h]

S = test stress at test temperature, [psi]

T_{ref} = reference temperature, [K]

T = test temperature, [K]

C = stress that will result in a ductile failure in one (1) hour, [psi/h]

n = characteristic creep rate exponent, [unitless]

V = vertical activation energy, [cal/(mol*K)] or [J/(mol*K)]

H = horizontal activation energy, [cal/(mol*K)] or [J/(mol*K)]

R = gas constant, 1.9872036 [cal/(mol*K)] or 8.3144598 [J/(mol*K)]

From Equation 14, the calculation of a time-based performance reduction factor is derived as follows with Equation 15, to Equation 16, to Equation 17:

$$t = \left(\frac{S}{\boldsymbol{f_s} \cdot C \cdot exp\left[\left(\frac{V + \frac{H}{n}}{R}\right)\left(\frac{1}{T} - \frac{1}{T_{ref}}\right)\right]} \right)^{-n}$$

Equation 15

$$\boldsymbol{f_t} \cdot t = \left(\frac{\mathbf{1}}{\boldsymbol{f_s}}\right)^{-n} \left(\frac{S}{C \cdot exp\left[\left(\frac{V + \frac{H}{n}}{R}\right)\left(\frac{1}{T} - \frac{1}{T_{ref}}\right)\right]} \right)^{-n}$$

Equation 16

$$f_t = \left(\frac{1}{f_s}\right)^{-n} = f_s{}^n$$

Equation 17

Where:

f_s = stress-based performance reduction factor

f_t = time-based performance reduction factor

APPENDIX 3 - Excerpt from Reference [90]

Material Property Uncertainty

Variance in material properties is a significant source of uncertainties and material properties are not always known. This fact is recognized by ASME FFS-1[5] and BS 7910[6] and, therefore, for example, Level 2 assessments offer generic Failure Assessment Lines (FAL) when no stress-strain data is available for a material. Figure 13 provides as an illustration of how failure assessment lines developed from actual stress-strain curves can vary from the generic FAL curves used in Level 2 assessments. As can be seen in Figure 13, depending on the specific steel, there are regions where the generic FALs are conservative and other regions where they are non-conservative. In the range from Lr=0 to Lr=1, the FAL curves of the vintage materials overlap each other – this is because they have the same elastic behavior up to their respective yield stresses (defined as Lr=1 on the FAD). Beyond Lr=1, the materials diverge, illustrating the variance in material behavior in the plastic deformation regions of the curves. The FALs terminate at the point corresponding to the UTS of the respective material; the scatter of the termination lines further illustrates the material variance.
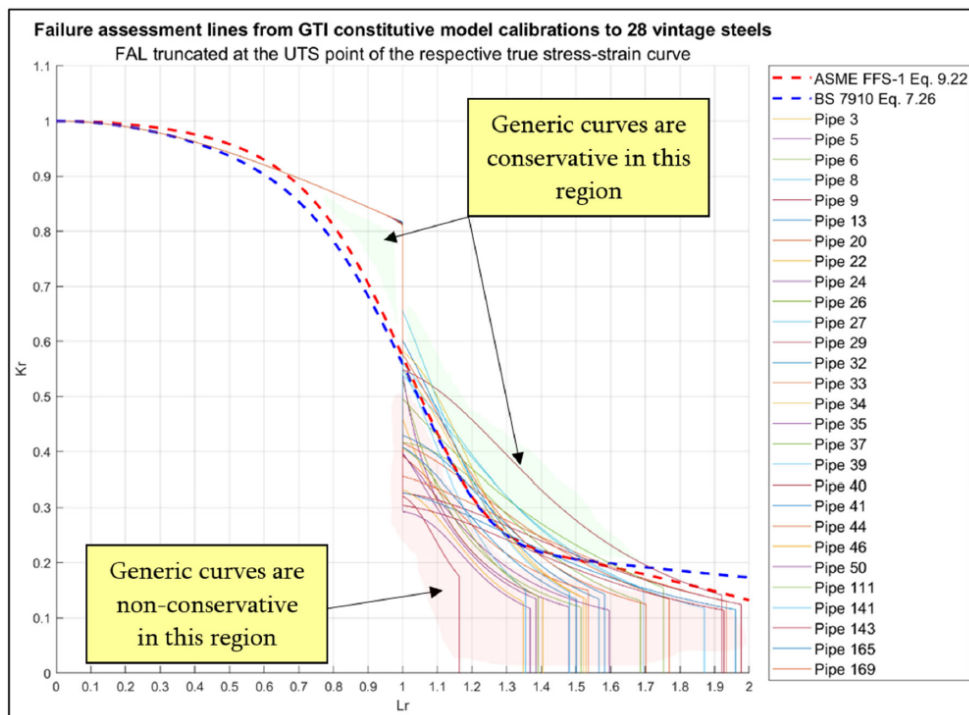

Figure 13. FAD with failure assesment lines of 28 vintage steels and two generic FAL curves

The FAD is very simple and elegant in the way that it portrays the limit state of the pipeline being assessed. We need to calculate two parameters: K_r, and L_r for each defect configuration

in a defect specific calculation such as the solution for a semi-elliptical internal axial defect shown in Figure 14 (RSCCLE1). This solution calculates Ki and σ_{ref} that are needed to determine the assessment point for a given geometry and loading. There are clearly many uncertainties that can be introduced into the result and we also need to have a good understanding of the underlying uncertainties inherent in the FFS standard [4].
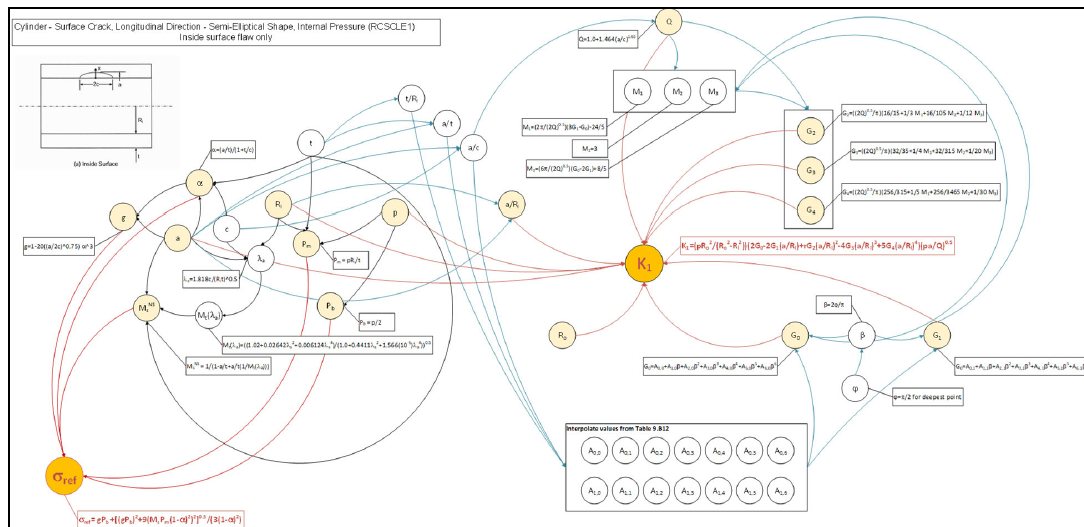
Figure 14. Flow of RSCCLE1 calculation

Assessing these uncertainties would be a massive undertaking and is well beyond the scope of this project. We accept the FFS calculations as correct and address the uncertainties in material properties in determining the reference Failure Assessment Line (FAL). Having a true-stress/true-strain curve for a specific material gives us the most accurate FAL possible. The true-stress/true-strain curve also gives us the yield stress needed in the RCSCLE1 calculation of L_r:

$$L_r = \frac{\sigma_{ref}}{\sigma_{yield}}$$

Kr is defined as:

$$K_r = \frac{K_I}{K_{mat}}$$

We need an estimate of the fracture toughness of the material K_{mat}. There are standardized conversion for calculating K_{mat} from full-size Charpy toughness such as the Welding Research Council WRc 265 conversion used in this report [7] that is in close agreement with the conversion reported by Antaki [5]. To address this need GTI developed a model for predicting the upper-shelf, full-size Charpy toughness from the true-stress/true-strain curves for each material. The model is discussed in the following section.

156

Prediction of Full Size Charpy Upper Shelf Energy from True Stress Strain Data

A preliminary model for predicting upper shelf Charpy energy based on 12 sets of material data showed promise. We enhanced the model by including all 28 sets of fully characterized stress-strain data we developed in conjunction with USDOT PHMSA Project 693JK31810003, "Validating Non-Destructive Tools for Surface to Bulk Correlations of Yield Strength, Toughness, and Chemistry" that will be published in 2021 [8].

In this project, the general approach to developing models for assessment of flaws, has been to rely heavily on detailed measurement of material properties and then to properly fuse the information gained into the various models used for prediction. The approach is graphically summarized in Figure 15.
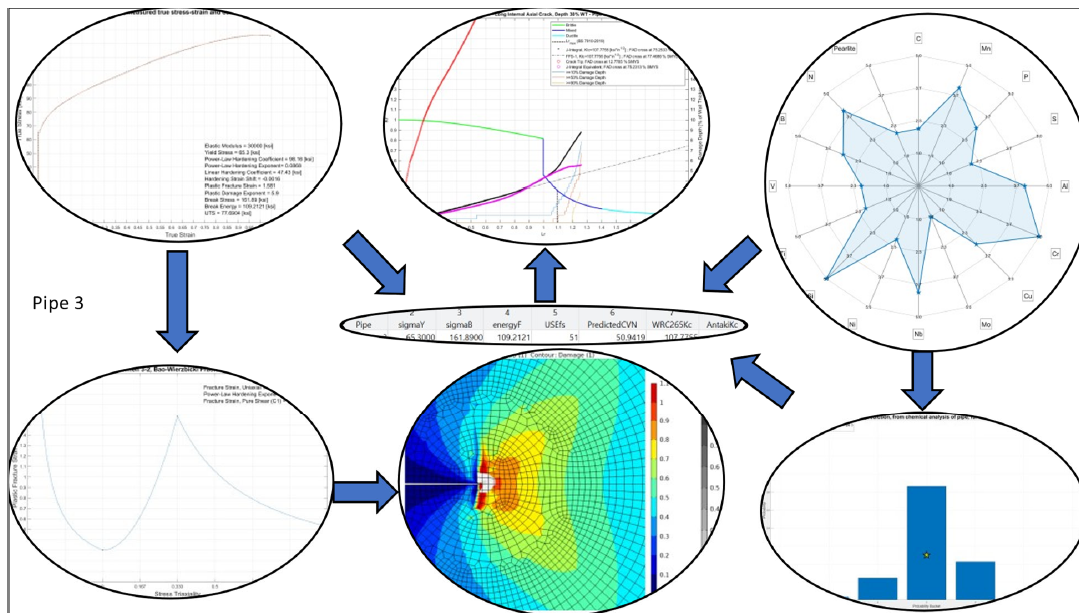
Figure 15. Data fusion approach applied in model development.

We start with a carefully developed true-stress/true-strain curve that is combined with models for damage propagation in ductile materials to develop FEM models as described above. The true-stress/true-strain curve information can be combined with steel chemistry to produce an approximation of the upper shelf Charpy energy for the steel in question. The red stars in Figure 16 show that the 28 pipes used in this analysis capture the full range of Yield Strength and Charpy Toughness measured in [8].

Figure 17 shows the remarkably good prediction obtained from the true-stress/true-strain curve information.

Figure 16. Spread of Yield Strength and Upper Shelf Charpy Toughness across the 28 pipes used in model development.

Figure 17. Upper Shelf Charpy Prediction

gti

Figure 18 shows how adding an error correction component developed from the detailed chemistry information improves the prediction slightly.
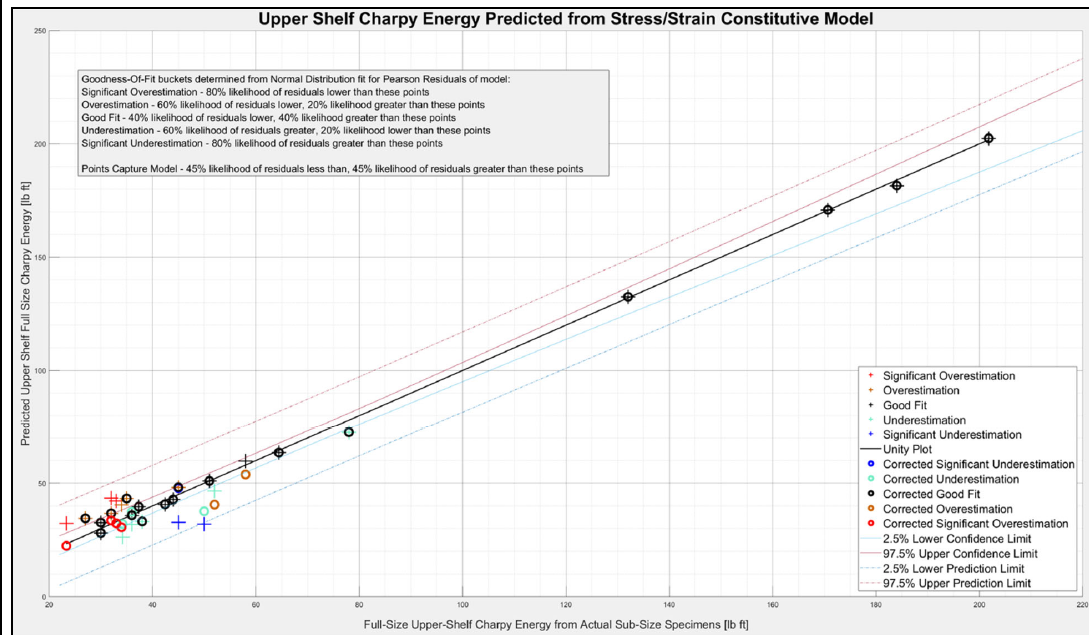
Figure 18. Upper Shelf Charpy Prediction with error correction from steel chemistry

The motivation for developing this upper shelf Charpy prediction model is to obtain the material K1c needed for a level 2 fitness for service evaluation directly from a true-stress/true-strain cu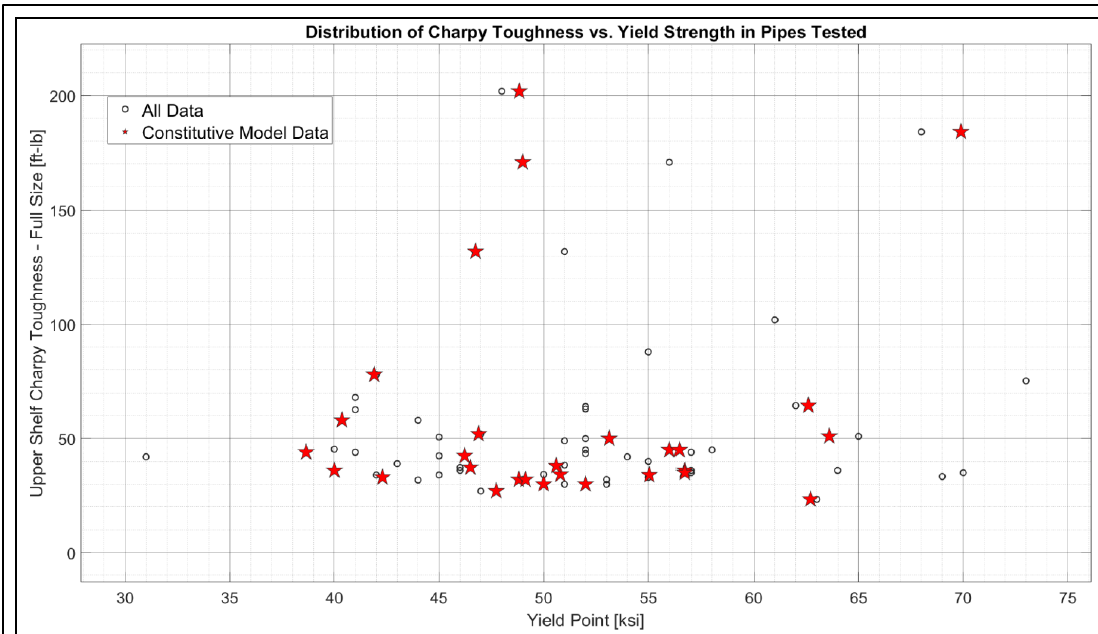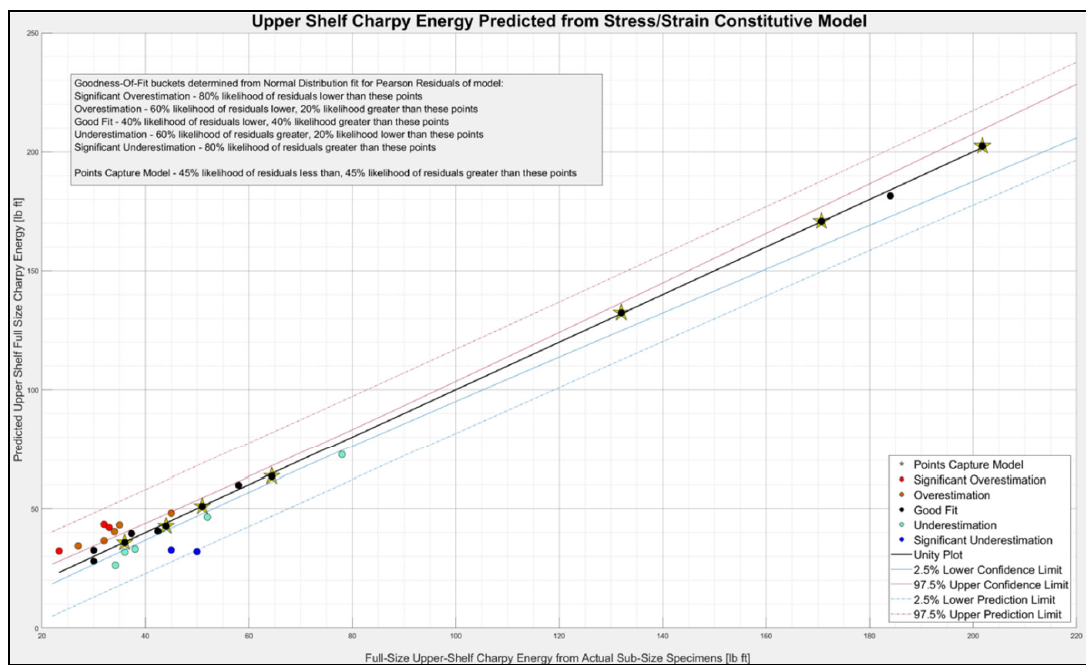rve. In the following section we apply the material data developed and listed in the Material Information Appendix to a total of 3780 level 2 assessments: 145 geometries across 28 materials, to examine uncertainties related to material properties.

Application to Minimum Yield Stress Boundaries

USDOT PHMSA Project 693JK31910001POTA "Review the Intent and Safety Impact of Hoop Stress and Percentage of Specified Minimum Yield Stress Boundaries on Natural Gas Transmission and Distribution Pipelines"[1] has provided a convenient framework for uncertainty analysis on the models used in this project. Aligning our analysis with the final report for Project 693JK31910001POTA will make it easier for reviewers of this body of work due to the use of a coherent set of metrics across projects.

GTI FEM modeling approach vs. API 579-1/ASME FFS-1 models

GTI adopted a Continuum Damage Modeling (CDM) formulation for the Finite Element Method (FEM) analyses to avoid the Linear Elastic Fracture Mechanics (LEFM) assumptions underpinning the currently accepted standard for Fitness for Service (FFS) calculations. The

CDM analyses and results are discussed in detail in the section Structural FEM Study and Appendix 1 through Appendix 14 below. A large assortment of defect types including interactions between cracks, corrosion, and dents were explored.

The CDM results for axial defects were rigorously compared to the API 579-1 results and were found to be conservative (Figure 19) for materials with greater plastic strain capacity due to the inherent non-linearity of the CDM analyses that capture the onset of damage propagation through the wall (see Appendix 8 for explanation).
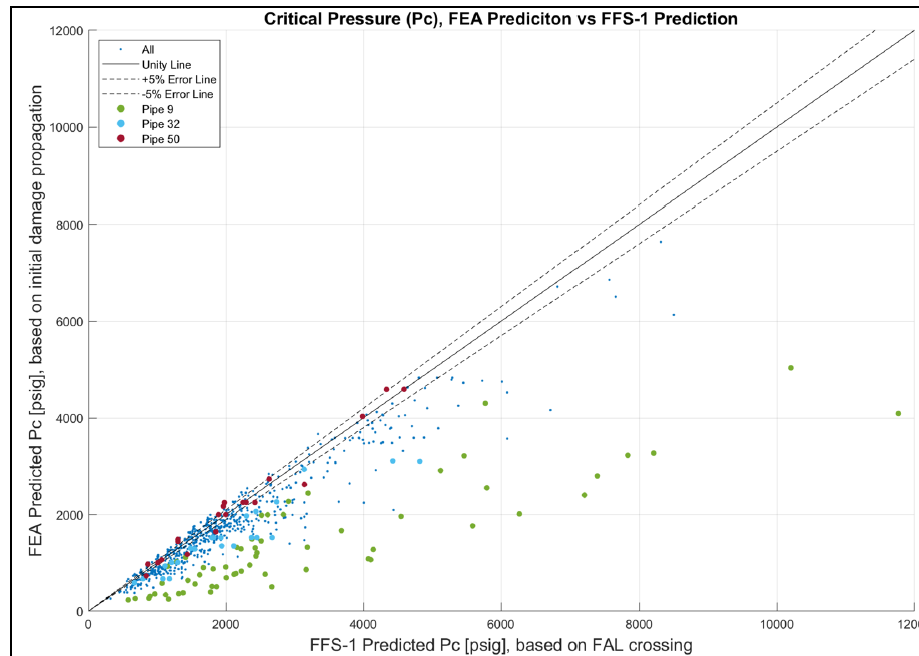
Figure 19. Comparison of GTI CDM FEM results to FFS-1

Considerable effort was put into developing a surrogate model that would capture the output of thousands of CDM analysis (see section: Step 7: Surrogate Model Development below). The motivation for developing a surrogate model is to simply the process of evaluating uncertainties using a simpler to implement closed-form solution for predicting critical pressure for the large range of geometry and material inputs that can occur in the field, Figure 20.

While the models could very accurately replicate the actual design points, and in doing so provide useful information on the value of better material knowledge in the assessment process, the surrogate models are useless between the design points as shown in Figure 21 where it is obvious that there is no correlation as opposed to what is seen in Figure 19 where the correlation is good and the deviations are explained by non-linear plastic damage propagation as opposed to LEFM considerations.

160

Figure 20. Schema for surrogate model development

Figure 21. Comparison of surrogate model results to FFS-1

Sensitivity analysis approach

Recognizing that a useful surrogate model for the more accurate CDM FEM models was not achievable, it was decided to use the Signal™ Fitness-For-Service (FFS) software with the GTI developed true-stress/true-strain curves, the upper shelf full-size Charpy e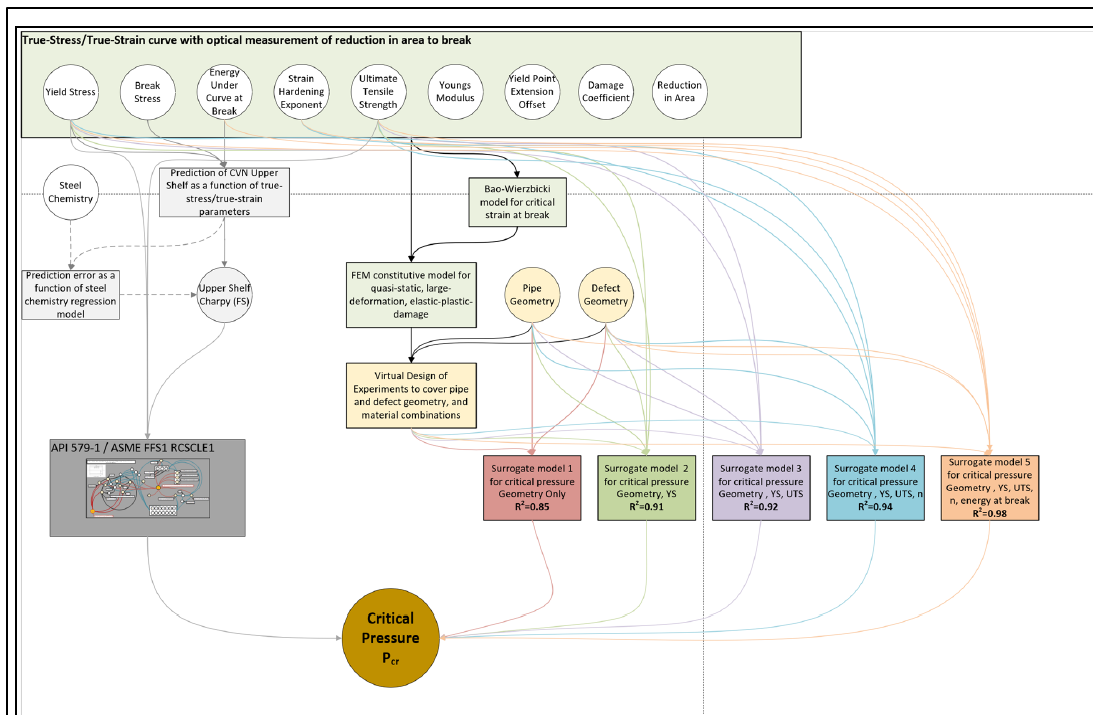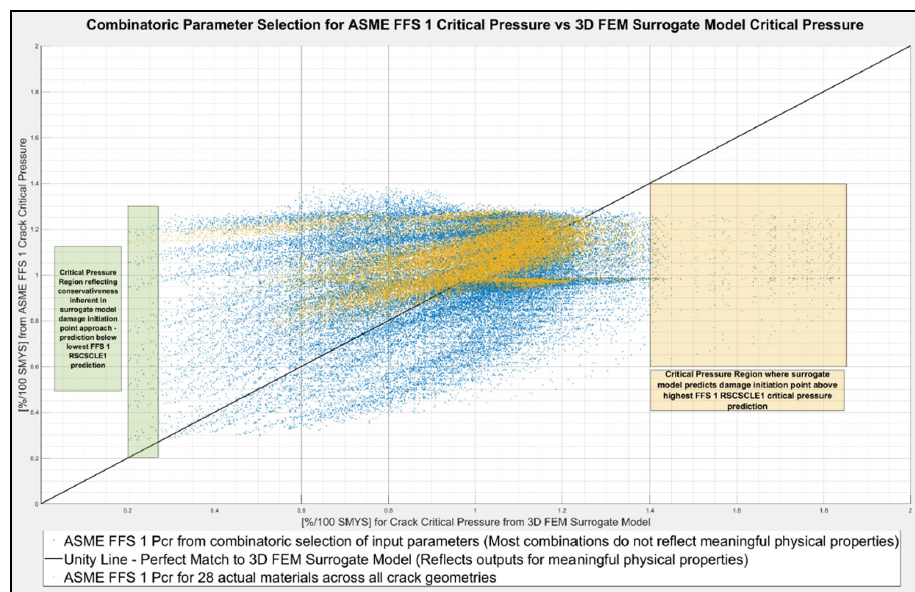nergy predictions, and the K_{mat} conversion described above to run a sensitivity study to assess the impact of material properties and geometry on the prediction of critical pressure. The full set of material properties for all 28 materials are listed in Appendix : Material Information below. Table 2 lists the geometry inputs that were investigated across all 28 materials. The information gained from the two modeling approaches is very similar as they both capture the governing physics of cracks propagating through the wall of the pipe.

Table 2. Input parameters for FFS model

	Value 1	Value 2	Value 3	Value 4	Value 5
Pipe OD [inch]	16	24	32		
Wall Thickness [inch]	0.25	0.375	0.5		
Crack Depth [% wall]	0.1	0.4	0.7		
Normalized Crack Length: L/sqrt(r*t) [1]	0.2475	0.495	1	3	6

The full test matrix comprised 145 geometries reflecting all possible combinations of OD, wall thickness, and crack length evaluated across 28 materials resulting in 3780 discreet analyses.

The calculated parameter is critical pressure, the internal pressure for a pipe of even combination of OD, wall thickness, crack depth, and crack length where the assessment point falls on the FAL (Figure 11).

Figure 22 is a plot of the critical pressures as a percent SMYS for each of the 145 geometries. We can immediately see that pipe OD has minimal impact of the result, justifying us in choosing a single OD to investigate sensitivities, Figure 23. All 3780 results are fully tabulated in Appendix - "Tabulated output of FFS calculations across materials, pipe geometries and defect geometries".
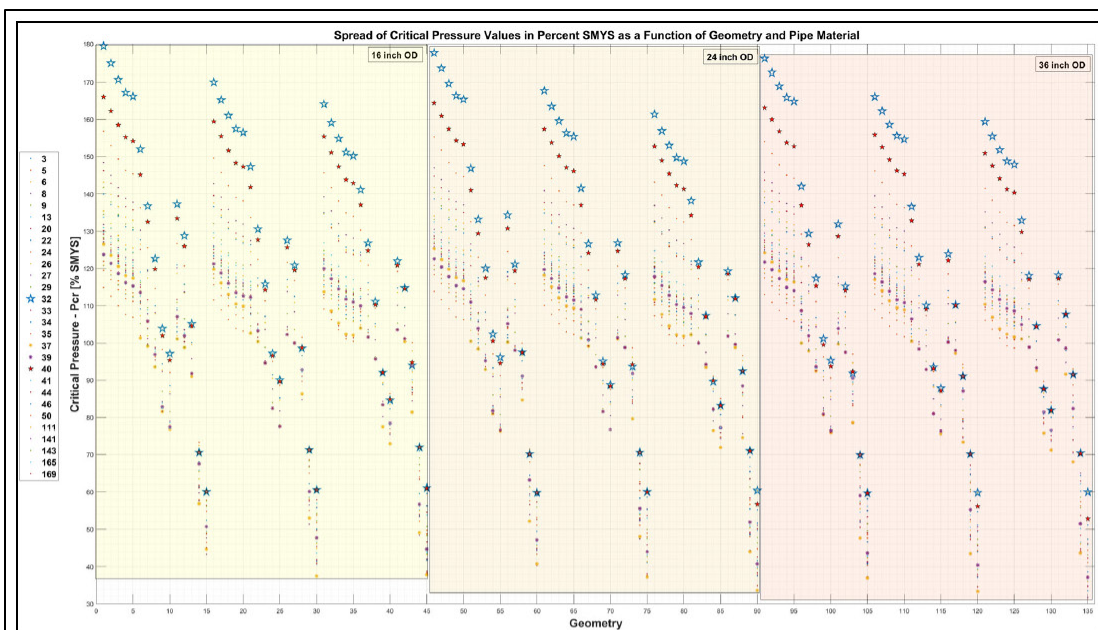
Figure 22. Output of FFS critical pressure calculations across 3780 material/geometry combinations
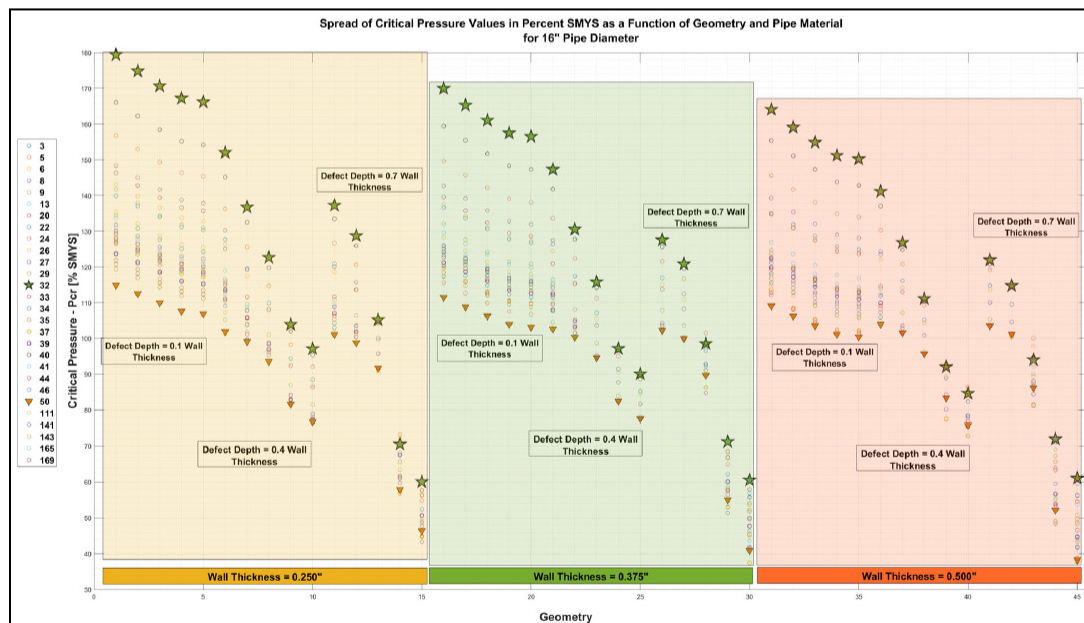

Figure 23. Zoom in to 16" OD from Figure 22.

Figure 22 and Figure 23 incorporate three levels of normalization that result in a meaningful plot:

1. Critical assessment pressure output normalized to the yield strength of each material and presented as %SMYS. This normalization allows the results across materials to be directly compared to a common reference point – 100% SMYS, where the internal pressure in the pipe generates a hoop stress that equals the material yield stress.
2. The defect depth is normalized to percent of wall thickness, and
3. The defect length is normalized to the square root of the multiple of pipe outside radius and wall thickness.

Without these normalizations we would not discern any meaningful relationships between the input parameters and the output.

With these normalizations we can directly see the contributions of material, crack depth, and crack length to assessment uncertainty.

We can also see that the sensitivity of critical pressure to these parameters is not constant across the ranges. This brings us back to Figure 4 and Figure 6 where we emphasize that proper definition of the context i.e., the combination of parameters in the assessment is essential to properly quantify uncertainty.

In Table 3 and Table 4 we examine the influence of crack depth and crack length on critical pressure respectively. In each table we quantify the influence of material on the output. The column headers and their explanations are described below:

D – Pipe outside diameter [inch],
t – Pipe wall thickness [inch],
anorm – Normalized crack depth [% wall thickness],
C – Normalized crack length (L/sqrt(R*t) where L is the full crack length,
Low Pc – The lowest critical pressure per geometry (combination of D, t, anorm, and C),
High Pc – The highest critical pressure per geometry (combination of D, t, anorm, and C),
Mat. Ratio – The material-based ratio – the Highest Pc divided by the lowest Pc per geometry that is always a function of material,
Low Pipe – The pipe (material) that produced the highest Pc,
High Pipe – The pipe (material) that produced the lowest Pc,
Low Ratio – The ratio across the low Pc values for a set of geometric combinations where either crack depth or crack length is varied while the other geometric parameters are held constant,
High Ratio – The ratio across the high Pc values for a set of geometric combinations where either crack depth or crack length is varied while the other geometric parameters are held constant.

gti.

	D	t	anorm	C	Low Pc	High Pc	Mat. Ratio	Low Pipe	High Pipe	Low Ratio	High Ratio
							Table 3. Effect of Crack Depth				
C=0.2475	16	0.25	10	0.2475	115	179	**1.56**	50	32		
	16	0.25	40	0.2475	101	152	**1.50**	37	32	1.14	1.31
	16	0.25	70	0.2475	101	137	**1.36**	37	32		
	16	0.375	10	0.2475	111	170	**1.53**	50	32		
	16	0.375	40	0.2475	103	147	**1.43**	143	32	1.09	1.34
	16	0.375	70	0.2475	102	127	**1.25**	143	32		
	16	0.5	10	0.2475	109	164	**1.50**	50	32		
	16	0.5	40	0.2475	104	141	**1.36**	143	32	1.05	1.33
	16	0.5	70	0.2475	104	123	**1.18**	143	32		
C=0.495	16	0.25	10	0.495	112	175	**1.56**	50	32		
	16	0.25	40	0.495	99	137	**1.38**	143	32	1.13	1.36
	16	0.25	70	0.495	99	129	**1.30**	37	32		
	16	0.375	10	0.495	109	168	**1.54**	50	32		
	16	0.375	40	0.495	100	131	**1.31**	143	32	1.09	1.39
	16	0.375	70	0.495	100	121	**1.21**	111	32		
	16	0.5	10	0.495	106	159	**1.50**	50	32		
	16	0.5	40	0.495	102	127	**1.25**	109	32	1.06	1.38
	16	0.5	70	0.495	100	115	**1.15**	37	32		
C=1	16	0.25	10	1	110	171	**1.55**	50	32		
	16	0.25	40	1	94	123	**1.31**	143	32	1.21	1.63
	16	0.25	70	1	91	105	**1.15**	37	32		
	16	0.375	10	1	106	161	**1.52**	50	32		
	16	0.375	40	1	95	116	**1.22**	169	32	1.25	1.58
	16	0.375	70	1	85	102	**1.20**	27	5		
	16	0.5	10	1	104	155	**1.49**	50	32		
	16	0.5	40	1	81	104	**1.28**	169	32	1.28	1.55
	16	0.5	70	1	81	100	**1.23**	27	5		

	D	t	anorm	C	Low Pc	High Pc	Mat. Ratio	Low Pipe	High Pipe	Low Ratio	High Ratio
C=3	16	0.25	10	3	107	167	**1.56**	50	32		
	16	0.25	40	3	81	104	**1.28**	169	32	1.91	2.29
	16	0.25	70	3	56	73	**1.30**	37	32		
	16	0.375	10	3	104	157	**1.51**	50	32		
	16	0.375	40	3	82	97	**1.18**	169	32	2.04	2.18
	16	0.375	70	3	51	72	**1.41**	27	5		
	16	0.5	10	3	101	151	**1.50**	50	32		
	16	0.5	40	3	78	93	**1.19**	37	5	2.10	2.10
	16	0.5	70	3	48	72	**1.50**	27	9		
C=6	16	0.25	10	6	106	166	**1.57**	50	32		
	16	0.25	40	6	77	97	**1.26**	169	32	2.47	2.77
	16	0.25	70	6	43	60	**1.40**	27	6		
	16	0.375	10	6	103	157	**1.52**	50	32		
	16	0.375	40	6	78	90	**1.15**	169	32	2.78	2.62
	16	0.375	70	6	37	60	**1.62**	37	9		
	16	0.5	10	6	100	150	**1.50**	50	32		
	16	0.5	40	6	73	86	**1.18**	37	5	2.63	2.46
	16	0.5	70	6	38	61	**1.61**	37	9		

	D	t	anorm	C	Low Pc	High Pc	Mat. Ratio	Low Pipe	High Pipe	Low Ratio	High Ratio
	16	0.25	10	0.2475	115	179	1.56	50	32		
	16	0.25	10	0.495	112	175	1.56	50	32		
	16	0.25	10	1	110	171	1.55	50	32		
	16	0.25	10	3	107	167	1.56	50	32	1.08	1.08
	16	0.25	10	6	106	166	1.57	50	32		
	16	0.375	10	0.2475	111	170	1.53	50	32		
	16	0.375	10	0.495	109	168	1.54	50	32		
a = 10	16	0.375	10	1	106	161	1.52	50	32		
	16	0.375	10	3	104	157	1.51	50	32	1.08	1.08
	16	0.375	10	6	103	157	1.52	50	32		
	16	0.5	10	0.2475	109	164	1.50	50	32		
	16	0.5	10	0.495	106	159	1.50	50	32		
	16	0.5	10	1	104	155	1.49	50	32		
	16	0.5	10	3	101	151	1.50	50	32	1.09	1.09
	16	0.5	10	6	100	150	1.50	50	32		
	16	0.25	40	0.2475	101	152	1.50	37	32		
	16	0.25	40	0.495	99	137	1.38	143	32		
	16	0.25	40	1	94	123	1.31	143	32		
	16	0.25	40	3	81	104	1.28	169	32	1.31	1.57
	16	0.25	40	6	77	97	1.26	169	32		
	16	0.375	40	0.2475	103	147	1.43	143	32		
	16	0.375	40	0.495	100	131	1.31	143	32		
a = 40	16	0.375	40	1	95	116	1.22	169	32		
	16	0.375	40	3	82	97	1.18	169	32	1.32	1.63
	16	0.375	40	6	78	90	1.15	169	32		
	16	0.5	40	0.2475	104	141	1.36	143	32		
	16	0.5	40	0.495	102	127	1.25	109	32		
	16	0.5	40	1	81	104	1.28	169	32		
	16	0.5	40	3	78	93	1.19	37	5	1.42	1.64
	16	0.5	40	6	73	86	1.18	37	5		

Table 4. Effect of Crack Length

	D	t	anorm	C	Low Pc	High Pc	Mat. Ratio	Low Pipe	High Pipe	Low Ratio	High Ratio
a = 70	16	0.25	70	0.2475	101	137	**1.36**	37	32	2.35	2.28
	16	0.25	70	0.495	99	129	**1.30**	37	32		
	16	0.25	70	1	91	105	**1.15**	37	32		
	16	0.25	70	3	56	73	**1.30**	37	32		
	16	0.25	70	6	43	60	**1.40**	27	6		
	16	0.375	70	0.2475	102	127	**1.25**	143	32	2.76	2.12
	16	0.375	70	0.495	100	121	**1.21**	111	32		
	16	0.375	70	1	85	102	**1.20**	27	5		
	16	0.375	70	3	51	72	**1.41**	27	5		
	16	0.375	70	6	37	60	**1.62**	37	9		
	16	0.5	70	0.2475	104	123	**1.18**	143	32	2.74	2.02
	16	0.5	70	0.495	100	115	**1.15**	37	32		
	16	0.5	70	1	81	100	**1.23**	27	5		
	16	0.5	70	3	48	72	**1.50**	27	9		
	16	0.5	70	6	38	61	**1.61**	37	9		

From the above tabulation we can see that material driven variance dominates up to normalized crack lengths C=1 for all crack depths.

For normalized crack lengths C>1, crack depth becomes critical.

For normalized crack depth anorm = 0.7, crack length is critical.

Hydrotest equivalent

A useful addition to Figure 23 is to add horizontal lines at various levels of %SMYS as shown in Figure 24. The lines added to Figure 24 reflect a maximum operating envelope of 60% SMYS and lines at 90% SMYS and 120% SMYS to reflect 150% and 200% pressure spikes.

Minimum defect resolution requirements

What is immediately get from these added horizontal lines is:

1. At 60% SMYS we are concerned with defects penetrating 70% of the wall with a normalized length of C=3 for the lowest performing materials.
2. At a normalized defect length C=6 we will be concerned about all materials with a 70% wall defect as the critical pressure for these defects ranges from about 35% SMYS to 60% SMYS.

3. To use NDE methods as an equivalent to a 150% SMYS hydrotest we would have to be able to resolve defects down to 40% wall depth and a normalized crack length less than or equal to 3.

4. For a 200% SMYS equivalent we would have to resolve defects down to 10% wall and C=0.2475 for the lower performing materials.

5. Alternatively, the chart defines which defect sizes per material will be triggered by a pressure spike of known magnitude.
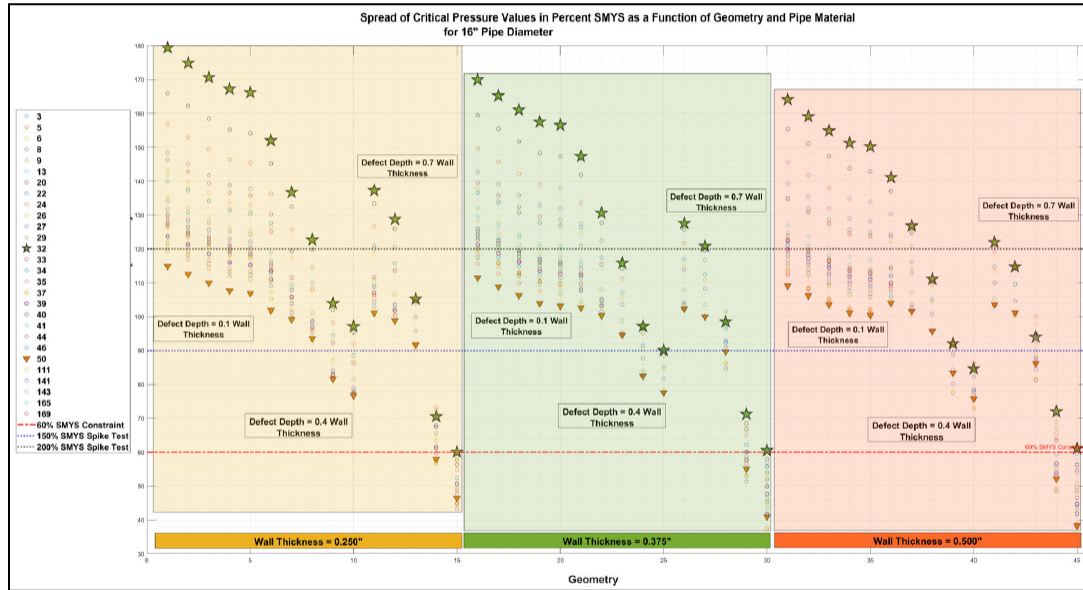

Figure 24. Hydrotest lines added to Figure 23

Caveat

While this method of determining the NDE resolution needed for a hydrotest equivalent is conceptually sound, it does not consider several additional aspects that need to be considered such as leak before rupture and interacting threats that will be discussed below.

(END OF ATTACHMENT A1)